

Electronic Thesis and Dissertation Repository

3-14-2010 12:00 AM

Catalytic Steam Gasification of Biomass Surrogates: A Thermodynamic and Kinetic Approach

Enrique Salaices, *The University of Western Ontario*

Supervisor: Dr. Hugo deLasa, *The University of Western Ontario*

A thesis submitted in partial fulfillment of the requirements for the Doctor of Philosophy degree in Chemical and Biochemical Engineering

© Enrique Salaices 2010

Follow this and additional works at: <https://ir.lib.uwo.ca/etd>

 Part of the [Catalysis and Reaction Engineering Commons](#)

Recommended Citation

Salaices, Enrique, "Catalytic Steam Gasification of Biomass Surrogates: A Thermodynamic and Kinetic Approach" (2010). *Electronic Thesis and Dissertation Repository*. 51.
<https://ir.lib.uwo.ca/etd/51>

This Dissertation/Thesis is brought to you for free and open access by Scholarship@Western. It has been accepted for inclusion in Electronic Thesis and Dissertation Repository by an authorized administrator of Scholarship@Western. For more information, please contact wlsadmin@uwo.ca.

Title – CATALYTIC STEAM GASIFICATION OF BIOMASS SURROGATES: A
THERMODYNAMIC AND KINETIC APPROACH.

(Spine title: Steam Gasification of Biomass Surrogates over a Ni/ α -alumina Catalyst)

(Thesis format: Monograph)

by

Enrique Salaices

Graduate Program in Chemical and Biochemical Engineering

A thesis submitted in partial fulfillment
of the requirements for the degree of
Doctor of Philosophy

The School of Graduate and Postdoctoral Studies
The University of Western Ontario
London, Ontario, Canada

© Enrique Salaices 2010

CERTIFICATE OF EXAMINATION

Supervisor

Examiners

Dr. Hugo de Lasa

Dr. Ajay Kumar Ray

Dr. Amarjeet Bassi

Dr. Ronald Martin

Dr. Nicolas Abatzoglou

The thesis by

Enrique Salaices

entitled:

**CATALYTIC STEAM GASIFICATION OF BIOMASS SURROGATES:
A THERMODYNAMIC AND KINETIC APPROACH**

is accepted in partial fulfillment of the
requirements for the degree of
Doctor of Philosophy

Date

Chair of the Thesis Examination Board

Abstract

Gasification of biomass is an environmentally important technology that offers an alternative to the direct use of fossil fuel energy. Steam gasification is getting increased attention as a potential source of renewable energy since it produces a gaseous fuel suitable for industrial applications in highly efficiently power/heat energy production, transport fuel, and as a feedstock for chemical synthesis. Furthermore, catalytic steam gasification has other advantages hence (i) it produces a gas with higher heating value; (ii) it reduces the diluting effect of N_2 from air; (iii) it eliminates the need of cleaning, upgrading and/or conditioning the product gas for certain applications; and (iv) it eliminates the need for an expensive oxygen plant when both air and oxygen are used as gasification mediums. Catalytic steam gasification of biomass in fluidized beds is a promising approach given its rapid biomass heating, its effective heat and mass transfer between reacting phases, and its uniform reaction temperature. Moreover, fluidized beds tolerate wide variations in fuel quality as well as broad particle-size distributions.

However, catalytic steam gasification is a more complex process resulting from: (i) the heat necessary to sustain the process is directly supplied by the partial combustion of the feedstock during the process, as it happens when air or oxygen is used, (ii) the rapid catalyst deactivation that occurs due to heavy coking, and (iii) tar formed during the process.

This Ph.D. dissertation reports a research study on the steam gasification of biomass over a Ni/ α -alumina catalyst using model compounds. This research allows elucidating the factors inherent to this process such as thermodynamic restrictions and mechanistic reaction steps. The ultimate aim is to establish the chemical reaction engineering tools that will allow the

design and operation of large scale fluidized bed units for biomass steam catalytic gasification.

On this basis, a thermodynamic equilibrium model based on evaluations involving C, H and O elemental balances and various product species (up to C₆ hydrocarbons) was developed. This model establishes the effect of biomass composition, temperature, and steam on the various gas product molar fractions. Based on the proposed equilibrium model and using glucose, as a model biomass species, an optimum gasification temperature close to 800°C and a steam/biomass ratio between 0.5 and 0.7 g/g is established.

Experiments were carried out in the CREC fluidized Riser Simulator under gasification conditions using a) glucose as a model compound for the cellulose contained in biomass, and b) 2-methoxy-4-methoxyphenol as a model compound for the lignin that is found in biomass. The experimental data show that for reaction times longer than 30 seconds, chemical species are essentially equilibrated and that the proposed thermodynamic model does provide an adequate description of various product fractions. Data obtained also demonstrate the shortcomings of equilibrium models for gasifiers with reaction times shorter than 10 seconds and the need for non-equilibrium models to describe gasifier performance at such conditions.

Taking the above into consideration, a reaction network and a kinetic model for biomass catalytic steam gasification were proposed. This kinetic model was developed using a coherent reaction engineering approach where reaction rates for various species are the result of the algebraic addition of the dominant reactions. It is also demonstrated that using an experimental-modeling procedure, where intrinsic kinetic parameters and adsorption constants are decoupled in their evaluation in the CREC Riser Simulator eliminates overparametrization with successfully parameter correlation. Numerical regression of the

experimental data leads to kinetic parameters with narrow spans suggesting that the proposed kinetic model satisfactorily describe the catalytic conversion of glucose and 2-methoxy-4-methyphenol under gasification conditions.

Keywords

Steam Gasification, Biomass, Ni/ α -Al₂O₃ catalyst, Tars, Thermodynamic equilibrium, Kinetics.

Acknowledgments

I would like to thank all people who made this doctoral study possible.

I especially want to express my sincere gratitude to my supervisor, Dr. Hugo de Lasa, whose expertise, understanding, and guidance added considerably to my graduate experience at The University of Western Ontario. His hard work and enthusiasm in research have motivated me.

I recognize that this research would not have been possible without the financial assistance of the National Council for Science and Technology (CONACyT - Mexico) and Electrical Power Research Institute (IIE – Mexico). I express my gratitude to those agencies that allowed me to pursue my Ph.D. studies

I am indebted to my fiends and student colleagues for providing a stimulating and fun environment in which to learn and grow. I am especially grateful to Randy, Valery Georges, Lissette Jaimes. Aaron Ortiz, Jesús Moreira, Juan Manuel García, Salvador Escobedo, Yira Aponte and Gabriela Navarro. A very special thanks goes out to Cassandra Derks for her help in the tar experiments and manuscript preparation.

I am grateful to Joanna Bloom, the graduate affairs coordinator, for helping the department to run smoothly and for assisting me in many different ways.

My deepest gratitude goes to my family for their unflagging love and support throughout my life; this dissertation would be simply impossible without them. Special thanks to my brother, Miguel Salaices, who has been a key part of my life and M^a Santos Rinconi, simply for believe in me.

Lastly, and most importantly, I wish to thank my beautiful wife, Tina Rinconi, not a single word can fully describe her patience and love to me; my son and daughter (Sebastian and Valentina), just for being the reason of my life; and my mom M^a del Carmen Arredondo (†), who truly believed that I can be whoever I want to be. To them I dedicate this thesis.

Table of Contents

CERTIFICATE OF EXAMINATION	ii
Abstract	iii
Acknowledgments	vi
Table of Contents	vii
List of Tables	xii
List of Figures	xiv
List of Appendices	xxi
List of Abbreviations, Symbols, Nomenclature	xxii
Chapter 1 Introduction	1
1 Introduction	1
Chapter 2 Scope	6
2 Scope of the Research	6
Chapter 3 Literature Review	8
3 Literature Review	8
3.1 Introduction	8
3.2 Design of Gasifiers	11
3.2.1 Fixed bed gasification	11
3.2.2 Fluidized Bed Gasification	14
3.2.3 Advantages/disadvantages of the different gasifying reactor	18
3.3 Gasification Conditions	19
3.3.1 Temperature	19
3.3.2 Pressure	20
3.3.3 Gasifying Medium	20
3.3.4 Equivalence Ratio (ER)	21

3.3.5	Residence Time.....	22
3.3.6	Conclusions and Recommendations for Design of Gasifiers	24
3.4	Catalysts for Steam Gasification of Biomass.....	24
3.4.1	Dolomite, Olivine and Alkali metal Based Catalysts	25
3.4.2	Nickel Based Catalysts	27
3.4.3	Conclusion and Recommendations for Catalysts	31
3.5	Thermodynamic Studies of Steam Gasification of Biomass	31
3.5.1	Equilibrium Model for Biomass Gasification.....	31
3.5.2	Improved Thermodynamic Approach.....	34
3.5.3	Conclusions and Recommendations for Thermodynamic Studies	34
3.6	Kinetic Studies of Catalytic Steam Gasification of Biomass.....	35
3.6.1	Characteristic Time Analysis.....	35
3.6.2	Models at Particle Scale.....	36
3.6.3	Kinetic Models of Pyrolysis.....	38
3.6.4	Model for Biomass Gasification in a Bubbling Fluidized Bed Reactor ...	38
3.6.5	Conclusions and Recommendations the Present PhD study.....	39
Chapter 4	Experimental Methods	40
4	Experimental Methods	40
4.1	Introduction.....	40
4.2	Catalyst and Materials.....	42
4.3	Reaction System.....	43
4.4	Experimental Procedure.....	48
4.5	Pressure Profiles, Varying S/B Ratios and Varying Contact Times.....	49
4.6	Analytical System: Identification and Quantification of Products	51
4.7	Conclusions.....	55
Chapter 5	Ni/ α -alumina Catalyst.....	56

5	Preparation and Characterization	56
5.1	Ni/ α -alumina Catalyst Preparation	56
5.1.1	Fluidizable Catalyst	56
5.1.2	Catalyst Materials	57
5.1.3	Catalyst Preparation	57
5.2	Catalyst Characterization	60
5.2.1	Particle Size Distribution and Particle Apparent Density	61
5.2.2	X-Ray Fluorescence (XRF)	63
5.2.3	NH ₃ Temperature Programmed Desorption	64
5.2.4	Temperature Programmed Reduction (TPR)	65
5.2.5	Temperature Programmed Oxidation (TPO)	67
5.2.6	Pulse Chemisorption	68
5.2.7	Catalyst Surface Area	70
5.2.8	Conclusions	71
	Chapter 6 Experimental Results	73
6	Experimental Results	73
6.1	Introduction	73
6.2	Glucose - Product Gas Partial Pressures Distribution	74
6.3	2-methoxy-4-methylphenol - Product Gas Partial Pressures Distribution	79
6.4	Conclusions	84
	Chapter 7 Tars from Biomass Gasification	85
7	Introduction	85
7.1	Tar Composition and Maturation	86
7.2	Reduction of Tars	92
7.2.1	Thermal	92
7.2.2	Steam	92

7.2.3	Partial Oxidation	92
7.2.4	The Catalytic Reduction of Tars	93
7.3	Tar Quantities as a Function of Gasifier Type.....	93
7.4	Experimental Tar Measurements in the CREC Riser Simulator	95
7.4.1	Tar Composition as a Function of Temperature, SB ratio and Contact Time	100
7.4.2	Tar Quantities.....	101
7.5	Conclusions.....	105
Chapter 8	Thermodynamic Modeling.....	107
8	Thermodynamic Equilibrium Modeling	107
8.1	Introduction.....	107
8.2	Thermodynamic Equilibrium Model for Steam Gasification	107
8.3	Equilibrium Constants	111
8.3.1	Effect of Temperature on the Equilibrium Constant.....	111
8.3.2	Effect of Pressure on the Equilibrium Gas Composition.....	111
8.4	Thermodynamic Equilibrium Model Predictions	112
8.4.1	Effect of Fuel Composition on the Steam Gasification of Biomass	112
8.4.2	Steam/Biomass Ratio and Temperature Effect on the Steam Gasification of Biomass	118
8.5	Equilibrium Model Prediction versus Experimental Results.....	120
8.5.1	Glucose: Equilibrium Model vs. Experimental Data at 700°C.....	120
8.5.2	2-methoxy-4-methylphenol: Equilibrium Model vs. Experimental Data at 700°C.....	128
8.6	Conclusions.....	131
Chapter 9	Kinetic Modeling.....	133
9	Kinetic Model.....	133
9.1	Introduction.....	133

9.2 Steam Gasification of Biomass	135
9.3 Overall Kinetic Model	136
9.4 Water-Gas Shift Mechanism.....	138
9.5 Steam Reforming of Methane (SR)	140
9.6 Dry Reforming of Methane (DRM).....	141
9.7 Postulated “Additive” Rate Equation Model	142
9.8 Parameter Estimation	145
9.9 Kinetic Parameter Estimation	146
9.10 Kinetic Parameters as a Function of Temperature	147
9.11 Intrinsic Kinetic Parameters Estimation	148
9.12 Gasification Kinetic Modeling Results	153
9.13 Conclusions.....	159
Chapter 10 Conclusions and Recommendations.....	160
10 Conclusions and Recommendations	160
10.1 Main Contributions	160
10.1.1 Related Contributions	161
10.2 Recommendations.....	162
Bibliography	163
Appendix A Volume Calculations	177
Appendix B Adsorption Isotherms at High Temperatures	185
Appendix C Calibration Curves.....	194
Appendix D Thermodynamic Equilibrium Model for Steam Gasification of Biomass .	212
Appendix E Kinetic Parameters Estimation Example	225
Appendix F Mass Balances.....	228
Curriculum Vitae	239

List of Tables

Table 1. Advantages and technical challenges of different gasifier designs, gasifying agents and operations for syngas production (Dhepe and Fukuoka, 2008).....	23
Table 2. Physical properties, catalytic activities and deactivation characteristic of various oxides-supported Ni catalysts (Wang and Lu, 1998).	30
Table 3. Typical chemical composition of biomass (Balat, 2009)	41
Table 4. Mass selective detector parameters.....	53
Table 5. Gas chromatograph method	54
Table 6. Ni/ α -alumina catalyst PSD results.....	62
Table 7. Elemental analysis results using XRF spectrometer.....	63
Table 8. Pulse chemisorption analysis summary	70
Table 9. BET surface area analysis.....	71
Table 10. Chemical components in biomass tar (Elliott, 1988).....	87
Table 11. Tars reported in raw gases for fluidized gasifiers (Milne et al., 1998).....	94
Table 12. MS peak integration for catalytic steam gasification of 2-methyl-4-methoxyphenol at 700°C, atmospheric pressure, S/B ratio of 0,4, and 30s of reaction time	98
Table 13. Tar mass fraction composition at 600 and 700°C for a) thermal, and b) catalytic steam gasification of 2-methoxy-4-methylpehnol.....	100
Table 14. Tars reported in raw gases at 600, 650 and 700°C for catalytic steam gasification of 2-methyl-4-methoxyphenol over Ni/ α -alumina	102
Table 15. Comparison of tar wt% for experimental runs with catalyst and without catalyst	104
Table 16. Chemical steam reactions in the steam gasification of biomass.....	109

Table 17. Ultimate analysis of a diverse variety of biomass composition.....	112
Table 18. <i>Formate</i> mechanism for the WGS reaction (Campbell and Daube, 1987).....	139
Table 19. Kinetic parameters at 700°C for 2-methyl-4-methoxyphenol mixtures.....	148
Table 20. Activation energies and heat of adsorption guesses	149
Table 21. Intrinsic kinetic parameters of the proposed “additive” kinetic model with their 95% confidence	150
Table 22. Activation energy review with the reported in the literature [kJ/mol]	152

List of Figures

Figure 1. Schematic of (a) updraft and (b) down draft gasifier (McKendry, 2002a)	12
Figure 2. Schematic of dual fluidized bed steam gasification reactor or FICFB-gasification system (Pfeifer et al., 2009).....	16
Figure 3. Glucose as a model compound of cellulose	41
Figure 4. 2-methoxy-4-methylphenol as a model compound of lignin	42
Figure 5. Schematic diagram of the CREC Riser Simulator : quarter section view, upper and lower shells exposed.....	44
Figure 6. Schematic description of CREC Riser Simulator, associated valves and accessories	45
Figure 7. Front view of the CREC Riser Simulator showing the control panel	46
Figure 8. Manual injector switch with syringe	47
Figure 9. Change in pressure in CREC Riser Simulator for injection of 12.5 μ L of phenol at 650 $^{\circ}$ C, reaction time of 20s and steam/biomass ratios of 0.4, 0.6, 0.8, 1.0.....	50
Figure 10. Change in pressure in CREC Riser Simulator for injection of 12.5 μ L of phenol at 650 $^{\circ}$ C, steam/biomass ratio of 0.6, reaction times of 5, 10, 20 and 30s.....	51
Figure 11. Fluidized bed reactor for Ni based catalyst preparation: a) exhaust gas exit port (9/16") b) inconel reactor wall c) fluidized catalyst d) inconel porous gas distribution grid plate and e) hydrogen/helium gas inlet port (9/16").....	59
Figure 12. Catalysis preparation flow chart (nickel supported on α -alumina).....	60
Figure 13. Particle Size Distribution of Ni/ α -alumina catalyst	61
Figure 14. TPD spectrum for Ni/ α -alumina catalyst	64
Figure 15. TPR Spectrum for Ni/ α -alumina Catalyst.....	67

Figure 16. Results for pulse chemisorption on Ni/ α -alumina catalyst	69
Figure 17. Hydrogen partial pressure experimental data for glucose as a function of temperature, S/B ratio, and reaction time. Note: This figure was plotted with at least 16 experimental data points at every temperature level. Typical standard deviations for repeats were 4%.	74
Figure 18. Carbon monoxide partial pressure experimental data for glucose as a function of temperature, S/B ratio, and reaction time. Note: This figure was plotted with at least 16 experimental data points at every temperature level. Typical standard deviations for repeats were 6%.	75
Figure 19. Carbon dioxide partial pressure experimental data for glucose as a function of temperature, S/B ratio, and reaction time. . Note: This figure was plotted with at least 16 experimental data points at every temperature level. Typical standard deviations for repeats were 5%.	76
Figure 20. Water partial pressure experimental data for glucose as a function of temperature, S/B ratio, and reaction time. Note: This figure was plotted with at least 16 experimental data points at every temperature level. Typical standard deviations for repeats were 4%.	77
Figure 21. Methane partial pressure experimental data for glucose as a function of temperature, S/B ratio, and reaction time. Note: This figure was plotted with at least 16 experimental data points at every temperature level. Typical standard deviations for repeats were 4%.	78
Figure 22. Hydrogen partial pressure experimental data for 2-methoxy-4-methylphenol as a function of temperature, S/B ratio, and reaction time. Note: This figure was plotted with at least 16 experimental data points at every temperature level. Typical standard deviations for repeats were 3%.	79
Figure 23. Carbon monoxide partial pressure experimental data for 2-methoxy-4-methylphenol as a function of temperature, S/B ratio, and reaction time. Note: This	

figure was plotted with at least 16 experimental data points at every temperature level. Typical standard deviations for repeats were 3%.	80
Figure 24. Carbon dioxide partial pressure experimental data for 2-methoxy-4-methylphenol as a function of temperature, S/B ratio, and reaction time. Note: This figure was plotted with at least 16 experimental data points at every temperature level. Typical standard deviations for repeats were 3.8%.	81
Figure 25. Water partial pressure experimental data for 2-methoxy-4-methylphenol for glucose as a function of temperature, S/B ratio, and reaction time. Note: This figure was plotted with at least 16 experimental data points at every temperature level. Typical standard deviations for repeats were 5%.	82
Figure 26. Methane partial pressure experimental data for 2-methoxy-4-methylphenol as a function of temperature, S/B ratio, and reaction time. Note: This figure was plotted with at least 16 experimental data points at every temperature level. Typical standard deviations for repeats were 5%.	83
Figure 27. Tar maturation scheme proposed by Elliott, 1988.....	86
Figure 28. Tar yield as a function of the maximum temperature exposure (Baker et al., 1988).	86
Figure 29. The distribution of the four tar component classes as a function of temperature at 300 ms (0.3 s) gas-phase residence time (reprinted from Evans and Milne, 1997) .	89
Figure 30. Composition of tar from atmospheric-pressure, air gasification of biomass at 780°C (Bangala et al., 1997)	91
Figure 31. Composition of permanent gases for catalytic steam gasification of biomass at 700°C, atmospheric pressure, S/B ratio of 0.4, and 30 seconds reaction time	96
Figure 32. Composition of tar for catalytic steam gasification of biomass at 700°C, atmosphere pressure, S/B ratio of 0.4, and 30 seconds of reaction time	97

Figure 33. Tar experimental data [wt%, $g_{\text{Tar}}/g_{\text{Feed}}$] for catalytic steam gasification of 2-methoxy-4-methylphenol as a function of temperature, S/B ratio, and reaction time. 3D plot established with 16 data points for each temperature. Data set with σ of 2.3.	103
Figure 34. Comparison of tar wt% experimental data with and without catalyst for steam gasification of 2-methoxy-4-methylphenol as a function of S/B ratio and reaction time at $P = 1$ atm and 600°C . 3D plot established with 16 data points. Data set with σ of 2.3 for 600°C catalytic and 4.7 for 600°C no catalytic.	105
Figure 35. Chemical reactions considered in the steam gasification of biomass.....	108
Figure 36. Hydrogen mole fraction versus steam/biomass ratio at 800°C and 1 atm; equilibrium model predictions for different biomass compositions; from higher to lower H_2 mole fractions, (1) jute stick, (2) heterotrophic, (3) glucose, (4) potato starch, (5) pine sawdust, (6) legume straw, (7) softwood bark, (8) wasted wood and (9) coal.....	113
Figure 37. Carbon monoxide mole fraction versus steam/biomass ratio at 800°C and 1 atm; equilibrium model predictions for different biomass compositions, (1) jute stick, (2) heterotrophic, (3) glucose, (4) potato starch, (5) pine sawdust, (6) legume straw, (7) softwood bark, (8) wasted wood and (9) coal	114
Figure 38. Carbon Dioxide mole fraction versus steam/biomass ratio at 800°C and 1 atm; equilibrium model predictions for different biomass compositions, (1) jute stick, (2) heterotrophic, (3) glucose, (4) potato starch, (5) pine sawdust, (6) legume straw, (7) softwood bark, (8) wasted wood and (9) coal	115
Figure 39. Methane mole fraction versus steam/biomass ratio at 800°C and 1 atm; equilibrium model predictions for different biomass compositions, (1) jute stick, (2) heterotrophic, (3) glucose, (4) potato starch, (5) pine sawdust, (6) legume straw, (7) softwood bark, (8) wasted wood and (9) coal	116
Figure 40. Hydrogen to carbon monoxide ratio versus steam/biomass ratio at 800°C and 1 atm; equilibrium model predictions for different biomass compositions, (1) jute	

stick, (2) heterotrophic, (3) glucose, (4) potato starch, (5) pine sawdust, (6) legume straw, (7) softwood bark, (8) wasted wood and (9) coal	117
Figure 41. Equilibrium fractional distribution of H ₂ on a dry basis at P = 1 atm and various steam/glucose (S/B) ratios and temperatures	119
Figure 42. Equilibrium fraction distribution of H ₂ , CO, CO ₂ , CH ₄ , and H ₂ O at P = 1 atm, S/B = 0.1 and various temperatures.....	119
Figure 43. Equilibrium fraction distribution of H ₂ , CO, CO ₂ , CH ₄ , and H ₂ O at P = 1 atm, S/B = 0.5 and various temperatures.....	119
Figure 44. Equilibrium fraction distribution of H ₂ , CO, CO ₂ , CH ₄ , and H ₂ O at P = 1 atm, S/B = 1.0, and various temperatures.....	120
Figure 45. Equilibrium fraction distribution of H ₂ , CO, CO ₂ , CH ₄ , and H ₂ O at P = 1 atm, S/B = 1.5, and various temperatures.....	120
Figure 46. H ₂ mole fraction of product gas for gasification of glucose at different steam/glucose ratios, 700°C and P = 1 atm. Solid line (—) equilibrium model, (*) non-catalytic gasification runs, experimental data using Ni supported catalyst at (⊕) 5 seconds, (⊕) 10 seconds, (▲) 20 seconds and (♠) 30 seconds of reaction time.	121
Figure 47. CO mole fraction of product gas for gasification of glucose at different steam/glucose ratios, 700°C and P = 1 atm. Solid line (—) equilibrium model, (*) non-catalytic gasification runs, experimental data using Ni supported catalyst at (⊕) 5 seconds, (⊕) 10 seconds, (▲) 20 seconds and (♠) 30 seconds of reaction time.	123
Figure 48. CO ₂ mole fraction of product gas for gasification of glucose at different steam/glucose ratios 700°C and P = 1 atm. Solid line (—) equilibrium model, (*) non-catalytic gasification runs, experimental data using Ni supported catalyst at (⊕) 5 seconds, (⊕) 10 seconds, (▲) 20 seconds and (♠) 30 seconds of reaction time.	124
Figure 49. CH ₄ mole fraction of product gas for gasification of glucose at different steam/glucose ratios, 700°C and P = 1 atm. Solid line (—) equilibrium model, (*)	

non-catalytic gasification runs, experimental data using Ni supported catalyst at (⊕) 5 seconds, (⊕) 10 seconds, (▲) 20 seconds and (♠) 30 seconds of reaction time. 125

Figure 50. H₂/CO ratio for gasification of glucose at different steam/glucose ratios, 700°C and P = 1 atm. Solid line (—) equilibrium model, (✱) non-catalytic gasification runs, experimental data using Ni supported catalyst at (⊕) 5 seconds, (⊕) 10 seconds, (▲) 20 seconds and (♠) 30 seconds of reaction time. 126

Figure 51. CO/CO₂ ratio for gasification of glucose at different steam/glucose ratios, 700°C and P = 1 atm. Solid line (—) equilibrium model, (✱) non-catalytic gasification runs, experimental data using Ni supported catalyst at (⊕) 5 seconds, (⊕) 10 seconds, (▲) 20 seconds and (♠) 30 seconds of reaction time. 127

Figure 52. Hydrogen mole fraction composition for steam gasification of 2-methoxy-4-methylphenol; equilibrium calculations and experimental data using Ni supported catalyst at 700°C as a function of S/B ratio and reaction time 128

Figure 53. Carbon monoxide mole fraction composition for steam gasification of 2-methoxy-4-methylphenol; equilibrium calculations and experimental data using Ni supported catalyst at 700°C as a function of S/B ratio and reaction time 129

Figure 54. Carbon dioxide mole fraction composition for steam gasification of 2-methoxy-4-methylphenol; equilibrium calculations and experimental data using Ni supported catalyst at 700°C as a function of S/B ratio and reaction time 130

Figure 55. Methane mole fraction composition for steam gasification of 2-methoxy-4-methylphenol; equilibrium calculations and experimental data using Ni supported catalyst at 700°C as a function of S/B ratio and reaction time 131

Figure 56. Chemical reaction network considered in the steam gasification of biomass 136

Figure 57. Predicted and experimental hydrogen yields from catalytic steam gasification of 2-methoxy-4-methylphenol over Ni/α-alumina at various temperatures, residence times, and steam biomass ratios. 154

Figure 58. Predicted and experimental water yields from catalytic steam gasification of 2-methoxy-4-methyphenol over Ni/ α -alumina at various temperatures, residence times, and steam biomass ratios.	154
Figure 59. Predicted and experimental carbon dioxide yields from catalytic steam gasification of 2-methoxy-4-methyphenol over Ni/ α -alumina at various temperatures, residence times, and steam biomass ratios.	155
Figure 60. Predicted and experimental carbon monoxide yields from catalytic steam gasification of 2-methoxy-4-methyphenol over Ni/ α -alumina at various temperatures, residence times, and steam biomass ratios.....	155
Figure 61. Predicted and experimental methane yields from catalytic steam gasification of 2-methoxy-4-methyphenol over Ni/ α -alumina at various temperatures, residence times, and steam biomass ratios.	156
Figure 62. Predicted and experimental hydrogen yields from catalytic steam gasification of glucose over Ni/ α -alumina at various temperatures, residence times, and steam biomass ratios.	156
Figure 63. Predicted and experimental carbon monoxide yields from catalytic steam gasification of glucose over Ni/ α -alumina at various temperatures, residence times, and steam biomass ratios.	157
Figure 64. Predicted and experimental water yields from catalytic steam gasification of glucose over Ni/ α -alumina at various temperatures, residence times, and steam biomass ratios.	157
Figure 65. Predicted and experimental carbon dioxide yields from catalytic steam gasification of glucose over Ni/ α -alumina at various temperatures, residence times, and steam biomass ratios.	158
Figure 66. Predicted and experimental methane yields from catalytic steam gasification of glucose over Ni/ α -alumina at various temperatures, residence times, and steam biomass ratios.	158

List of Appendices

Appendix A Volume Calculations	177
Appendix B Adsorption Isotherms at High Temperatures	185
Appendix C Calibration Curves.....	194
Appendix D Thermodynamic Equilibrium Model for Steam Gasification of Biomass	212
Appendix E Kinetic Parameters Estimation Example	225
Appendix F Mass Balances.....	228

List of Abbreviations, Symbols, Nomenclature

A	A constant
AD	Particle apparent density (g/cc)
A_p	Area of the surface occupied by a single adsorbent gas molecule
BET	Brunauer, Emmett and Teller method
C_i	Molar concentration of species “i”
ΔC_p	Standard heat capacity change (J/°K)
CREC	Chemical Reactor Engineering Centre
$C_x H_y O_z$	Unit composition of biomass
DRM	Dry reforming of methane
d_p	Particle diameter (μm)
ECCMB	External Circulating Concurrent Moving Bed
E_i	Activation energy (KJ/mol) for component “i”
ER	Equivalence ratio
FB	Fluidized bed
FICFB	Fast Internally Circulating Fluidised Bed
f	Fraction of reduced metal
\hat{f}_i	Fugacity coefficient of species “i” in an ideal gaseous solution
f_i^o	Fugacity coefficient of pure species “i”
GC/MS	Gas chromatograph/Mass spectrometer
ΔG^o	Standard Gibbs energy change of reaction (KJ/mole)
$\Delta G_{f(298)}^o$	Standard Gibbs free energy change of formation at 298 °K (KJ/mole)
ΔH^o	Standard enthalpy change of reaction (KJ/mole)
$\Delta H_{f(298)}^o$	Standard enthalpy change of formation at 298 °K (KJ/mole)

$\Delta H_{ads}^{CO_2}$	Carbon dioxide heat of adsorption (KJ/mol)
j	Component in denominator term
k_i	Reaction rate constant for component “i”
k_i^0	pre-exponential factor or reaction rate constant for component “i”
k_i^k	Kinetic constant for component “i” (mol/gcat min)
K_i^A	Adsorption constant for component “i” (l/atm)
K_j	Equilibrium reaction constant for “j” reaction (-)
LHV	Lower Heating Value (MJ/Nm ³)
m_i	Mass of component “i”
m/z	Mass-to-charge ratio
MBMS	Molecular beam mass spectrometry
MS	Mass spectrometer
MW_i	Molecular weight of component “i” (g mol ⁻¹)
n	Number of chemical species
N_A	Avogadro’s number
n_{cr}	Number of nickel crystals
Ni/ α -Al ₂ O ₃	Nickel supported on alpha-alumina
NR	Newton-Raphson
P	Total pressure (Kpa, unless specified otherwise)
P_i	Partial pressure of component “i”
P_o	Saturation pressure
PAH	Polynuclear aromatic hydrocarbons
PSD	Particle size distribution
R	Gas constant (J /mol °K)
r_i	Rate of reaction of component “i” (mol/gcat)

S	Surface site
S/B	Steam/biomass feed ratio (g/g)
SR	Steam reforming of methane
S_m	Average surface area (m ² /g catalyst)
STP	Standard temperature and pressure
T	Temperature (°K)
T ₀	Reference temperature (°K)
T _{avg}	Average temperature (K)
TCD	Thermal conductivity detector
TPD	Temperature programmed desorption
TPR	Temperature programmed reduction
TPO	Temperature programmed oxidation
V	Volume of reactor (cc)
V_{ads}	Volume of gas adsorbed
V _i	Volume of specie “i”
V_m	Volume of a monolayer
Vol%	Volume percent
W _{cat}	Catalyst weight (g)
WGS	Water-gas shift reaction
Wt%	Weight percent
X	Total hydrogen chemisorbed (μmol of H ₂ /g catalyst)
x _{Ni}	Percent metal loading
X _{purity}	Percent purity
$X_{w,Ni}$	Percentage of weight nickel metal
XRF	X-Ray fluorescence
y _i	Moles fraction of species i

%D	Percent dispersion
%-mol	Mole percent

Greek Symbols

α	Product H ₂ /biomass feed ratio (mole/mole)
β	Product CO/biomass feed ratio (mole/mole)
β_{\min}	Minimum allowable value of β
β_{\max}	Maximum allowable value of β
γ	Product CO ₂ /biomass feed ratio (mole/mole)
γ_{\max}	Maximum allowable value of γ
ε	Product C ₂ H ₄ /biomass feed ratio (mole/mole)
ζ	Product CH ₄ /biomass feed ratio (mole/mole)
η	Product C ₂ H ₆ /biomass feed ratio (mole/mole)
θ	Product C ₃ H ₈ /biomass feed ratio (mole/mole)
λ	Product C ₄ H ₁₀ /biomass feed ratio (mole/mole)
μ	Product C ₅ H ₁₂ /biomass feed ratio (mole/mole)
ν	Product C ₆ H ₁₄ /biomass feed ratio (mole/mole)
ν_i	Stoichiometric coefficient of specie "i"
ν_T	Sum of stoichiometric coefficients
Π_i	Product over all species "i"
ϕ	Particle shape constant
Φ_i	Fugacity coefficient of species "i"
σ	Standard deviation
ψ	Product H ₂ O/biomass feed ratio (mole/mole)
ω	steam/biomass feed ratio (mole/mole)

Chapter 1 Introduction

1 Introduction

Biomass, a hydrocarbon material mainly consisting of carbon, hydrogen, oxygen, nitrogen and minerals, is considered an ideal renewable resource given its abundance, its lower sulfur content and its CO₂ neutral emissions (Balat, 2009; Chen et al., 2008). As a result, it is becoming one of the most important renewable energy sources in our planet's immediate future. However, in order to utilize biomass, it is necessary to investigate and develop an efficient and clean conversion technology.

Bio-chemical and thermo-chemical biomass conversion processes are utilized to produce heat and electricity, as well as various chemicals. Thermo-chemical processes which have been studied to date are combustion, pyrolysis and gasification. Among them, gasification of biomass is considered one of the most economical and efficient technologies. This finding is based on consideration of the greater overall conversion efficiency of gas production via gasification and the proven operational history and performance of gasifiers (McKendry, 2002b). Biomass is mainly composed of hemicellulose, cellulose and lignin lumps, along with ash and moisture. Theoretically, almost all kinds of biomass with moisture content of 5-30% can be gasified. However, it is known that feedstock (biomass) properties such as surface, size, shape as well as moisture content, volatile matter and carbon content affect this process (Kirubakaran et al., 2009). Other variables which affect gasification are the gasifier configuration, the specific gasification process conditions used, and the gasifying agent. It is in this respect, essential to understand the gasification chemistry in order to determine the influence of each type of lump on the gasification process. Furthermore, one must also study the full feedstock in order to establish both the contribution by the individual lumps as well as the interactive effects of various biomass constituents.

In recent years, biomass steam gasification has become an area of growing interest because it produces a gaseous fuel with relatively higher hydrogen content that could be

used for industrial applications, both for highly efficient electricity production and as a feedstock for chemical synthesis. Furthermore, steam gasification has other advantages in that: (i) it produces a gas with higher heating value; (ii) it reduces the diluting effect of N₂ from air and (iii) it eliminates the need for an expensive oxygen plant when both air and oxygen are used as gasification mediums (Franco et al., 2003). Catalytic steam gasification of biomass in fluidized beds is a promising approach given its rapid biomass heating, its effective heat and mass transfer between reacting phases, and its uniform reaction temperature (Munir et al., 2009). Moreover, fluidized beds tolerate wide variations in fuel quality as well as broad particle-size distributions.

A serious issue for the broad implementation of this technology is the generation of unwanted contaminants like tars, particles, nitrogen compounds, alkali metals (Banowetz et al., 2009). Tar is a complex mixture of condensable hydrocarbons, which includes single ring to 5-ring aromatic compounds along with other oxygen-containing hydrocarbons species (Tasaka et al., 2007). These product species condense in gasifier pipe outlets and in particulate filters which leads to blockages and filter clogging. Tar causes further downstream problems and clogs fuel lines and injectors in internal combustion engines. Moreover, tars contain significant amounts of energy that could be transferred to the fuel gases such as H₂, CO, CO₂, CH₄, etc. According to Milne et al., 1998; *“tar is the most cumbersome and problematic parameter in any gasification commercialization effort”*. For commercial applications, tar components have to be limited to less than 1 g/m³ of gas at STP conditions. Therefore, considerable efforts are currently being made towards tar removal from fuel gas. The different approaches for tar removal to date can be categorized as follows (Devi et al., 2003): i) direct syngas treatment is inside the gasifier, and ii) hot gas cleaning after the gasification process (secondary methods).

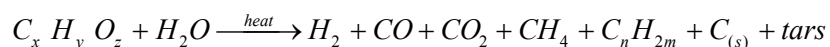
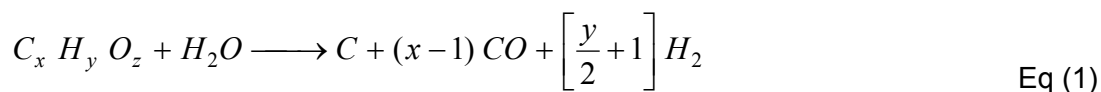
Primary treatment methods are the ones gaining much attention nowadays as they may eliminate the need for installation and maintenance of downstream processing steps using hot-gas cleaning technology. There are several factors to consider in one's approach to the development of an effective primary treatment method: (a) the proper selection of

operating parameters, (b) the type of additive/catalyst used, and (c) gasifier modifications to prevent tar build-up (Devi et al., 2003).

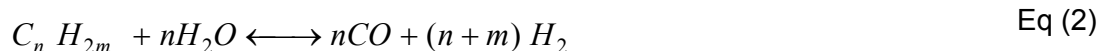
Tar can be reduced thermally. However, this typically requires very high temperatures, greater than 1000°C. It is highly desirable however, to keep the operating temperature of the gasifier below 700°C, to prevent ash agglomeration. Ash frequently contains CaO, K₂O, P₂O₅, MgO, SiO₂, SO₃, and Na₂O that can sinter, agglomerate, deposit on surfaces and contributes to erosion and corrosion of the gasifier. Furthermore, alkaline metals react readily in the gasifier with silica forming silicates or with sulfur producing alkali sulfates, leaving a sticky deposit and in many instances causing bed sintering and defluidization (Wang et al., 2008; Banowetz et al., 2009; Liao et al, 2007).

According to Devi et al., 2003 catalytic reforming of tar into gaseous products is an effective method for tar removal, avoiding costly tar disposal. In this respect, Ni-based catalysts have high activity for tar conversion, have water-gas-shift activity and decrease the amount of nitrogenous compounds such as ammonia. However, several deactivation mechanisms occur with nickel-based catalysts including poisoning by sulphur, chlorine, and alkali metals, sintering of Ni particles and coke formation (Albertazzi et al., 2009). Ni-based catalysts deactivate rapidly due to coke formation and catalyst attrition. While coke can be removed by combustion, coke removal can lead, if not carefully performed, to poor catalyst activity and selectivity and limited catalyst life. Coke deposition can be minimized through the use of excess steam vis-a-vis the one required by gasification stoichiometry. In practice, this increases the overall energy costs for the gasifier plant operation.

Catalytic steam gasification of biomass is a complex network of heterogeneous reactions (Huber et al., 2006). Primary reactions break down the vaporized biomass molecules, forming coke and permanent gases:



Secondary reactions crack the higher hydrocarbons into gases that further combust or become reduced:



Furthermore, permanent gases react to alter the gas composition depending on gasifier conditions:



Extensive researches have been made to develop stable and highly active catalysts for biomass gasification producing high quality syngas and /or hydrogen. However, designing an optimum steam gasification process requires additional insights into gasification kinetics, reaction mechanism and thermodynamics in order to predict the end-reaction product composition distribution.

New catalysts for biomass steam gasification are required to provide to the catalyst the long life required in large scale processes, preventing tar formation and crystallite agglomeration. Furthermore, better understanding of both fundamentally based kinetics and thermodynamics of gasification will be valuable in order to establish processes which operate in the 600-700°C range, yielding H₂/CO ratios of one or even higher for subsequent alternative fuel manufacture of ethanol and diesel.

To date, a significant volume of research on thermodynamics models provides valuable tools to predict the end-product composition distribution under various gasification operating conditions. Although these models provide satisfactory predictions of the

H₂/CO ratio and changes of chemical species with operating conditions, in most of the cases the experimental syngas composition deviates from equilibrium composition. Specifically experimental methane composition, a very critical parameter that is used to define the heating value of the syngas, deviates considerably from most of the model predicted values. The main reasons for this deviation are due to inadequate assumptions adopted such as the following: i) assumed equilibrium conditions for some key reaction steps, ii) char and tar accumulation being considered as solid carbon and iii) ash being treated as an inert species. It is well acknowledged that in an actual process, various gasification reactions cannot reach equilibrium and that the above mentioned deviation is affected by the different reactivity of char/tar. Furthermore, even the ash can have positive catalytic activity in the pyrolysis step which may influence the syngas fraction predictions.

Therefore, reactor design and operation call for suitable physicochemically based kinetics adaptable to various biomass feedstocks and suitable for unit scale-up. It is our view that research on gasification reaction mechanism and kinetics, as it is the case of this PhD dissertation, will provide valuable reaction engineering information and future directions for establishment of advanced biomass catalytic gasification processes.

Chapter 2 Scope

2 Scope of the Research

The main objective of this PhD research is to gain understanding on the thermodynamics and kinetics of the catalytic steam gasification of biomass using model compounds. More specifically, the purpose of the research is to elucidate the kinetic factors inherent to this process such as thermodynamic restrictions and mechanistic reaction steps. The ultimate aim is to establish the chemical reaction engineering tools that will allow the design and operation of large scale fluidized bed units for biomass steam catalytic gasification.

The specific proposed objectives for this research set at the beginning of the PhD studies included the following:

1. The preparation and characterization of a Ni on α -Al₂O₃ (Ni/ α -Al₂O₃) catalyst using advanced surface science characterization techniques.
2. The development of reaction runs in the CREC Riser Simulator to establish the performance of the prepared Ni/ α -Al₂O₃ steam gasification catalysts. The planned experimental runs were intended to examine the effects of reaction temperature, steam/biomass ratio, fuel type, and reaction contact time. The study was planned to be carried out by using a catalyst at short residence times and high heating rates. Another goal of the experimental work was to investigate the reaction factors involved in determining the gas composition and tars during biomass steam gasification.
3. The establishment of a comprehensive thermodynamic model suitable to determine the equilibrium product compositions at chemical equilibrium conditions for several biomass feedstock types.
4. The elucidation of the mechanistic reaction steps involved in catalytic gasification of biomass using two different classes of model compounds representing cellulose and lignin. It was expected that the planned runs with

these model compounds will be done under the experimental conditions typical of biomass gasification.

5. The establishment of a heterogeneous kinetic model that describes the product gas composition during catalytic steam gasification of biomass. It was expected this heterogeneous kinetic model will supersede thermodynamic predictions. It was also anticipated that this kinetic model will be physicochemical based and will include intrinsic reaction kinetic parameters calculated using a statistically-based parameter estimation.

Chapter 3 Literature Review

3 Literature Review

3.1 Introduction

Gasification of biomass is an environmentally favourable technology that may contribute to the fulfillment of the Kyoto protocol by offering an alternative to the direct use of fossil fuel energy. Biomass can be converted into a vast array of chemical products and fuel, and it can be utilized to produce power/electricity. There are however, still major limitations of biomass gasification technology, which presently make biomass gasification economically not viable. These limitations arise from the presence of condensable organic compounds (tar), and particulate matter in the product gas, which renders the gas unsuitable for specific applications and potentially may damage downstream process equipment, harm the environment, and hinder economic efficiency (Milne et al., 1998). Elimination of tar by a suitably low cost technology will enhance the economic viability of biomass gasification.

It is well known that biomass properties such as composition, structure, reactivity, physical properties as well as moisture content affect this process (Kirubakaran et al., 2009). Other variables which affect gasification are the gasifier configuration, the specific gasification process conditions used (temperature, residence time, heating rate, etc.), and the gasifying agent. It is in this respect, essential to understand the gasification chemistry in order to determine the influence of each type of lump on the gasification process. Furthermore, one must also study the full feedstock in order to establish both the contribution by the individual lumps as well as the interactive effects of various biomass constituents.

One of the conventional methods for the production of synthesis gas (syngas) from biomass is the non-catalytic gasification of biomass. The drawback of non-catalytic gasification is the high reaction temperature required (above 1273°K) for significant tar

reduction. High reaction temperature may result in expensive reactor equipment, which would hamper the overall economical efficiency of this gasification process.

According to Devi et al., 2003, the catalytic reforming of tars into gaseous products is an effective method for tar removal, avoiding costly tar disposal. In this respect, dolomite, olivine, and silica sand have been used as catalysts. Nevertheless, the effect of these materials is not so significant, with the required reaction temperature being close to the one used in non-catalytic gasifiers. On the other hand, the utilization of metal supported catalysts in biomass gasification systems is an effective approach to reduce the tar content in the product gas as well as to improve the thermal balance of the unit, thus promoting the gas shift reaction.

One of the promising metal components for catalytic gasification of biomass is the low-cost nickel. One of the issues however is that commercial nickel catalysts, which were developed for steam reforming of methane and hydrocarbons, have been reported to display low performance. As a result, nickel catalysts have to be specifically adapted for the gasification of biomass, with these modified nickel catalyst displaying promising performance. Using these materials at a typical reaction temperature of 823°K, both tar and coke yields are decreased drastically. However, designing an optimum steam gasification process requires additional insights into gasification kinetics, reaction mechanism and thermodynamics in order to predict the end-reaction product composition distribution.

Given the potential contribution of catalytic processes to biomass gasification, other catalysts, such as Rh/CeO₂/SiO₂, are being considered. The Rh/CeO₂/SiO₂ catalyst, while showing interesting performance, has a potentially less viable application given its high manufacturing costs due to the limited availability of Rhodium.

Long life catalysts for biomass steam gasification are required in large scale processes to prevent tar formation and catalyst crystallite agglomeration. Furthermore, a better understanding of both fundamentally based kinetics and the thermodynamics of gasification will be valuable. This is will be required in order to establish processes

which operate in the 700-800°C range, yielding H₂/CO ratios of one or even higher suitable for alternative fuel manufacturing such as ethanol and biodiesel.

To date, a significant volume of research on thermodynamic models provides valuable tools to predict the proximate end-product composition distribution under various gasification operating conditions. Although these models offer satisfactory predictions of the H₂/CO ratio, in most cases, the observed syngas compositions deviate from chemical equilibrium predictions. Specifically, experimental methane composition, a very critical parameter that is used to define the heating value of the syngas, deviates considerably from most of the model predicted thermodynamic values. The main reasons for this deviation are due to some inadequate assumptions adopted such as the following: (i) assumed equilibrium conditions for some key reaction steps, (ii) char and tar accumulation being considered as solid carbon and (iii) ash being treated as an inert species. It is well acknowledged that in an actual process, various gasification reactions cannot reach equilibrium and that the above mentioned deviations are affected by the different reactivity of char/tar. Furthermore, even the ash can have positive catalytic activity in the pyrolysis step which may influence the syngas composition predictions.

Therefore, reactor design and operation call for suitable physicochemically based kinetics adaptable to various biomass feedstocks and suitable for unit scale-up. It is our view that a critical and up-to-date review on gasification reaction mechanisms and kinetics, as it is provided in this review, provides valuable information and future direction for reaction engineering and process design in the context of biomass catalytic gasification.

Several books, book chapters and a significant volume of review articles have been published in the technical literature focusing on different issues such as: (i) tar removal, (ii) catalyst for biomass gasification, (iii) hot gas cleaning, and (iv) characteristics of biomass. These are all important factors in biomass gasification technology. However and in spite of the significance of all this, there is no comprehensive review on biomass catalytic gasification with emphasis on thermodynamics, kinetics, and catalyst properties as well as feedstock characteristics.

In this literature review, research contributions are reported according to the following sections:

1. In Section 3.2 and Section 3.3, we review the steam gasification process with main emphasis given to the gasifier designs and operating conditions. This is done in order to understand the influence of these variables on the conversion process.
2. In Section 3.4, we report different catalysts previously used for steam gasification. Main emphasis is given to the nickel catalyst.
3. In Section 3.5, we discuss thermodynamics studies of steam gasification of biomass published in the technical literature.
4. In Section 3.6, we discuss reaction engineering with mechanism and kinetics studies already established for these processes.

3.2 Design of Gasifiers

Gasifiers can be divided into two principal types: fixed beds and fluidized beds, with variations within each type. A third type, the entrained suspension gasifier has been developed for finely divided coal gasification (<0.1–0.4 mm). This type of gasifier is not recommended for fibrous materials such as wood, which makes the process largely unsuitable for most biomass materials (Huber et al., 2006).

3.2.1 Fixed bed gasification

Fixed-bed gasifiers are the oldest and historically most common reactors used to produce syngas. In the last two decades however large scale (higher than 10 MW) fixed-bed gasifiers have lost a part of their industrial market appeal (Dhepe and Fukuoka, 2008). Yet, small scale (lower than 10 MW) fixed-bed gasifiers with high thermal efficiency and minimal pretreatment of the supplied biomass have maintained a commercial interest especially for locally based power generation (Klimantos et al., 2009). Fixed-bed gasifiers are widely used and studied because of their simplicity in construction and

operation. Depending on the direction of airflow, the gasifiers are classified as updraft (Figure 1a), downdraft (Figure 1b), or cross-flow (Chaiwat et al., 2009).

In downdraft gasifiers and updraft gasifiers, the gas composition by volume is typically in the following ranges: CO (20-30%), H₂ (5-15%), CH₄ (1-3%), and CO₂ (5-15%) (Gordillo et al., 2009). The reaction distribution regions in a fixed-bed reactor are different depending on the type of gasifier design.

3.2.1.1 Updraft Gasifier

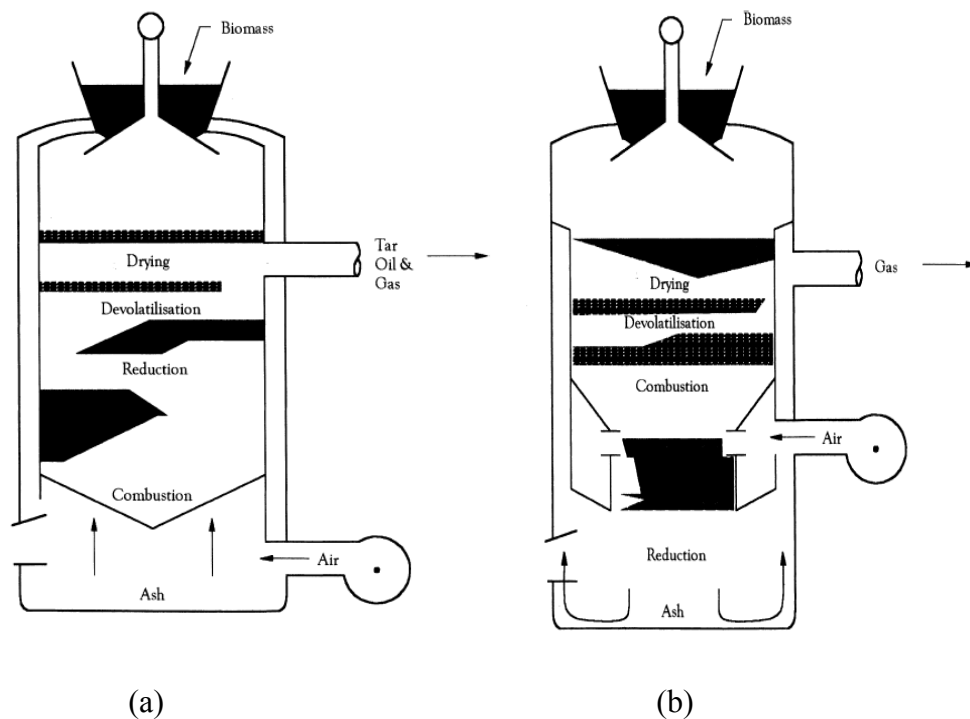


Figure 1. Schematic of (a) updraft and (b) down draft gasifier (McKendry, 2002a)

In an updraft gasifier, the feed is introduced at the top of the gasifier while air is fed at the bottom of the unit via a grate (Figure 1a). In the top gasifier section, the fed biomass is dried. Moving downwards, the dry biomass reaches the devolatilization zone, where the volatile species are released and considerable quantities of tars are formed. Following this, the volatiles freed of biomass evolve in the reduction zone where permanent gases are formed. The residual biomass finally reaches the grate where the solid char, and the remaining biomass, is combusted at 1000°C. Once char combustion with air is complete, the formed ash falls through the grate. Regarding the upflow of gases following

combustion, the hot gases move upwards while being reduced. Tar condenses partially on the descending biomass while also leaving the gasifier with the product gas. Thus, in the updraft gasifier, biomass may have a favorable filtering effect producing a gas with low tar content. The temperature in the gasification zone can also be controlled by co-feeding steam and air or by humidifying the air. Formed gases are cooled down to 200–300° C. Due to the low temperature of the gas leaving the gasifier; the overall updraft gasifier energy efficiency is high (Nagel et al., 2009).

3.2.1.2 Downdraft Gasifier

In a downdraft gasifier, both biomass and air move in the same downward direction in the lower section of the gasifier unit (Figure 1b). The downdraft gasifier has four distinct zones: (1) upper drying zone, (2) upper medium pyrolysis section, (3) lower medium oxidation zone and (4) lower reduction zone. The product gases leave the upper medium section, moving towards the lower medium zone enabling the partial cracking of the formed tars and producing a gas with low tar content. The temperature in the oxidation zone is 1000-1400 °C, and the tars produced are almost exclusively tertiary tars. The product gas contains a low concentration of particulates and tars (approximately 1 g/Nm³) as most of the tars are combusted in the gasifier. The downdraft gasifier is ideal when clean gas is desired (Sheth et al., 2009). The disadvantages of this type of gasifier include a relatively low overall thermal efficiency and difficulties in handling biomass with high moisture and ash content.

3.2.1.3 Cross-flow Gasifier

In a cross-flow gasifier, the biomass fed at the top of the unit moves downwards while the air is introduced from the unit side. Gases are withdrawn from the upper side of the unit at about the same level that the biomass is fed. A hot combustion/gasification zone forms around the air entrance, with both, pyrolysis and drying zones being formed higher up in the vessel. Ash is removed at the unit bottom and the temperature of the gas leaving the unit is about 800–900°C: As a result, low overall energy efficiency with a gas having high tar content are expected in cross-flow gasifier units.

In general, fixed-bed gasifiers have the advantage of involving simple designs but have the shortcoming of producing a low gas calorific value with high tar content. The product gas composition is typically 40–50% N₂, 15–20% H₂, 10–15% CO, 10–15% CO₂ and 3–5% CH₄, with a net CV of 4–6 MJ/Nm³. When using air as the gasifying medium, the resulting high N₂ content increases the volume of the product gas and augments the need for downstream gas cleaning equipment of larger capacity. To obtain a high gas calorific value, the moisture content of the feed should remain below 15–20wt% which is typical biomass moisture content. Therefore pre-drying of the biomass feedstock is usually not required. Fixed bed gasifiers generally produce outlet gases with a lower particulate loading (e.g. ash, tar, char) than fluidized bed gasifiers.

3.2.2 Fluidized Bed Gasification

Among the technologies that can be used for biomass combustion, fluidized beds are emerging as the best given their flexibility and high efficiency. Fluidized bed (FB) gasification has been used extensively for coal gasification for many years. Its advantage over fixed bed gasifiers is the uniform temperature distribution achieved in the gasification zone. This temperature uniformity is accomplished using a bed of fine granular material (e.g. sand) into which air is circulated, fluidizing the bed. Intense bed fluidization promoting solid circulation, favors the mixing of the hot bed material, the hot combustion gases and the biomass feed. Fluidized beds are used for a broad variety of fuels. This flexibility with respect to different fuels is actually another critical advantage of fluidized beds (Bartels et al., 2008). Furthermore, the typical tar level of 10 g/Nm³ in fluidized beds is an intermediate tar yield versus the ones observed in updraft and the downdraft gasifiers. Tar created forms a blend of secondary and tertiary tars (Huber et al., 2006).

Loss of adequate fluidization or defluidization due to bed agglomeration is a major problem in fluidized bed gasifiers. The most common problem found in fluidized beds as a preamble to defluidization in commercial-scale installations is the “coating-induced” agglomeration of the fine granular material forming the bed. During reactor operation, a coating is formed on the bed sand particle surface. At certain critical coating thicknesses and/or temperature levels, the sintering of the bed particles is promoted by biomass

sodium content. Sodium lowers the melting point of the silicates and aluminosilicates of the bed particles.

Agglomeration associated with fluidized bed gasifiers is still a major issue when used to gasify certain herbaceous biofuels. However, there are successful solutions that have been reported for other biomass feedstocks (Khan et al., 2009). These solutions are mainly based on lowering and controlling the bed temperature.

Two main types of fluidized bed gasifiers are in current use: a) circulating fluidized bed, b) bubbling bed. A third type of FB gasifier, an internally circulating bed, which combines the design features of the other two types is currently being investigated at the pilot plant scale.

3.2.2.1 Circulating Fluidized Beds

Circulating fluidized bed gasifiers are able to cope with high capacity biomass throughputs and are used in the paper industry for the gasification of bark and other forestry residues. The bed material is circulated between the reaction vessel and a cyclone separator, where the ash is removed and the bed material and char are returned to the reaction vessel. Circulating fluidized bed gasifiers can be operated at elevated pressures. Output gases produced in this case, are delivered at gas turbine operating pressure without requiring further compression.

3.2.2.2 Bubbling bed

Bubbling bed FB gasifiers consist of a vessel with a grate at the bottom through which air is introduced. Above the grate there is a moving bed of fine-grained material into which the prepared biomass feed is introduced. Regulation of the bed temperature to 700–900°C is maintained by controlling the air/biomass ratio. The biomass is pyrolyzed in the hot bed forming char, gaseous compounds and tar. The high molecular weight tar is cracked by contact with the hot bed material, giving a product gas with lower tar content ($< 1\text{--}3 \text{ g/Nm}^3$). For steam gasification without a catalyst, the tar produced in the gasifier is about 12 wt % of the fed cellulose. The main components of tar are celotriosan, cellobiosan, and levoglucosan (Tasaka et al., 2007).

There is another type of technology called dual fluidized bed (DFB) which has been developed in Austria using steam as the gasification agent and providing the heat for the gasification reactor by circulating bed material (Pfeifer et al., 2009). As shown in Figure 2, the biomass enters a bubbling fluidized bed gasifier where the steps of drying, devolatilization, and partially heterogeneous char gasification take place at temperatures of 850- 900 °C. Residual biomass char leaves the gasifier together with the bed material through an inclined, steam fluidized chute towards the combustion reactor. The combustion zone (riser) serves to heat up the bed material and is designed for high solid transport rates controllable by staged air introduction. After particle separation from the flue gas in a cyclone, the hot bed material flows back to the gasifier via a loop seal (Proll et al., 2007).

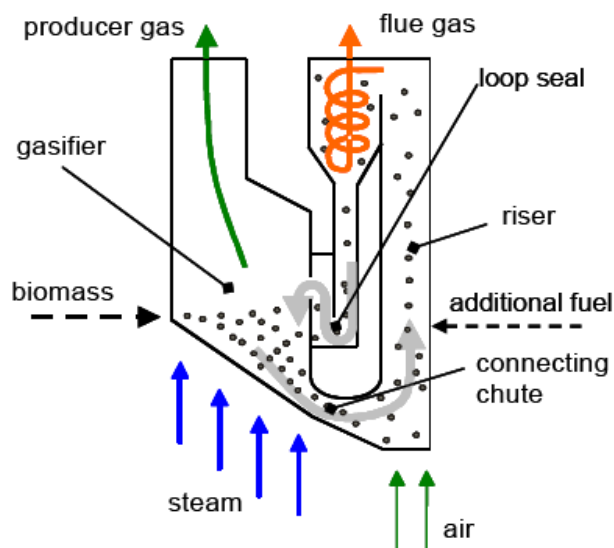


Figure 2. Schematic of dual fluidized bed steam gasification reactor or FICFB-gasification system (Pfeifer et al., 2009)

Dual circulating fluidized beds have been commercially demonstrated in coal-fired power stations (Osowski et al., 2006). The process involves two reactions steps. In the first one, the catalytic decomposition of methane to H_2 and carbon which deposits on the catalyst takes place. In the second step, the carbon deposited on the catalyst is gasified by steam into H_2 and CO_2 . The reactions steps are carried out separately in two parallel reactors both containing the same Ni-based catalyst. These two steps are carried out in cyclic manner by switching from a methane-containing feed stream to a steam-containing feed

stream at set time intervals (Choudhary et al., 2001). In spite of these claimed advantages, there are still issues concerning circulating fluidized bed gasifiers as follows: (i) particle content in the raw gas is close to the one in fixed beds while tar formed is higher (ii) investments and operating costs are higher than in fixed bed gasifiers (Corella et al., 2007; Osowski et al., 2005).

More recently, a new process of biomass gasification designated as the external circulating concurrent moving bed gasifier or ECCMB system has been proposed. This system is composed of a moving-bed with gasification and combustion zones. A circulation loop allows transport of bed material and as a result heat transfer between the two zones. The char deposited on the catalyst is burned off in the combustion zone and as a result the catalyst is continuously regenerated. The combustion also provides the energy for the endothermic steam gasification in the gasification zone. A lab-scale facility was established to demonstrate this process concept, where steam gasification of biomass and combustion of the produced char can occur simultaneously. A H₂ content of 53.3 mol % in dry gas and the tar yield of 0.7 g/Nm³ dry gas were obtained with a 40 cm bed height an S/B ratio (steam/biomass mass ratio) of 0.4 g/g at 800 °C using calcined olivine as the catalyst. The obtained results show that this new concept of biomass gasification for hydrogen rich gas is feasible. It also appears that concurrent biomass and catalyst transport in the gasification zone is a good alternative to enhance process and tar yield reduction.

Viking Company proposes a 500 kW LTCFB gasifier (Low-Temperature Circulating Fluid Bed) specially developed for difficult fuels with high alkali contents. Until now, it has successfully been operated on straw containing more than 12wt% ash, pig manure and chicken litter.

Furthermore, gasification systems in an integrated plant for synthetic natural gas production shows that dual circulating bed gasifiers of Figure 5 are more suitable overall, due to a more advantageous energy conversion related to the producer gas composition (Gassner and Maréchal, 2009).

3.2.3 Advantages/disadvantages of the different gasifying reactor

While there are a limited number of studies directly comparing fluidized and fixed-bed reactors, a recent study reports that the fluidized-beds for both steam and dry methane reforming with Ni-based catalysts provide a high CH₄ conversion and low coke formation as compared to the fixed bed. Chen et al., 2009, reported a similar result with a Ni/ Al₂O₃ catalyst used for the dry reforming of methane at 800 °C. Neither study reported catalyst attrition.

However, catalyst attrition may be an issue limiting catalyst utilization in fluidized bed reactors. Materials such as dolomite and many conventional, high surface area metal oxide supports may experience high attrition. High-strength materials, such as olivine and specially designed catalysts are recommended.

Listed below are key criteria that need to be addressed when selecting a gasifier reactor:

- Capital costs
- Operating and maintenance
- Gasifier configuration robust and without moving parts,
- Avoiding as much as possible feedstock preparation such as drying, separation, size reduction or pelletization.

A reported comparison between fixed beds and fluidized bed reactors based on technology, use of material, use of energy, environment and economy shows that there is no significant advantage between these two systems (Warnecke, 2000). Selection of a particular gasifier type and its design will require however a close scrutiny of a number of other factors such as the properties of the feedstock (both chemical and physical), the quality of product gas required, the heating method and the various operational variables involved (Demirbas, 2004).

The features of a fluidized bed gasifier that make it appear less attractive are a more complex design and operation and energy expenses in biomass particle size reduction. Particle size reduction as well entails the formation of dust unsuitable for fluidization.

The product gas contains as well a higher tar content requiring extensive external gas cleaning. High plant costs make fluidized bed gasification economical at the 5 to 10MW scale.

In comparison to fluidized bed gasifiers, the fixed bed gasifier appears the most adaptable for the production of low calorific value gas in small-scale power generation stations with gas turbines. The fixed bed gasifier plant is simpler in this application and has no or very few moving parts (McKendry et al., 2002c).

3.3 Gasification Conditions

The operating conditions play a very important role in biomass gasification in all respects, including carbon conversion, product gas composition, tar formation, and tar reduction. The most important influencing parameters include temperature, pressure, gasifying medium, catalyst and additives, and residence time. The selection of these parameters also depends on the type of gasifier used. A homogeneous bed temperature profile and well functioning bed fluidization are of the utmost importance in avoiding disturbances in the operation of a fluidized bed gasifier.

3.3.1 Temperature

Researchers have conducted extensive studies reviewing the influence of temperature on tar production during biomass gasification (Skoulou et al., 2009). To achieve high carbon conversion of biomass as well as low tar content in the resultant product gas, a high operating temperature (above 800°C) in the gasifier is recommended. With the increase in temperature, combustible gas content, gas yield, hydrogen, and LHV (Lower Heating Value) all increased significantly, while the tar content decreased sharply. This showed that high temperature is favorable for biomass gasification (Chen et al., 2008; Luo et al., 2009; Gao et al., 2009).

Moreover, Mahishi and Goswami, 2007 and Salaices et al. 2010, reported that the hydrogen at chemical equilibrium initially increased with temperature, reached a maximum and then gradually decreased at the highest temperatures.

Temperature not only affects the amount of tar formed, but also the composition of tar by influencing the chemical reactions involved in the gasification network (Wolfesberger et al., 2009). To produce a relatively clean gas by increasing temperature, several operational strategies are reported in the literature. Fagbemi et al., 2001, showed that tar yields augmented first while temperature rose up to 600°C, and then dropped after this temperature was surpassed. At higher temperatures, primary C_nH_m were less significant in the reaction network and secondary reaction (i.e. tar cracking) prevailed. This led to considerable tar decomposition (Han and Kim, 2008). In the oxidization zone, reactions between char and oxygen had however a more dominant role (Zhao et al., 2009).

Therefore, Mahishi and Goswami, 2007, mentioned several factors that limit the operating temperature. He presents a typical gasification temperature for various feedstocks and the influence of temperature change on some critical factors. Besides tar content, these factors are the gas heating value, char conversion and the risk of sintering.

3.3.2 Pressure

Several researchers have investigated pressurized biomass gasification. Knight, 2000 investigated the effect of system pressure for biomass gasification. When the pressure was increased to 21.4 bars, almost complete elimination of phenols was observed for whole Wisconsin tree chips. Although the amount of total tar decreased, the fraction of polycyclic aromatic hydrocarbons increased with increasing pressure. Pressurized gasification (5–20 bar) was also investigated in the Lund University (Wang et al., 2000; Padban, 2000). Wang et al., 2000, observed a decrease in the amount of light hydrocarbons (LHC, lower than naphthalene) and tar in the fuel gas with an increasing equivalence ratio (ER) for pressurized gasification with 100% carbon conversion.

3.3.3 Gasifying Medium

Different gasifying agents such as air, steam, steam–oxygen and carbon dioxide have been reported in the literature. Selectivity of the gasification reaction varies with different gasifying media. In general, the gasifying agent determines the overall calorific value of the gas exiting the gasifier. A low energy gas results from using air as the gasifying agent, which is mainly because the gas is diluted by nitrogen from the air (Li et al., 2004;

Mathieu and Dubuisson, 2002; Fiaschi and Michelini 2001; Li et al., 2001; Gil et al., 1999). A medium energy gas is produced from using steam or a combination of steam and oxygen (Ginsburg and de Lasa, 2005; Zhang et al., 2004; Tomishige et al., 2004) Rapagna et al., 2002; Coll et al., 2001; Schuster et al., 2001; Garcia et al., 1999; Minowa and Inoue, 1999; Gil et al., 1999; Rapagna and Latif, 1997). In addition, combined use of steam and air gave much higher H₂ yields than with air alone. This also helps to reduce the process energy requirements which are normally provided by combusting a fraction of the biomass (Mahishi and Goswami, 2007; Brown et al., 2009; Swami and Abraham, 2006).

3.3.4 Equivalence Ratio (ER)

The Equivalence Ratio (ER) is a key parameter which considers the actual air/biomass ratio divided by the stoichiometric air/biomass ratio as follows:

$$ER = \frac{n_{oxidant} / n_{wood}}{n_{oxidant,stoich} / n_{wood}}$$

The ER strongly influences the type of gasification products. Tar yield and tar concentration decreases as the ER increases because more oxygen is available to react with volatiles in the flaming pyrolysis zone. This effect of the ER is more significant at higher temperatures. The ER is very crucial because a higher value of the ER results in lower concentrations of H₂, and CO, and higher CO₂ content in the product gas, thus decreasing the heating value of the gas. Although the total tar concentration decreased by almost 30 % when the ER was increased from 0.22 to 0.32 for a temperature of 700°C, the fraction of PAH (polynuclear aromatic hydrocarbons) increased in the total tar. The decrease in total tar concentration could be even more significant at higher temperatures. Almost all phenols were converted at an ER of 0.27. An increase in the amount of benzene, naphthalene, and 3- and 4-ring compounds, were reported by Narvaez et al., 1996.

Lv et al., 2004, divided biomass gasification into two stages based on the ER. In the first stage, the ER varied from 0.19 to 0.23. The gas yield was also increased from 2.13 to 2.37Nm³/kg biomass and the LHV of the gas was augmented from 8817 to 8839 kJ/Nm³. In the second stage, the ER ranged from 0.23–0.27 and the LHV decreased with ER, with this being the result of the combustion influence. However, according to Zhou et al., 2000, ER does not significantly influence the concentration of nitrogen containing products during biomass gasification. A slight increase in NH₃ was observed when the ER was increased from 0.25 to 0.37 at 800 °C for sawdust gasification.

3.3.5 Residence Time

Residence time has a significant influence on the amount and composition of the produced tars. According to Kinoshita et al., 1994, the fraction of oxygen-containing compounds tends to decrease by increasing residence time. Furthermore, yields of one and two aromatic ring compounds (except benzene and naphthalene) decrease with residence time whereas that of three and four ring species increases. Corella et al., 1999, observed a decrease in the total tar content when the space time was augmented in biomass gasification with a bed of dolomite.

Advantages and technical challenges of different gasifying agents, gasifier designs and operations for syngas production are summarized in Table 1.

Table 1. Advantages and technical challenges of different gasifier designs, gasifying agents and operations for syngas production (Dhepe and Fukuoka, 2008)

	Main Advantages	Main Technical Challenges
Gasifier design		
Fixed/moving bed	<ol style="list-style-type: none"> 1. Simple and reliable design 2. Capacity for wet biomass gasification 3. Favorable economics on a small scale 	<ol style="list-style-type: none"> 1. Long residence time 2. Non-uniform temp distribution 3. High char or/and tar contents 4. Low cold gas energy efficiency 5. Low productivity
Fluidized bed	<ol style="list-style-type: none"> 1. Short residence time 2. High productivity 3. Uniform temperature distribution 4. Low char or/and tar contents 5. High cold gas energy efficiency 6. Reduced ash-related problems 	<ol style="list-style-type: none"> 1. High particulate dust in syngas 2. Favorable economics on a medium to large scale
Gasifying agents		
Air	<ol style="list-style-type: none"> 1. Partial combustion for heat supply of gasification 2. Moderate char and tar content 	<ol style="list-style-type: none"> 1. Low heating value (4-6MJ/Nm³) 2. Large amount of N₂ in syngas (e.g., > 50% by volume) 3. Difficult determination of ER (usually 0.2–0.4)
Steam	<ol style="list-style-type: none"> 1. High heating value syngas (13–20 MJ/Nm³) 2. H₂-rich syngas (e.g., > 50% by volume) 	<ol style="list-style-type: none"> 1. Require indirect or external heat supply for gasification 2. High tar content in syngas 3. Require catalytic tar reforming
Carbon dioxide	<ol style="list-style-type: none"> 1. High heating value syngas 2. High H₂ and CO in syngas, and low CO₂ in syngas 	<ol style="list-style-type: none"> 1. Require indirect or external heat supply 2. Required catalytic tar reforming

Gasifier operation		
Increase of temperature	<ol style="list-style-type: none"> 1. Decreased char and tar content 2. Decreased methane in syngas 3. Increased carbon conversion 4. Increased heating value 	<ol style="list-style-type: none"> 1. Decreased energy efficiency 2. Increased ash-related problems
Increase of pressure	<ol style="list-style-type: none"> 1. Low char and tar content 2. No costly syngas compression required for downstream utilization of syngas 	<ol style="list-style-type: none"> 1. Limited design and operational experience 2. Higher costs of a gasifier at a small scale
Increase of ER	<ol style="list-style-type: none"> 1. Low char and tar content 	<ol style="list-style-type: none"> 1. Decreased heating value of syngas

3.3.6 Conclusions and Recommendations for Design of Gasifiers

As described in the previous sections gasification in fluidized beds offers special features for biomass gasification. Furthermore, catalytic gasification in fluidized beds brings new opportunities for implementing this technology at lower temperatures (lower than 700°C) as follows: a) limits tar content, b) reduces ash agglomeration, c) promotes the water gas shift reaction, an exothermic reaction, reducing gasification energy requirements.

3.4 Catalysts for Steam Gasification of Biomass

Some catalysts have been used as active bed additives inside the gasifier during gasification. There is a great potential of in-bed additives in terms of tar reduction and thus avoidance of complex downstream tar removal methods. These bed additives act as in-situ catalysts, promoting several chemical reactions in the same gasifier. The presence of additives influences not only the gas composition, but also the heating value of the product gas. The use of catalysts during biomass gasification promotes char gasification, changes the product gas composition, and reduces the tar yield. The addition of active bed materials also prevents the solid agglomeration tendencies and subsequent choking of

the bed. These are the reasons why the major part of ongoing biomass gasification research deals with the development of new catalysts or the improvement of existing active materials to produce high quality tar free syngas and /or hydrogen. A significant number of studies have been carried out using dolomite, olivine, alkali and noble metals catalysts for this purpose.

3.4.1 Dolomite, Olivine and Alkali metal Based Catalysts

Dolomite, a magnesium ore with the general formula $MgCO_3 \cdot CaCO_3$, has been considered as a catalyst in biomass gasification. It has attracted much attention as it is a cheap disposable material that can significantly reduce the tar content of the product gas. The main issue with these materials is their fragility as they are soft and quickly attrite in fluidized beds under the prevalent high turbulence conditions.

Dalai et al., 2003, studied the performance of a CaO catalyst by varying the catalyst loading from 0 to 8.9 wt.% during temperature programmed gasification (TPG) and constant temperature gasification (CTG) processes. The experiments showed that the use of CaO as a catalyst reduced the maximum gasification temperature by 150°C. Also, total fuel yields (H_2), and carbon yields were significantly increased with the impregnation of CaO in cellulose, cedar, and aspen. The rate of production and cumulative production of H_2 from cedar and aspen were significantly higher than those from cellulose for catalytic and non-catalytic TPG and CTG processes.

A few studies have been done recently about the catalytic activity of olivine for tar elimination. Hu et al., 2006, tested calcined olivine and dolomite as downstream catalysts in a fixed-bed reactor. The results show that the catalytic activities of calcined catalysts are higher than the activities of the natural catalysts. A similar system was used by Lopamudra et al., 2005, who observed that tar conversion increases with a temperature rise from 800 to 900°C. They found that water soluble heterocyclic compounds can be 100% converted at 900°C. Additionally, the conversion of heavy polyaromatics can increase from 48% to 71% with the use of 17 wt% olivine in sand at 900°C, compared to a conversion of up to 90% with 17 wt% of calcined dolomite. A total tar amount of 4.0 g/m^3 could be reduced to 1.5 and 2.2 g/m^3 using dolomite and olivine, respectively.

Aznar et al., 2006, conducted parametric studies using dolomite as a tar cracking catalyst. The feedstock was composed of blends of plastic waste with pine wood sawdust and coal, at flow rates of 1–4 kg/h. The operating variables that were studied were: gasifier bed temperature (750 – 880°C), equivalence ratio (0.30 – 0.46), feedstock composition, and the influence of secondary air insertion in freeboard. As a result, a gas with medium hydrogen content (up to 15% dry basis) and low tar content (less than 0.5 g/m³) was obtained. Additionally, these authors found that the injection of secondary air in the freeboard reduces tar content by 50 %. Tar content obtained was less than 0.5 g/m³ and as a result an essentially clean gas was obtained under these conditions

Xu et al., 2005, demonstrated that for atmospheric gasification of biomass, CaO could also be an effective on-site CO₂ acceptor, provided the reaction temperature is controlled at appropriately low values, such as 973°K. It was shown that at temperatures <1000°K, the acceptor captured CO₂ with fuel gasification, lowering the CO₂ content in the product gas to a few percent (<10 vol%), and increasing the gas's heating value considerably. The addition of CaO into the fuel increased the H₂ content of the gas, while decreasing its CO concentration, irrespective of the reaction temperature. This result corroborates the commonly known catalytic effect of CaO on CO shift and tar reforming/cracking reactions.

Monovalent alkali metals such as lithium (Li), sodium (Na), potassium (K), rubidium (Rb), cesium (Cs), and francium (Fr), belong to group 1A of the periodic table. They are all highly reactive and electropositive. Alkali metals, principally K and to a lesser extent Na, exist naturally in biomass and accumulate in the gasifier ashes. Furthermore, the use of ash itself, as a catalyst, solves the problem of ash waste handling and gives an added value to the gasification by increasing the gasification rate and reducing the tar content in the produced gas. However, the major disadvantage of these ash based catalysts is their activity losses due to particle agglomeration. Sutton et al., 2001, reported several disadvantages related to the direct addition of alkali metals, such as the difficult and the expensive recovery of the catalyst, increased char content after gasification, and ash disposal problems. On the other hand, Lee et al., 2000 found that the addition of Na₂CO₃ enhances the catalytic gasification of rice straw over a nickel catalyst and significantly

increases the formation of permanent gases. The same authors found that the formation of permanent gases depends on the nature of the alkali metal carbonate with the following reactivity order being proposed as $\text{Na} \geq \text{K} > \text{Cs} > \text{Li}$.

The use of activated alumina as a secondary catalyst for tar reduction comes from its high catalytic activity, comparable to dolomite (Simell et al. 1992), although it deactivates by coke faster than dolomite. Sami et al (Juutilainen et al. 2006), tested its activity in the selective oxidation of tar and ammonia using catalysts containing zirconia and alumina. Their performance was compared with that of nickel and dolomite catalysts. Synthesis gas with toluene as a tar model compound was used as feed in a fixed bed tube reactor. In the presence of oxygen, zirconia and alumina-doped zirconia yielded high toluene and ammonia conversions, below 600°C. These catalysts were the most active catalysts for toluene oxidation below 700°C and for ammonia oxidation below 650°C. At higher temperatures, these impregnated $\text{ZrO}_2/\text{Al}_2\text{O}_3$ catalysts performed better. Oxidation selectivity was improved and toluene and ammonia conversions were higher. These authors concluded that the both zirconia and alumina promoted toluene and ammonia conversions at lower temperatures. This shows the enhanced oxidation activity of zirconia with alumina improving oxidation selectivity. H_2S had little effect on the activity of alumina-doped zirconia.

3.4.2 Nickel Based Catalysts

Among the transition metals (group VIII), nickel is the most widely used in the industry to catalyze steam reforming and dry reforming reactions (Rostrup-Nielsen and Hansen, 1993). Commercially available nickel reforming catalysts have been used extensively for biomass gasification (Aznar et al., 1993; Aznar et al., 1998; Baker et al., 1987; Caballero et al., 1997; Elliott et al., 1993; Mudge et al., 1985). Heavy hydrocarbon steam-reforming catalysts are according to Aznar et al., 1998 more active than light hydrocarbon steam reforming catalysts for tar removal. These catalysts promote steam and dry reforming reactions and water-gas-shift reactions. They are very effective in tar conversion and in adjusting the gas composition to syngas desired H_2/CO ratios. According to Olivares et al., 1997 nickel reforming catalysts display 8-10 times more reactivity than calcined dolomite.

However, when using nickel-based catalysts, several deactivation mechanisms occur including poisoning by sulphur, chlorine, and alkali metals, sintering of Ni particles and coke formation (Abu El-Rub et al. 2004). Ni-based catalysts deactivate rapidly due to coke formation and catalyst attrition. Coke formation is inherent in the steam reforming processes and in the high temperatures associated with reforming. These conditions promote higher hydrogen and carbon yields. Coking of Ni-based steam reforming catalysts is reasonably well understood (Trimm, 1997). High temperatures promote dissociation of tars, light and unsaturated hydrocarbons both in the gas phase and on the catalyst surface producing carbon deposits. They can block the access to the catalyst pore network resulting in catalyst activity loss. The formed carbon may be gasified, encapsulated on the surface or diffused through the nickel crystallites. Carbon may at a later reaction stage nucleate and/or precipitate lead to the formation of carbon whiskers. Formation of carbon whiskers lifts nickel crystallite from the surface resulting in catalysts sintering. Therefore, nickel-based catalysts deactivate by carbon in two ways: (1) encapsulation of nickel crystallites by layers of inactive carbonaceous material, and (2) formation of inactive bulk nickel carbide phases (Bangala et al., 1998; Bartholomew et al., 1980; Bartholomew and Sorensen, 1983; Rostrup-Nielsen, 1997; Trimm, 1997). Furthermore, there is a tendency for coke to be formed with the increase of unsaturation, molecular weight and aromaticity of the feed.

Regarding coke formation, it can be minimized through the use of excess steam as required by gasification stoichiometry. In this respect, it is possible to estimate a minimum steam/carbon ratio required to avoid coke formation (Dibbern et al. 1986). This provides a very useful guideline to establish the desired operating conditions. However, the practical negative effect is that it increases the overall energy costs for plant operation. Therefore and given the above mentioned consideration, it is crucial to maintain as low steam/C ratio as possible (Trimm, 1997).

However, if coke deposits on the catalyst surface at the same rate as it is removed by combustion, the catalyst surface remains clean. Thus, the catalyst remains effective in cracking newly formed tar and/or preventing char formation yielding gas products with increased ability (Baker et al., 1987). This is the ideal scenario that may happen in auto-

thermal gasification of biomass where the air fluidizing the bed (catalyst and biomass) may contribute to keeping the catalyst free of coke. Otherwise, if coke removal is not carefully performed it can lead to poor catalyst activity, selectivity and limited catalyst life.

The formulation of nickel catalysts involves (i) an active phase (i.e. Ni), (ii) promoters and (iii) a support phase. Generally, higher nickel content results in lower tar yield and higher H₂ and CO yields. On the other hand, according to Bartholomew et al, 1980, nickel content has a significant effect on the catalyst deactivation by coking. They suggested that lower metal crystallite concentration results in stronger interaction with the support phase. This normally yields higher metal dispersion and therefore more resistance to deactivation caused by carbon fouling. Metal dispersion may be improved by addition of promoters and thus minimizing the coking tendency. It has been proven that the activity and life (deactivation) of nickel based catalysts depend greatly on the type of support and the presence of additives and promoters.

The support phase gives the catalyst mechanical strength and protection against severe conditions such as attrition and heat (Abu El-Rub et al., 2004). The pore structure of the support, the metal-support interactions, and the acidity-basicity of the support significantly influence the metal dispersion, metal crystallite size and carbon deposition on the catalyst surface; thus affecting the overall catalytic performance and catalyst coking resistance (Wang and Lu 1998b). Baker et al., 1988 also reported that the acidity of the support affects coke deposition and catalyst deactivation. For instance, higher acidity of support materials favors tar cracking reactions causing higher carbon buildup on the catalyst surface. On the contrary, Mark and Maier.1996 reported that the pore structure or the support type did not influence the rate of dry-reforming of methane. It is considered that the support role is to stabilize the metal surface, which in turn is responsible for catalytic activity.

Alumina-based materials are considered to be the primary support material for most reforming catalysts. Gadalla and Bower, 1988, investigated performance of α -Al₂O₃ and γ -Al₂O₃ supported Ni catalysts for the reforming of methane with CO₂. They reported

that Ni/ α -Al₂O₃ catalyst provided lower methane conversion than Ni/ γ -Al₂O₃, given the stable allotropic form and smaller surface area of α -Al₂O₃. They also reported that Al₂O₃ supports with MgO/CaO addition were more stable than with silica, which favor rapid Ni/Al₂O₃ catalyst deactivation. Wang and Lu, 1998a; also reported higher conversion and lower deactivation rate for Ni/ γ -Al₂O₃ over the Ni/ α -Al₂O₃ catalysts. They found that nickel aluminate (Ni Al₂O₄) was formed due to phase transformation of γ -Al₂O₃ supported Ni catalyst during calcinations. While this aluminate is hard to reduce at lower temperatures, reduced Ni/Al₂O₄ appears active for reforming reactions, being quite resistant to coking.

Wang and Lu, 1998b investigated the effect of various oxide-supports with respect to the catalytic performance and stability of Ni catalysts for dry reforming of methane. Results of their investigation are summarized in Table 2.

Table 2. Physical properties, catalytic activities and deactivation characteristic of various oxides-supported Ni catalysts (Wang and Lu, 1998).

Catalyst	Support S _{BET} (m ² /g)	Catalyst S _{BET} (m ² /g)	Ni crystallite size (nm)		CH ₄ Conversion @ 800 ^o C (%)	Deactivation <i>Conv</i> _{3 h} / <i>Conv</i> _{10 min}	Carbon deposition (g of C / g of Cat)	Sintering d ₂ /d ₁
			Fresh (d ₁)	Used (d ₂)				
Ni/La ₂ O ₃	6.4	16.4	15.5	37.5	98	0.97	0.48	2.4
Ni/SiO ₂	290	239	12	21.8	96.2	0.87	0.068	1.8
Ni/TiO ₂	9.4	8.4	27.6		10			
Ni/ α -Al ₂ O ₃	0.8	1.2	31.7	37.5	92.4	0.72	0.15	1.2
Ni/ γ -Al ₂ O ₃		157			95.8	0.95		
Ni/MgO	147.8	55.5			95.6	1.1	0.049	
Ni/CeO ₂	52	34			65	0.65	0.02	

Ni crystallites formed on the SiO₂ surface were smaller in size, as a result of the high surface area and well developed support porosity. Lower porosity of Ni/ α -Al₂O₃ and Ni/TiO₂ resulted in lower dispersion of metal and thus larger crystallite sizes. On the

other hand and in spite of La_2O_3 being nonporous, Ni crystallites formed on this material are smaller in size. La_2O_3 has a higher ability of disperse metal particles on the surface. Regarding Ni catalysts supported on MgO, it is apparent that NiO-MgO forms a solid solution. As a result, it is a very hard to reduce Ni in the Ni/MgO catalyst. This catalyst has to be pre-reduced at more than 800°C to become active.

3.4.3 Conclusion and Recommendations for Catalysts

While there have been a number of catalysts proposed for catalytic gasification of biomass, it was felt given the previous experience of CREC group that Ni- α alumina provided a good basis for this PhD study. This was done with the understanding that emphasis of this research will be placed on thermodynamic and kinetic models of catalytic gasification. It was anticipated from the initiation of this research that the thermodynamics and kinetic models proposed will be developed in such a manner that could be easily extended to other catalysts with enhanced properties (higher specific surface area, lower tar formation). These catalysts with enhanced properties are currently being considered by the CREC research team.

3.5 Thermodynamic Studies of Steam Gasification of Biomass

Since modeling studies of the thermo-chemical conversion of biomass have received considerable attention, different modeling approaches have been taken into account. Two of these models are of interest for this review.

3.5.1 Equilibrium Model for Biomass Gasification

One possible approach to describe biomass gasification is to take advantage of thermodynamics equilibrium. The input data are: the amount of elements C, H, and O in the system, the temperature, and the pressure (Schuster et al., 2001). A mathematical solver is used to minimize the Gibbs energy of a closed system to calculate the composition of the product mixture. This tool relies on thermodynamic databases that contain the values of the standard Gibbs energy of the components. Most gaseous components can be found in such databases, but concerning solid phase, only pure carbon

is taken into account. Such a model does not require any knowledge of the mechanisms of transformation. Moreover, the model is independent of the reactor configuration and not limited to a specified range of operating conditions.

Li et al., 2004, developed an equilibrium model applied to air gasification of biomass in a circulating fluidized bed. Comparisons were made by Boissonnet et al., 2002, and 2003, between the predictions of the equilibrium model applied to steam gasification and experimental results from Schuster et al., 2001, and Rapagna et al., 2000. It can be seen that the model gives correct orders of magnitude and trends. However, the equilibrium model always overestimates the yield of H_2 and CO , whereas it underestimates the yield of CO_2 . It predicts a gas nearly free of CH_4 , free of tars (modeled as $C_{10}H_8$), and no solid residue. Thus, this type of model does not seem to be accurate enough for the purpose of designing gasifiers.

Melgar et al., 2007, present a mathematical model for the thermochemical processes in a downdraft biomass gasifier. The model combines the chemical equilibrium and the thermodynamic equilibrium of the global reaction, predicting the final composition of the producer gas as well as its reaction temperature. According to the authors, the model helps to predict the behavior of different biomass types and is a useful tool for optimizing the design and operation of downdraft biomass gasifiers.

Yan et al., 2006, developed a non-stoichiometric thermodynamic model based on minimum free energy to predict the performance of hydrogen production from biomass gasification in super critical water. The trend of the prediction results is in strong agreement with the trend of the experimental data, especially as we take into consideration the carbon conversion efficiency.

Ginsburg and de Lasa, 2005 modified a non-stoichiometric equilibrium model from the literature to analyze experimental data. Only major product species such as H_2 , CO , CO_2 , H_2O , and CH_4 , were considered for the equilibrium calculations. From the elemental analysis of the wood, it was shown that the compositions of nitrogen and sulfur species evolving from the reactor are negligible in terms of the equilibrium calculations. This is in agreement with previous models (Schuster et al., 2001).

This model considers two main reactions occurring in the gas phase, which are considered to be at equilibrium: a) steam reforming of methane, and b) water-gas-shift. However, the experimental product gas composition deviates from the equilibrium model as a result of the inaccurate assumption that the dry reforming reaction reaches equilibrium over the given reaction times. Ginsburg and de Lasa, 2005, concluded that a comprehensive kinetic model for dry reforming under the conditions of catalytic gasification of biomass is required.

Li et al., 2001, 2004, proposed a phenomenological model adapted from the pure equilibrium model incorporating experimental results regarding unconverted carbon and methane to account for non-equilibrium factors. This model calculates product gas compositions, heating value and cold gas efficiency in sound agreement with the experimental data. This group found that experimental evidence indicated that the pilot gasifier deviated from chemical equilibrium due to kinetic limitations. The experimental study was completed on a circulating fluidized bed gasifier to examine the effects of operating parameters on the gas composition (air ratio), gasification efficiency and tar yield.

Schuster et al., 2001, developed a model for steam gasification of biomass by applying thermodynamic equilibrium calculations. Fuel composition (ultimate analysis and moisture content), temperature, and amount of gasification agent were varied over a wide range. The influence of these parameters on amount, composition, and heating value of product gas and process efficiencies were evaluated. It was shown that the accuracy of an equilibrium model for the gas composition is sufficient for thermodynamic considerations. Sensitivity analysis showed that gasification temperature and fuel oxygen content were the most significant parameters determining the chemical efficiency of the gasification. The thermodynamic model offered the opportunity to evaluate different gasification processes as well as fuel variations. The results of the equilibrium model for the gasifier (LHV gas yield) were in the range of measured results, though the CH₄ content in the product gas was overestimated. It was shown that the discrepancies in the prediction of the gas composition did not significantly influence the overall efficiency.

Ruggiero and Manfrida, 1999, emphasized the potential of the equilibrium model when the Gibbs free energy is taken into consideration. This proceeding can be used under different operating conditions for predicting producer gas composition and the corresponding heating value.

Altafini and Mirandola, 1997, present a coal gasification model by means of chemical equilibrium, minimizing the Gibbs free energy. These authors analyzed the influence of the ultimate analysis and the gasifying agents/fuel ratio on the equilibrium temperature (adiabatic case) in order to obtain the producer gas composition and the overall and conversion efficiency. They concluded that the equilibrium model fits the real process well.

Kilpinen et al., 1991, also showed that solid carbon and CH_4 content were under predicted to some extent by an equilibrium approach. This was mainly caused by the slow kinetics of the heterogeneous gasification and the decomposition of CH_4 .

3.5.2 Improved Thermodynamic Approach

It was also found that improvements of these models have been examined only in the case of air gasification. Kersten et al., 2002, have developed a quasi-equilibrium temperature (QET) model based on equilibrium calculations made at a temperature lower than the reactor temperature. Kersten et al., 2002, Li et al. 2004, and Jand et al., 2006, added empirical relations to their initial thermodynamic models to calculate the carbon conversion and the yield of CH_4 . The use of these correlations is limited to the reactors under study. The QET and correlation based models are empirical and dead end approaches restricted to the studied systems.

3.5.3 Conclusions and Recommendations for Thermodynamic Studies

Given the lack of a comprehensive thermodynamic equilibrium model which includes the expected main gasification reactions (reacting system described by two independent reactions, WGS and SRM) it was set as a goal for this PhD dissertation research the establishment of an equilibrium model based on C, H and O elemental balances and

various product species up to C₆ hydrocarbons. It was expected that this model should be developed to establish the effect of biomass composition, temperature, and steam on the various gas product molar fractions. On this basis, it was anticipated at the onset of this research that the significant parameters determining the chemical inter-conversions and distribution of chemical species during biomass catalytic gasification will be identified.

3.6 Kinetic Studies of Catalytic Steam Gasification of Biomass

The global steam gasification chemistry can be described by Eq (9):



An initial solid of known formula C_xH_yO_z reacts under heat and steam to give two kinds of products:

- A solid residue of generic formula C_{x'}, H_{y'}, O_{z'}.
- Gases.

3.6.1 Characteristic Time Analysis

Some authors have developed a rational approach to simplify the kinetic models. A comparison is made between the time scales of the different phenomena involved in the reaction.

Pyle and Zaror, 1985, accounted for external heat transfer limitations. Experimental data were used to validate the simplified models for different particle sizes under slow pyrolysis conditions. Bryden et al., 2002, considered the case in which internal and external heat transfer processes were both limiting.

In order to show which particle size could be used for an intrinsic kinetic study of biomass pyrolysis, Simmons and Gentry, 1986, plotted the boundaries between thermal and chemical regimes as a function of temperature and particle size. According to their calculations, at 773°K, particles smaller than 100 μm are required to be under chemical control but according to his flash pyrolysis experiments, this size is reduced to 10 μm.

The relative influence of the different heat transfer phenomena on the transformation was shown for different gas velocities.

More recently, Peters and Bruch, 2003, plotted the ratio of the characteristic time of the chemical reaction to the internal heat conduction time, versus particle diameter, for different temperatures up to 873°K. At this temperature, the transition zone between the chemical and thermal regimes was found to be between 50 and 500 μm . One can notice that the limits found by Peters and Bruch, 2003, and Simmons and Gentry, 1986, are not in agreement. This may be due to the large discrepancies in the data used for the study and to the different operating conditions considered, namely the heating rate.

The characteristic times analysis is an efficient way to derive simplified models that have a physical significance. Nevertheless, such simplified models lose some generality since they are restricted to the range of operating conditions under which adopted model assumptions apply.

It is worth noting that time scales analysis has been mainly used in the case of pyrolysis. No similar study could be found concerning biomass steam gasification.

3.6.2 Models at Particle Scale

Sophisticated models have been derived for gasification at particle scale. They are focused only on one of the two main stages of steam gasification of biomass:

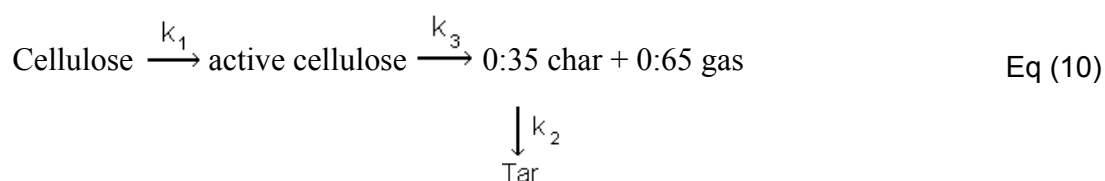
- Pyrolysis reaction which accounts for the decomposition of the initial solid into permanent gases, condensable gases often called tars, and a solid residue often called char;
- Gasification reaction which considers the reaction of the solid residue with reactive gases such as steam.

The first of these models is based on mass and energy balances over the particle, and the associated boundary conditions. The differences between the two models are found in the hypotheses of the models, mainly concerning the description of the physical properties of the solid during the transformation. The evolution with time or conversion of these

properties is sometimes taken into account, which dramatically increases the number of adjustable parameters of the model.

Significant effort has been made on the description of different transport processes involved. However, these models describe the complex chemical phenomena inadequately. Contrary to the physical phenomena, there is no universal law to describe rates of reaction and the nature of the chemical pathways. It is also believed that these various pathways can vary in importance with the operating conditions, especially with changes in the heating rates. Additionally, more detailed description of the chemical pathways increases the number of model parameters to be determined. Finally, the reliability, confidence intervals, and the consistency of the derived kinetic parameters are rarely discussed

For the description of the pyrolysis chemistry, semi global mechanisms are proposed, which are given in Eq (10). These descriptions are interesting since they seem to be a first step towards understanding the complex chemistry of pyrolysis. Nevertheless, the composition of the gases produced cannot be predicted by this model. One possible cause is the lack of adequate consideration of the solid C, H, and O elemental fractions as input data of these models. The material to be gasified is considered as a single pseudospecies, such as biomass or wood, or as a mixture of species (Koufopoulos and Papayannakos, 1991), but it is never referred to by its elemental composition of C, H and O.



Concerning the chemistry of steam gasification of biomass residue, most authors assume that the solid residue is pure carbon. Kinetic laws obtained on coal or pure carbon are then used [(Raman et al., 1981); (Golfier et al., 2004)]. As already stated for pyrolysis reactions, using kinetic laws implies that kinetic parameters are added to the physical parameters to be determined. Note that Di Blasi, 2000, approximately accounts for the true nature of biomass by considering the amount of H and O in the residue. Matsui et al., 1985, compiled the heterogeneous reaction of carbon with steam and the homogeneous

reaction of the water–gas shift into a single reaction, with a stoichiometric coefficient of $(1 + \beta)$ associated to H_2O . From a thermodynamic or kinetic viewpoint, lumping together two independent reactions is risky and should be avoided, especially when one of these reactions, namely the water–gas shift, is well documented.

3.6.3 Kinetic Models of Pyrolysis

Lv et al., 2004, proposed a kinetics model of biomass catalytic pyrolysis, in which the entire process is treated as a single reaction. It assumes that biomass first decomposes to gaseous products, tars, and chars via three competitive reactions and then tars go through a second cracking reaction to produce gases and chars. Through the proposed model, the calculated data fit well with the experimental data obtained from pyrolysis tests of pine sawdust, lignin, and cellulose. The calculated reaction order is in the range of $n = 0.66$ – 1.57 .

3.6.4 Model for Biomass Gasification in a Bubbling Fluidized Bed Reactor

Radmanesh et al., 2006, developed a model for biomass gasification in a bubbling fluidized bed reactor. The model takes into account the pyrolysis and heterogeneous and homogeneous reaction kinetics, as well as the hydrodynamics of the bed and freeboard. The model does not have adjustable parameters. A two-phase model was used to describe the gas phase in the bed, whereas a countercurrent back-mixing model was applied for the char mixing in the bed. It was shown that pyrolysis is an important step in the overall gasification model that can determine the distribution of products and thus the heating value of the product fuel gas. The bubbling fluidized bed gasifier model also showed agreement with experiments on steam gasification of wood.

Corella and Sanz, 2005, presented a 1-dimensional model for an atmospheric circulating fluidized bed biomass gasifier under stationary state. The model is based on the kinetic equations for the reaction network which are solved together with mass and heat balances and with several hydrodynamic considerations. On this basis the axial concentration profiles of ten different species and the temperature were calculated. Even if this model is developed using more rigorous considerations, several important assumptions were left

without proper justification. Thus, this model can only be considered a first model approximation.

Fiaschi and Michelini, 2001, developed a mathematical model of biomass gasification kinetics in bubbling fluidized beds. It is one-dimensional, as it is able of predicting temperature and concentration gradients along the reactor axis. This model considers two phases, a bubble and a dense phase. Mass transfer between the two phases and a quantitative estimation of local bubble and particle properties are included. Too simplistic reaction kinetics is used in the dense phase. The authors claimed that the proposed model showed substantial agreement with experimental data from the literature and other available gasification kinetics. It is felt however that further validation of this model is still required with more adequate kinetics.

3.6.5 Conclusions and Recommendations the Present PhD study.

Various kinetic models for catalytic steam gasification of biomass of differing complexity have been proposed in the literature (Fiaschi and Michelini, 2001; Radmanesh et al., 2006; Corella and Sanz, 2005; Orfao et al., 1999; Aznar et al., 1998; Perez et al., 1997). These reported models lump together a complex network of heterogeneous reactions in one single kinetic rate equation. The resulting rate equation does not provide a distinction between intrinsic kinetic constants and adsorption parameters. Furthermore, the models have no connection with the physicochemical events of either adsorption or reaction taking place. In addition, there is no proper calculation of kinetic parameters and adsorption constants with their adequate statistical indicators (e.g. spans for the 95% interval).

The present study addresses these issues considering as it will be described in Chapter 9,

- a) An additive gasification kinetic model which include the dominant reactions (water gas-shift reaction, steam reforming of methane and dry reforming of methane),
- b) Decoupling of the evaluation of intrinsic kinetic constants of adsorption constants,
- c) Kinetic and adsorption parameters are calculated with narrow spans for the 95% confidence interval and minimum parameter cross correlation.

Chapter 4 Experimental Methods

4 Experimental Methods

4.1 Introduction

Biomass, a hydrocarbon material mainly consisting of carbon, hydrogen, oxygen, nitrogen and minerals, is considered an ideal renewable resource given its abundance, its low sulfur content and its CO₂-neutral emissions (Chen et al., 2008; Balat, 2009). As a result of this, it is becoming one of the most important renewable energy sources in our planet's immediate future. However, in order to utilize biomass, it is necessary to research and develop an efficient and clean technology. Biomass is mainly composed of hemi-cellulose, cellulose and lignin lumps, along with ash and moisture. Theoretically, almost all kinds of biomass with moisture content between 5-30% can be gasified.

Cellulose is the principal carbohydrate constituent of biomass. It is a polymer of glucose with a repeating unit of C₆H₁₀O₅ strung together by β-glycosidic linkages. A typical composition of biomass is presented in Table 3, where cellulose ranges from 22.5 to 50.3 wt%. On the other hand, lignin is the major noncarbohydrate, polyphenolic structural constituent of biomass. It is a highly polymeric substance, with a complex, cross-linked, highly aromatic structure. Lignin is known as the main contributor to tar formation during the gasification process. It ranges from 10.9 to 28.8 wt%.

Table 3. Typical chemical composition of biomass (Balat, 2009)

ASTM Method	E-1821-96 E-1758-95	E-1821-96 E-1758-95	E-1721-95 T-250	E-1755-95
Biomass	Cellulose [Wt%]	Hemi-cellulose [Wt%]	Total Lignin [Wt%]	Ash [Wt%]
Agricultural Residues	30.6 - 43.4	12.2 - 25.5	16.9 - 27.6	2.8 - 13.5
Hardwood	36.4 - 50.3	12.7 - 23.2	16.6 - 28.6	0.4 - 9.7
Herbaceous Energy Crops	22.5 - 39.4	13.8 - 28.8	10.9 - 31.9	2.1 - 12.1
Other wastes	30.7 - 31.4	9.8 - 16.9	15.3 - 16.9	6.6 - 34.2

On this basis, glucose, as a model compound for the cellulose contained in biomass (Figure 3), and 2-methoxy-4-methylphenol representing the lignin species in biomass (Figure 4) were chosen as the key species to evaluate the steam gasification performance of the Ni/ α -alumina catalyst in this research.

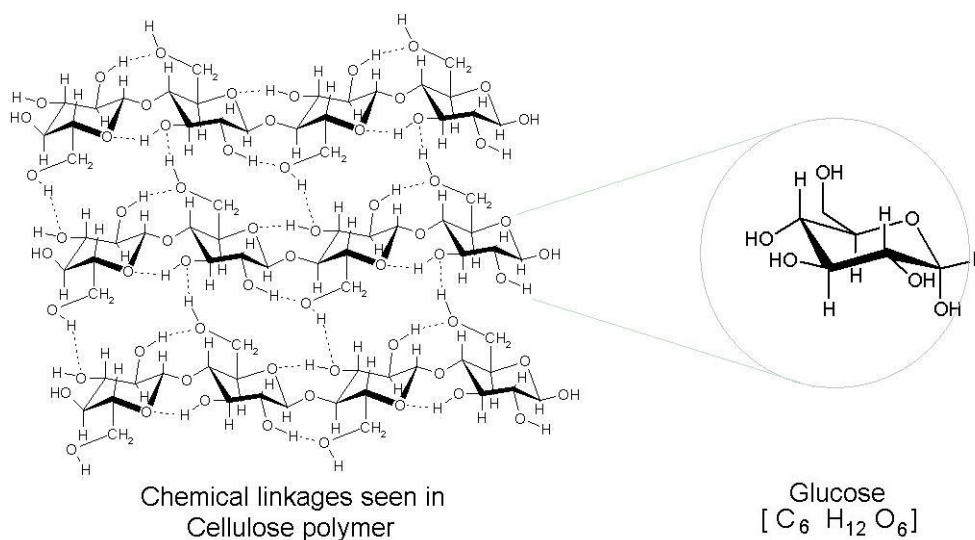


Figure 3. Glucose as a model compound of cellulose

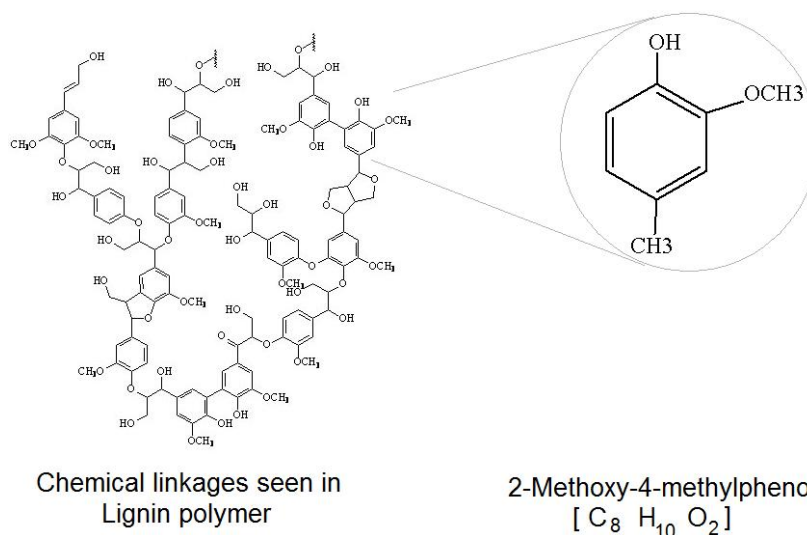


Figure 4. 2-methoxy-4-methylphenol as a model compound of lignin

Experiments were developed using a CREC Riser Simulator (de Lasa, 1992), which works under a fluidized regime and operates in conjunction with a series of sampling valves that allow the experimenter to inject reactants and withdraw products in short periods of time, while following a pre-determined sequence of steps. The identification of gaseous reaction products were analyzed in a Shimadzu 2010 GC/MS system. The coke deposited on the catalysts was measured in a Total Organic Carbon analyzer (TOC-V).

Catalytic steam gasification of biomass experiments were run with mixtures of both glucose–water, and 2-methoxy-4-methylphenol–water at different steam/biomass ratios, varying the reaction contact time from 5 to 30 seconds, and the reaction temperature from 600°C to 700°C. The product distribution obtained from these experiments helped to understand the reaction mechanisms involved in the process.

The detailed reaction system, experimental procedure, and analytical techniques are described in Section 4.3, Section 4.4, and Section 4.6 of this chapter.

4.2 Catalyst and Materials

The α -alumina supported nickel catalyst was prepared according to the incipient wetness technique. Alpha alumina, which acts as support to the active metal, was obtained from Stream Chemicals Incorporated, and its composition was 65% Al₂O₃, 34.8% H₂O, and 0.15% Na₂O. The source of the nickel came in the form of nickel-nitrate hexa-hydrate (Ni

(NO_3)₃·6H₂O) powder. Physical and chemical characterization of the Ni/ α -alumina catalyst included Particle Size Distribution (PSD), Apparent Density (AD), X-Ray Fluorescence (XRF), Temperature Programmed Desorption (TPD), Temperature Programmed Reduction (TPR), Pulse Chemisorption and Surface Area (BET and T-Plot). A detailed catalyst preparation and physical chemical characterization is presented in Chapter 5.

Glucose and 2-methoxy-4-methylphenol were used as model compounds of the cellulose and lignin contained in biomass, respectively. A solution at steam/biomass ratios of 0.4, 0.6, 0.8, and 1.0 were prepared using: a) high purity D-(+)-Glucose, minimum 99.5%, CAS 50-99-7 purchased from Sigma Aldrich, Inc. St. Louis, and b) 2-methoxy-4-methylphenol, minimum 99%, CAS 93-51-6 purchased from Sigma Aldrich Canada, Ltd.

4.3 Reaction System

Experiments were developed using a CREC Riser Simulator (de Lasa, 1992). The Riser Simulator consists of two outer shells, a lower section and an upper section that permit the loading and unloading of the catalyst easily. A quarter-section view of the upper and lower shells of the reactor is shown in Figure 5.

This reactor was designed in such way that an annular space is created between the outer portion of the basket and the inner part of the reactor shell. A metallic gasket seals the two chambers, and an impeller is located in the upper section. A packing gland assembly and a cooling jacket surround the shaft that supports the impeller. Upon rotation of the shaft, an inert gas is forced outward from the center of the impeller towards the walls. This creates a lower pressure in the center region of the impeller thus, inducing a flow of gas upward through the catalyst chamber from the bottom of the reactor annular region where the pressure is slightly higher. The impeller provides a fluidized bed of catalyst particles as well as intense gas mixing inside the reactor.

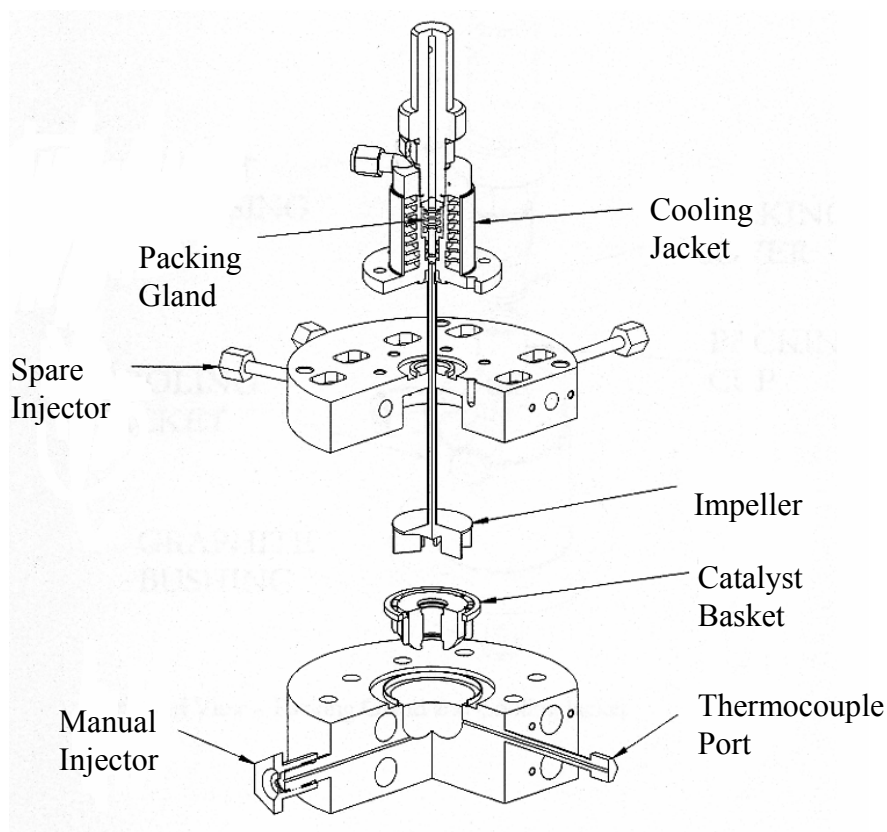


Figure 5. Schematic diagram of the CREC Riser Simulator : quarter section view, upper and lower shells exposed

The reactor volume was found to be $50.7 \pm 0.30 \text{ cm}^3$. This volume includes the reactor and the connecting lines within the reactor and the 4-port valve. The procedure followed to measure the reactor volume is detailed in Appendix A.

The CREC Riser Simulator operates in conjunction with a series of sampling valves that allow, following a predetermined sequence, the injection of hydrocarbons and the withdraw products in short periods of time. The sampling system also allows sending the reaction product sample to the analytical system. Figure 6 reports a schematic diagram of the CREC Riser Simulator experimental setup.

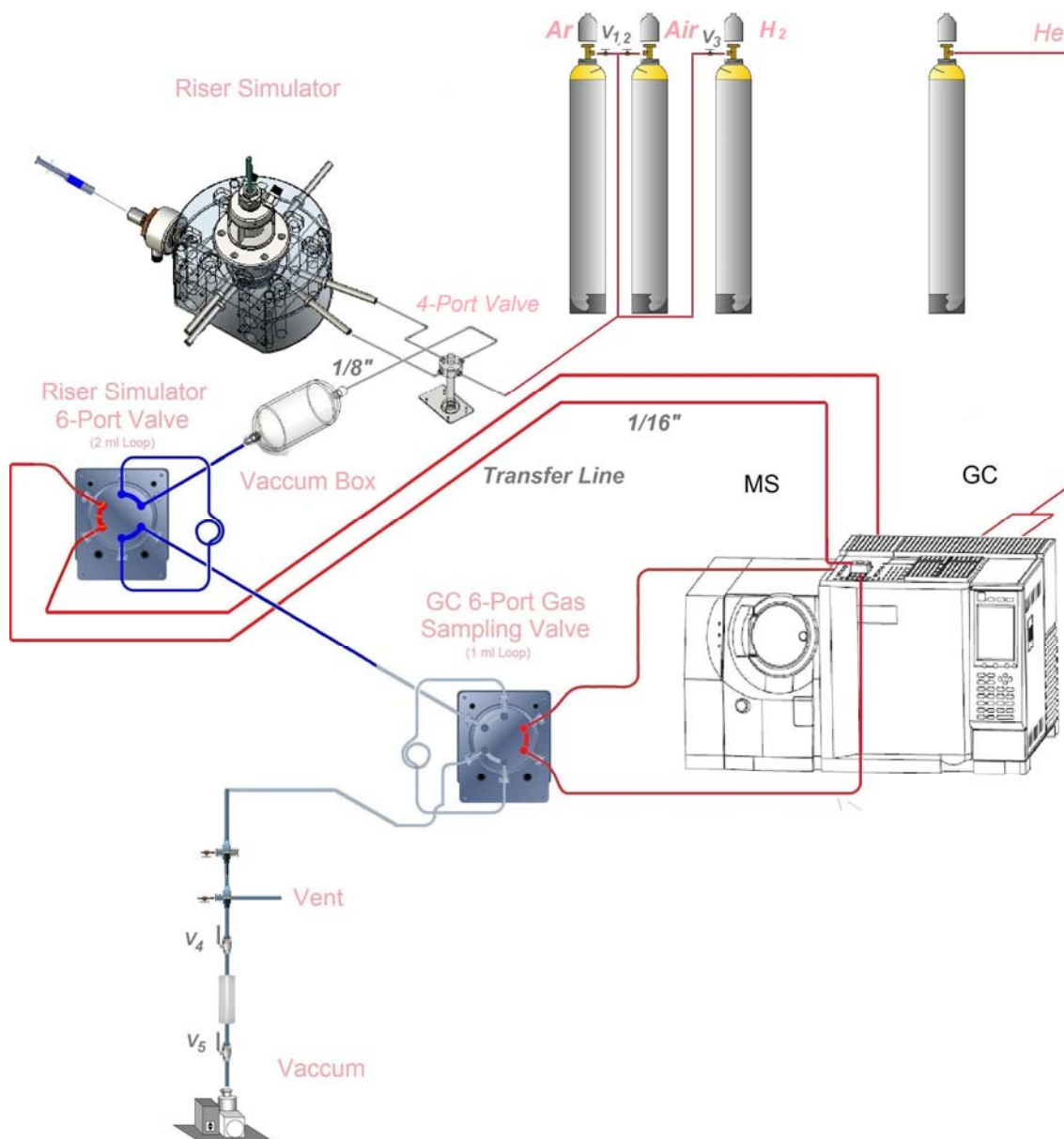


Figure 6. Schematic description of CREC Riser Simulator, associated valves and accessories

All the connections of the CREC Riser Simulator are manufactured using 1/8" stainless steel tubing, except the transfer line that connects and carries the reaction product sample to the analytical system (Figure 6), which is 1/16". The vent is a three way valve. Valve V_1 , V_2 and V_3 are used to select the gas source (air, argon or hydrogen) to the reactor and vacuum system. Argon is used during reaction periods as an inert gas, and air and hydrogen are used during catalyst regeneration (oxidation-reduction cycles). The vent valve is used to vent the system or create a vacuum in the system. Valves V_4 and V_5 are

on-off valves and separate the vacuum box from the vacuum pump. The reactor 4-port and 6-port valves are solenoid type and are controlled from the reactor control panel (Figure 7). The GC 6-port gas sampling valve is controlled from the gas chromatograph control panel.

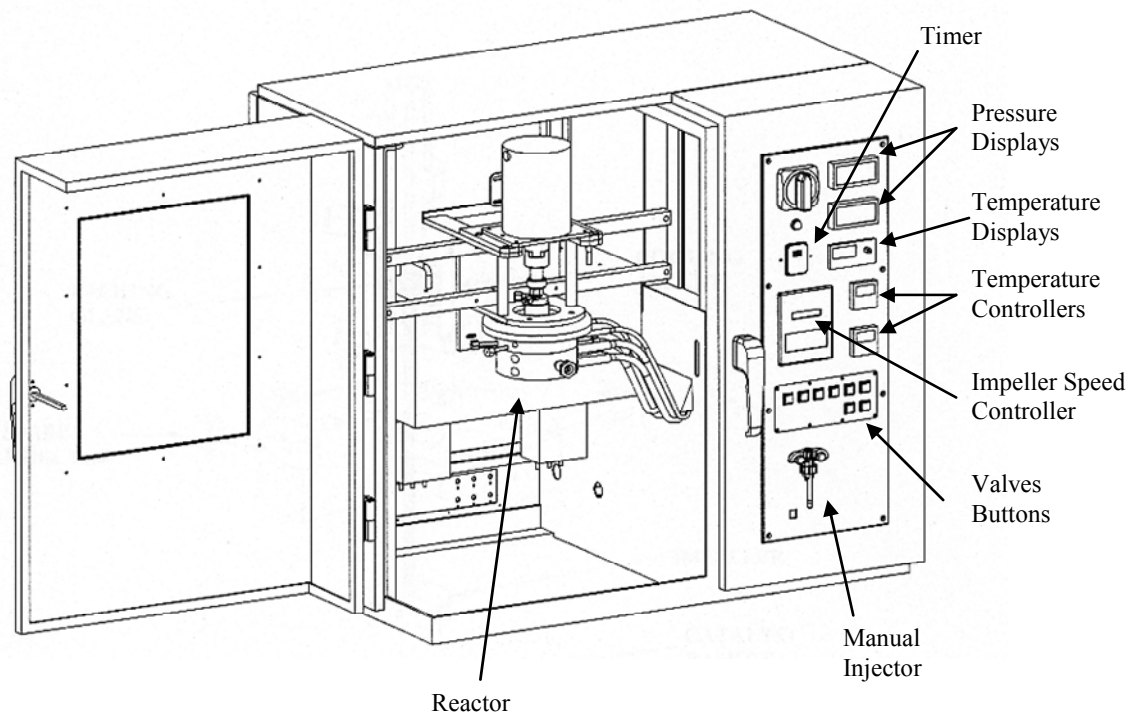


Figure 7. Front view of the CREC Riser Simulator showing the control panel

A 1/8" 4-port chromatographic valve (4-PV) connects the reactor with the argon/air/hydrogen supply at one end, and with the vacuum system at the other end (Figure 6). In the open position, the gases pass through the 4-port valve, enter into the reactor through the inlet port, out of the reactor through the outlet port, back into the valve and finally go to the vacuum box. While in the closed position, the reactor is completely isolated from the rest of the system; thus any gas going to the 4-PV will bypass the reactor and go straight to the vacuum chamber.

A stainless steel vacuum chamber is connected to the 4-PV. This vacuum box volume was found to be $1098.8 \pm 3.1 \text{ cm}^3$ (refer to Appendix A). The volume of the vacuum box

system includes the vacuum chamber, sample loop reactor 6-PV, sample loop GC 6-PV and connecting lines. Its large volume allows quick and easy removal of gas products as well as unreacted feed from the small riser reactor ($50.7 \pm 0.3 \text{ cm}^3$). Additionally, a pressure difference is attained using a vacuum pump in order to effectively remove the reactor contents. The reactor and vacuum system are measured and displayed on an Omega DP series digital pressure display. The currently selected pressure transducers allow pressure readings up to 50 psi. The pressure data of the reactor and vacuum box is saved on a computer disk using a Personal Daq acquisition card.

The reaction time is set with a timer connected to the actuator of the 4-PV. This timer is linked to a micro-switch located in the manual injector (see Figure 8). When the plunger of the syringe is pushed all the way forward to deliver its contents to the reactor, the injector switch is pressed and the timer is started. Once the desired reaction time is reached, the actuator opens the 4-PV and the reactor is emptied due to the pressure difference between the reactor and the vacuum box. Then, the reactor can be isolated again using the manual actuator of the 4-PV.

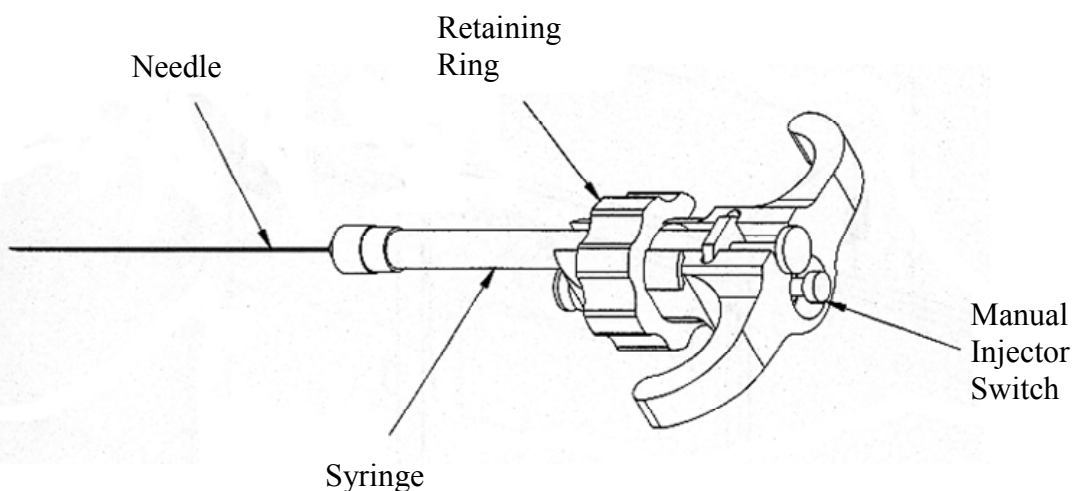


Figure 8. Manual injector switch with syringe

A $1/8''$ 6-port chromatographic valve (6-PV) is installed after the vacuum box. This valve has two permitted positions, load and inject, each having an independent path for the gases to move through. The load position is used to fill up both, the reactor 6-PV sample

loop and the GC 6-PV sample loop. This path leads from the vacuum box to the vent/vacuum pump. The inject position connects the sample loop with the helium carrier gas supply, and sends the sample to the Shimadzu MS. The GC 6-PV is controlled from the gas chromatograph control panel connecting the helium carrier gas to the sample loop and sending the sample to the Shimadzu GC/TCD.

The reactor valves (4-PV and 6-PV) and vacuum chamber are located inside a heated box. The GC 6-PV is heated using an independent temperature controller from Valco Instruments Co. Inc. A thermocouple placed inside the heated box is used to measure and control the temperature of the vacuum system. The vacuum box temperature was always set at 300°C to avoid condensation of products. The temperature of the product transfer line connecting the vacuum box and GCMS was also kept at 300°C, using a heating tape.

Additional temperatures such as: room temperature, reactor cooling jacket water temperature and transfer line different point temperatures were displayed and/or controlled through the control panel (Figure 7).

Regarding the application of the CREC Riser Simulator to the present study, it is important to mention that this unit is particularly well equipped for mechanistic studies. The sample collected in the vacuum box at vacuum pressure (e.g. 3 psia) provides information about the combined abundance of species both in the gas and in the catalyst phases. This combined measurement is essential to argue about species formed in a catalytic reaction network such as the one of this study.

4.4 Experimental Procedure

Thermal and catalytic runs were performed in the reactor configuration that is described above. The conditions of the catalytic experiments were set as follows:

a) mixtures of glucose-water at steam biomass ratios of 0.4, 0.6, 0.8 and 1.0 (g/g) wt%, 2 atm. of argon, catalyst/biomass ratio of ~25, residence times of 5, 10, 20, and 30 s, and reaction temperatures 600, 650, and 700°C. The maximum reaction time (30s) was selected after preliminary runs to maximize the interconversion of the product gas and the

maximum temperature (700°C) was chosen to prevent ash agglomeration. The impeller velocity was set at 6000 rpm to get a well fluidized bed.

b) mixtures of 2-methoxy-4-methylphenol-water at 0.4, 0.6, 0.8 and 1.0 steam/biomass ratios (g/g) wt%, 2 atm. of argon, catalyst/feedstock ratio of ~25, residence times of 5, 10, 20, and 30 s, and reaction temperatures of 600, 650, and 700°C.

c) mixtures of glucose-2 methoxy 4 methylphenol-water at 0.4, 0.6, 0.8 and 1.0 steam/biomass ratios (g/g) wt%, 2 atm. of argon, catalyst/feedstock ratio of ~25, residence times of 5, 10, 20, and 30 s, and reaction temperature of 700°C.

The Ni/ α -alumina catalyst, already thermally treated during the preparation process, was loaded in the catalyst basket, the reaction system was sealed, leak tested and heated to the reaction temperature in an argon atmosphere. Then, the reactant mixture was injected, and once the reaction time was reached, the reaction products were evacuated from the reactor and sent to the analytical system, through the heated transfer line. All experiments were repeated at least 3 times to secure the reproducibility of the results.

For the 2-methoxy-4-methylphenol experimental runs, a regeneration cycle was required after 1 run because it was found that a significant amount of coke was formed, since conversion of reactants vary considerably. The regeneration conditions were set at 700°C, 25 min of air flow and 25 min of hydrogen flow (oxidation-reduction cycle). Under these conditions the coke was completely removed.

4.5 Pressure Profiles, Varying S/B Ratios and Varying Contact Times

The following two figures display typical pressure profiles in the CREC Riser Simulator changes as a result of the catalytic steam biomass gasification reaction (when 2-methoxy-4-methyl phenol is used as the biomass feedstock). The curves in Figure 9 display the pressure changes in the reactor (upper curves) and vacuum box (lower curves) simultaneously for a reaction time of 20s, and for S/B ratios of 0.4, 0.6, 0.8, and 1.0. The vertical sections of the reactor pressure curves indicate the injection of 2-methoxy-4-methylphenol into the reactor, and the release of the products into the vacuum box

(displayed in that order on the graph). As the S/B ratio increases, Figure 9 shows increasingly higher pressure readings for the injection of 2-methoxy-4-methylphenol. The curved section of the graph (between the two vertical lines), represents the gasification reaction and displays an increase in pressure as the injected phenol compound cracks into various gas and tar products.

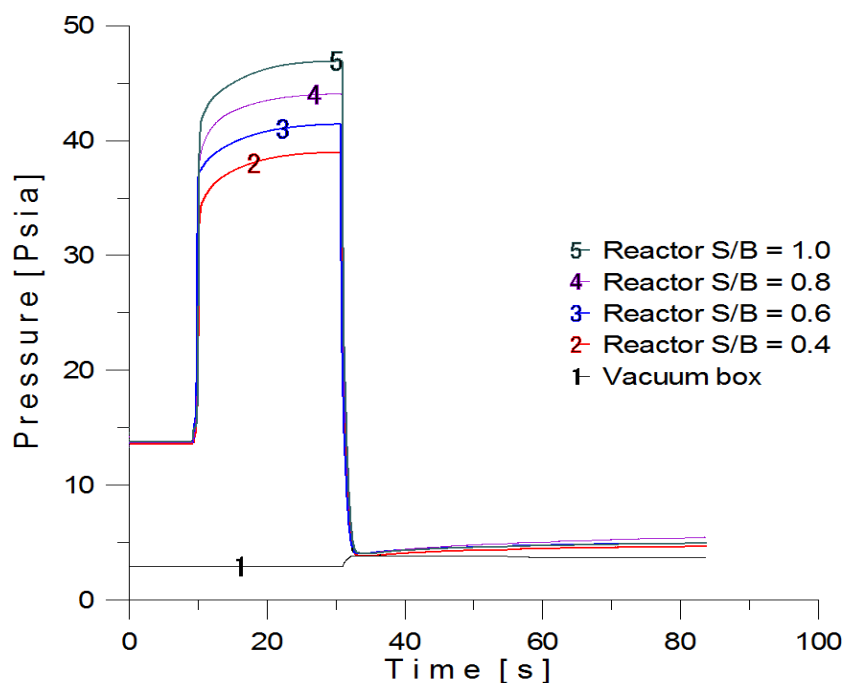


Figure 9. Change in pressure in CREC Riser Simulator for injection of 12.5 μ L of phenol at 650°C, reaction time of 20s and steam/biomass ratios of 0.4, 0.6, 0.8, 1.0

Figure 10 depicts the pressure changes in the reactor and vacuum box for the gasification of 2-methoxy-4-methyl phenol, when the S/B ratio remains constant at 0.6, and the reaction time varies from 5 to 30s. The straight (vertical) and curved sections of this figure also denote the phenol injection/product release and the gasification reaction, respectively. For increasing reaction times, the curved sections of the graph become longer, but follow a consistent shape. The consistency of the shape of the curves, in both Figure 9 and Figure 10 confirms that the CREC Riser Simulator produces precise results. This verifies the excellent repeatability in the reported experimental results, and that the findings in this study can be stated with a high degree of certainty.

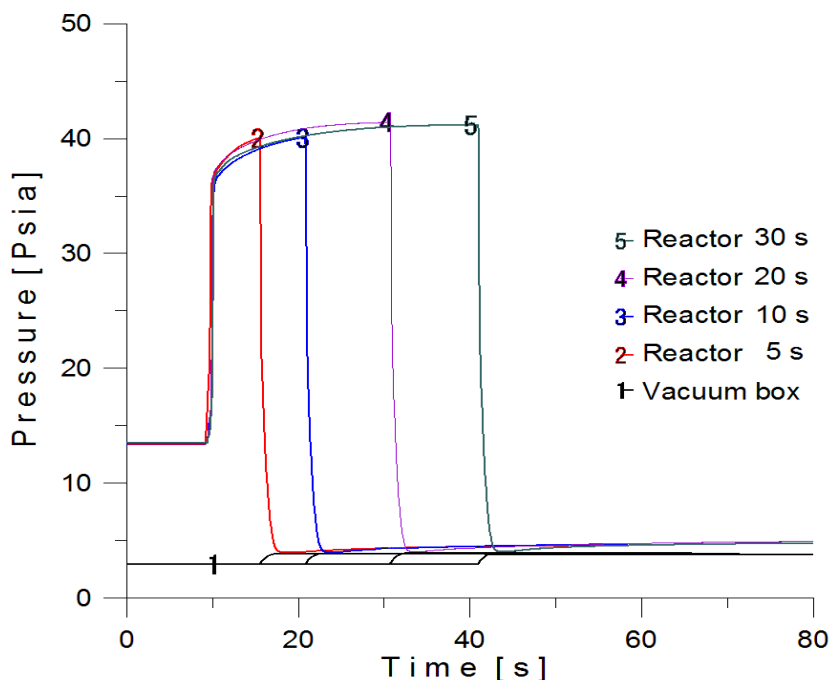


Figure 10. Change in pressure in CREC Riser Simulator for injection of 12.5 μ L of phenol at 650°C, steam/biomass ratio of 0.6, reaction times of 5, 10, 20 and 30s

4.6 Analytical System: Identification and Quantification of Products

A Shimadzu 2010 GC/TCD (thermal conductivity detector) with a packed column HayeSep D 100/120 Pours Polymer, 30 ft x 1/8" O.D. S.S. was used for the separation and quantification of permanent gases (H_2 , CO, CO_2 , CH_4), water, and light hydrocarbons up to C_6 hydrocarbons. A Shimadzu 2010 mass selective detector with a HP-5MS silica capillary column, 30 m \times 0.25 m I.D. (5% phenyl-/95% methylpolysiloxane) also allowed the separation, identification and quantification of the components present in the tars. A detailed list of the entire components identified in the tars is presented in Chapter 7. The mass spectrometer was operated in the scan mode using the parameters presented in Table 4.

The product gas components identified in the GC/TCD were quantified using calibration curves. The calibration curves of hydrogen (H_2), carbon monoxide (CO), carbon dioxide (CO_2), methane (CH_4), ethylene (C_2H_4), ethane (C_2H_6), propylene (C_3H_6), propane

(C₃H₈), i-butene (C₄H₈), n-butane (C₄H₁₀), i-pentene (C₅H₁₀), n-pentane (C₅H₁₂), i-hexene (C₆H₁₂), and n-hexane (C₆H₁₄) are given in the Appendix C.

The tar components were quantified in the MS spectrum; the procedure for this quantification is explained in Chapter 7.

The detailed method used for each detector is detailed in Table 4 and Table 5.

Table 4. Mass selective detector parameters

Column	HP-5MS silica capillary column, 30 m×0.25 m I.D. (5% phenyl-/95% methylpolysiloxane)		
Column Oven Temperature [°C]	35		
Injection Temperature [°C]	300		
Injection Mode	Split		
Flow Control Mode	Lineal Velocity		
Pressure [Kpa]	61.8		
Total Flow [mL/min]	722.2		
Column Flow [mL/min]	1.2		
Lineal Velocity [cm/s]	39.4		
Purge Flow [mL/min]	1		
Split Ratio	600		
High Pressure Injection	OFF		
Carrier Gas Saver	ON		
Carrier Gas Server Split Ratio	10		
Carrier Gas Server time [mn]	5		
Splitter Hold	OFF		
Oven Temperature Program	Rate	Temperature [°C]	Hold Time [min]
	–	35.0	3.00
	25	250.0	13.40
Start Time [min]	0.01		
End Time [min]	10		
ACQ Mode	Scan		
Event Time [sec]	0.1		
Scan Speed	2500		
Start m/z	5		
Emd m/z	200		
Ion Source Temperature [°C]	250		
Interface Temperature [°C]	250		
Solvent Cut Time [min]	0		
Detector Gain Mode	Relative		
Detector Gain Mode [kV]	-0.2		
Threshold	0		
MS Program	OFF		

Table 5. Gas chromatograph method

Column	HayeSep D 100/120 Porous Polymer, 30 ft x 1/8" o.d. S.S.				
Injection Temperature [°C]	200				
Injection Mode	Direct				
Flow Control Mode	Flow				
Column Flow [mL/min]	30				
Lineal Velocity [cm/s]	115.1				
Purge Flow [mL/min]	1				
Oven Temperature Program	Rate	Temperature [°C]	Hold Time [min]		
	–	35.0	3.00		
	25	250.0	13.40		
Flow Program	Rate	Flow [mL/min]	Hold Time [min]		
	–	25.0	3.00		
	0.7	31.0	13.43		
[TCD]					
Temperature [°C]	250				
Makeup Gas	He				
Makeup Flow [mL/min}	8				
Current [mA]	85				
Polarity	+				
Signal Acquire	ON				
Sampling Rate [msec]	40				
Stop Time [min]	25				
Subtract Detector	None				
Delay Time [min]	0				
GC Program					
Time Program	No.	Time [min]	Device	Event	Value
	1	0.00	Relay	Relay 91	0
	2	0.01	Relay	Relay 91	1
	3	0.50	Relay	Relay 91	0

Finally, the coke deposited on the catalysts after the experimental run was measured in a total organic carbon analyzer (TOC-V) with a solid sample module (SSM-5000) from Mandel.

4.7 Conclusions

- a. The CREC Riser Simulator of the present study offers a valuable tool for evaluation of catalytic steam gasification of biomass reactions. This unit provides minimum temperatures differences inside the reactor at any reaction time, with excellent contacting between catalyst and the vapor phase. The CREC Riser Simulator allows direct sampling of reaction products to the GC/MS, which allows an excellent repeatability of the experimental results.
- b. The analytical system employed consists of GC and MS which was considered the best arrangement to identify and quantify permanent gases and tar composition.
- c. The model compounds selected to evaluate the performance of Ni/ α -alumina catalyst biomass conversion were glucose, representing cellulose, and 2-methoxy-4-methylphenol representing lignin
- d. The glucose-2-methoxy-4-methylphenol-water mixtures were also employed to account for potential interactive effects between biomass components.

Chapter 5 Ni/ α -alumina Catalyst

5 Preparation and Characterization

5.1 Ni/ α -alumina Catalyst Preparation

5.1.1 Fluidizable Catalyst

Fluidizable supported catalysts for catalytic gasification of biomass, being developed at the Chemical Reactor Engineering Center (CREC), typically consist of two primary components: the catalyst itself (a metal in the reduced state) and the appropriate catalyst support over which the active metal is dispersed. The metals in group VIII of the periodic table are active for gasification as are the noble metals.

However, economic considerations rule out the use of the noble metals and from the group VIII metals, only nickel has suitable resistance to oxidation (Jarosch et al., 1999). The catalyst support is also an important catalyst design parameter. Supports have to be mechanically strong, stable under steam atmospheres and high temperatures ($\sim 1000^\circ\text{C}$), and resistant to metal-support interactions. Given all these facts, α -alumina formed by the decomposition of hydrated alumina (Tsuchida, 1993), is a preferred support as it is mechanically strong at 1200°C as potentially required by the conditions of biomass gasification.

In selecting a catalyst for biomass gasification, a number of characteristics have to be met. The catalyst should be stable at high temperatures, be mechanically strong, resistant to the effects of coking, have a minimal support-metal interaction and have suitable activity (El Solh et al., 2001). In addition, a catalyst for the biomass gasification process has to be fluidizable and stable when exposed to repeated oxidation and reduction cycles.

With the above in mind, CREC researchers concluded that nickel should be used as the active metal with loadings of 2.5 wt%, as this level bracket the loadings found on commercially available catalysts. Alpha-alumina, which was readily available in a fluidizable form, was chosen as the appropriate support for nickel. The results, found by

El Solh, 2002, provide the basis for the catalyst selection, which is a nickel catalyst supported on α -alumina.

5.1.2 Catalyst Materials

5.1.2.1 Alpha-Alumina

Alpha-alumina is thermally stable, chemically inert and mechanically strong. These characteristics make it an effective support material for a catalyst used in biomass gasification.

The α -alumina tri-hydrate used was purchased from Stream Chemicals Incorporated; its chemical composition being 65% Al_2O_3 , 34.8% H_2O , 0.15% Na_2O . This material has low specific surface area and pore volume, and an average diameter of 60 μm .

5.1.2.2 Nickel

Nickel offers many characteristics that are advantageous for a catalyst that is used in biomass gasification. Nickel oxides show negligible volatility below 1000°C and nickel oxides are well assessed for high temperature applications (Villa et al., 2003). Although there are precious metals that may be more active than nickel, nickel is sufficiently active and inexpensive, producing an economically suitable catalyst.

For this study, nickel (II) nitrate hexa-hydrate, $(\text{Ni}(\text{NO}_3)_2 \cdot 6\text{H}_2\text{O})$, crystal was obtained from Aldrich chemical company.

5.1.3 Catalyst Preparation

The α -alumina supported nickel catalyst was prepared according to the incipient wetness technique.

The catalyst preparation began by obtaining the α -alumina, which acts as a support to the active metal. The alpha alumina was obtained from Stream Chemicals Incorporated, with 65% Al_2O_3 , 34.8% H_2O , and 0.15% Na_2O composition. The α -alumina was calcined prior to metal loading impregnation. Calcination consisted of heating the α -alumina in a

furnace oven to a temperature of 1000°C for 8 hours. This process removed excess water and eliminated potential thermal instability in the alumina powder.

Nickel loading was achieved according to the following steps: a) the alumina powder was placed into a quartz flask, b) a magnetic stirrer was inserted into the flask and then the flask was sealed with a rubber septum, and c) the system was kept under 250 mmHg vacuum.

A nickel-nitrate solution was prepared by dissolving nickel-nitrate hexa-hydrate, (Ni(NO₃)₃·6H₂O), powder in water. 0.8 ml of water was used for every gram of α-alumina support. The amount of desired nickel-nitrate hexa-hydrate powder to be dissolved in water and added to the support was calculated by the formula:

$$m_{\text{Ni(NO}_3)_3 \cdot 6\text{H}_2\text{O}} = \frac{x_{\text{Ni}} \text{MW}_{\text{Ni(NO}_3)_3 \cdot 6\text{H}_2\text{O}} m_{\text{Al}_2\text{O}_3}}{\text{MW}_{\text{Ni}} x_{\text{purity}}} \quad \text{Eq (11)}$$

where:

$m_{\text{Ni(NO}_3)_3 \cdot 6\text{H}_2\text{O}}$, represents the mass of nickel-nitrate hexa-hydrate to be added

x_{Ni} , represents the percent metal loading

$\text{MW}_{\text{Ni(NO}_3)_3 \cdot 6\text{H}_2\text{O}}$, represents the molecular weight of nickel-nitrate hexa-hydrate

$m_{\text{Al}_2\text{O}_3}$, represents the mass of α-alumina support

MW_{Ni} , represents the molecular weight of nickel, and

x_{purity} , represents the percentage purity of nickel-nitrate hexa-hydrate.

The nickel solution was introduced into the flask using a syringe. The magnetic stirrer was used to mix the impregnated α-alumina until the mixture was homogeneous in color (uniformly coloured emerald green paste).

In order to dry the impregnated α-alumina solution, the resulting paste was heated in a furnace oven to a temperature of 140°C at a 20°C/hour heating rate during 6 hours.

The next step was to decompose the nickel-nitrate and to lay the nickel on the α-alumina support. To do this, the catalyst powder was placed in the specially designed

fluidized bed reactor (Figure 11) located in a furnace oven, and the temperature was kept at 750°C for a period of 8 hours. During this time, a stream of gas containing hydrogen flowed through the bed of catalyst. The nickel-nitrate decomposed first to nickel oxide with the nickel oxide being reduced in a second step. This occurred according to the following series of reactions:

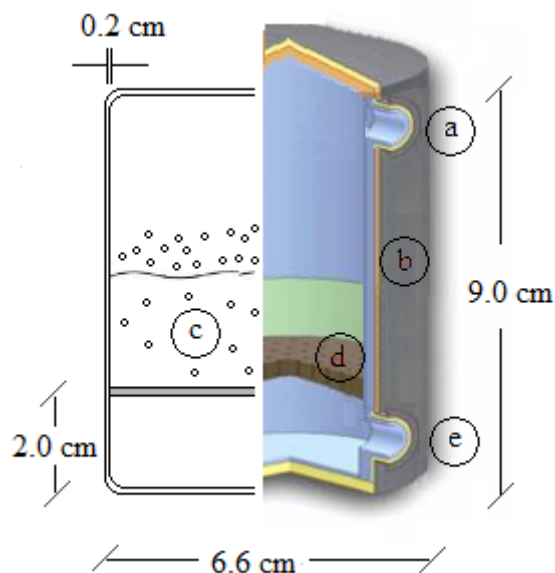
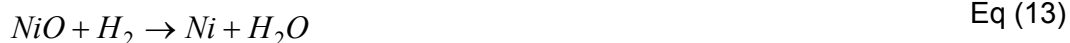


Figure 11. Fluidized bed reactor for Ni based catalyst preparation: a) exhaust gas exit port (9/16") b) inconel reactor wall c) fluidized catalyst d) inconel porous gas distribution grid plate and e) hydrogen/helium gas inlet port (9/16")

Water and HNO₃ vapors exited the fluidized bed reactor through an exhaust stream. The HNO₃ in the exhaust stream was then scrubbed in a sodium hydroxide solution inside the fume hood. The HNO₃ reacted with the sodium hydroxide to form nitrate and water vapor according to the following reaction mechanism:



Multiple metal loadings were accomplished according to the procedure above. Each metal loading presumably added 2.5wt% nickel to the α -alumina support.

When the desired metal loading was reached, the impregnated α -alumina solution was calcined under an air atmosphere. The catalyst was placed in the furnace oven and heated to a temperature of 750°C for 8 hours. A flow chart of all steps included in the catalyst preparation is given in Figure 12.

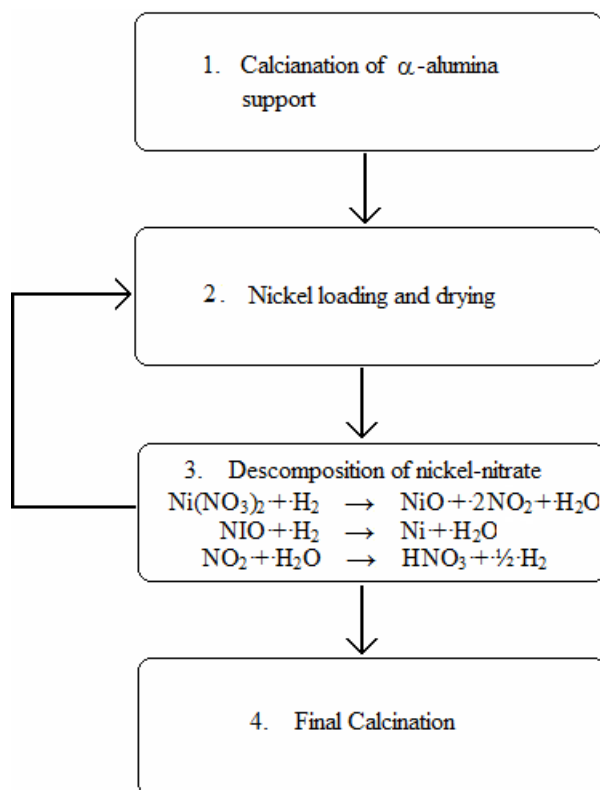


Figure 12. Catalysis preparation flow chart (nickel supported on α -alumina)

5.2 Catalyst Characterization

Physical and chemical characterization of Ni/ α -alumina catalyst included Particle Size Distribution (PSD), Apparent Density (AD), X-Ray Fluorescence (XRF), Temperature Programmed Desorption (TPD), Temperature Programmed Reduction (TPR), Pulse Chemisorption and Surface Area (BET and T-Plot). This section presents a description of the physical and chemical analyses that were carried out in order to predict the catalytic performance of Ni/ α -alumina.

5.2.1 Particle Size Distribution and Particle Apparent Density

Fluidizability is an important characteristic that a catalyst should have for its application in biomass gasification. Therefore, it is important to analyze the particle size and size distribution on the prepared catalyst to confirm its adequacy for fluidized bed conditions. Beside the fluidization properties, the size of particle also plays a significant role in the gas-solid reaction involved in the reactor. For instance, large particles limit the gas phase reactant access to the inner layers of the catalyst. As a result, using smaller particles can minimized the diffusional resistance and reduction/oxidation rates can be maximized. On the other hand, excessive smaller particles can cause fluidization problems, channeling and loss of fines.

Taking into consideration the importance of the above mentioned facts, the PSD of the Ni/ α -alumina catalyst was measured using a Mastersizer 2000 from Malvern Instruments. Figure 13 shows the PSD of the Ni/ α -alumina catalyst while Table 6 reports the results. The average particle size was assessed at 46.6 μm ($d(0.5)$), with the 80-120 μm and 120-160 μm catalyst fractions being limited to 7.9 and 3.2 vol%, respectively. This shows that there was a considerable amount of catalyst particles that were smaller than 80 μm in size.

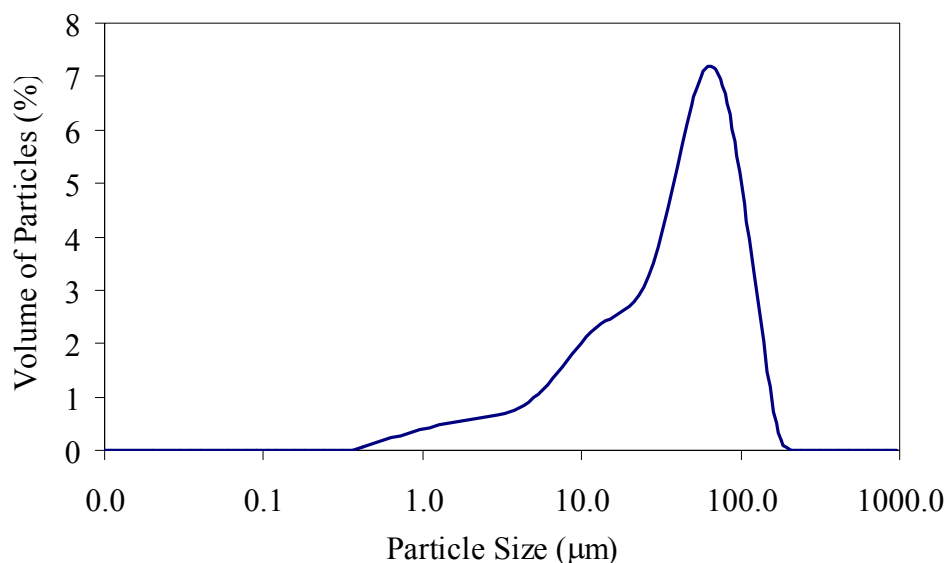


Figure 13. Particle Size Distribution of Ni/ α -alumina catalyst

Table 6. Ni/ α -alumina catalyst PSD results

Particle Size	Vol%
0-40 μm	55.36
0-80 μm	88.9
0-120 μm	96.8
0-160 μm	99.98
Surface Weighted Mean, D[3,2]	12.3 μm
Volume Weighted Mean, D[4,3]	52.3 μm
d(0.1)	6.3 μm
d(0.5)	46.6 μm
d(0.9)	107.8 μm

The apparent particle density of the catalyst was assessed to be 1929 kg/m^3 , using a method established at the CREC. This method enables the determination of the AD of a catalyst by introducing a known amount of catalyst to a 5 mL flask, filling the flask with cyclohexane, and using the following equation:

$$AD = \frac{W_{cat}}{V_T - V_{CyH}} \quad \text{Eq (16)}$$

where AD is the particle apparent density (g/cc), W_{cat} is the catalyst weight (0.5 g), V_T is the flask volume (5 cc), and V_{CyH} the volume of cyclohexane (4.7 cc) calculated as the ratio of the weight of cyclohexane needed to fill the flask (3.8 g) and the density of cyclohexane (0.8 g/cc).

Using the average particle size, the particle apparent density, and Geldart's powder classification chart (Geldart, 1973), it was concluded that the Ni/ α -alumina catalyst particles belong to the group A, a particle group considered to display good fluidization. These characteristics were further confirmed experimentally using a plexiglas model of the CREC Riser Simulator, specially manufactured for flow visualization.

5.2.2 X-Ray Fluorescence (XRF)

XRF was used to confirm the metal loading of the presumed 2.5% wt Ni/ α -alumina catalyst. The XRF analysis was performed at the Department of Earth Sciences at The University of Western Ontario. Table 7 reports the chemical composition of the Ni/ α -alumina catalyst sample after normalisation to 100%. In addition, the sum of the concentrations before normalisation to 100% was 48.4%. Therefore, the nickel loading of this catalyst was 3.3% (0.068×48.4), a value which is slightly higher than what was initially anticipated.

Table 7. Elemental analysis results using XRF spectrometer

Element	Wt%
Al	92.32
Ni	6.84
Na	0.388
Ba	0.086
Ca	0.0844
S	0.0616
Cs	0.0526
Au	0.0481
Fe	0.0347
K	0.0282

5.2.3 NH₃ Temperature Programmed Desorption

Temperature-programmed desorption (TPD) of ammonia is one of the most widely used techniques to characterize the acid sites on oxide surfaces. Determining the quantity and strength of the acid sites on alumina, is crucial to understanding and predicting the performance of the Ni/ α -alumina catalyst. The method assumes that the amines adsorb quantitatively on surface acid sites, and that desorption from acid sites can be distinguished from desorption of physisorbed base on other sites. The concentration of surface acid sites can be calculated from the amount of amine that desorbs from these sites, and some limited indication of the relative strengths of the acid sites can be obtained from the temperatures needed to bring about desorption.

TPD experiments were performed using an AutoChem II analyzer from Micromeritics. A 0.171 g, sample was pre-treated by a helium purge for 2 h at 500°C. Ammonia was adsorbed for 1 hour at 100°C using an NH₃/He gas mixture (4.5% ammonia, 95.5% helium). After dosing, the sample was purged in He for 1 hour at the adsorption temperature. During the TPD experiments, the temperature of the sample was increased linearly by 15°C min⁻¹ until 300°C in flowing helium. Ammonia TPD for Ni/ α -alumina catalyst and α -alumina are reported in Figure 14.

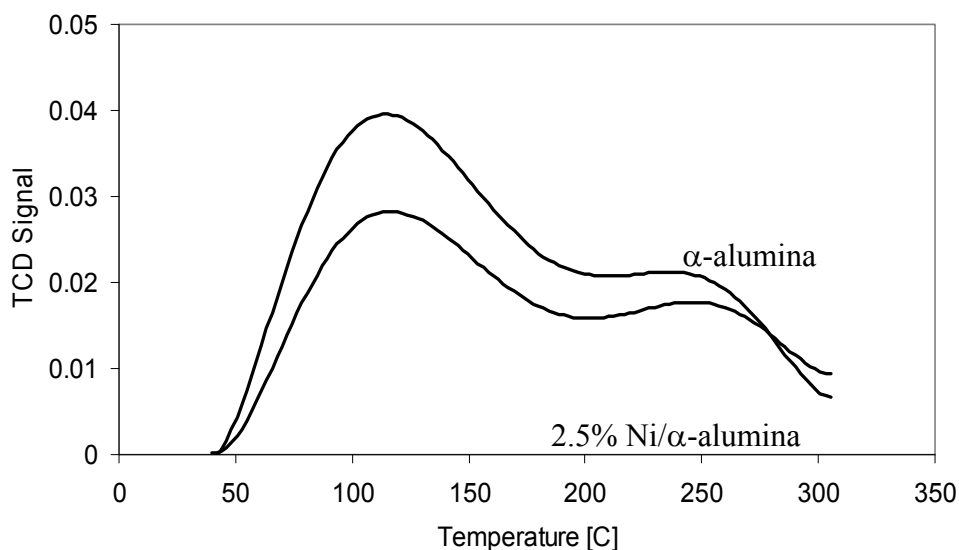


Figure 14. TPD spectrum for Ni/ α -alumina catalyst

TPD spectra displays two consistent desorption peaks centered at 110°C and 280°C, confirming that Ni/ α -alumina catalyst and α -alumina contain weak acidic sites and strong acidic sites. Furthermore, total acidity for both Ni/ α -alumina catalyst and α -alumina were determined by integrating the TPD spectrums (Figure 14). Ni/ α -alumina catalyst displayed an acidity of 0.036 mmol NH₃/g while α -alumina reference showed a higher 0.058 mmol NH₃/g value. This allows hypothesizing that nickel crystallites while covering the support acidic sites on the support surface, they reduce the total acidity of the α -alumina.

5.2.4 Temperature Programmed Reduction (TPR)

In a supported metal/metal oxide system, metal species may be present in different oxide phases. The formation of each phase depends on parameters such as properties of the metal and the support material, preparation techniques and calcination temperature. The reaction rate of the supported metal is mainly dictated by the availability of the reactive phase for the desired reaction conditions. Temperature programmed reactions (TPR/TPO) provide information about the formation of metal oxide phase(s), the interaction between those phase(s), the interaction between metal oxide and support material, and the reduction characteristics of the oxide metal phase(s).

The number of reducible species available in the Ni/ α -alumina catalyst and the reduction temperature can be determined using TPR. TPR was performed using an AutoChem II ASAP 2920 analyzer by Micromeritics. A stream of gas containing 10% H₂ in Ar flowed through a bed containing approximately 150–200 mg of the catalyst at a rate of 50.25 mL/min. The temperature of the bed was raised from ambient temperature to 950°C at a rate of 10°C/min. A thermal conductivity detector (TCD) was used to analyze the gas leaving the catalyst.

Once the bed temperature reaches the reduction temperature of NiO, reduction occurs and hydrogen is consumed according to the reaction



where: NiO represents the nickel catalyst in its oxidized form, and Ni represents the nickel catalyst in its reduced form.

The hydrogen that is consumed during the reaction is used to calculate the number of reducible species available on the catalyst as follow:

$$W_{Ni} = \frac{MW_{Ni} V_{H_2}}{\nu MV} \quad \text{Eq (17)}$$

where: W_{ni} represents the weight of reducible species, MW_{Ni} represents the molecular weight of reducible specie, V_{H_2} represents the volume of hydrogen consumed, ν represents the stoichiometric number of the reduction reaction, and MV represents the molar volume at STP.

The percentage reduction is then calculated as follow:

$$\% \text{ reduction} = \frac{W_{ni}}{W_o} \cdot 100\% \quad \text{Eq (18)}$$

where: W_o represents the actual metal amount on the catalyst.

In repeated cycles of TPR and TPO, the Ni/ α -alumina catalyst displays a consistent peak centered at approximately 500°C as presented in Figure 15. This result indicates that the reducible phase is primarily NiO and there are no changes of the Ni available with the successive oxidation-reduction cycles (Sedor et al., 2008).

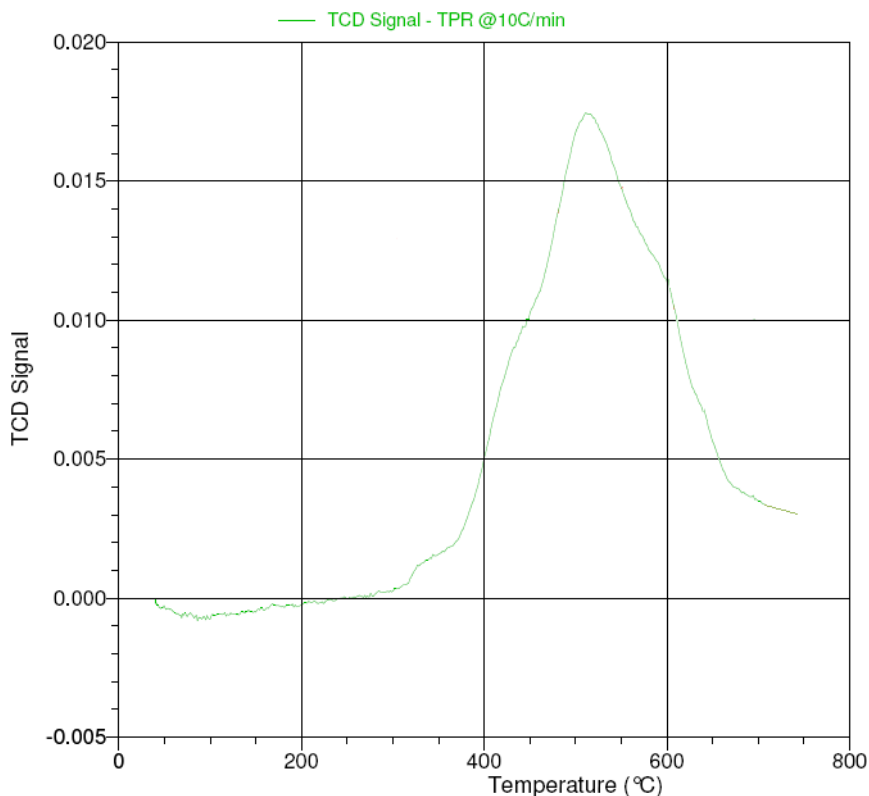
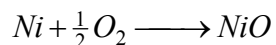


Figure 15. TPR Spectrum for Ni/ α -alumina Catalyst

5.2.5 Temperature Programmed Oxidation (TPO)

Temperature programmed oxidation (TPO) was performed following a TPR experiment in order to oxidize the reduced catalyst using the Autochem II ASAP 2920 analyzer. In the oxidation cycle a stream of gas containing 5% oxygen in helium flowed through the bed of oxygen carrier at a rate of 50 mL/min. The temperature of the bed was raised from ambient to 750°C at a rate of 10°C/min. As the temperature of the sample increases, oxidation of the metal occurs according to the reaction



where, Ni represent the active metal of the catalyst in its reduced form, and NiO the active metal of the catalyst in its oxidized form.

In the case of our study, it was observed using TPR that within the studied temperature range (25 to 700°C) the major reducing species present is NiO . Therefore, only NiO was

considered to establish the relationship between metal loading and oxygen available for reduction. On this basis the average of oxygen consumed was estimate at 0.4470 mmol per gram of catalyst.

5.2.6 Pulse Chemisorption

The pulse chemisorption technique provides valuable information on the dispersion and on the crystal site of the supported metal. Metal dispersion can vary depending on several factors such as the type of meta/support, the surface area of the support, and the sample preparation methods. A pre-reduced sample of catalyst was used in order to perform the pulse chemisorption experiments. A stream of Ar gas flowed through a bed containing approximately 150–200 mg of Ni/ α -alumina at a rate of 50 mL/min. H₂ gas was injected in a series of pulses containing 1.01 mL STP and the injected H₂ was chemisorbed onto the active sites of the catalyst sample. A TCD analyzed the gas leaving the catalyst bed. As H₂ gas was adsorbed by the sample, peaks were created in the thermal conductivity reading of the outlet stream. When two consecutive peaks have the same area, the catalyst is considered as saturated with hydrogen gas with no more hydrogen being chemically adsorbed.

The amount of hydrogen chemically adsorbed on the active site or the catalyst is used to calculate the percent dispersion (%D) as follow:

$$\%D = \frac{AX}{X_{w,Ni} f} \quad \text{Eq (19)}$$

where, A represents a constant, X represents the total hydrogen chemisorbed [μmol of H₂/g catalyst], $X_{w,Ni}$ represents the percentage of weight metal, and f represents the fraction of reduced metal.

To calculate the average crystal size (d_p), the following expression is used:

$$\%D = \frac{\sum [n_{cr} \pi d_{pi}^2] \cdot V_m}{\sum \left[\frac{n_{cr} \pi d_{pi}^3}{\phi} \right] \cdot S_m} = \frac{\phi V_m}{S_m} \cdot \frac{1}{d_p} \quad \text{Eq (20)}$$

Rearranging to solve for d_p , we have:

$$d_p = \frac{\phi V_m}{S_m} \cdot \frac{1}{\%D} \quad \text{Eq (21)}$$

where, n_{cr} represents the number of nickel crystals of d_{pi} size, V_m represents the volume of metal atoms, ϕ represents the particle shape constant, and S_m represents the average surface area of metal particle exposed per surface metal atom.

Figure 16 illustrates the results of this process.

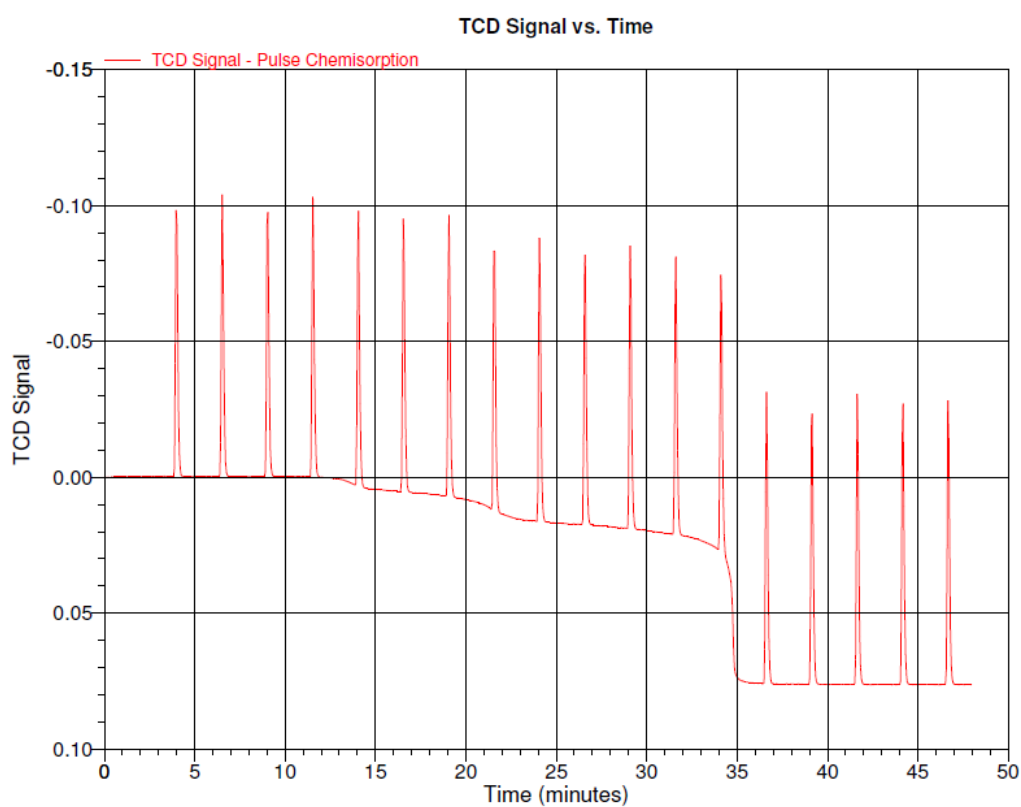


Figure 16. Results for pulse chemisorption on Ni/ α -alumina catalyst

Each peak in Figure 16 represents the adsorption of H_2 onto the Ni/ α -alumina catalyst.

Additionally, quantitative results for the pulse chemisorption experiment are summarized below in Table 8.

Table 8. Pulse chemisorption analysis summary

Parameter	Value
Metal Dispersion	3.4%
Metallic Surface Area	0.56 m ² /g catalyst
Metallic Surface Area 2	22.56 m ² /g metal
Active Particle Diameter	29.89 nm

5.2.7 Catalyst Surface Area

Surface area is another fundamental physical property of the supported active metal involved in heterogeneous reactions. The surface area is one of the important parameters that determine the dispersion of the active sites present in the solid materials. The BET surface area of the metal loaded catalyst was calculated using nitrogen adsorption isotherms. The amount of nitrogen adsorbed on the surface of the catalyst and the equilibrium adsorption pressure are used to calculate the volume of a monolayer of nitrogen using BET expression:

$$\frac{P_A}{V_{ads} (P_o - P_A)} = \frac{1}{V_m C} + \frac{(C-1)}{V_m C} \frac{P_A}{P_o} \quad \text{Eq (22)}$$

where: V_{ads} represents the amount of gas adsorbed at pressure P_A , P_o represents the saturation pressure at the gas, V_m represent the quantity of gas adsorbed when the entire surface is cover with a monomolecular layer, and C is a constant.

The specific surface area can be calculated by:

$$S = \frac{V_m A_p N_A}{MV} \quad \text{Eq (23)}$$

With S being the specific surface area, A_p the area of the surface occupied by a single adsorbent gas molecule, A_p the area of the surface occupied by a single adsorbent gas molecule N_A Avogadro's number and MV the molecular volume at STP.

The specific surface of the Ni/ α -alumina catalyst was measured using an ASAP 2010 analyzer (from Micromeritics). Before the measurements, samples weighing from 0.15 to 0.2 g were degassed at 643 °K for 4 hour. Adsorption isotherms were measured under the relative pressure range from $\sim 10^{-6}$ to 1.

Table 9. BET surface area analysis

Calcined α -alumina [m ² /g sample]	2.5% Ni/ α -alumina [m ² /g sample]
30.1	22.4

Table 9 summarized the finding of the BET analysis on the Ni/ α -Alumina catalyst. These results indicate a decrease in the total surface area of the catalyst after nickel is loaded on the calcined α -alumina support. The decrease of the surface area of the Ni/ α -Alumina catalyst is likely principally due to the plugging of support pores by nickel species. These results agree with those found in the literature. Khodakov et al., 2002 found that the observed decrease in surface area after impregnation of cobalt is attributed to clogging of the support pores by the cobalt species, making the support pores inaccessible to nitrogen adsorption.

5.2.8 Conclusions

On the basis of the above data and results the following are the conclusions for the Ni/ α -alumina characterization:

- More than 80wt% of the catalyst particles are in a size range smaller than 80 μ m. Thus securing good fluidization in the CREC Riser Simulator
- The TPD spectra displays two consistent desorption peaks centered at 110°C and 280°C, confirming that Ni/ α -alumina catalyst and α -alumina contain weak acidic sites and strong acidic sites. TPD analysis on the α -alumina and the Ni/ α -alumina catalyst reports a decrease in the acidity of the catalyst after nickel is loaded. This acidity reduction can be attributed to nickel crystallites while

covering the support acidic sites on the support surface will reduce the total acidity of the α -alumina.

- c) The XRF and Pulse Chemisorption confirm a metal loading of 3-4wt% Ni on the α -alumina support.
- d) The prepared catalyst show crystallite sizes in the range of 30 nm.
- e) Repeated TPR and TPO cycles show that, the Ni/ α -alumina catalyst displays a single peak of reproducible magnitude centered at approximately 500°C. This result indicates a reducible phase primarily composed by NiO.
- f) BET analysis on the α -alumina and the Ni/ α -alumina catalyst shows a moderate decrease in the total surface area of the catalyst after nickel is loaded on the calcined α -alumina support. The decrease of the surface area is assigned to the plugging of some of the support pores by nickel species.

Chapter 6 Experimental Results

6 Experimental Results

6.1 Introduction

This chapter reports experimental results obtained during catalytic runs using glucose – water and 2-methoxy-4-methylphenol-water mixtures. A discussion is provided regarding the effect of the operating variables (temperature, steam biomass ratio and reaction time) on product distribution.

Thermal and catalytic runs with Ni/a-alumina catalyst were performed in a CREC fluidized riser simulator. Mixtures of glucose-water and 2-methoxy-4-methylphenol-water at different steam biomass ratios (0.4, 0.6, 0.8 and 1.0 (g/g) wt%) were reacted in an argon environment (2 atm.), catalyst/biomass ratio of ~25, residence times of 5, 10, 20, and 30 s, and reaction temperatures 600, 650, and 700°C and 6000 rpm of impeller velocity. All thermal and catalytic runs were repeated at least 3 times to secure reproducibility of results. An important observation from these runs was that the mass balance closures, which consider permanent gases (H₂, CO, CO₂, H₂O, and CH₄), ethylene, ethane, propylene, acetaldehyde, carbon deposited over the catalyst and tar, were in the ±7% range, with most of the balances in the ±2% range. More details of this calculation are provided in Appendix F Mass Balances.

The gaseous reaction products were analyzed in a Shimadzu 2010 GC/MS with a thermal conductivity detector and a mass spectrometer, the pressure data of the reactor and vacuum box was saved on a computer disk using a Personal Daq acquisition card as described in Sections 4.3 and 4.6, respectively. The coke deposited on the catalysts after the every single experimental run was measured in a total organic carbon analyzer with a solid sample module from Mandel.

6.2 Glucose - Product Gas Partial Pressures Distribution

Figure 17 through Figure 21 present the experimental results data of the product gases acquired during catalytic runs using glucose as a feedstock.

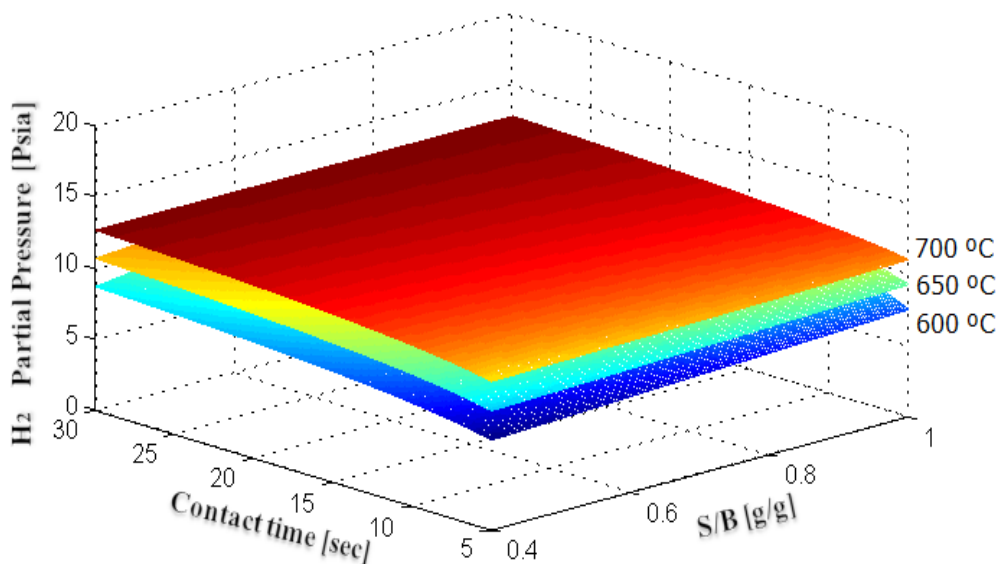


Figure 17. Hydrogen partial pressure experimental data for glucose as a function of temperature, S/B ratio, and reaction time. Note: This figure was plotted with at least 16 experimental data points at every temperature level. Typical standard deviations for repeats were 4%.

Figure 17 reports how the partial pressure of H_2 changes as a result of changes in temperature (600, 650, and 700°C), contact time (5-30s), and S/B ratio (0.4-1.0). It is quite apparent in the graph that the H_2 partial pressure increases as all three experimental parameters augment. In terms of S/B ratio, the partial pressure of H_2 slightly changes from 12.67 to 12.71 psia (700°C and 30s), as the S/B ratio ascends from 0.4 to 1.0. For conditions of 700°C and S/B ratio equal to 1.0, the partial pressure of H_2 upward trend is more noticeably from 11.03 to 12.71 psia, as the contact time increment from 5 to 30s. Additionally, when temperature raises from 600 to 700°C, the partial pressure of H_2 increases from 12.58 to 12.70 psia, at S/B ratio of 1.0 and contact time of 30s. From this experimental data it appears that the reaction contact time and temperature have the most significant effect on the production of H_2 .

These experimental results are consistent with the thermodynamic equilibrium calculations, as discussed in Chapter 8. It is predicted that augmenting the steam/biomass ratio does not lead to a significantly higher concentration of H_2 in the product gas.

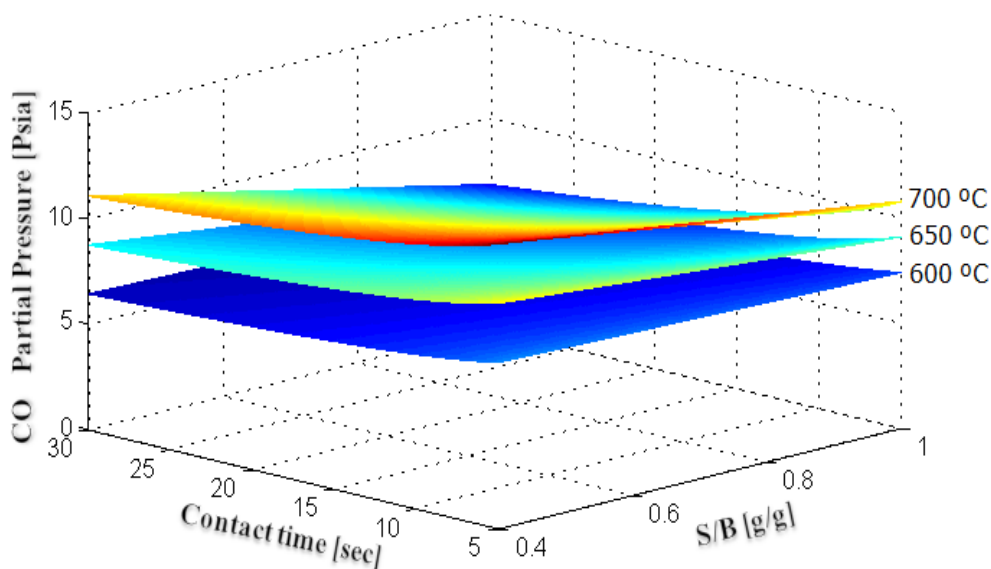


Figure 18. Carbon monoxide partial pressure experimental data for glucose as a function of temperature, S/B ratio, and reaction time. Note: This figure was plotted with at least 16 experimental data points at every temperature level. Typical standard deviations for repeats were 6%.

At thermodynamic equilibrium conditions, the CO mole fraction composition in the product gas decreases with an increment in the steam/biomass ratio according to the water-gas shift reaction, Eq (26). The same trend can be seen in Figure 18, where an increase in both contact time and S/B ratio has a negative effect on the partial pressure of CO. In this case, when the temperature and contact time are set at 700°C and 30s, the partial pressure of CO changes from 11.09 to 6.87 psia, as the S/B ratio varies from 0.4 to 1.0. Furthermore, as the contact time arises from 5 to 30s at 700°C and S/B ratio of 1.0, the CO partial pressure is reduced from 10.76 to 6.87 psia, at 700°C and S/B of 1.0. Finally, it can be observed that changing the temperature from 600 to 700°C at set S/B and contact time values of 1.0 and 30s respectively, the CO partial pressure evolves from 6.07 to 6.87 psia. Therefore, from the different operational parameters, the S/B ratio seems to have the largest influence on CO production, while the temperature displays the smallest.

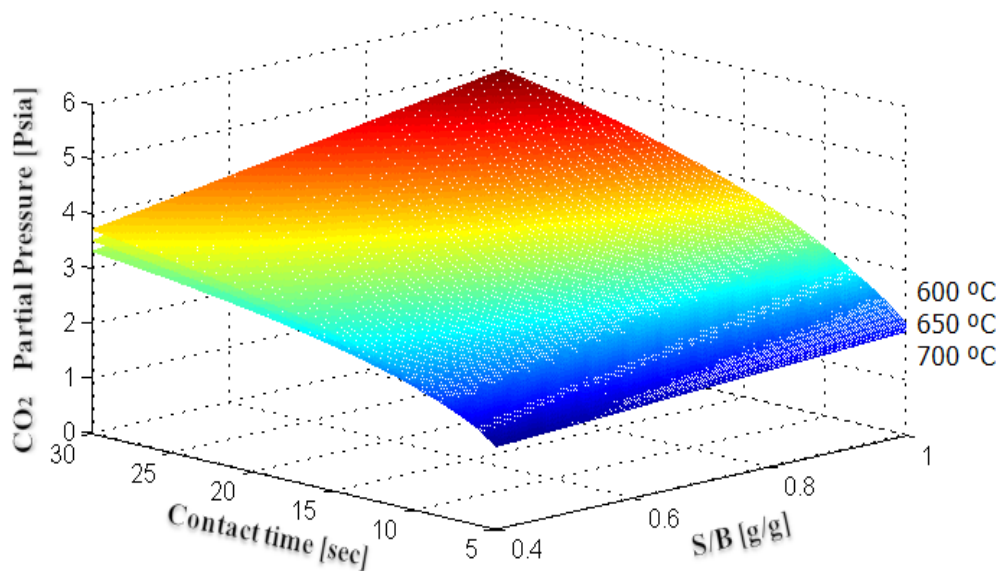


Figure 19. Carbon dioxide partial pressure experimental data for glucose as a function of temperature, S/B ratio, and reaction time. . Note: This figure was plotted with at least 16 experimental data points at every temperature level. Typical standard deviations for repeats were 5%.

As reported in Figure 19, the CO₂ partial pressure increases as the contact time and the S/B ratio augment. Temperature variations have the opposite effect. One can notice that these trends are reverse with respect to the ones observed for CO (Figure 18).

Furthermore, when the temperature remains constant at 600°C and the contact time is set at 30s and the S/B ratio increases from 0.4 to 1.0, the partial pressure of CO₂ changes from 3.72 to 4.92 psia,. Similarly, when the operating temperature is 600°C and the S/B ratio is 1.0, the partial pressure of CO₂ raises with contact time (5 to 30s) from 1.90 to 4.92 psia, As the temperature ascends from 600°C to 700°C, the partial pressure of CO₂ decreases slightly from 4.92 to 4.57 psia, at S/B ratio of 1.0 and contact time of 30s. In this case, the contact time has the most noticeable effect on the production of CO₂.

All the above reported results suggest that a combination of reactions govern the overall gasification reaction network, with the water-gas-shift reaction being a major influence on the observed product yields. The cause of this observed behavior may be assigned to the role of the nickel catalyst. This metal supported catalyst enhances the water-gas-shift reaction, and thus an increment in the CO₂ and H₂ production can be seen, while a downward trend in CO is observed.

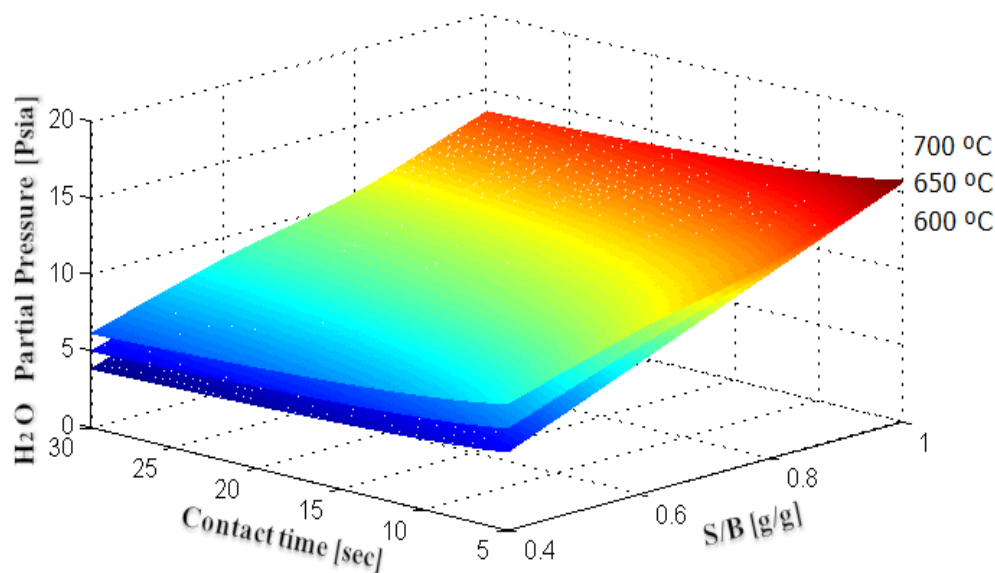


Figure 20. Water partial pressure experimental data for glucose as a function of temperature, S/B ratio, and reaction time. Note: This figure was plotted with at least 16 experimental data points at every temperature level. Typical standard deviations for repeats were 4%.

Figure 20 depicts how the partial pressure of H₂O changes as reaction temperature, contact time, and S/B ratio change. It can be observed a proportional increase in the partial pressure of H₂O with the S/B ratio. This increase could be attributed to the excess of gasification agent present in the system.

As contact time scales up, the H₂O partial pressure slightly decreases. The cause of this observed downward trend may be assigned to the role of the steam reforming of methane reaction (kinetically limited). For gasification conditions of 700°C and 30s, the partial pressure of H₂O ascends from 6.15 to 13.53 psia, as the S/B ratio moves from 0.4 to 1.0. In this case, when the temperature and S/B ratio are set at 700°C and 1.0, the partial pressure of H₂O is reduced from 15.74 to 13.53 psia, as the contact time progress form 5 to 30s. Finally, the temperature shows a positive effect on the partial pressure of H₂O. Thus, it is show as expected, that the S/B ratio has the most significant impact on the partial pressure of H₂O.

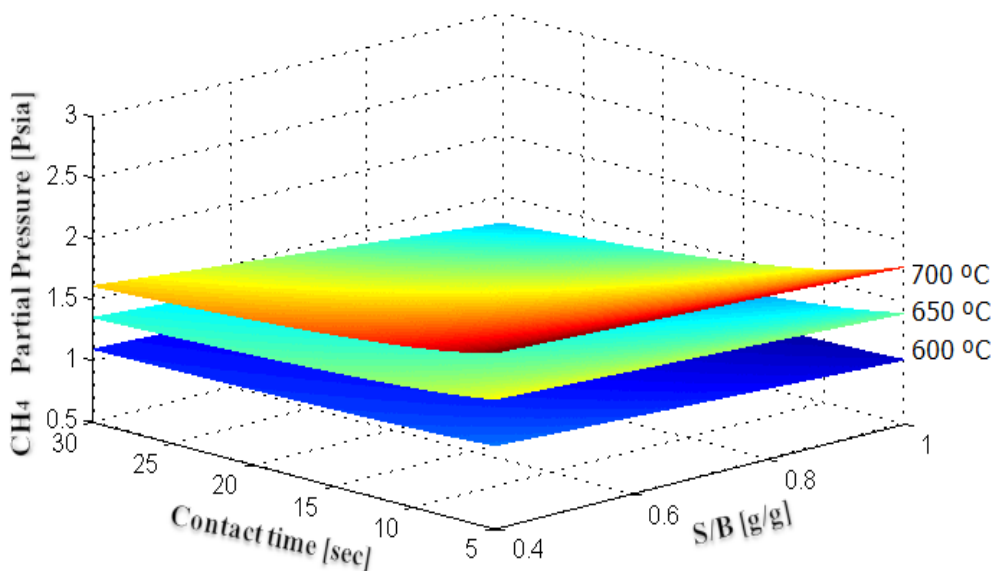


Figure 21. Methane partial pressure experimental data for glucose as a function of temperature, S/B ratio, and reaction time. Note: This figure was plotted with at least 16 experimental data points at every temperature level. Typical standard deviations for repeats were 4%.

Lastly, Figure 21 displays the trend for the partial pressure of CH₄ as a function of temperature, S/B ratio, and contact time. At 700°C and 30s, the partial pressure of CH₄ slightly changes from 1.61 to 1.27 psia, as the S/B ratio moves from 0.4 to 1.0. Additionally, at temperature of 700°C and S/B ratio of 1.0, the partial pressure of CH₄ presents a downward trend from 1.79 to 1.27 psia, when the contact time goes from 5 to 30s. Temperature shows an opposite influence on the CH₄ partial pressure. In this particular case, all three reaction parameters have a similar impact, in magnitude, on the partial pressure of CH₄.

The predictions of the thermodynamic equilibrium model show that almost no methane is produced over the span of experimental S/B ratios (0.4–1.0) and temperatures (600–700°C). This indicates that a state of equilibrium is not reached during experiments. The de-volatilization of the glucose gives high contents of methane which do not react completely leading to equilibrium concentrations of H₂, CO, CO₂, and H₂O according to the steam reforming and dry reforming of methane reactions.

6.3 2-methoxy-4-methylphenol - Product Gas Partial Pressures Distribution

Figure 22 through Figure 26 present the experimental results of the main product gases obtained during catalytic gasification of 2-methoxy-4-methylphenol including H₂, CO, CO₂, H₂O and CH₄.

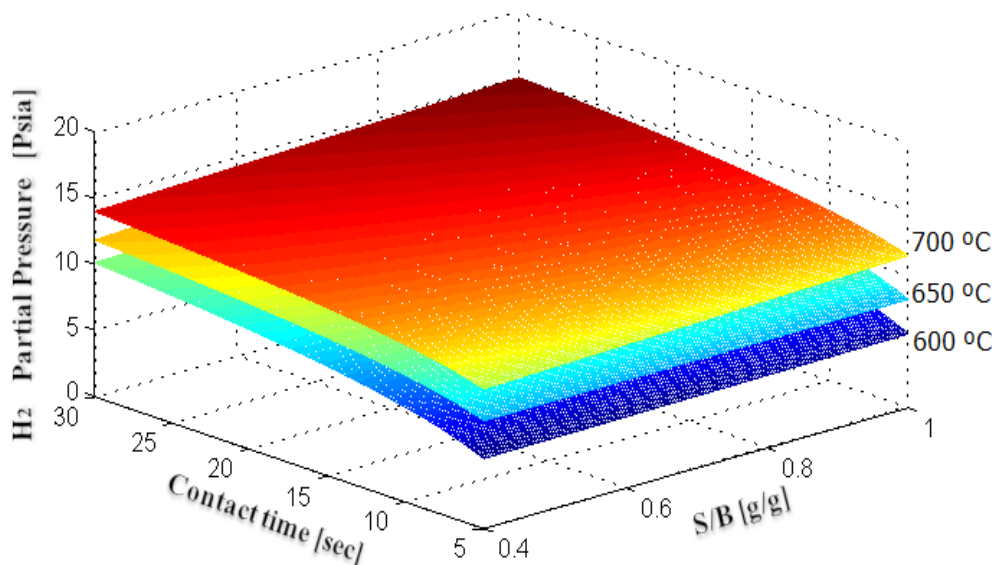


Figure 22. Hydrogen partial pressure experimental data for 2-methoxy-4-methylphenol as a function of temperature, S/B ratio, and reaction time. Note: This figure was plotted with at least 16 experimental data points at every temperature level. Typical standard deviations for repeats were 3%.

Figure 22 shows the change on the partial pressure of H₂ as a function of the variation in temperature (600, 650, and 700°C) S/B ratio (0.4-1.0) and contact time (5-30s), when 2-methoxy-4-methylphenol is used as the biomass feed. As reported for glucose, it can also be notice in the graph that the H₂ partial pressure builds up as all three experimental variables augment. With reference to S/B ratio, the H₂ partial pressure gradually rises from 13.97 to 14.95 psia, when the S/B ratio escalates form 0.4 to 1.0 at 700°C and 30s. As the contact time moves up from 5 to 30s, the H₂ partial pressure increases from 11.48 to 14.95 psia at 700°C and S/B ratio of 1.0. In addition, when the temperature ascends from 600 to 700°C, and the contact time and S/B ratio are 30s and 1.0 respectively, the partial pressure of H₂ shows an increment from 10.97 to 14.95 psia. Taking into

consideration the data trends it seems that the reaction contact time and temperature have the most noticeable effect on the production of H_2 .

Once more time, these experimental results are consistent with the thermodynamic equilibrium calculations that predict a small influence of the steam/biomass ratio on the concentration of H_2 in the product gas.

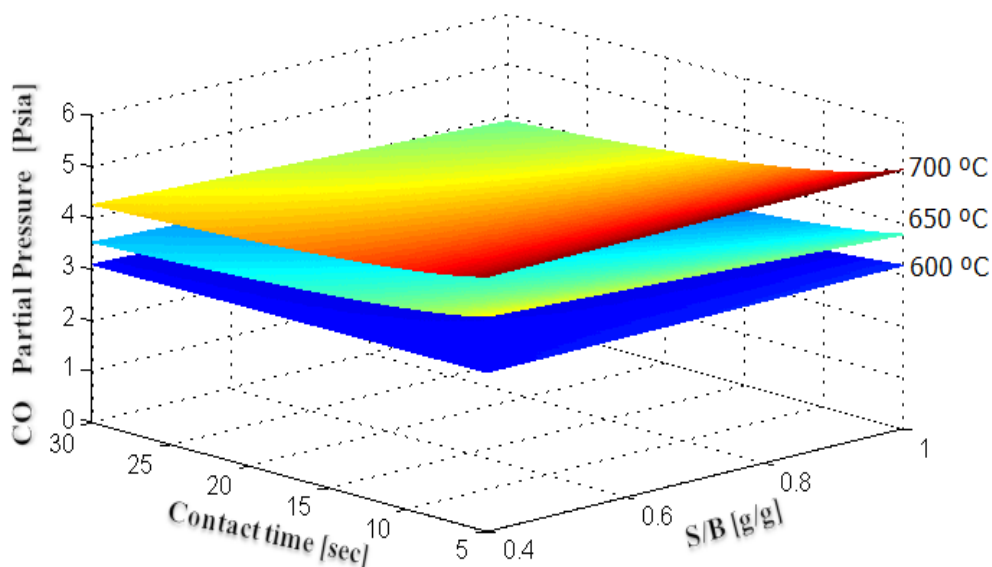


Figure 23. Carbon monoxide partial pressure experimental data for 2-methoxy-4-methylphenol as a function of temperature, S/B ratio, and reaction time. Note: This figure was plotted with at least 16 experimental data points at every temperature level. Typical standard deviations for repeats were 3%.

A close trend than for equilibrium predictions for CO, as reported in Chapter 8, can be seen in Figure 23. It can be observed that an increment in S/B ratio has a negative influence on the partial pressure of CO according to the water gas shift reaction. In this case, when the temperature and contact time are kept at 700°C and 30s, the partial pressure of CO change from 4.26 to 3.88 psia as the S/B ratio augments from 0.4 to 1.0. Moreover, as the contact time arises from 5 to 30s, the CO partial pressure decreases from 5.06 to 3.88 psia, when the temperature is 700°C and the S/B ratio is 1.0. And finally, it can also be observed that a raise in temperature from 600 to 700°C results in a CO partial pressure ascends from 2.84 to 3.88 psia, when the S/B ratio and contact time remain at 1.0 and 30s, respectively. All three experimental parameters appear to have close influence in magnitude on the partial pressure of CO.

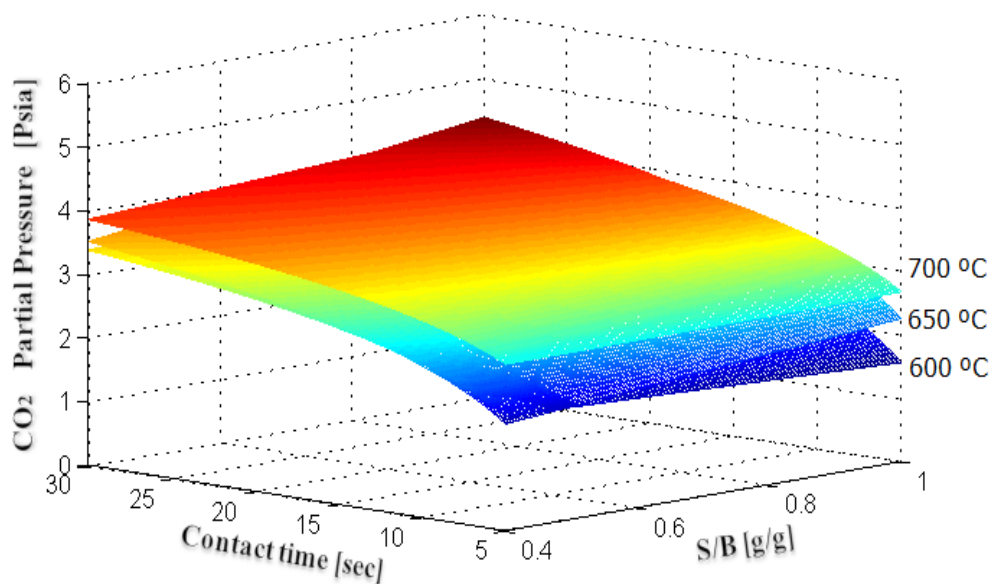


Figure 24. Carbon dioxide partial pressure experimental data for 2-methoxy-4-methylphenol as a function of temperature, S/B ratio, and reaction time. Note: This figure was plotted with at least 16 experimental data points at every temperature level. Typical standard deviations for repeats were 3.8%.

As seen in Figure 24, the CO₂ partial pressure increases as contact time, S/B ratio, and temperature move upwards. This is a similar behaviour that is seen for the partial pressure of H₂ (Figure 22). The cause of this observed trend may be assigned to the role of the nickel catalyst that enhances the water-gas-shift reaction. As a result of this, an increment in the CO₂ and H₂ production can be seen, while a downward trend in CO is observed. In the same way, when the temperature remains constant at 700°C and the contact time is set at 30s, the partial pressure of CO₂ changes from 3.85 to 4.22 psia, as the S/B ratio moves from 0.4 to 1.0. Similarly, at 700°C and S/B ratio of 1.0, the partial pressure of CO₂ increases from 2.66 to 4.22 psia, when the contact time raises from 5 to 30s. Finally, the temperature has a positive effect on the partial pressure of CO₂ where a slightly increment from 3.82 to 4.22 psia can be seen when temperature ascents from 600 to 700°C at S/B ratio of 1.0 and contact time 30s. In this case, the contact time has the most noticeable effect on the production of CO₂.

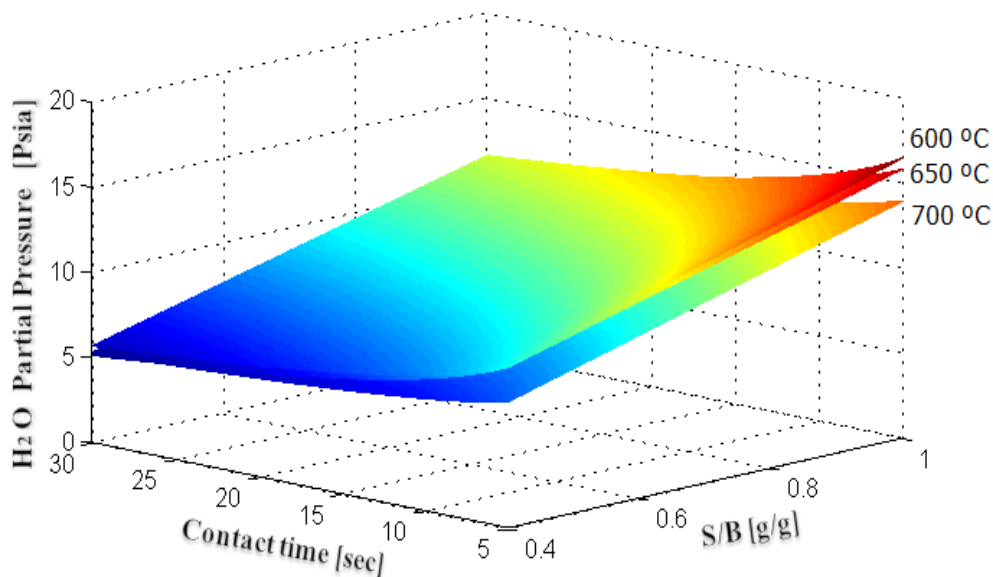


Figure 25. Water partial pressure experimental data for 2-methoxy-4-methylphenol for glucose as a function of temperature, S/B ratio, and reaction time. Note: This figure was plotted with at least 16 experimental data points at every temperature level. Typical standard deviations for repeats were 5%.

Figure 25 reports how the partial pressure of H₂O changes as reaction temperature, contact time, and S/B ratio vary. One can observe a proportional increase in the partial pressure of H₂O with the S/B ratio. This proportional increase is attributed to the excess of gasification agent introduced to the system.

As contact time goes up, the H₂O partial pressure slightly decreases. The cause of this observed downward trend may be assigned mainly to the role of the steam reforming of methane reaction. For reaction conditions of 700°C and 30s contact time, the partial pressure of H₂O evolves from 5.28 to 11.16 psia, as the S/B ratio moves from 0.4 to 1.0. In the case, when the temperature and S/B ratio are set at 700°C and 1.0, the partial pressure of H₂O is attenuated from 13.90 to 11.16 psia, as the contact time augments from 5 to 30s. Finally, the temperature shows a slightly negative effect on the partial pressure of H₂O. Thus, it is shown as expected, that the S/B ratio has the most significant impact on the partial pressure of H₂O.

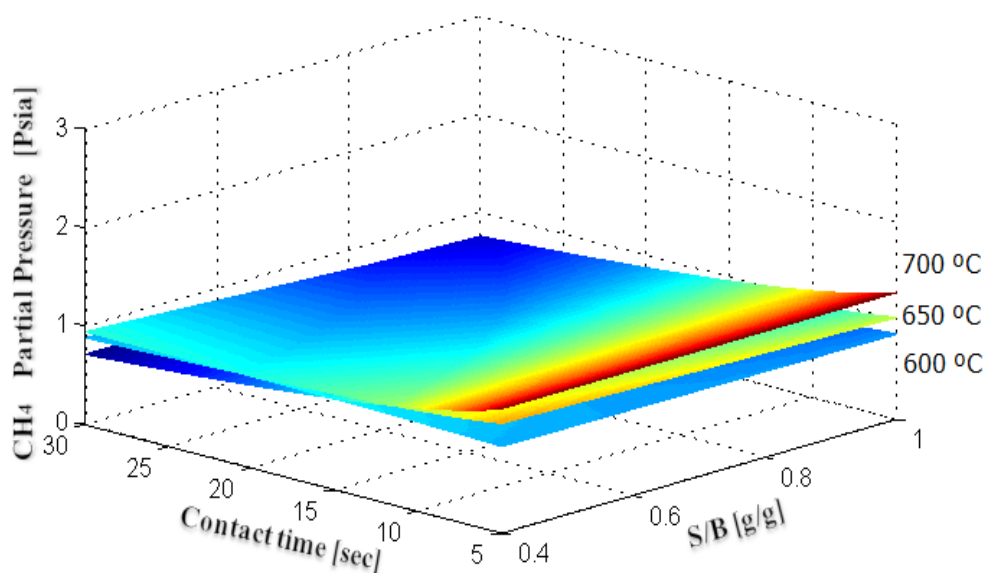


Figure 26. Methane partial pressure experimental data for 2-methoxy-4-methylphenol as a function of temperature, S/B ratio, and reaction time. Note: This figure was plotted with at least 16 experimental data points at every temperature level. Typical standard deviations for repeats were 5%.

Lastly, Figure 26 displays the trend for the partial pressure of CH₄ as a function of temperature, S/B ratio, and contact time. At thermodynamic equilibrium, almost no CH₄ is produced over the span of experimental S/B ratios (0.4–1.0) and temperatures (600–700°C). It can be observed in the graph that the experimental data shows a CH₄ partial pressure of around 1.0 psia. These experimental results which differ from the equilibrium predictions indicate that a state of chemical equilibrium for methane is not reached during experiments.

As reported in Figure 26, the partial pressure of CH₄ augments very slightly from 0.72 to 0.75 psia, as the S/B ratio changes from 0.4 to 1.0 at 700°C and contact time of 30s. Additionally, at 700°C and S/B ratio equal to 1.0, the partial pressure of CH₄ presents a downward trend from 1.28 to 0.75 psia as the contact time increases from 5 to 30s. In terms of temperature, the partial pressure of CH₄ has a small contribution from 0.73 to 0.75 psia, as the temperature goes from 600 to 700°C, with the contact time and S/B ratio remaining constant at 30s and 1.0, respectively. In this case, the contact time seems to have the greatest impact on the partial pressure of CH₄.

6.4 Conclusions

1. It is reported the effect of the operating variables such as temperature, SB ratio and contact time on the product gas distribution during catalytic runs using glucose – water and 2-methoxy-4-methylphenol-water mixtures.
2. It is proven that at the operating conditions of the CREC Riser Simulator the methane experimental results differ from the thermodynamic equilibrium predictions indicating that the reforming of methane is a kinetically controlled chemical reaction.
3. It is shown that reported experimental runs were affected with mass balance closures in the $\pm 7\%$ range, with most of the balances in the $\pm 2\%$ range.

Chapter 7

Tars from Biomass Gasification

The main purpose of this chapter is to provide information and experimental results on “tar” formation. Tar is an expected biomass gasification product. According to Milne et al., 1998; *tar is the most cumbersome and problematic parameter in any gasification commercialization effort*. Both the fraction of tar and type of tar formed are closely related with the biomass or the model compound considered to represent the biomass to be gasified. While for glucose gasification, tar formation is minimal, for the 2-methoxy-4-methylphenol gasification there is considerable amounts of tar obtained along permanent gases being formed.

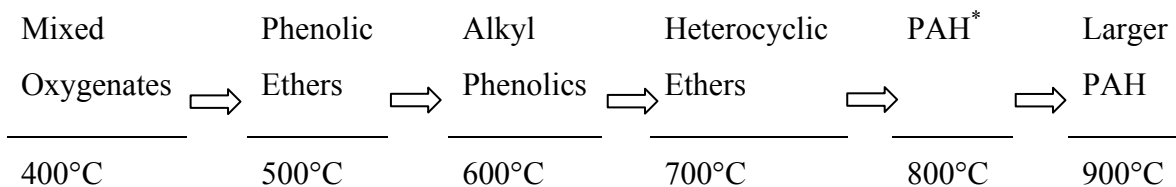
7 Introduction

Tar is a complex mixture of condensable hydrocarbons, which includes single ring to 5-ring aromatic compounds along with other oxygen-containing hydrocarbons species (Tasaka et al., 2007). These product species condense in gasifier pipe outlets and in particulate filters which leads to blockages. Tar causes further downstream problems and clogs fuel lines and injectors in internal combustion engines. Moreover, tars contain significant amounts of energy that could be transferred to the fuel gases such as H₂, CO, CO₂, CH₄, etc. Considerable efforts are currently being made towards tar removal from fuel gas. The different approaches for tar removal to date can be categorized as direct syngas treatment inside the gasifier and hot gas cleaning after the gasification process.

In this work, tar is defined as *“the C₆+ organics produced under gasification conditions from any organic feedstock and generally assumed to be largely composed by aromatic molecules.”* Although this definition does not allow for distinction between classes and families of tar compounds, which will be presented comprehensively in Section 7.1, it is a useful as a starting definition.

7.1 Tar Composition and Maturation

Elliott, 1988; reviewed the composition of biomass pyrolysis products and gasifier tars from various processes. Figure 27 shows the expected transition from primary products to phenolic compounds to aromatic hydrocarbons as a function of process temperature, and Table 10 shows the classes of chemical components in each major regime based on a GC/MS analysis of collected tars.



* High molecular weight polynuclear aromatic hydrocarbons (PAHs)

Figure 27. Tar maturation scheme proposed by Elliott, 1988.

In a later publication, Baker et al., 1988, described a conceptual relationship between the yield of tars and the reaction temperature as shown in Figure 28.

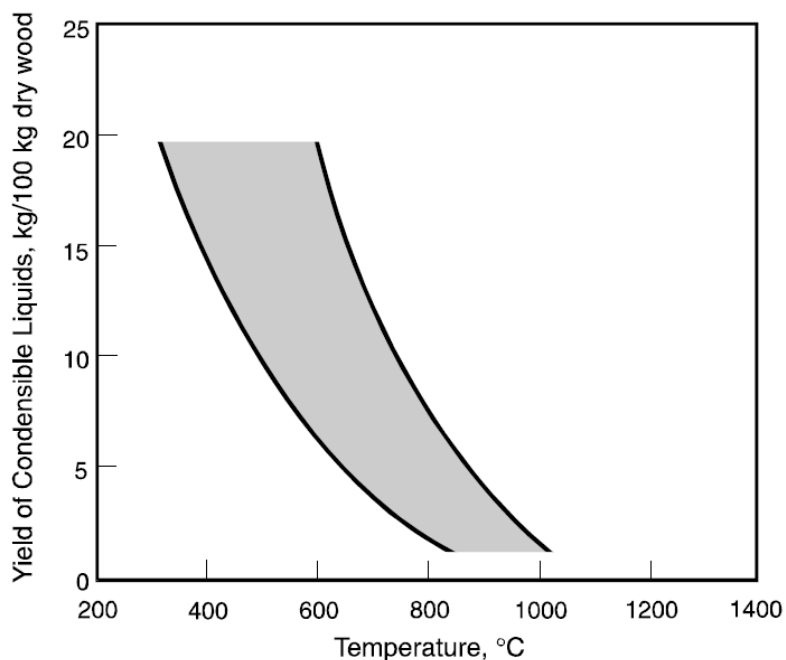


Figure 28. Tar yield as a function of the maximum temperature exposure (Baker et al., 1988).

They cited the level of tars for various reactors types, with the updraft gasifiers having 12 wt% of wood fed and the downdraft gasifiers forming less than 1 wt%. Steam-blown fluid-bed gasifiers had tar levels of 15% at 600°C and 4% at 750°C. For oxygen-blown fluid beds, the levels of tar were 4.3% and 1.5% at 750°C and 810°C, respectively. The entrained flow gasifier of Battelle Columbus Laboratories operated at 1,000°C, and had tar levels of 1% (Baker et al., 1988). Table 10 reports chemical species groups observed in tars at various temperature ranges.

Table 10. Chemical components in biomass tar (Elliott, 1988).

Conventional Flash Pyrolysis (450–500°C)	High-Temperature Flash Pyrolysis (600–650°C)	Conventional Steam Gasification (700–800°C)	High-Temperature Steam Gasification (900–1000°C)
Acids	Benzenes	Naphthalenes	Naphthalene
Aldehydes	Phenols	Acenaphthylenes	Acenaphthylene
Ketones	Catechols	Fluorenes	Phenanthrene
Furans	Naphthalenes	Phenanthrenes	Fluoranthene
Alcohols	Biphenyls	Benzaldehydes	Pyrene
Complex Oxygenates	Phenanthrenes	Phenols	Acephenanthrylene
Phenols	Benzofurans	Naphthofurans	Benzanthracenes
Guaiacols	Benzaldehydes	Benzanthracenes	Benzopyrenes
Syringols			226 MW PAHs
Complex Phenols			276 MW PAHs

The influence of process changes can be seen as a function of reaction severity, which accounts for both temperature and time. Evans and Milne, 1987a,b, show the trade-off in product distribution as a function of these two parameters by using multivariate analysis of product composition. In this respect, an important consideration is the gas-phase reactions leading to tar synthesis. Hydrocarbon chemistry, based on free radical

processes, occurs in this thermal regime where olefins react to give aromatics. This process occurs at the same time as dehydration, while decarbonylation reactions can be considered as the main drivers of the chemical transformations reported in Figure 27.

Evans and Milne, 1987 a, b, used molecular beam mass spectrometry (MBMS) to establish that a systematic approach to classifying pyrolysis products as primary, secondary, and tertiary. This approach can be also employed to compare products from the various reactors that are used for pyrolysis and gasification. Four major product classes were identified as a result of gas-phase thermal cracking reactions.

- a. Primary products: characterized by cellulose-derived products such as levoglucosan, hydroxyacetaldehyde, and furfurals; analogous hemicellulose-derived products; and lignin-derived methoxyphenols;
- b. Secondary products: characterized by phenolics and olefins;
- c. Alkyl tertiary products: include methyl derivatives of aromatics, such as methyl acenaphthylene, methylnaphthalene, toluene, and indene;
- d. Condensed tertiary products: show the PAH series without substituents: benzene, naphthalene, acenaphthylene, anthracene/phenanthrene, and pyrene.

The primary and tertiary products were mutually exclusive as shown by the distribution in Figure 29 (Evans and Milne, 1997). That is, the primary products are converted before the tertiary products are formed. The tertiary aromatics can be produced from cellulose and lignin, although higher molecular weight aromatics were formed faster from the lignin-derived chemical species (Evans and Milne, 1987 a, b).

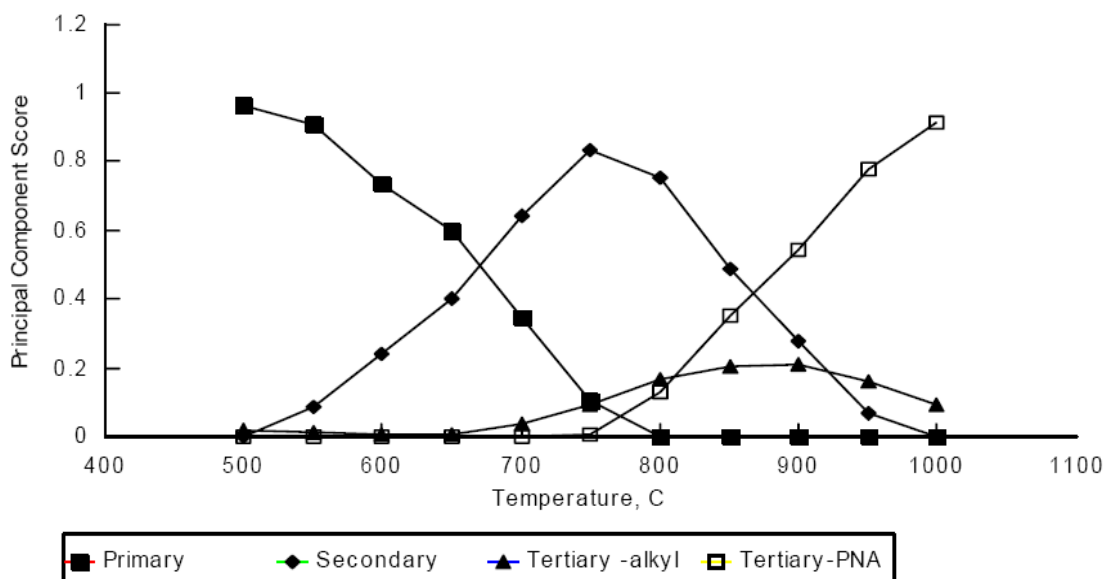


Figure 29. The distribution of the four tar component classes as a function of temperature at 300 ms (0.3 s) gas-phase residence time (reprinted from Evans and Milne, 1997)

Ekstrom et al., 1985, showed the catalytic effects of char on tar cracking. Gas was circulated over a char bed resulting in reduced yields of tar and increased yields of CH₄, CO₂, and H₂. These and other results quoted by Ekstrom et al., 1985, indicate that the temperature and the type of wood are important factors in tar composition. These results lead to the conclusion that intra-particle phenomena are likely to be important and add complexity to the severity equation that governs tar yields and composition.

The assumption often made is that tars thermally crack to CO, H₂, and other light gases with this being a function of temperature. This can be seen in primary product cracking wherein yields of 50% by weight of CO are possible by thermal cracking. However, this is not true for the condensable tertiary products, which grow in molecular weight with reaction severity. Evans and Milne, 1997, show that the ratio of benzopyrene to naphthalene (m/z 252/128) increases with both temperature and gas-phase residence time. Simell et al., 1993, found that the relative proportion of heavy PAH components in the tar increased as the gasification temperature increased in high pressure, air-blown, fluid-bed wood gasifiers.

One should notice that the decision to run a gasification system at high severity to crack tars should be balanced taking into consideration the remaining tar composition. Elliott,

1986, pointed out the processing dilemma that arises when high temperatures favor greater efficiency and reaction rates, whilst also leading to a more refractory nature of the remaining tar. The condensed aromatics in these tertiary tars may prove harder to remove by downstream catalytic cracking than the larger amount of primary or secondary tars produced under less severe gasification conditions. In fact the molecular weight of PAHs increases through the tertiary cracking zone; hence, maturation of tar to soot should be kept in mind both in running gasifiers and in performing chemical analysis to determine the effectiveness of tar cracking.

Conventional analysis of tars from various gasifiers by GC/MS shows the relationship between reaction severity and tar composition. This always comes with the caveat that incomplete product collection, post-condensation reactions, and the averaging of sample composition over time can mask the true underlying chemical processes. These analyses are particularly valuable for evaluating tar composition before and after catalytic operations. Bangala et al., 1997, published a representative GC of the tars from the atmospheric-pressure, fluidized-bed gasification of wood at 780°C, as reported in Figure 30. This shows a mixture of primary products such as furfural, secondary products such as cresols, and tertiary products such as phenanthrene. There are no correlations allowing a statistically valid quantification of the residence-time distribution as a function of the formed tar profile.

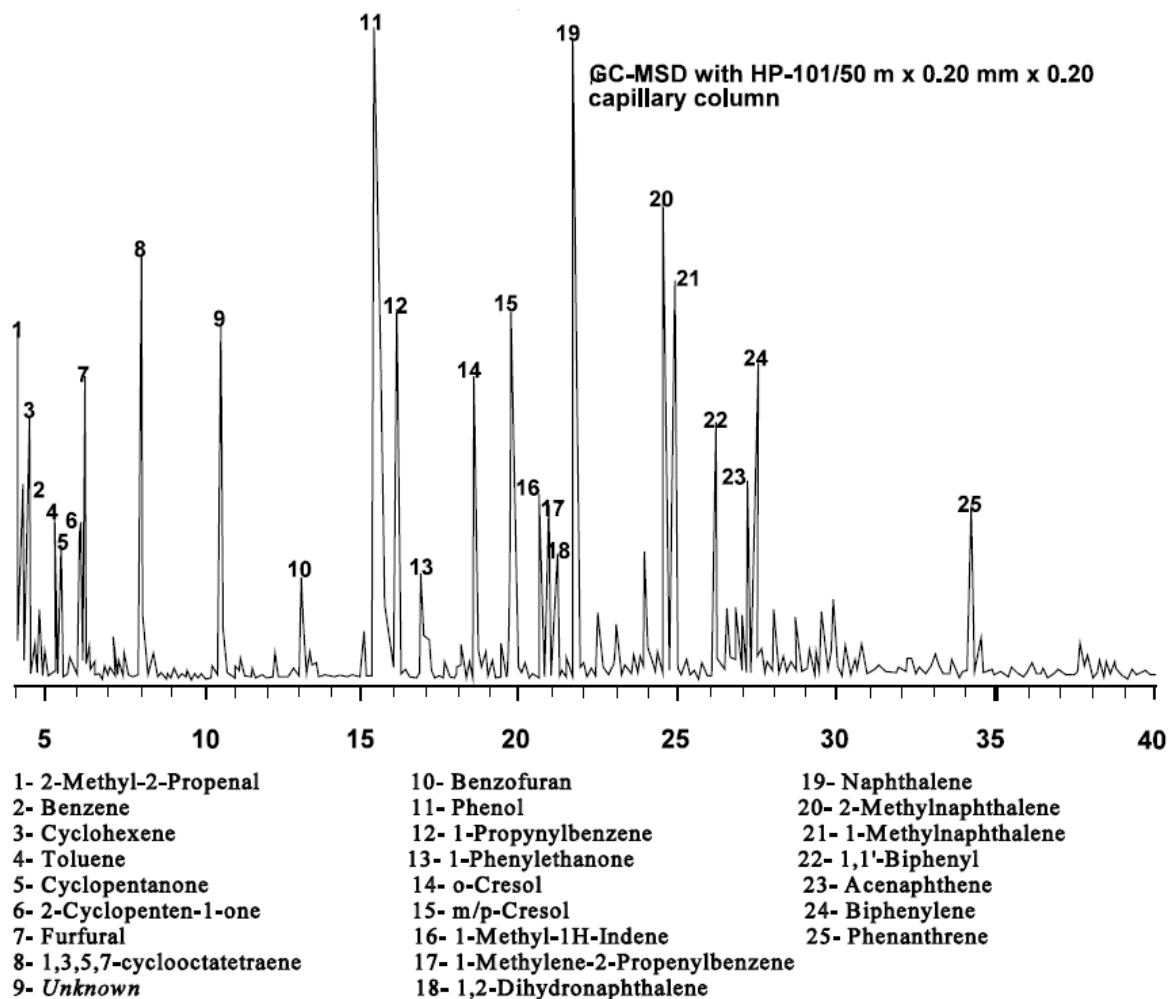


Figure 30. Composition of tar from atmospheric-pressure, air gasification of biomass at 780°C (Bangala et al., 1997)

Aldén et al., 1988, developed a two-stage reactor system to study tar formation and thermal and catalytic cracking where the gas-phase cracking temperature can be independently varied. GCs of tars generated at temperatures from 400 to 900°C show the systematic maturation of the low temperature tars to the high temperature tars. The former has many peaks at short retention times, while the latter has fewer peaks at short retention times, but more peaks in higher quantities at longer retention times.

7.2 Reduction of Tars

7.2.1 Thermal

There is a literature consensus that supports the view that temperatures in excess of 1000°C, at reasonable residence times, are necessary to destroy the refractory unsubstituted aromatics without a catalyst. However, such thermal decomposition can produce a soot (the fine black particles produced by incomplete combustion) that can be even more troublesome than the aromatic species for some processes. Benzene seems to be the least reactive, thermally, of the light aromatics.

7.2.2 Steam

The addition of steam, over and above that formed from the water and oxygen in the biomass feedstock, has been reported to produce fewer refractory tars, enhance phenol formation, reduce the concentration of other oxygenates, have a small effect on the conversion of aromatics, and produce tars that are easier to reform catalytically.

7.2.3 Partial Oxidation

The effects of steam and oxygen on biomass gasification rates were reported by Wang and Kinoshita, 1992, and by Narváez et al., 1996, among others. Equivalence ratios (ratio of oxygen in the mixture to that required for complete combustion) of 0.2 to 0.45 were explored. The thermal cracking of tars with steam and oxygen added in the cracking zone was reported by Jönsson, 1985. Both additives increased the cracking rate over the temperature range studied (950–1250°C). The partial oxidation of the primary, secondary, and tertiary products has been studied by MBMS (Evans and Milne, 1997). Under these conditions, oxygen can influence the cracking of these products before complete oxidation occurs. The presence of oxygen at 600–700°C accelerates the destruction of primary pyrolysis products but has no significant effect on benzene destruction once it is formed. Secondary and tertiary products are generally less susceptible to oxidation than primary products, and each primary product appears to have its own reaction rate, which indicates a selective bimolecular process.

7.2.4 The Catalytic Reduction of Tars

Many types of catalysts have been investigated to reduce tars to lower levels and at lower temperatures than by thermal, oxidative, or steam reforming alone. Non-metallic catalysts such as dolomites, and metallic catalysts such as nickel (Ni), have been extensively studied. A literature review of catalyst for gasification of biomass and tar conversion is presented in Section 3.4 (Chapter 3).

7.3 Tar Quantities as a Function of Gasifier Type

Numerous publications report the quantities of tar produced by various types of gasifiers, under various geometries and operating conditions; e.g., (Abatzoglou et al., 1997; Bangala, 1997; CRE Group Ltd., 1997; Graham et al., 1993; Hasler et al., 1998; Mukanda et al., 1994a; Mukanda et al., 1994b; Nieminen et al., 1996). The lack of standard quantification procedures renders a successful comparison difficult (CRE Group Ltd., 1997). Generally it has been proven and explained scientifically and technically that updraft gasifiers produce more tar than fluidized beds while fluidized beds produce more than downdraft gasifiers. Table 11 presents the amount of tar reported in raw gases for fluidized gasifiers.

Table 11. Tars reported in raw gases for fluidized gasifiers (Milne et al., 1998)

Amount of tar	Gasifier	Conditions	Reference
10 wt% feed		Typical Steam	Corella et al. 1991
8-4 wt% feed	Steam	650-780°C 780°C	Corella et al. 1989
15 wt% feed	Top-fed.	750°C	Corella et al. 1988
3 wt%	Bottom-fed		
10 wt% feed	Indirect	620°C	Flanigan et al. 1988
7.5 wt% feed		760°C	
46 wt% feed	Waterloo-type	650°C	Garcia et al. 1997
39 wt% feed		700°C	
18.2 wt% feed	Laboratory	Top-fed, inert gas 600°C	Gulyurthu et al. 1994
10.7		790°C	
9.2		990°C	
24		700°C Steam	
6		900°C	
4.3 wt% feed	HNEI,	700°C	Kinoshita et al. 1994
5.4	indirectly	750°C	
2.5	heated	900°C	
5.4 wt% feed	Bench	800°C, no steam	Wang et al. 1994

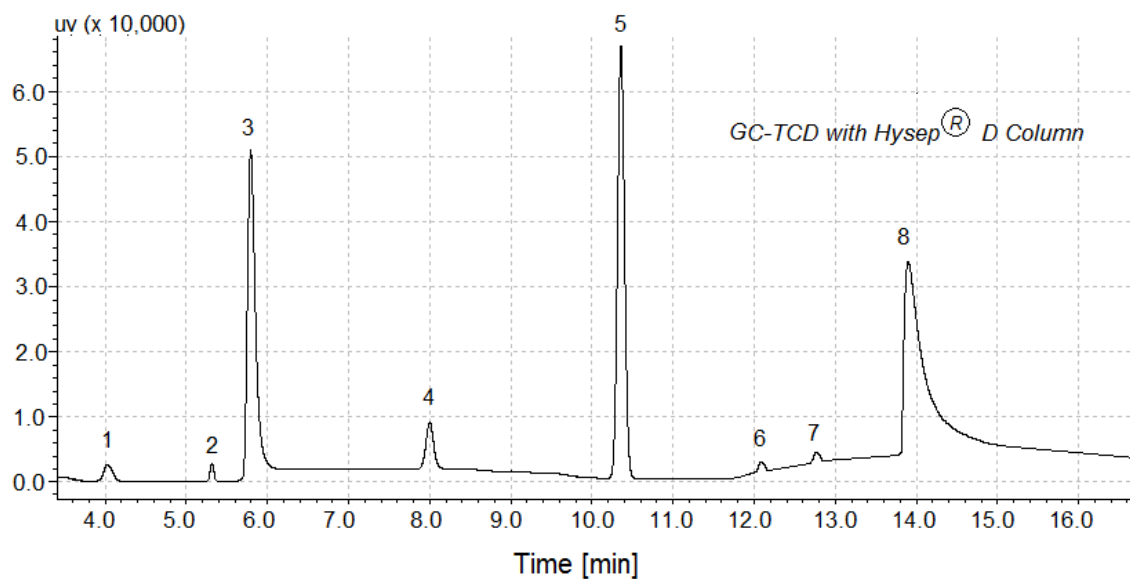
7.4 Experimental Tar Measurements in the CREC Riser Simulator

Steam gasification experiments over Ni/ α -alumina catalyst were developed using the CREC Riser Simulator. Mixtures of glucose-steam and 2-methoxy-4-methylphenol-steam were used as model compounds of the cellulose and lignin contained in biomass, respectively. The gaseous reaction products were analyzed in a Shimadzu GC/MS system with a thermal conductivity detector and a mass spectrometer. A detailed experimental method is presented in Chapter 4.

The tar formation is closely related with the model compound considered to represent the biomass to be gasified. While for glucose gasification, there is minimal to no tar formation, for the 2-methoxy-4-methylphenol gasification there is considerable amounts of tar obtained along permanent gases being formed.

The components present in the tars were quantified based on the size of the peaks in the MS spectrum in relation to the size of the methane peak in the same spectrum. Since methane was visible in both the GC and MS spectrums that analyzed the products of the catalytic steam biomass gasification, the concentration of methane reported in the GC analysis (quantified using calibration curves), dictated an equal concentration of methane in the MS analysis. Thus, a concentration/area ratio, based solely on methane, was established and compared to all peak areas in the MS spectrum. This led to the quantification of the unknown concentrations of all reported tar species.

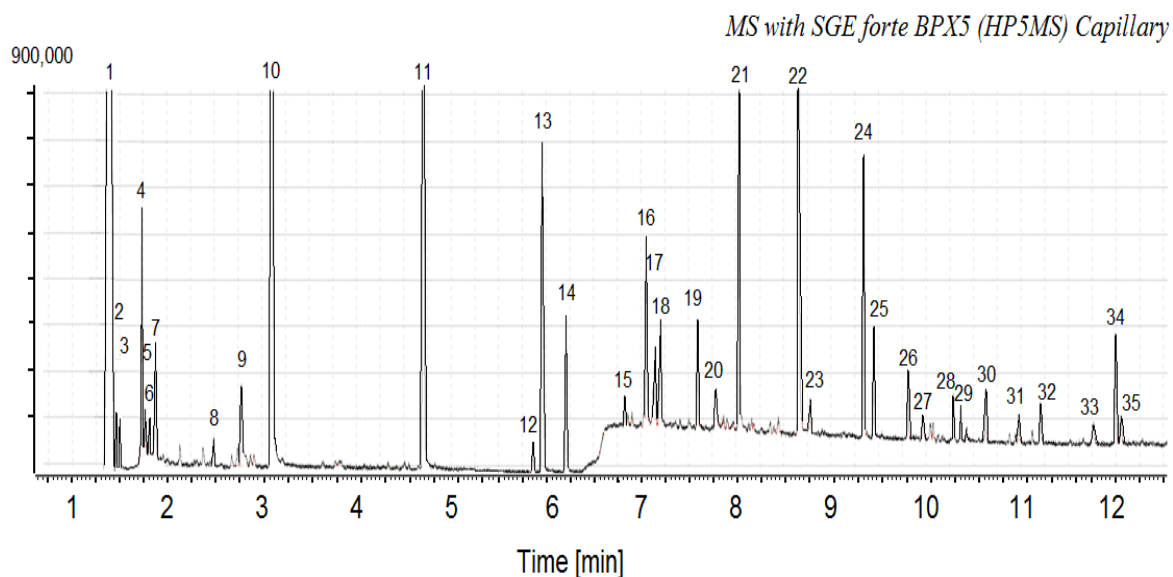
Figure 31 shows the product gas components identified in the Shimadzu GC/TCD when gasifying 2-methoxy-4-methylphenol. The different components were quantified using calibration curves.



1	Hydrogen	5	Carbon Dioxide
2	Nitrogen	6	Ethylene
3	Carbon Monoxide	7	Ethane
4	Methane	8	Water

Figure 31. Composition of permanent gases for catalytic steam gasification of biomass at 700°C, atmospheric pressure, S/B ratio of 0.4, and 30 seconds reaction time

A Shimadzu 2010 mass selective detector with a HP-5MS silica capillary column was used for identification of the components present in the tars. Figure 32 displays the main component identified in tars for catalytic steam gasification of 2-methoxy-4-methylphenol at 700°C, S/B ratio of 0.4 and 30 seconds of contact time. A detailed list of the entire components identified in the tars is presented in Table 12.



1	Methane	18	Benzocyclobuten-1(2H)-one
2	Ethylene	19	Indene
3	Ethane	20	Phenol, 3-methyl-
4	1,3-Pentadiene	21	2-Propenal, 3-phenyl-
5	2-Butene, 2-methyl-	22	Naphthalene
6	1,3-Pentadiene, (Z)-	23	Phenol, 2-ethyl-5-methyl-
7	1,3-Cyclopentadiene	24	Naphthalene, 2-methyl-
8	1,3-Butadiene, 2,3-dimethyl-	25	Naphthalene, 1-methyl-
9	1,3-Cyclohexadiene	26	Naphthalene, 1,7-dimethyl-
10	Benzene	27	Naphthalene, 2,3-dimethyl-
11	Toluene	28	1,1'-Biphenyl, 3-methyl-
12	Ethylbenzene	29	1-Naphthalenol
13	o-Xylene	30	2-Naphthalenol
14	p-Xylene	31	7-Methyl-1-naphthol
15	Benzene, 1-ethyl-3-methyl-	32	9H-Fluoren-9-ol
16	Phenol	33	Naphtho[2,1-b]furan, 1,2-dimethyl-
17	Benzene, 1-ethenyl-2-methyl-	34	Anthracene
		35	Phenanthrene

Figure 32. Composition of tar for catalytic steam gasification of biomass at 700°C, atmosphere pressure, S/B ratio of 0.4, and 30 seconds of reaction time

Table 12. MS peak integration for catalytic steam gasification of 2-methyl-4-methoxyphenol at 700°C, atmospheric pressure, S/B ratio of 0,4, and 30s of reaction time

Component	Area	Height	Formula	Mass (g)
Methane	9523960	11440397	CH ₄	2.42E-03
1,3-Pentadiene	465573	631983	C ₅ H ₈	1.18E-04
2-Butene, 2-methyl-	88994	121962	C ₅ H ₁₀	2.26E-05
1,3-Pentadiene, (Z)-	79907	100666	C ₅ H ₈	2.03E-05
1,3-Cyclopentadiene	151042	124570	C ₅ H ₆	3.84E-05
1,3-Butadiene, 2,3-dimethyl-	77709	73581	C ₆ H ₁₀	1.97E-05
1,3,5-Hexatriene, (Z)-	19895	16387	C ₆ H ₈	5.05E-06
1,3-Cyclohexadiene	32106	24672	C ₆ H ₈	8.15E-06
Benzene	8706184	6476668	C ₆ H ₆	2.21E-03
Cyclopentene,3-methylene-	4544	6663	C ₆ H ₈	1.15E-06
Toluene	4966881	4813976	C ₇ H ₈	1.26E-03
Ethylbenzene	110351	103275	C ₈ H ₁₀	2.80E-05
o-Xylene	1051568	803027	C ₈ H ₁₀	2.67E-04
p-Xylene	373395	368065	C ₈ H ₁₀	9.48E-05
Benzene, 1-ethyl-3-methyl-	262414	144364	C ₉ H ₁₂	6.66E-05
Benzene, 1-ethyl-3-methyl-	188503	100179	C ₉ H ₁₂	4.79E-05
2-Cyclopenten-1-one, 3-methyl-	19284	51328	C ₆ H ₈ O	4.90E-06
.alpha.-Methylstyrene	140356	75868	C ₉ H ₁₀	3.56E-05
Phenol	66876	44552	C ₆ H ₆ O	1.70E-05
Benzene, 1,2,3-trimethyl-	93399	91511	C ₉ H ₁₂	2.37E-05
Benzene, 1-ethenyl-2-methyl-	156150	147858	C ₉ H ₁₀	3.96E-05
Benzene, 1-ethenyl-3-methyl-	257947	215827	C ₉ H ₁₀	6.55E-05
Benzocyclobuten-1(2H)-one	257947	215827	C ₉ H ₁₀	6.55E-05
Indene	55523	54982	C ₉ H ₈	1.41E-05
Phenol, 2-methyl-	7405	9585	C ₇ H ₈ O	1.88E-06
Phenol, 3-methyl-	35004	32899	C ₇ H ₈ O	8.89E-06
Benzene, (2-methyl-1-propenyl)-	4959	11773	C ₁₀ H ₁₂	1.26E-06
Benzene, 2-ethenyl-1,3-dimethyl-	31229	27016	C ₁₀ H ₁₂	7.93E-06

2-Propenal, 3-phenyl-	527773	516947	C ₉ H ₈ O	1.34E-04
Benzene, (2-methyl-1-propenyl)-	13568	16305	C ₁₀ H ₁₂	3.45E-06
Benzene, 2-ethenyl-1,3-dimethyl-	13568	16305	C ₁₀ H ₁₂	3.45E-06
Phenol, 2,4-dimethyl-	12935	12651	C ₈ H ₁₀ O	3.28E-06
Benzene, (1-methyl-2-cyclopropen-1-yl)-	11578	13227	C ₁₀ H ₁₀	2.94E-06
Phenol, 2-ethyl-	5423	14149	C ₈ H ₁₀ O	1.38E-06
Benzaldehyde, 2-hydroxy-4-methyl-	1797	12024	C ₈ H ₈ O ₂	4.56E-07
Phenol, 2,3-dimethyl-	4309	11120	C ₈ H ₁₀ O	1.09E-06
Phenol, 2-,methoxy-4-methyl-	8776	8960	C ₈ H ₁₀ O ₂	2.23E-06
Phenol, 3,4-dimethyl-	8776	8960	C ₈ H ₁₀ O	2.23E-06
1,2-Benzenediol	8776	8960	C ₆ H ₆ O ₂	6.34E-04
Naphthalene	2496185	2628057	C ₁₀ H ₈	6.34E-04
Phenol, 2,4,6-trimethyl-	2496185	2628057	C ₉ H ₁₂ O	4.60E-06
Phenol, 2-ethyl-5-methyl-	18119	9529	C ₉ H ₁₂ O	1.60E-06
Phenol, 2-ethyl-5-methyl-	6287	9803	C ₉ H ₁₂ O	8.54E-07
Benzofuran, 2,3-dihydro-2-methyl-	3363	12467	C ₉ H ₁₀ O	3.28E-07
1,2-Benzenediol, 4-methyl-	1291	7066	C ₇ H ₈ O ₂	1.01E-06
Thymol	3959	8168	C ₁₀ H ₁₄ O	8.21E-07
Naphthalene, 2-methyl-	3235	8012	C ₁₁ H ₁₀	1.27E-04
Naphthalene, 1-methyl-	500160	539649	C ₁₁ H ₁₀	4.50E-05
1H-Indenol	177331	183558	C ₉ H ₈ O	3.27E-06
Naphthalene, 1,7-dimethyl-	12867	8143	C ₁₂ H ₁₂	5.84E-06
Naphthalene, 2,3-dimethyl-	22985	20095	C ₁₂ H ₁₂	3.96E-06
1,1'-Biphenyl, 3-methyl-	15591	14568	C ₁₃ H ₁₂	1.63E-05
1-Naphthalenol	64014	69157	C ₁₀ H ₈ O	4.88E-06
2-Naphthalenol	19205	25106	C ₁₀ H ₈ O	4.88E-06
4,4'-Dimethylbiphenyl	19205	25106	C ₁₄ H ₁₄	2.24E-06
7-Methyl-1-naphthol	8827	10860	C ₁₁ H ₁₀ O	1.91E-06
9H-Fluoren-9-ol	7527	6261	C ₁₃ H ₁₀ O	1.18E-05
(2-Methyl-3-biphenyl)methanol	46421	40297	C ₁₄ H ₁₂	0.00E+00
Naphtho[2,1-b]furan, 1,2-dimethyl-	0	0	C ₁₄ H ₁₂ O	1.88E-06
Sum	7390	6952		6.16E-03

7.4.1 Tar Composition as a Function of Temperature, SB ratio and Contact Time

The experimental program was designed to analyze the tar formation for thermal and catalytic cracking where the gas-phase cracking temperature, SB ratio and the reaction contact time were independently varied. The mass spectrometers of tars generated at temperatures from 600 to 700°C show the systematic maturation of the 600°C temperature tars to the 700°C temperature tars. The mass spectrum has many peaks at short retention times, while the latter has fewer peaks at short retention times, but more peaks in higher quantities at longer retention times. In order to establish a quantification procedure to analyze the effect of temperature, steam and contact time on the tar composition, a classification based on the number of carbon molecules contained in the tar components was made. Table 13 presents the tar mass fraction composition at 600 and 700°C when gasifying 2-methoxy-4-methylphenol with and without catalyst and 30 second of contact time.

Table 13. Tar mass fraction composition at 600 and 700°C for a) thermal, and b) catalytic steam gasification of 2-methoxy-4-methylphenol.

Aromatic Molecules [No. Carbon]	Thermal		Catalytic	
	Tar @ 600°C [%]	Tar @ 700°C [%]	Tar @ 600°C [%]	Tar @ 700°C [%]
6	5.8	31.4	12.7	50.4
7	27.0	23.5	13.2	19.1
8	31.4	11.7	10.8	10.5
9	22.5	15.6	35.5	12.3
10	4.2	7.2	4.3	6.4
11	1.3	3.9	2.2	0.2
12	0.5	0.6	0.5	0.7
13	0.5	0.8	1.0	0.1
14	0.9	0.5	0.8	0.1

7.4.1.1 Aromaticity

Taking into consideration the tar definition, *C₆+ organics produced under gasification conditions from any organic feedstock*, it was found that at 700°C, 97% of the total component found in the tars are composed by aromatic molecules ranging from MW of 78 (Benzene, C₆H₆) to 196 (Naphtho[2,1-b]furan, 1,2-dimethyl-, C₁₄H₁₂O). At 600°C, the total aromatic molecules contained in the tars were 95%.

7.4.1.2 Effect of Temperature on the Tar Composition

It was also found a decrease on the aromatic molecules containing C₇, C₈ and C₉ (Phenols, Benzofurans, Benzaldehydes), while an increase in the C₆ (Benzenes) components when temperature increases from 600 to 700°C. In addition, an increase in the C₁₀ components (Naphtalenes) was observed while a decrease in the C₁₁₋₁₄ components for the same increment in temperature.

7.4.1.3 Effect of SB ratio and reaction contact time on the Tar Composition

The SB ratio and reaction contact time have the same effect than temperature on tars composition. An increase from 5.9 to 12.7 was observed on the C₆ components when SB was varied from 0.4 to 1.0 at 600°C and 30 seconds of contact time. On the other hand, an increase from 31.9 to 50.4 was reported when the reaction time increase from 5 to 30 seconds at 700°C and SB of 1.0.

7.4.2 Tar Quantities

Table 14 summarizes the total concentration of tars as well as the wt% of tar (based on the mass of 2-methyl-4-methoxyphenol injected into the reactor) for all operating conditions in the CREC Riser Simulator.

Table 14. Tars reported in raw gases at 600, 650 and 700°C for catalytic steam gasification of 2-methyl-4-methoxyphenol over Ni/ α -alumina

Conditions		Tar, wt% [$\text{g}_{\text{tar}}/\text{g}_{\text{C}_8\text{H}_{10}\text{O}_2}$]		
S/B [g/g]	Reaction time [s]	600 [°C]	650 [°C]	700 [°C]
0.4	5	85.8	62.6	42.2
0.4	10	85.8	61.3	39.6
0.4	20	85.8	58.7	34.4
0.4	30	85.8	56.0	29.2
0.6	5	86.1	63.3	41.3
0.6	10	86.1	62.3	39.4
0.6	20	86.1	60.4	35.6
0.6	30	86.1	58.4	31.8
0.8	5	70.2	52.9	35.5
0.8	10	70.2	52.6	34.8
0.8	20	70.2	51.9	33.5
0.8	30	70.2	51.3	32.2
1	5	51.9	34.9	24.2
1	10	51.9	35.4	25.3
1	20	52.0	36.4	27.5
1	30	51.9	37.4	29.8

Figure 33 shows how tars changes as a function of temperature, S/B ratio and contact time, when 2-methoxy-4-methylphenol is used as a feedstock in the catalytic steam gasification of biomass. As the S/B ratio increases from 0.4 to 1.0, the tars decreases from 17.1 to 6.7 wt%- $\text{g}_{\text{Tar}}/\text{g}_{\text{Feed}}$ when the temperature and contact time are kept constant at 700°C and 30s, respectively. As the contact time increases from 5 to 30s, the tars wt%

decreases from 13.8 to 6.7 wt%- $g_{\text{Tar}}/g_{\text{Feed}}$, when the temperature is 700°C and the S/B ratio is 1.0. Finally, when the temperature increases from 600 to 700°C, and the contact time and S/B ratio are 5s and 0.4 respectively, the tars decreases from 38.1 at 600°C to 23.6 wt%- $g_{\text{Tar}}/g_{\text{Feed}}$ at 700°C.

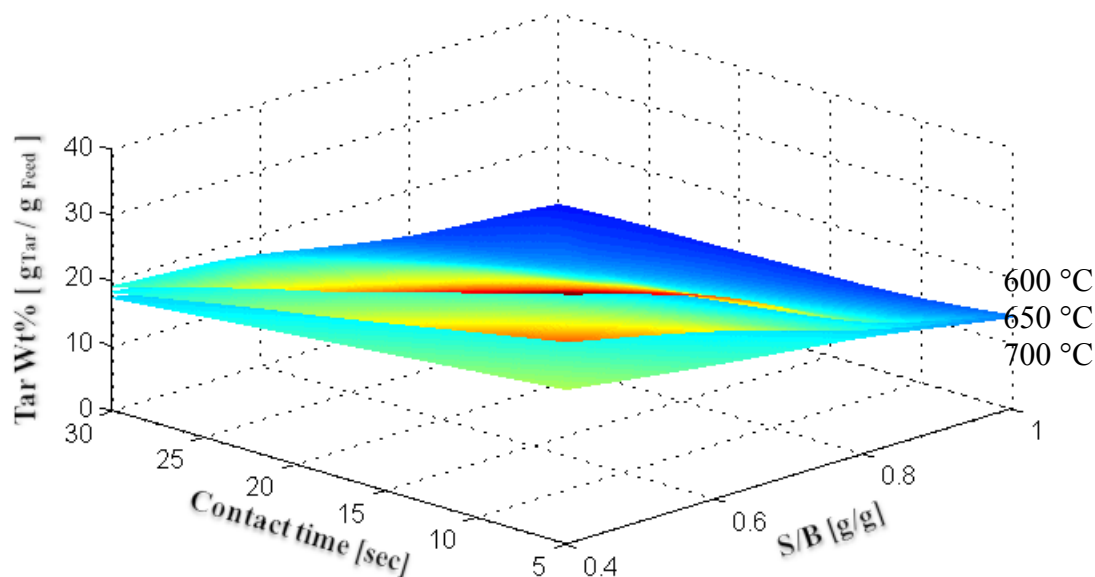


Figure 33. Tar experimental data [wt%, $g_{\text{Tar}}/g_{\text{Feed}}$] for catalytic steam gasification of 2-methoxy-4-methylphenol as a function of temperature, S/B ratio, and reaction time. 3D plot established with 16 data points for each temperature. Data set with σ of 2.3.

Additionally, the total amount of tar produced from the gasification reaction is largely dependent on the presence of the Ni/ α -alumina catalyst. As Table 15 indicates, there is a noticeable reduction in the tar wt% when the catalyst is employed in the reaction, especially at reaction temperatures of 600 and 650°C. At 700°C the wt% reduction of tar when a catalyst is used is less significant and, for operating conditions of 700°C, 5s, and S/B ratios of 1.0 and 0.8, there is little to no wt% reduction in tars. This is indicative of the fact that at higher temperatures, shorter reaction times and larger S/B ratios, *thermal* cracking, as opposed to catalytic cracking, is predominantly responsible for the production of tars.

Table 15. Comparison of tar wt% for experimental runs with catalyst and without catalyst

Conditions			Tar wt% [$\text{g}_{\text{Tar}}/\text{g}_{\text{C}_8\text{H}_{10}\text{O}_2}$]		Tar reduction using catalyst [%]	Average tar reduction [%]
Temp. [$^{\circ}\text{C}$]	S/B [g/g]	Reaction time [s]	Thermal (no catalyst)	Catalytic		
700	1.0	30	29.8	13.0	56.3	36
700	0.8	30	32.2	18.9	41.2	
700	0.6	30	31.8	22.9	28.0	
700	0.4	30	29.2	23.1	20.8	
700	1.0	5	24.2	26.9	0.0	13
700	0.8	5	35.5	31.6	11.0	
700	0.6	5	41.3	33.9	17.7	
700	0.4	5	42.2	31.8	24.6	
650	1.0	30	37.4	12.1	67.7	61
650	0.8	30	51.3	19.5	62.0	
650	0.6	30	58.4	24.1	58.7	
650	0.4	30	56.0	23.6	57.9	
650	1.0	5	34.9	19.5	44.3	39
650	0.8	5	52.9	31.7	40.1	
650	0.6	5	63.3	40.1	36.5	
650	0.4	5	62.6	40.2	35.8	
600	1.0	30	51.9	11.1	78.5	73
600	0.8	30	70.2	20.0	71.5	
600	0.6	30	86.1	25.3	70.6	
600	0.4	30	85.8	24.0	71.9	
600	1.0	5	51.9	12.0	76.8	55
600	0.8	5	70.1	31.8	54.7	
600	0.6	5	86.1	46.3	46.2	
600	0.4	5	85.8	48.6	43.4	

Figure 34 displays the effect of the catalyst in the production of tars at 600°C, different S/B ratios and different reaction times. The tar decreases from 61.7 – 25.9 wt%-g_{Tar}/g_{Feed} for non-catalytic experimental gasification runs when S/B ratio increases from 0.4 - 1.0 at 5 seconds of reaction time. For catalytic experimental gasification runs, the tar decreases from 38.1 – 14.0 wt%-g_{Tar}/g_{Feed} for the same non-catalytic conditions. No significant reduction in the tar wt% can be seen at different contact times for non-catalytic runs when for catalytic experimental runs, tar wt% decreases from 38.1 – 18.9 wt%-g_{Tar}/g_{Feed} as contact time increases form 5 – 30 seconds. An average of tar reduction of 73.1 and 39.2 % can be observed when the catalyst is employed in the reaction for 30 and 5 seconds, respectively.

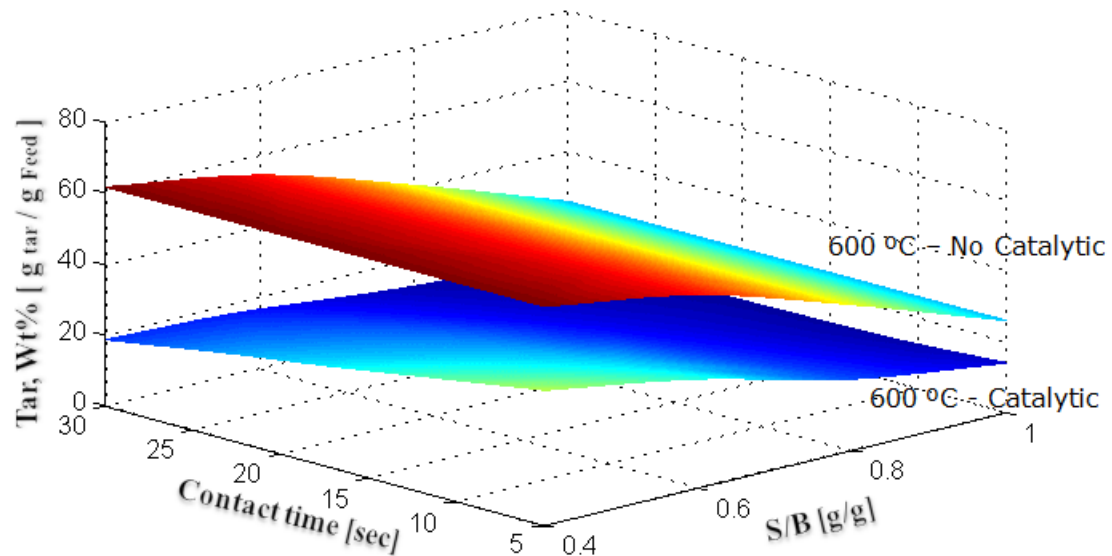


Figure 34. Comparison of tar wt% experimental data with and without catalyst for steam gasification of 2-methoxy-4-methylphenol as a function of S/B ratio and reaction time at P = 1 atm and 600°C. 3D plot established with 16 data points. Data set with σ of 2.3 for 600°C catalytic and 4.7 for 600°C no catalytic.

7.5 Conclusions

- a. It is shown that the configuration of CREC Riser Simulator - GC and MS offers a valuable tool for evaluation and quantification of tars from catalytic steam gasification of biomass.

- b. It is proven that the fraction of tar and type of tar formed are closely related with the biomass or the model compound considered to represent the biomass to be gasified. While for glucose gasification, there is minimal to no tar formation, for the 2-methoxy-4-methylphenol gasification there is considerable amounts of tar obtained along permanent gases being formed.
- c. It is reported the effect of the catalyst, temperature, SB ratio and contact time on the tars quantity and composition.
- d. It is important to mention that although this work has shown the systematic nature of tar composition and quantities as a function of reaction temperature, SB ratio and contact time, a more extensive study is needed to characterize tar products in more detail, This more extensive study should involve the kinetics and reaction pathways describing primary tar conversion into secondary and tertiary processes.

Chapter 8 Thermodynamic Modeling

8 Thermodynamic Equilibrium Modeling

8.1 Introduction

A thermodynamic equilibrium model based on evaluations involving C, H and O elemental balances and various product species (up to C₆ hydrocarbons) is reported in this study. This model establishes the effect of biomass composition, temperature, and steam on the various gas product molar fractions. On this basis, significant parameters determining the chemical inter-conversions and distribution of chemical species are identified. Based on the proposed equilibrium model and using glucose, [C₆H₁₂O₆], as a model biomass species, an optimum gasification temperature close to 800°C and a steam/biomass ratio between 0.5 and 0.7 g/g is established.

This study has the special value of comparing thermodynamic equilibrium predictions with experimental data obtained in a CREC Riser Simulator using a fluidizable Ni/ α -alumina catalyst. Results are relevant for scaled-up gasifiers. They show that for reaction times longer than 30 seconds, chemical species are essentially equilibrated and that the proposed model does provide an adequate description of various product fractions. Data obtained also demonstrate the shortcomings of equilibrium models for gasifiers with reaction times shorter than 10 seconds and the need for non-equilibrium models to describe gasifier performance at such conditions.

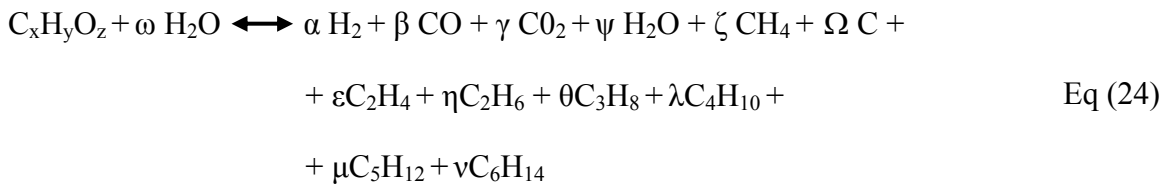
8.2 Thermodynamic Equilibrium Model for Steam Gasification

The product species considered for the equilibrium calculations are the following: H₂, CO, CO₂, H₂O, CH₄, C, C₂H₄, C₂H₆, C₃H₈, C₄H₁₀, C₅H₁₂, and C₆H₁₄.

From the elemental analysis of different biomasses, it can be proven that the contribution of nitrogen and sulphur species evolving from the reactor are negligible in terms of the equilibrium calculations, with this being in agreement with previously reported models

(Ginsburg and deLasa, 2005; Schuster et al., 2001). The formation of tar is neglected in the thermodynamic calculations given its low concentration; although it does have to be considered in full-scale gasifier plant operation.

Thus, the simplified overall mass balance for the gasification reaction can be written as follows:



This proposed equilibrium model considers the following gas phase reactions occurring after volatilization of the biomass, which are considered to be at equilibrium:

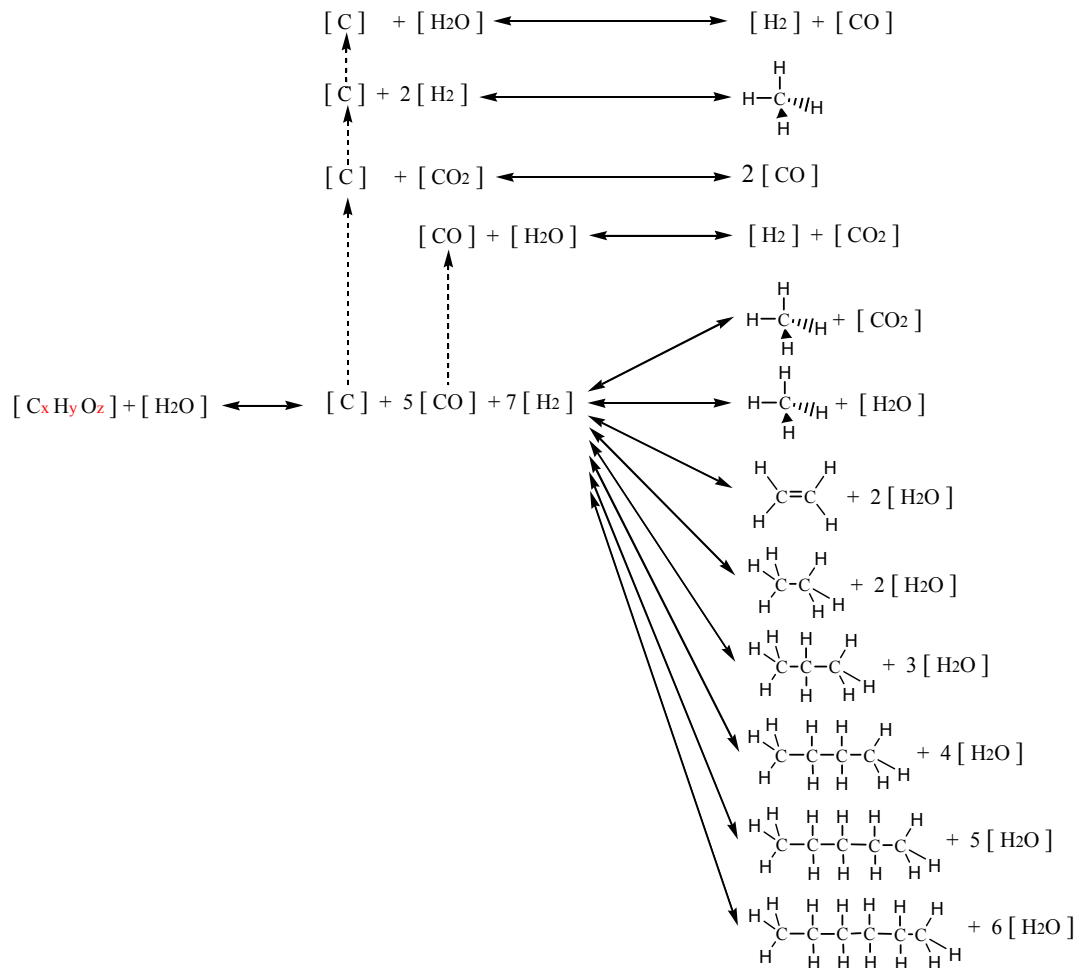


Figure 35. Chemical reactions considered in the steam gasification of biomass

Table 16. Chemical steam reactions in the steam gasification of biomass

Name of reaction	Chemical equation	$\Delta G_{f(298)}^o$ [kJ/ mol]	$\Delta H_{f(298)}^o$ [kJ/ mol]	$K_{(800\text{ C})}$	Eq.
Dry reforming of methane	$CH_4 + CO_2 \leftrightarrow 2CO + 2H_2$	168.635	123.760	132.013	Eq (25)
Steam reforming of methane	$CH_4 + H_2O \leftrightarrow CO + 3H_2$	140.098	205.310	169.182	
Water-gas shift reaction	$CO + H_2O \leftrightarrow H_2 + CO_2$	-28.538	-42.200	1.0051	Eq (26)
Heterogeneous water-gas shift	$C + H_2O \leftrightarrow H_2 + CO$	89.824	130.414	7.0401	
Boudouard equilibrium	$C + CO_2 \leftrightarrow 2CO$	118.362	172.615	6.499	Eq (27)
Hydrogenating gasification	$C + 2H_2 \leftrightarrow CH_4$	-50.273	-74.900	0.049	
Ethylene	$2CO + 4H_2 \leftrightarrow C_2H_4 + 2H_2O$	-111.651	-104.256	1.738e-08	Eq (28)
Ethane	$2CO + 5H_2 \leftrightarrow C_2H_6 + 2H_2O$	-212.787	-172.779	1.475e-08	Eq (29)
Propane	$3CO + 7H_2 \leftrightarrow C_3H_8 + 3H_2O$	-293.149	-165.051	8.743e-14	Eq (30)
Butane	$4CO + 9H_2 \leftrightarrow C_4H_{10} + 4H_2O$	-376.793	-161.968	7.669e-19	Eq (31)
Pentane	$5CO + 11H_2 \leftrightarrow C_5H_{12} + 5H_2O$	-457.916	-159.719	4.321e-24	Eq (32)
Hexane	$6CO + 13H_2 \leftrightarrow C_6H_{14} + 6H_2O$	-539.699	-158.303	2.785e-29	Eq (33)

Nine independent nonlinear equations with nine unknowns (as described in Appendix D) result from algebraic manipulation of this system of twelve variables ($\alpha, \beta, \gamma, \psi, \zeta, \Omega, \epsilon, \eta, \theta, \lambda, \mu, \nu$). The Newton-Raphson (NR) model is used to solve the nonlinear system of equations containing constrained variables. The NR method uses a truncated Taylor series estimate of the function values to obtain better estimates of the unknowns.

To solve the nonlinear equation system, initial guesses of $\beta, \gamma, \epsilon, \eta, \theta, \lambda, \mu,$ and ν are made with the following constraints: $K_{WGS}, K_{CH_4}, K_{C_2H_4}, K_{C_2H_6}, K_{C_3H_8}, K_{C_4H_{10}}, K_{C_5H_{12}},$ and

$K_{C_6H_{14}} \rightarrow 0$. This holds true if β , γ , ε , η , θ , λ , μ , and ν are selected using the following procedure:

i) The minimum allowable value of β for a given value of γ is found by taking the limit of $K_{WGS} \rightarrow 0$

$$K_{WGS \rightarrow 0} = \frac{y_{H_2} y_{CO_2}}{y_{CO} y_{H_2O}} = \frac{\alpha\gamma}{\psi\beta} = \frac{(0.5y - 2x - z + 3\beta + 4\gamma - \eta - 2\theta - 3\lambda - 4\nu - 5\nu)\gamma}{\beta(z + \omega - \beta - 2\gamma)}$$

$$\alpha > 0; \quad 0.5y - 2x - z + 3\beta_{\min} + 4\gamma - \eta - 2\theta - 3\lambda - 4\nu - 5\nu > 0$$

$$\beta_{\min} > \frac{1}{3}[2x + z - 0.5y - 4\gamma + \eta + 2\theta + 3\lambda + 4\nu + 5\nu]$$

ii) The maximum allowable value of β for a given value of γ is found by taking the limit of $K_{WGS} \rightarrow \infty$.

$$K_{WGS \rightarrow \infty} = \frac{y_{H_2} y_{CO_2}}{y_{CO} y_{H_2O}} = \frac{\alpha\gamma}{\psi\beta} = \frac{(0.5y - 2x - z + 3\beta + 4\gamma - \eta - 2\theta - 3\lambda - 4\nu - 5\nu)\gamma}{\beta(z + \omega - \beta - 2\gamma)}$$

$$\psi > 0; \quad (z + \omega - \beta_{\max} - 2\gamma) > 0,$$

$$\beta_{\max} > z + \omega - 2\gamma$$

iii) To ensure that for a given value of γ , $\beta_{\max} > \beta_{\min}$ the following inequality must be satisfied:

$$\beta_{\max} > \beta_{\min}$$

$$\left[\frac{2}{3}x + \frac{1}{3}z - \frac{1}{6}y - \frac{4}{3}\gamma_{\max} + \frac{1}{3}\eta + \frac{2}{3}\theta + \lambda + \frac{4}{3}\nu + \frac{5}{3}\nu \right] < [z + \omega - 2\gamma_{\max}]$$

and

$$\gamma_{\max} < \frac{3}{2} \left[\frac{2}{3}z + \omega - \frac{2}{3}x + \frac{1}{6}y - \frac{1}{3}\eta - \frac{2}{3}\theta - \lambda - \frac{4}{3}\nu - \frac{5}{3}\nu \right]$$

Additionally, the numerical solution of a partial set of the above equations (steam reforming of methane, Eq (25), and the water-gas shift reaction, Eq (26), was carried out using Aspen HYSYS[®] package to check the adequacy of the proposed model.

8.3 Equilibrium Constants

8.3.1 Effect of Temperature on the Equilibrium Constant

Since the standard-state temperature is that of the equilibrium mixtures, the standard property changes of reaction, such as ΔG° and ΔH° , vary with the equilibrium temperature.

The dependence of ΔG° on T is given by:

$$\frac{d(\Delta G^\circ / RT)}{dT} = \frac{-\Delta H^\circ}{RT^2} \quad \text{Eq (34)}$$

According to the definition of the *standard Gibbs energy change of reaction*:

$$\frac{d\Delta G^\circ}{RT} = -\ln K \quad \text{Eq (35)}$$

$$\text{with: } \Delta G^\circ = \Delta H_0^\circ - \frac{T}{T_0}(\Delta H_0^\circ - \Delta G_0^\circ) + R \int_{T_0}^T \frac{\Delta C_p^\circ}{R} dT - RT \int_{T_0}^T \frac{\Delta C_p^\circ}{R} \frac{dT}{T} \quad \text{Eq (36)}$$

Therefore,

$$\frac{d \ln K}{dT} = \frac{-\Delta H^\circ}{RT^2} \quad \text{Eq (37)}$$

Eq (37) establishes the effect of temperature on the equilibrium constant, and hence on the equilibrium conversion.

8.3.2 Effect of Pressure on the Equilibrium Gas Composition

At reaction equilibrium, the gas species composition is a function of the temperature and pressure. An analysis of this composition can be made by applying Le Chatelier's principle to the reaction network.

$$\left[\frac{K}{\prod_i (\phi_i)^{\nu_i}} \right] = \left[\frac{(y_{A3})^{\nu_3} (y_{A4})^{\nu_4}}{(y_{A1})^{\nu_1} (y_{A2})^{\nu_2}} \right] P^{\nu_T} \quad \text{Eq (38)}$$

8.4 Thermodynamic Equilibrium Model Predictions

In order to identify optimal reaction conditions for the maximum H₂ output from the steam gasification of biomass, the reaction parameters: (i) temperature; (ii) steam-to-biomass ratio; and (iii) fuel composition, were investigated.

8.4.1 Effect of Fuel Composition on the Steam Gasification of Biomass

The influence of different fuel compositions (Table 17) on the product gas composition is examined in the present study by varying firstly, the carbon to hydrogen content, and secondly, the carbon to oxygen content (both in wt%). This variation is carried out over a wide range of fuel compositions: from carbon to hydrogen content of 1:2.11 (Jute stick), to carbon to hydrogen content of 1:0.69 (Coal), and carbon to oxygen content of 1:1 (Glucose) to carbon to oxygen content of 1:0.111 (Heterotrophic).

Table 17. Ultimate analysis of a diverse variety of biomass composition

Biomass	Ultimate Analysis					C _x H _y O _z			Reference
	C	H	O	N	S	x	y	z	
Jute stick	47.18	8.36	44.10	0.36		1.00	2.11	0.70	Mohan et al., 2006
Glucose						1.00	2.00	1.00	
Heterotrophic	76.22	11.61	11.24	0.93		1.00	1.81	0.11	Mohan et al., 2006
Potato starch	42.50	6.40	50.80	0.00	0.00	1.00	1.79	0.90	Antal et al., 2000
Poplar wood sawdust	42.70	6.20	50.90	0.10	0.10	1.00	1.73	0.89	Antal et al., 2000
Pine Sawdust	50.26	6.72	42.66	0.16	0.20	1.00	1.59	0.64	Ligang et al., 2007
Legume straw	43.30	5.62	50.35	0.61	0.12	1.00	1.55	0.87	Ligang et al., 2007
Rice straw	36.90	4.70	32.50	0.30	0.06	1.00	1.52	0.66	Tomishige et al., 2004
Softwood bark	77.56	8.69	13.30	0.59		1.00	1.34	0.13	Mohan et al., 2006
Pine	51.60	4.90	42.60	0.90		1.00	1.13	0.62	Franco et al., 2003
Waste Wood	55.11	6.01	37.99	0.86	0.03	1.00	1.30	0.52	Ginsburg et al., 2005
Coal	75.80	4.40	16.70	1.89	1.22	1.00	0.69	0.17	Aznar et al., 2006

In order to obtain comparable results, the temperature and pressure is set constant at 800°C and 1 atm, respectively.

Figure 36 to Figure 40 report the mole fraction of the product gas (H_2 , CO, CO_2 and CH_4) as a function of steam/biomass ratio for different biomass compositions (on a dry basis).

The hydrogen concentration in the product gas is shown both to increase with increasing steam/biomass ratio from 0.0 to 1.2, and to be proportional to the carbon to hydrogen content in the biomass considered. This value is consistent with experimental data, as discussed in Section 8.5. It is predicted that increasing the steam/biomass ratio beyond 1.0 g/g does not lead to a significantly higher concentration of H_2 in the product gas.

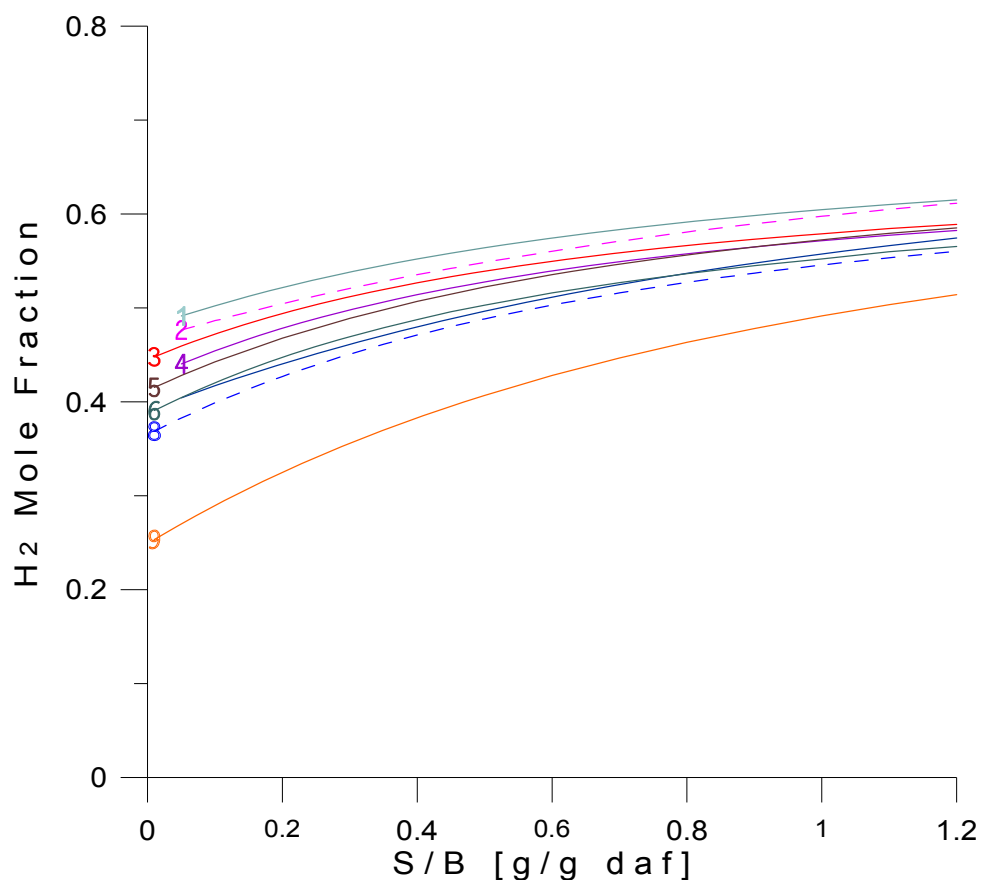


Figure 36. Hydrogen mole fraction versus steam/biomass ratio at 800°C and 1 atm; equilibrium model predictions for different biomass compositions; from higher to lower H_2 mole fractions, (1) jute stick, (2) heterotrophic, (3) glucose, (4) potato starch, (5) pine sawdust, (6) legume straw, (7) softwood bark, (8) wasted wood and (9) coal

The carbon monoxide mole fraction composition in the product gas decreases with an increase in the steam/biomass ratio, according to the water-gas shift reaction. When excess gasification agent is present in the system ($S/B > 0.8$), Figure 37 shows a decrease in carbon monoxide molar fraction proportionally to the oxygen to carbon contained in the biomass.

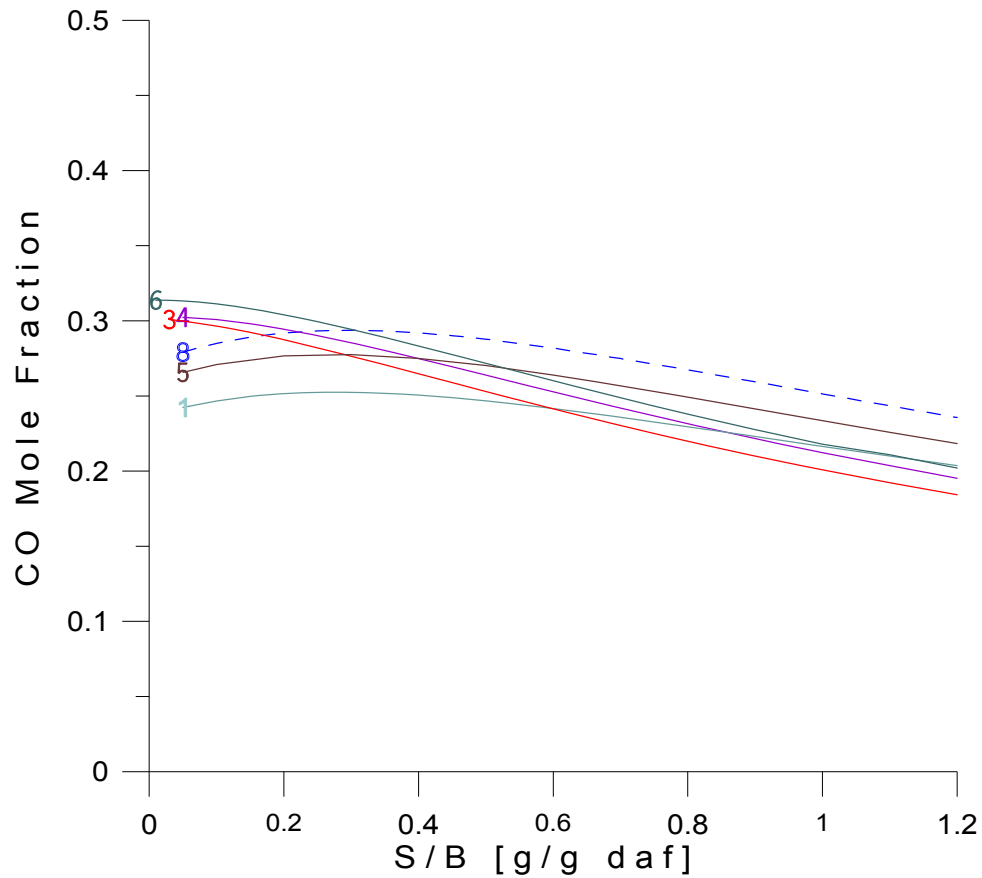


Figure 37. Carbon monoxide mole fraction versus steam/biomass ratio at 800°C and 1 atm; equilibrium model predictions for different biomass compositions, (1) jute stick, (2) heterotrophic, (3) glucose, (4) potato starch, (5) pine sawdust, (6) legume straw, (7) softwood bark, (8) wasted wood and (9) coal

An increasing trend in the mole fraction of CO₂ was also observed with increasing steam/biomass ratios. Figure 38 reports an increase in the CO₂ molar fraction of glucose from 0.70 at S/B ratio of 0.0, to 0.20 at S/B of 1.2. It can also be seen in Figure 38 that the increase in the carbon dioxide concentration is proportional with the carbon to oxygen content in the biomass considered.

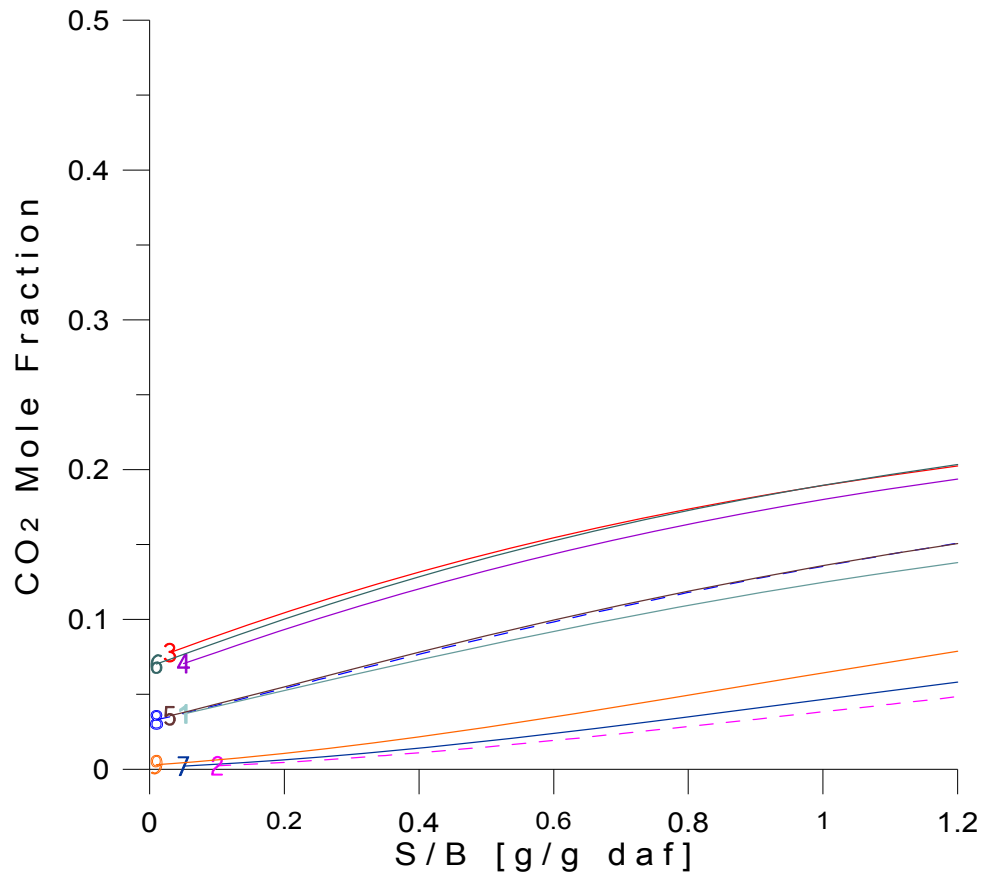


Figure 38. Carbon Dioxide mole fraction versus steam/biomass ratio at 800°C and 1 atm; equilibrium model predictions for different biomass compositions, (1) jute stick, (2) heterotrophic, (3) glucose, (4) potato starch, (5) pine sawdust, (6) legume straw, (7) softwood bark, (8) wasted wood and (9) coal

At equilibrium conditions, Figure 39 shows that the composition of methane is lower than 0.010%-mol for all the biomass considered. The methane concentration in the product gas decreases proportionally with the carbon to oxygen content in the biomass.

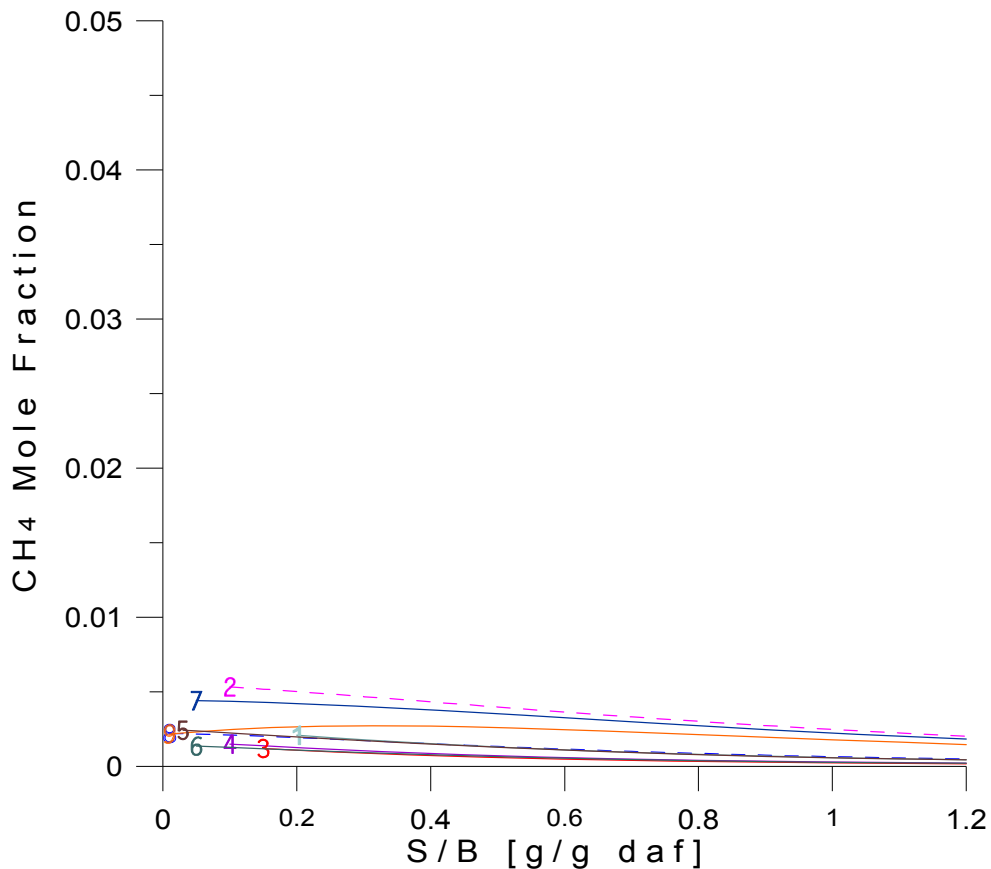


Figure 39. Methane mole fraction versus steam/biomass ratio at 800°C and 1 atm; equilibrium model predictions for different biomass compositions, (1) jute stick, (2) heterotrophic, (3) glucose, (4) potato starch, (5) pine sawdust, (6) legume straw, (7) softwood bark, (8) wasted wood and (9) coal

Figure 40 shows the hydrogen to carbon monoxide ratio (H_2/CO) as a function of S/B ratio and biomass composition. H_2/CO ratio shows: a) an increase when augmenting the S/B ratio from 0.0 to 1.2, and b) an increase in the ratio proportional to the carbon to hydrogen content in the biomass, which is tabulated in Figure 40.

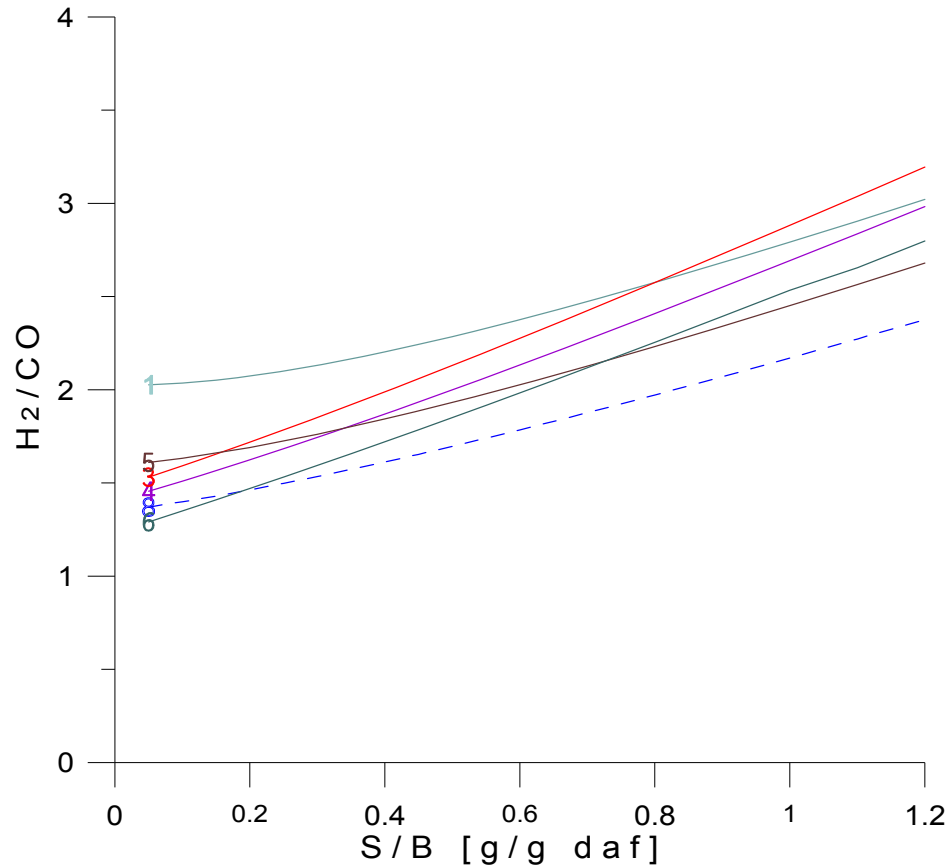


Figure 40. Hydrogen to carbon monoxide ratio versus steam/biomass ratio at 800°C and 1 atm; equilibrium model predictions for different biomass compositions, (1) jute stick, (2) heterotrophic, (3) glucose, (4) potato starch, (5) pine sawdust, (6) legume straw, (7) softwood bark, (8) wasted wood and (9) coal

8.4.2 Steam/Biomass Ratio and Temperature Effect on the Steam Gasification of Biomass

Previous experimental investigations (Franco et al., 2003; Ginsburg and deLasa, 2005; Herguido et al., 1992; Prasad and Kuester., 1988; Singh et al., 1986; Walawender et al., 1985; Wei et al., 2007) have demonstrated the effect of the steam/biomass ratio on the product gas composition. An increase in the steam/biomass ratio is expected to have an increase in the hydrogen output according to both the water gas shift reaction, and the steam reforming reaction. In addition, excess steam is often used to drive the cracking of higher hydrocarbons and reforming reactions.

However, an upper limit of hydrogen output is expected due to an increase in the steam in the product gas, and the energy associated with the generation of steam needs to be considered when excess steam is introduced to the system. Such considerations demonstrate the importance of selecting the optimal steam/biomass ratio in the steam gasification of biomass from the point of view of process efficiency.

Figure 41 reports the fractional distribution of hydrogen in the product gas as a function of the steam/biomass ratio and temperature (on a dry basis).

Figure 42 through Figure 45 present the predicted molar fractions of the product gases (H_2 , CO, CO_2 , CH_4 and H_2O) at S/B of 0.1, 0.5, 1.0 and 1.5 g/g, respectively. The horizontal axis corresponds to the temperature. The distribution of hydrogen increases with an increase in the steam/biomass ratio for a steam/biomass ratio of 0.1 to 0.8. For a steam/biomass ratio higher than 0.8, H_2 essentially reaches a plateau (0.38 at S/B=1.0 and 0.33 at S/B=1.5) at approximately 800°C, decreasing slightly after this temperature.

On the basis of this analysis, a steam/biomass ratio of 0.5 to 0.7 g/g and a temperature around 800°C are considered to be optimal conditions for the process, since it is at these conditions that the equilibrium model predicts a maximum H_2/CO ratio of 2.

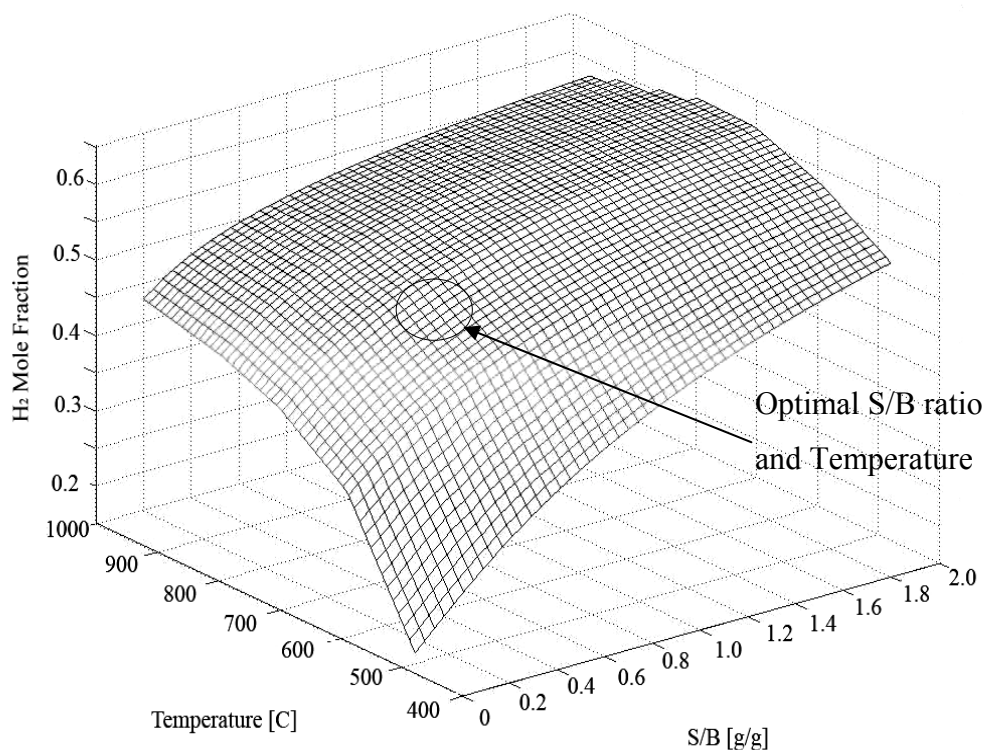


Figure 41. Equilibrium fractional distribution of H₂ on a dry basis at P = 1 atm and various steam/glucose (S/B) ratios and temperatures

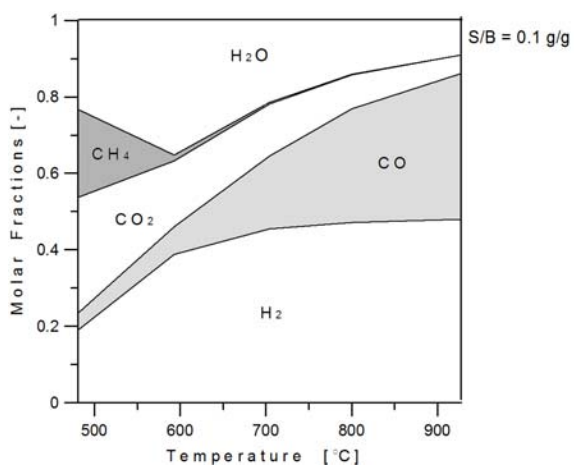


Figure 42. Equilibrium fraction distribution of H₂, CO, CO₂, CH₄, and H₂O at P = 1 atm, S/B = 0.1 and various temperatures.

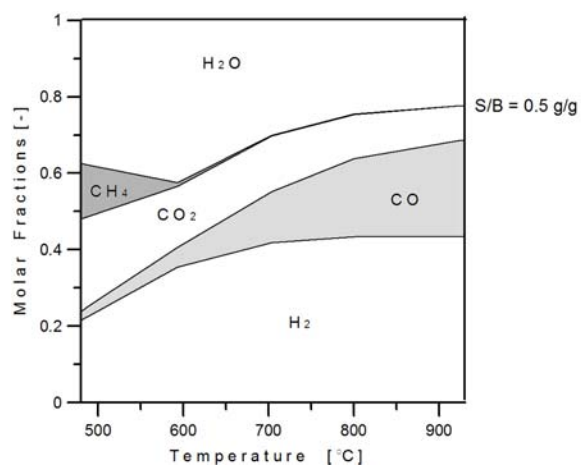


Figure 43. Equilibrium fraction distribution of H₂, CO, CO₂, CH₄, and H₂O at P = 1 atm, S/B = 0.5 and various temperatures.

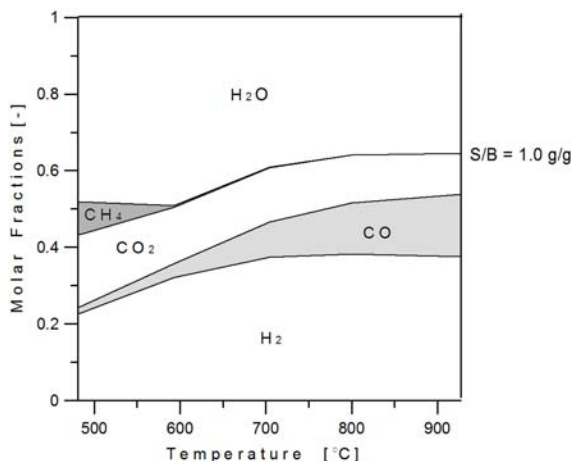


Figure 44. Equilibrium fraction distribution of H_2 , CO , CO_2 , CH_4 , and H_2O at $P = 1$ atm, $S/B = 1.0$, and various temperatures.

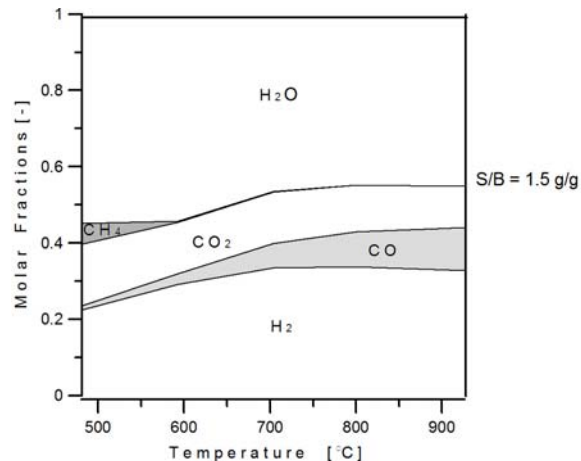


Figure 45. Equilibrium fraction distribution of H_2 , CO , CO_2 , CH_4 , and H_2O at $P = 1$ atm, $S/B = 1.5$, and various temperatures.

8.5 Equilibrium Model Prediction versus Experimental Results

Equilibrium studies can be used to predict the maximum possible conversion and product distribution in a chemical reacting system. By comparing experimental results with equilibrium calculations one can establish the relation between thermodynamics and chemical kinetics of the process. In the case of this study, the thermodynamic equilibrium model proved to be useful in analyzing and understanding the experimental results.

8.5.1 Glucose: Equilibrium Model vs. Experimental Data at 700°C

Using glucose as a model compound for biomass, steam gasification experimental runs were carried out at the following conditions:

- Non-catalytic steam gasification runs at 700°C and 30 seconds of reaction time
- Catalytic steam gasification runs at 700°C and reaction times of 5, 10, 20 and 30 seconds.

Figure 46 through Figure 49 report the molar fraction compositions of the major product species on a dry basis, including H_2 , CO , CO_2 and CH_4 as a function of steam/biomass ratio for: a) equilibrium model prediction (—), b) catalytic steam gasification using Ni

supported catalyst at 5 seconds (\oplus), 10 seconds ($\opl�$), 20 seconds (\blacktriangle), 30 seconds (\blacklozenge) and c) non-catalytic steam gasification runs (*).

The H_2 concentration in the product gas for glucose is shown in Figure 46. By augmenting the steam/biomass ratio from 0.2 - 1.0 g/g, the hydrogen fraction increases from 31.08 - 34.68%-mol for non-catalytic and from 46.86 - 51.02%-mol for catalytic experimental gasification runs at 30 seconds of reaction time. The equilibrium model over predicts the H_2 mole fraction by around 18.5%-mol for non-catalytic and 4.5%-mol for catalytic experimental runs for longer reaction times (> 20 sec) over the span of experimental steam/biomass ratios. This over predicted value is consistent with the previous non-catalytic experimental data analyzed (15, 18 and 21%-mol for Legume straw (Wei et al., 2007), $[C_{1.00} H_{1.55} O_{0.87}]$, pine sawdust (Wei et al., 2007), $[C_{1.00} H_{1.59} O_{0.64}]$ and pine (Franco et al., 2003), $[C_{1.00} H_{1.13} O_{0.62}]$, respectively).

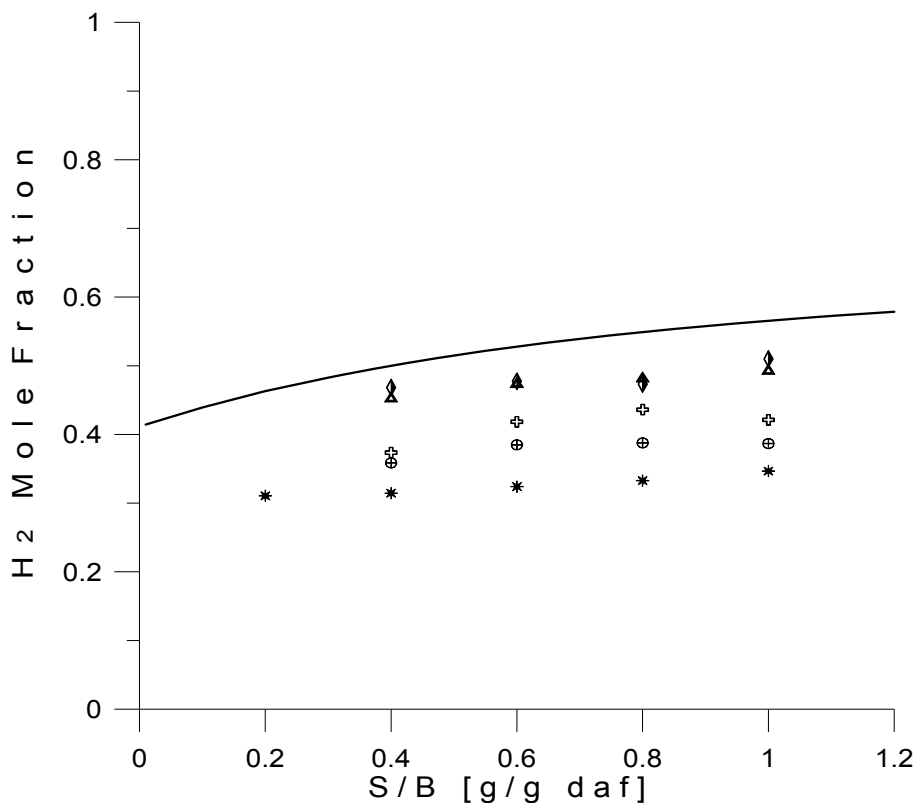


Figure 46. H_2 mole fraction of product gas for gasification of glucose at different steam/glucose ratios, 700°C and $P = 1$ atm. Solid line (—) equilibrium model, (*) non-catalytic gasification runs, experimental data using Ni supported catalyst at (\oplus) 5 seconds, ($\opl�$) 10 seconds, (\blacktriangle) 20 seconds and (\blacklozenge) 30 seconds of reaction time.

At thermodynamic equilibrium conditions, the CO mole fraction composition in the product gas decreases with an increase in the steam/biomass ratio according to the water-gas shift reaction, Eq (26), when an excess of gasification agent is present in the system. On the other hand, at low steam/biomass ratios (no excess of gasification agent), solid carbon remains in the equilibrium state and must be considered according to Eq (27).

Figure 47 displays the CO concentration in the product gas as a function of the steam/biomass ratio. The CO mole fraction decreases from 51.01 – 48.23%-mol for non-catalytic and from 38.42 – 30.20%-mol for catalytic experimental gasification runs at 30 seconds of reaction time. It can be seen in Figure 47 that the equilibrium model follows the trend of the experimental data showing 33 %-mol less CO for non-catalytic, and 15 %-mol less CO for catalytic gasification runs for longer reaction times (> 20 sec) for all steam/biomass ratios analyzed.

All this suggests that a combination of reactions govern the overall gasification reaction network, with the water-gas-shift reaction being a major influence on the observed product yields. The cause of this observed behavior may be assigned to the role of the nickel catalyst. This metal supported catalyst enhances the water-gas-shift reaction, and thus increases CO₂ and H₂ production, while a decrease in CO is observed.

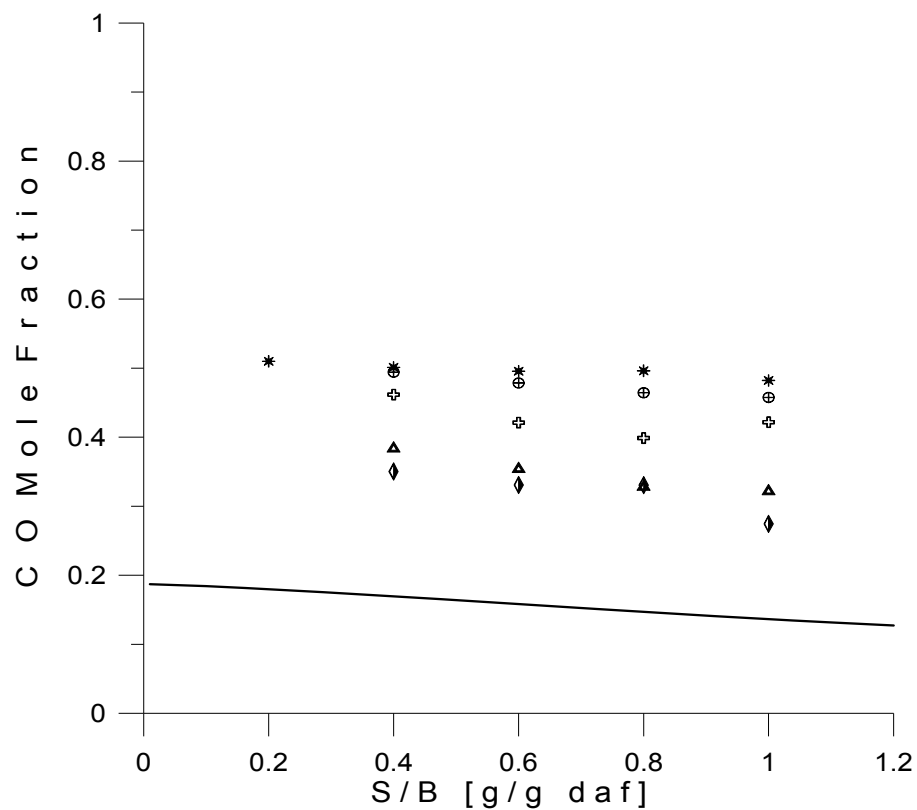


Figure 47. CO mole fraction of product gas for gasification of glucose at different steam/glucose ratios, 700°C and $P = 1$ atm. Solid line (—) equilibrium model, (*) non-catalytic gasification runs, experimental data using Ni supported catalyst at (⊕) 5 seconds, (⊕) 10 seconds, (Δ) 20 seconds and (◊) 30 seconds of reaction time.

An increasing trend in the CO_2 was also observed with increasing steam/biomass ratios. Figure 48 reports that the equilibrium model over predicts the quantity of CO_2 by 13.8%-mol and 4.6%-mol for non-catalytic and catalytic experimental runs, respectively, at 30 seconds of reaction time.

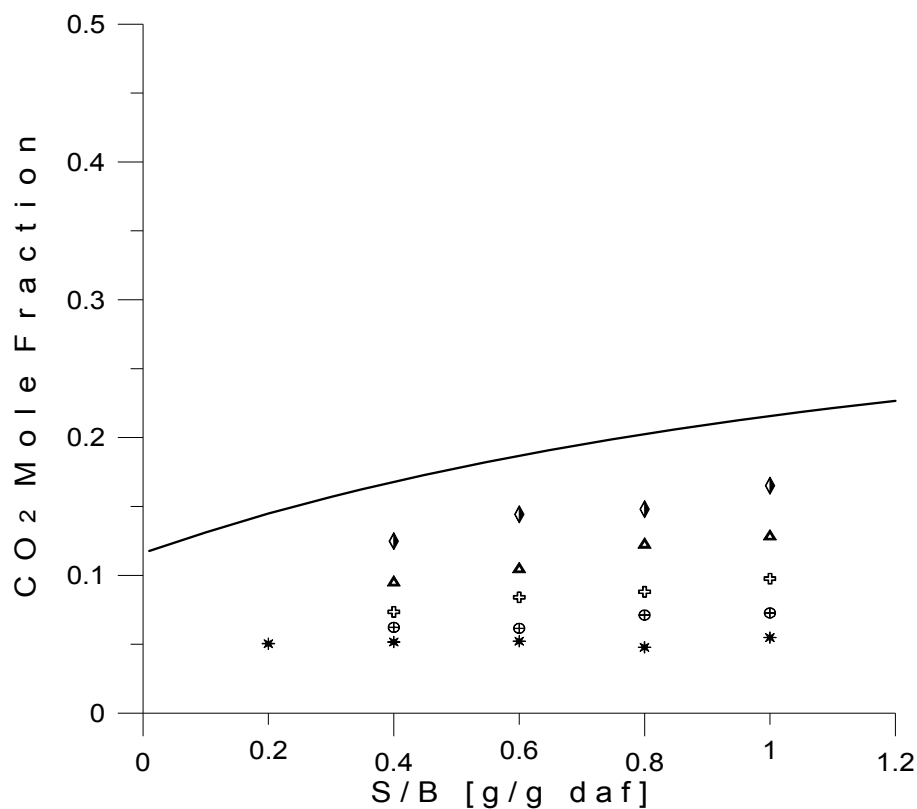


Figure 48. CO_2 mole fraction of product gas for gasification of glucose at different steam/glucose ratios 700°C and $P = 1$ atm. Solid line (—) equilibrium model, (*) non-catalytic gasification runs, experimental data using Ni supported catalyst at (⊕) 5 seconds, (⊕) 10 seconds, (▲) 20 seconds and (◆) 30 seconds of reaction time.

The equilibrium model, Figure 49, shows that almost no methane ($\sim 0.2\%$ -mol) is produced at 700°C and 1 atm. The equilibrium prediction differs from the experimental data showing around 10.3% -mol more CH_4 for non-catalytic and 4.3% -mol more CH_4 for catalytic experimental runs for longer reaction times (> 20 sec) over the span of experimental steam/biomass ratios. This indicates that a state of equilibrium is not reached during experiments. The de-volatilization of the biomass gives high contents of methane and higher hydrocarbons which do not react completely leading to equilibrium concentrations of H_2 , CO , CO_2 , and H_2O according to the reforming of methane reaction, Eq (25), and the higher hydrocarbons cracking reactions, Eq (28) to Eq (33).

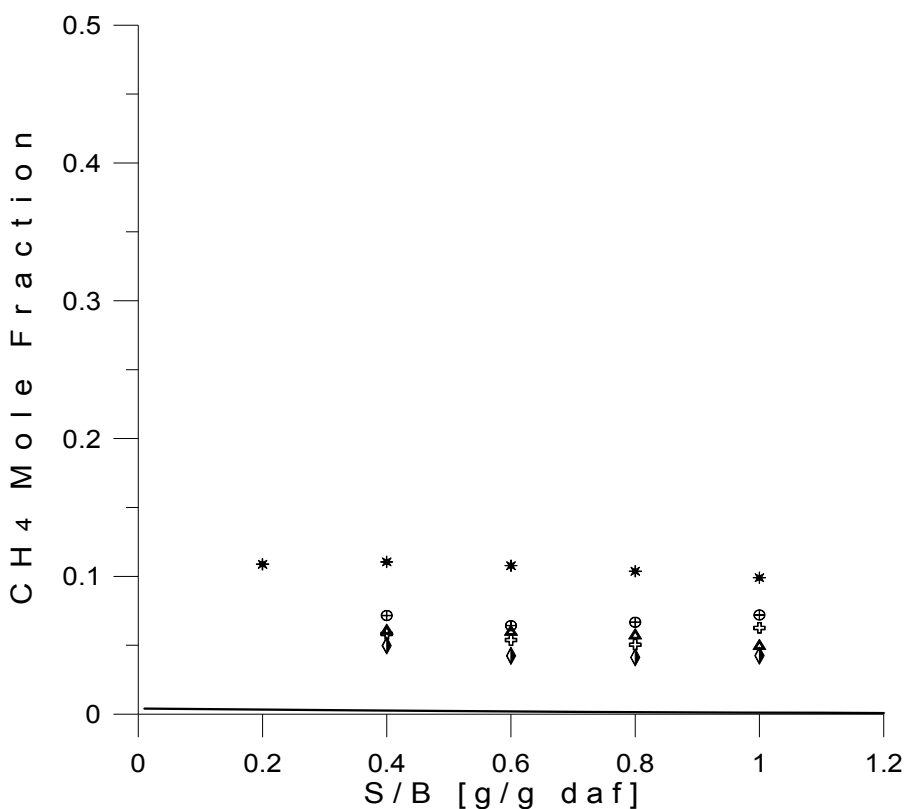


Figure 49. CH_4 mole fraction of product gas for gasification of glucose at different steam/glucose ratios, 700°C and $P = 1$ atm. Solid line (—) equilibrium model, (*) non-catalytic gasification runs, experimental data using Ni supported catalyst at (⊕) 5 seconds, (⊕) 10 seconds, (△) 20 seconds and (◇) 30 seconds of reaction time.

Figure 50 illustrates the trends of the experimentally determined H_2/CO . It can be seen that for non-catalytic experimental runs, the H_2/CO ratio increases from 0.61 – 0.71 by augmenting the S/B ratio from 0.2 – 1.0 g/g at 700°C. Similar trends for catalytic gasification runs were observed at 700°C and 30 seconds of reaction time, with H_2/CO ranging from 1.33 - 1.86, over the range of steam/biomass ratios.

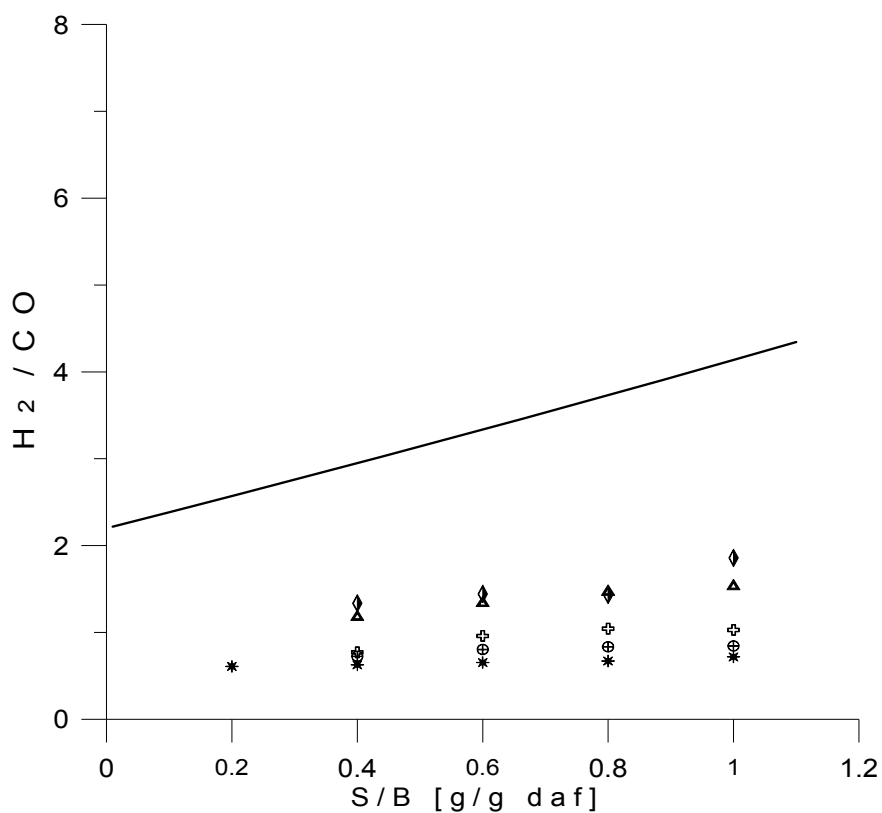


Figure 50. H_2/CO ratio for gasification of glucose at different steam/glucose ratios, 700°C and $P = 1$ atm. Solid line (—) equilibrium model, (*) non-catalytic gasification runs, experimental data using Ni supported catalyst at (⊕) 5 seconds, (⊕) 10 seconds, (Δ) 20 seconds and (◇) 30 seconds of reaction time.

It can be observed in Figure 51 that the CO/CO₂ ratio predicted by the model agrees quite well with the observed experimental values at 700°C for catalytic gasification experimental data at 30 seconds of reaction time. The model slightly over-predicts the CO/CO₂ ratio by 1.75 within the range of steam/biomass feed ratios. However, predictions become more accurate at higher steam/biomass ratios.

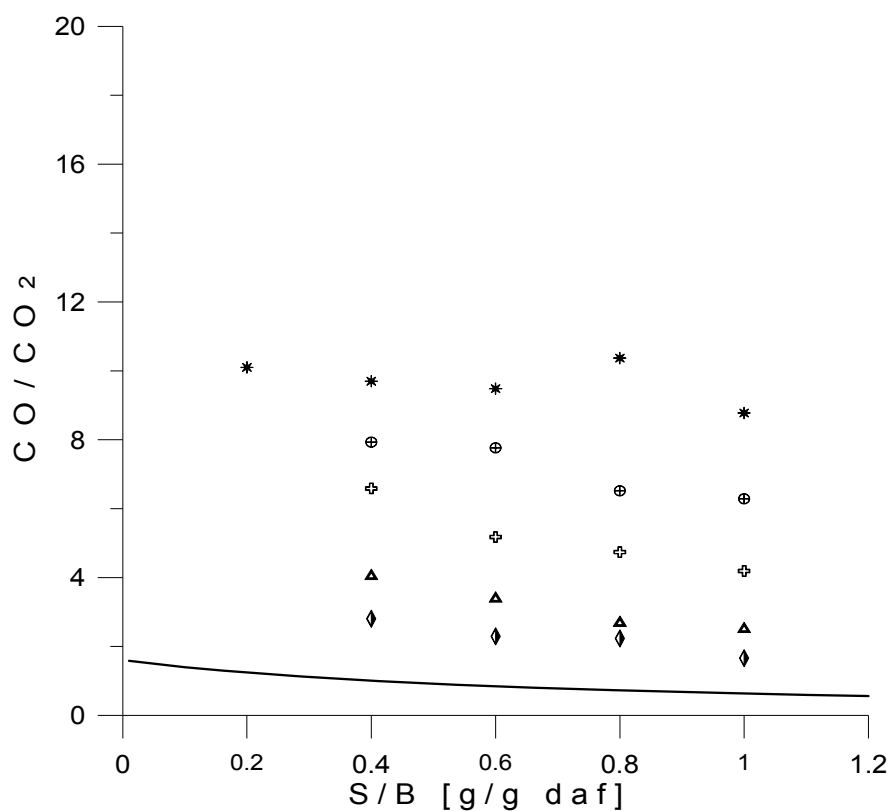


Figure 51. CO/CO₂ ratio for gasification of glucose at different steam/glucose ratios, 700°C and P = 1 atm. Solid line (—) equilibrium model, (*) non-catalytic gasification runs, experimental data using Ni supported catalyst at (⊕) 5 seconds, (⊕) 10 seconds, (Δ) 20 seconds and (◊) 30 seconds of reaction time.

8.5.2 2-methoxy-4-methylphenol: Equilibrium Model vs. Experimental Data at 700°C

Catalytic steam gasification experimental runs were also performed using 2-methoxy-4-methylphenol representing the lignin species in biomass at 700°C, reaction times of 5, 10, 20, 30 seconds, and S/B ratios of 0.4, 0.6, 0.8 and 1.0.

Figure 52 through Figure 49 report the molar fraction compositions of H₂, CO, CO₂ and CH₄ (on a dry basis), as a function of S/B ratio and reaction time for: a) equilibrium model prediction, b) catalytic steam gasification using Ni supported catalyst.

Figure 52 displays the H₂ concentration in the product gas as a function of the S/B ratio and contact time. The H₂ mole fraction slightly increases from 61.42 – 62.88 %-mol for catalytic steam gasification runs when S/B ratio changes from 0.4 to 1.0 at 30 seconds of reaction time and from 56.04 – 61.42 %-mol when reaction time augments from 5 - 30 seconds at S/B of 1.0. It can be also observed in Figure 52 that the equilibrium model follows the trend of the experimental data showing 9.56 and 2.72 %-mol less H₂ for catalytic gasification runs for 5 and 30 seconds, respectively.

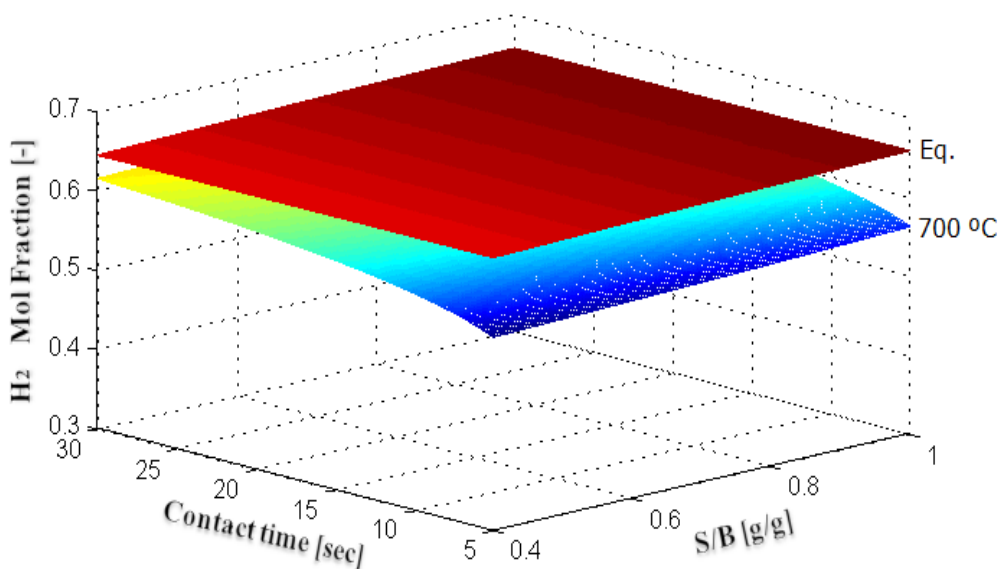


Figure 52. Hydrogen mole fraction composition for steam gasification of 2-methoxy-4-methylphenol; equilibrium calculations and experimental data using Ni supported catalyst at 700°C as a function of S/B ratio and reaction time

The CO concentration in the product gas for gasification of 2-methoxy-4-methylphenol is shown in Figure 53. By augmenting the S/B ratio from 0.4 - 1.0 g/g, the carbon monoxide fraction hardly decreases 18.54 – 16.12%-mol for catalytic steam gasification runs when S/B ratio increases from 0.4 to 1.0 at 30 seconds of reaction time and from 24.63 – 16.12 %-mol when reaction time moves from 5 - 30 seconds at S/B of 1.0. The equilibrium model under predicts the CO mole fraction by 9.47 and 0.97 %-mol more CO for catalytic experimental runs for 5 and 30 seconds, respectively.

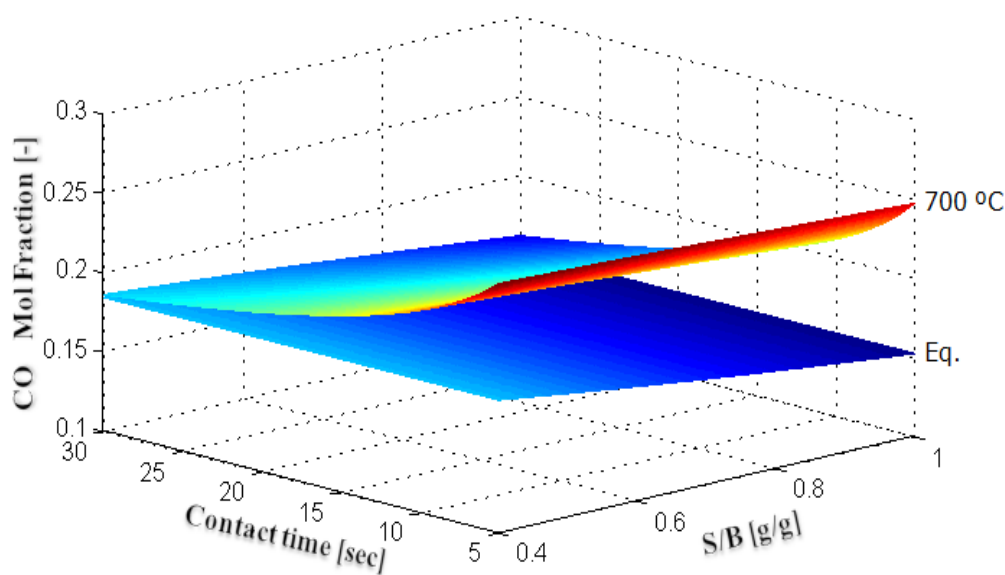


Figure 53. Carbon monoxide mole fraction composition for steam gasification of 2-methoxy-4-methylphenol; equilibrium calculations and experimental data using Ni supported catalyst at 700°C as a function of S/B ratio and reaction time

An upward trend in the CO_2 was observed with increasing S/B ratios and reaction time. Figure 54 reports that the equilibrium model over predicts the quantity of CO_2 by 5.56 %-mol and 1.17 %-mol more CO_2 for 5 and 30 seconds of contact time, respectively.

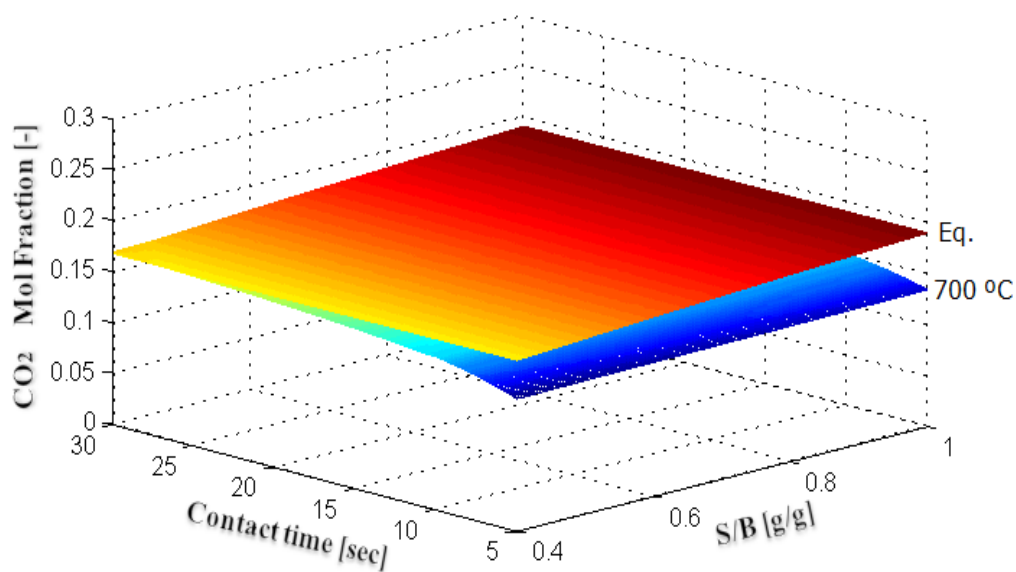


Figure 54. Carbon dioxide mole fraction composition for steam gasification of 2-methoxy-4-methylphenol; equilibrium calculations and experimental data using Ni supported catalyst at 700°C as a function of S/B ratio and reaction time

Finally, similar to the catalytic steam gasification of glucose, the equilibrium model, Figure 55, shows that almost no methane is produced at 700°C and 1 atm for the gasification of 2-methoxy-4-methylphenol. The equilibrium prediction differs from the experimental data showing around 6.10 %-mol and 2.93 %-mol more CH_4 for the experimental runs at 5 and 30 seconds of contact time, respectively.

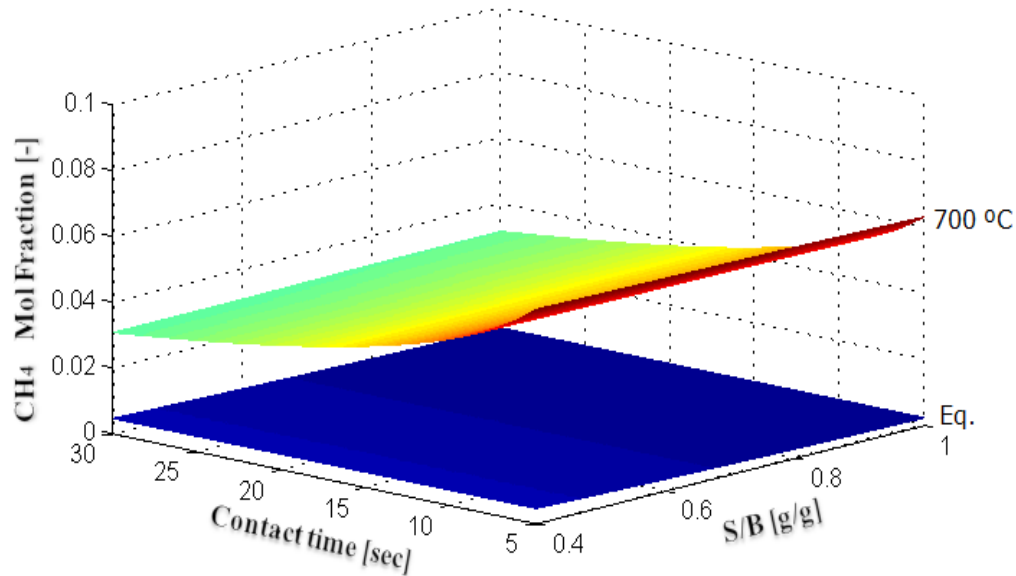


Figure 55. Methane mole fraction composition for steam gasification of 2-methoxy-4-methylphenol; equilibrium calculations and experimental data using Ni supported catalyst at 700°C as a function of S/B ratio and reaction time

In summary, while this equilibrium model provides satisfactory predictions for the catalytic experimental product gas composition for longer reaction times (>30 sec), the experimental product gas composition deviates from the equilibrium model at shorter reaction times (< 10 sec). In general, it is felt that the equilibrium model becomes less accurate at short reaction times (< 20 sec). As a consequence of these results, a comprehensive kinetic model under the conditions of catalytic steam gasification of biomass is required, and this in conjunction with the developed thermodynamic analysis.

8.6 Conclusions

The following points are the main conclusions of this study:

- a) It is shown that the thermodynamic equilibrium model involving a set of nine independent reactions is able to represent the molar fraction of various product species in a CREC Riser Simulator catalytic gasification unit for 30 seconds of contact time and a wide range of steam/glucose ratios and temperatures. The

CREC Riser Simulator unit closely mimics the expected fluidization conditions in a scaled-up catalytic gasifier.

- b) It is proven that at the operating conditions of the CREC Riser Simulator and at longer contact time (e.g. 30 seconds), the catalytic biomass gasification process is not a kinetically controlled chemical transformation. It is also shown that thermodynamics do provide an effective tool for assessing product distribution, with a temperature of 800°C and a steam/biomass ratio between 0.5 and 0.7 g/g being identified as optimal values for this process. Practical considerations to prevent ash agglomeration have shown that 700°C is a preferred temperature for operation and it is at this temperature level where all experiments are developed in this study. Mass balances were performed for each one of the experiments developed in the CREC Riser Simulator. Mass balances closed with an average value of 95%-103%.

- c) It is also demonstrated that at shorter contact time (e.g. 5 seconds), the catalytic gasification becomes a kinetically limited process, indicating that further kinetic studies are required to establish rate equations for product distribution predictions at various contact times, temperatures and steam/biomass ratios. The gathered data strongly suggest that the water-gas shift, reforming of methane, solid carbon and higher hydrocarbons reactions (C₂+) are the ones limiting the establishment of thermodynamic equilibrium.

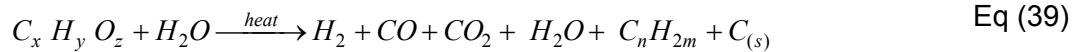
Chapter 9 Kinetic Modeling

9 Kinetic Model

9.1 Introduction

The steam gasification of biomass is a complex network of heterogeneous reactions.

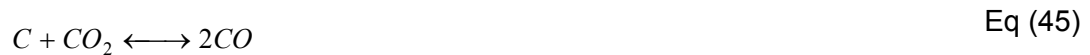
Primary reactions break down the vaporized biomass molecules, forming coke and permanent gases:



Secondary reactions crack the higher hydrocarbons into gases that further combust or become reduced:



Furthermore, permanent gases react to alter the gas composition depending on gasifier conditions:



Various kinetic models of differing complexity describing the gasification of various biomass feeds have been proposed in the literature (Fiaschi and Michelini, 2001; Radmanesh et al., 2006; Corella and Sanz, 2005; Orfao et al., 1999; Aznar et al., 1998; Perez et al., 1997). These models utilize subsets of reactions under a wide range of gasification conditions. These authors conclude that the following reaction have to be

considered: (i) the kinetically limited steam reforming of methane, and (ii) the close to equilibrium water–gas shift reaction [(Ginsburg and de Lasa, 2005); (Schuster et al., 2001); (Li et al., 2001); (Rapagna et al., 2000); (Ruggiero and Manfrida, 1999); (Kilpinen et al., 1991)].

However one can see that one of the main shortcomings of the proposed gasification kinetic models is given by the fact that they lump together a complex network of heterogeneous reactions in one single kinetic rate equation. While this in principle circumvents the overparametrization problem, the resulting rate equation provides an empirical fitting kinetic model. This model has little or no connection with the physicochemical events of either adsorption or reaction taking place.

Thus, one of the goals set for this research is to overcome this dilemma demonstrating the viability of establishing, as it is demonstrated in the upcoming sections, that kinetic models for biomass catalytic steam gasification can be developed using a coherent reaction engineering approach where reaction rates for various species are the result of the algebraic addition (“additive effect”) of the dominant reactions.

$$r_i = \sum r_{i,j} = r_{WGS} + r_{SR} + r_{DRM} \quad \text{Eq (47)}$$

where:

$$r_{WGS} = \frac{k'_{WGS} K_{CH_4}^A K_{CO_2}^A p_{CO} p_{H_2O}}{1 + K_{CH_4}^A p_{CH_4} + K_{CO_2}^A p_{CO_2}} \left(1 - \frac{p_{H_2} p_{CO_2}}{K_{WGS} p_{CO} p_{H_2O}} \right) \quad \text{Eq (48)}$$

$$r_{SR} = \frac{k'_{SR} K_{CH_4}^A p_{CH_4} p_{H_2O}}{1 + K_{CH_4}^A p_{CH_4}} \left(1 - \frac{p_{CO} p_{H_2}^3}{K_{SR} p_{CH_4} p_{H_2O}} \right) \quad \text{Eq (49)}$$

$$r_{DRM} = \frac{k'_{DRM} K_{CO_2}^A K_{CH_4}^A p_{CO_2} p_{CH_4}}{1 + K_{CH_4}^A p_{CH_4} + K_{CO_2}^A p_{CO_2}} \left(1 - \frac{p_{CO}^2 p_{H_2}^2}{K_{DRM} p_{CO_2} p_{CH_4}} \right) \quad \text{Eq (50)}$$

It can be noticed that each of these equations include physicochemically relevant intrinsic kinetic parameters, k'_i and adsorption constants, K_j^A .

One of the highlight of the CREC Riser Simulator is given by the fact that the determination of adsorption and intrinsic kinetic parameters can be *decoupled*. As a result, one has in the CREC Riser Simulator data analysis either adsorption or reaction tractable models with a limited number of parameters. This limited number of physicochemically relevant parameters is always established with their respective reduced statistical indicators: parameter spans for the 95% confidence interval and low cross-correlation.

The problem with initial conditions for gasification simulation can also be handled very effectively using the CREC Riser Simulator. Reaction times can be studied in a wide range of time spans using this device. Thus, by considering the gas composition trends at the shortest reaction time measured (e.g. 5 seconds) the various stoichiometric coefficients in Eq (24) can be set at close to zero reaction times.

Furthermore by using the chemical species composition close to initial reaction state and the intrinsic kinetic and adsorption parameters established as in section 9.7, the differential equations for various chemical species can be solved numerically.

Numerical solution of these equations can be done for the complete span of reaction times (e.g. 5 to 30 seconds).

9.2 Steam Gasification of Biomass

This research evaluates the catalytic steam gasification of biomass over a Ni/ α -alumina catalyst. Experiments were carried out in the CREC fluidized Riser Simulator under gasification conditions using a) glucose ($C_6H_{12}O_6$) – steam, and b) 2-methoxy-4-methylphenol ($C_8H_{10}O_2$) – steam as a model compounds for the cellulose and lignin contained in biomass. Experimental results (Chapter 6), along with thermodynamic evaluations (Chapter 8), allow for the identification of the most probable reaction scheme for the gasification of biomass over Ni/ α -alumina, as shown in Figure 56.

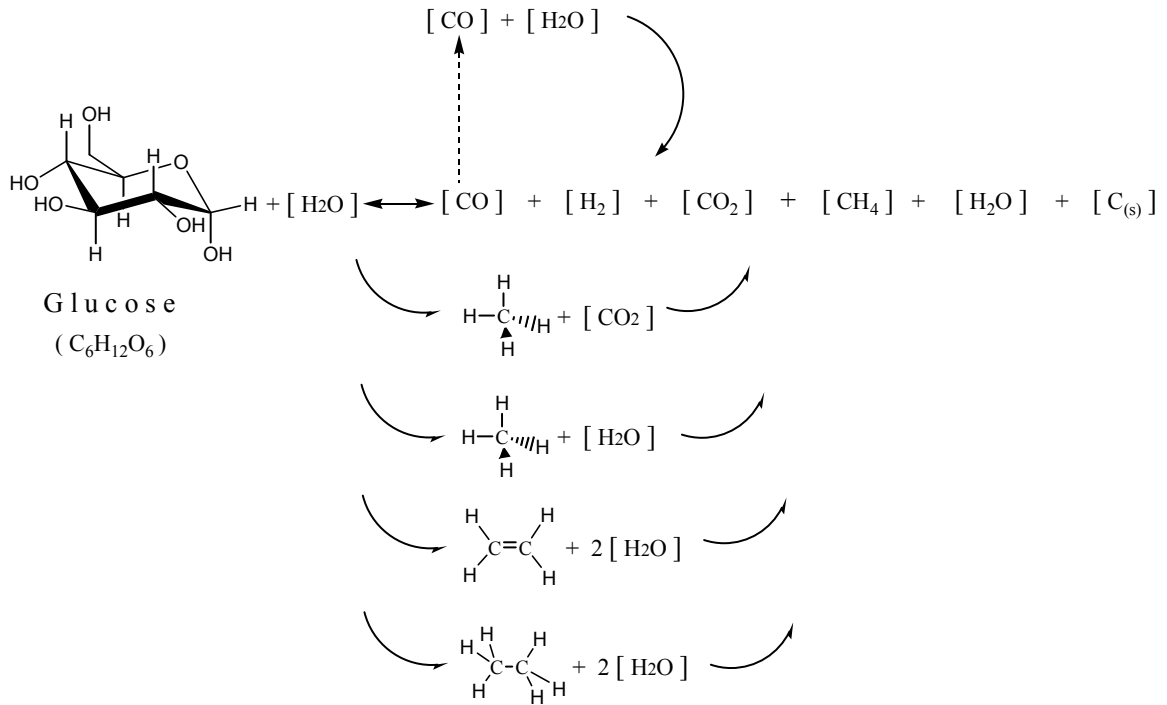


Figure 56. Chemical reaction network considered in the steam gasification of biomass

9.3 Overall Kinetic Model

The rate of formation and disappearance of all components can be modeled using a Langmuir-Hinshelwood type rate equation, which takes into consideration the adsorption of the reactants on the catalyst surface as well as the reaction kinetics. The general form of a Langmuir-Hinshelwood for this system is given by Ollis et al., 1989:

$$r_i = \frac{k_i^k K_i^A p_i}{1 + \sum_{j=1}^n K_j^A p_j} \quad \text{Eq (51)}$$

where, r_i is the rate of reaction of component “ i ” in $\text{mol}/\text{g}_{\text{cat}} \text{min}$, k_i^k is the kinetic constant for component “ i ” in $\text{mol}/\text{g}_{\text{cat}} \text{min}$, K_i^A is the adsorption constant for component “ i ” in $1/\text{atm}$, p is the partial pressure of component “ i ” in atm . The term “ n ” is the number of chemical species, while “ j ” is a subscript to denote each component in the denominator term.

Knowing that the CREC Riser Simulator in which the experimental runs were carried out operates as a well mixed batch reactor (Ginsburg and deLasa, 2005, Pekediz et al, 1992), a balance equation for each component “ i ” can be expressed as follows:

$$r_i = \frac{V}{W} \frac{d\left(\frac{p_i}{R T}\right)}{dt} \quad \text{Eq (52)}$$

with this equation being applicable to a bench-scale isothermal well-mixed batch reactor unit, where V is the volume of the reactor in cm^3 , W is the weight of the catalyst in *grams*, p_i is the partial pressure of specie “ i ”, R is the gas constant in $cm^3 \square atm \square K^{-1} \square mol^{-1}$, T is the reactor temperature in $^{\circ}K$ and t is the time in *seconds*.

By combining Eq (51) and Eq (52), the general rate of reaction for each chemical species is obtained as follow:

$$\frac{d\left(\frac{p_i}{R T}\right)}{dt} = \frac{\frac{W}{V} k_i^k K_j^A p_i}{1 + \sum_{j=1}^n K_j^A p_j} \quad \text{Eq (53)}$$

Let set $k_i' = \frac{W}{V} R T k_i^k K_j^A$, then Eq (53) can be simplified to:

$$\frac{dp_i}{dt} = \frac{k_i' p_i}{1 + \sum_{j=1}^n K_j^A p_j} \quad \text{Eq (54)}$$

with all “ k_i' ” rate constants in Eq (54) representing kinetic constants lumping adsorption and intrinsic kinetic parameters.

Thus, by developing one equation with the form of Eq (54) for each component, one can obtain a set of differential equations to represent the catalytic steam gasification of biomass. This set of differential equations is presented in Section 9.7

9.4 Water-Gas Shift Mechanism

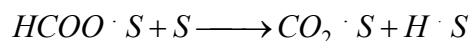
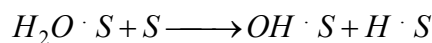
Due to the industrial significance of the water-gas-shift (WGS) reaction, many researchers have investigated the reaction mechanism and developed kinetic models to reflect the behavior of the reaction over commercial industrial catalysts (i.e., copper, iron, or nickel-based). The results of several of these investigations suggest that the WGS reaction occurs largely via four specific mechanisms: i) the *redox* mechanism [(Nakamura et al., 1990); (Ovesen et al., 1992); (Ovesen et al., 1996); (Tserpe and Waugh, 1997); (Waugh, 1999); (Campbell and Daube, 1987); (Schumacher et al., 2005); ii) the *formate* mechanism [(Ovesen et al., 1996); (Campbell and Daube, 1987); (Askgaard et al., 1995); (Shido and Iwasawa, 1993);]; iii) the *associative* mechanism [(Fishtik and Datta, 2002); (Rhodes et al., 1995); (Callaghan et al., 2003)], and, more recently, iv) the *carbonate* mechanism [(Tserpe and Waugh, 1997); (Waugh, 1999); (Millar et al., 1991); (Ma and Lund, 2003)].

The *redox* mechanism implies successive oxidation and reduction of the reactive catalyst surface by adsorbed oxygen (from water) and carbon monoxide (as it is oxidized to carbon dioxide), respectively.



where S represents a surface site.

In the *formate* mechanism, adsorbed water dissociates into an adsorbed hydroxyl group and adsorbed atomic hydrogen. The hydroxyl group then combines with adsorbed carbon monoxide to form adsorbed formate, which eventually decomposes into carbon dioxide and hydrogen, yielding the WGS products.

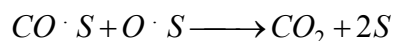


Campbell and Daube, 1987, explored the WGS reaction in terms of the *formate* mechanism, given in Table 18.

Table 18. Formate mechanism for the WGS reaction (Campbell and Daube, 1987)

Formate Reaction Mechanism	
$CO + S \longrightarrow CO \cdot S$	Step 1
$H_2O + S \longrightarrow H_2O \cdot S$	Step 2
$H_2O \cdot S + S \longrightarrow OH \cdot S + H \cdot S$	Step 3
$CO \cdot S + OH \cdot S \longrightarrow HCOO \cdot S + S$	Step 4
$HCOO \cdot S + S \longrightarrow CO_2 \cdot S + H \cdot S$	Step 5
$2H \cdot S \longrightarrow H_2 + 2S$	Step 6
<hr/>	
$CO + H_2O \longrightarrow CO_2 + H_2$	(OR)

Experimental investigation of the catalyst's surface suggested that CO and H₂O coverage are very low under reaction conditions resulting in a rate that is nearly independent of the partial pressure of CO and that strongly increases with the partial pressure of H₂O. This was explained by the inclusion of a hydroxyl intermediate formed from the surface dissociation of adsorbed water. Furthermore, step 3 – the dissociation of H₂O to form a surface hydroxyl and an adsorbed hydrogen atom – was identified as the rate-limiting step. Campbell and Daube, 1987, also considered a *surface redox* mechanism in which the OH·S produced in step 3 of the *formate* mechanism further dissociates into O·S and H·S. The O·S was then assumed to be consumed rapidly by adsorbed CO in the following step:



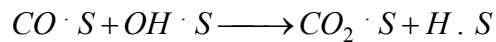
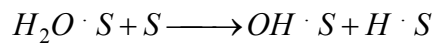
This alternate mechanism also assumes that step 3 is rate-limiting and is reinforced by the experimental findings of Campbell and Daube, 1987. That is to say, the surface reaction proceeds rapidly to equilibrium. Campbell and Daube, 1987, also utilized the analytical

expression proposed earlier by van Hewijnen and de Jong, 1980, to correlate and predict their experimental results accurately. Assuming Langmuir adsorption, the numerical data are manipulated to indicate the form of the rate expression. The rate is reported, in general, as:

$$r_{WGS} = \frac{k p_{CO} p_{H_2O}}{1 + K_{CO_2}^A p_{CO_2} + K_{H_2O}^A p_{H_2O} + K_{H_2}^A p_{H_2} + K_{CO}^A p_{CO}} \left(1 - \frac{p_{CO_2} p_{H_2}}{K p_{CO} p_{H_2O}} \right) \quad \text{Eq (55)}$$

In the third possible *associative* WGS reaction mechanism, adsorbed water dissociates into an adsorbed hydroxyl group and atomic hydrogen. The adsorbed hydroxyl then oxidizes adsorbed carbon monoxide resulting in adsorbed carbon dioxide and atomic hydrogen.

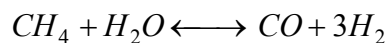
In addition to the *redox*, *formate*, and *associative* mechanisms, researchers have also proposed that the WGS reaction may proceed via a *carbonate* species. Even more, in attempts to model and predict the real behavior of the WGS reaction some researchers have considered more general mechanisms often comprising elementary reaction steps from the more recognized mechanisms as follows:



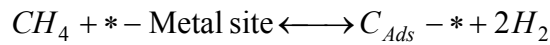
For the present study, the WGS reaction is assumed to occur via the *formate* mechanism assuming Langmuir adsorption as reported in Eq (55).

9.5 Steam Reforming of Methane (SR)

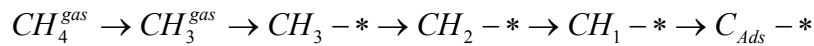
The chemical processes involved in the steam reforming of methane can be expressed using the following endothermic reforming reaction:



A considerable number of rate expressions for the steam reforming of methane have been proposed in literature. These kinetic models range in complexity from simple first order expressions that are dependent on methane and contain only two parameters [(Munster and Grabke, 1981); (Prokopiev et al., 1992)], to complex Langmuir-Hinshelwood models with over 10 parameters [(Xu and Froment, 1989); (Jarosch et al., 2002)]. It is generally accepted that the rate of methane reforming displays a first order dependency on methane. Furthermore, it is also agreed that the rate determining step in the reforming process is the formation of adsorbed carbon (Munster and Grabke, 1981).



The formation of adsorbed carbon from methane is a stepwise process that requires a C-H bond to be broken while methane is in the gas phase. The resultant CH_3 species must then come into contact with an open site on the surface of the metal crystal. After being adsorbed to the surface of the metal crystal, the CH_3 is transformed into adsorbed carbon by stepwise dehydrogenation (Rostrup-Nielsen, 1993).



The kinetic expression reported by Munster and Grabke, 1981 was adopted for the steam reforming of methane reaction in the present study. In this model, adsorption of methane is assumed to play a role in determining the apparent rate of methane consumption as follow:

$$r_{CH_4} = \frac{k_{SR} K_{CH_4}^A p_{CH_4}}{1 + K_{CH_4}^A p_{CH_4}} \left(1 - \frac{p_{CO} p_{H_2}^3}{K_{SR} p_{CH_4} p_{H_2O}} \right) \quad \text{Eq (56)}$$

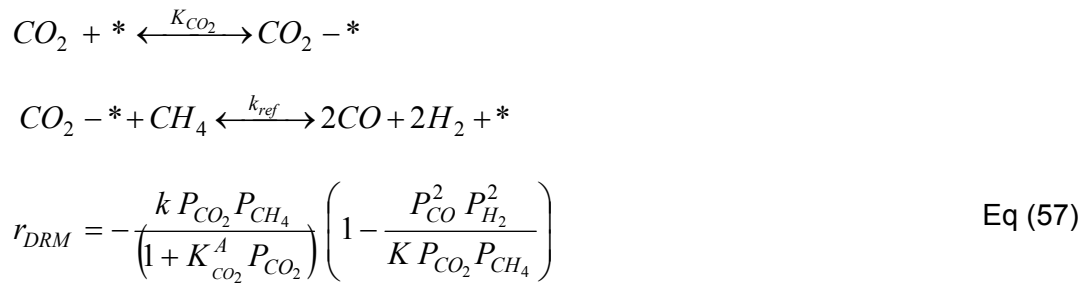
In addition, the formation of an adsorbed carbon species is assumed to be the direct result of methane adsorption to the nickel crystal surface. The products, hydrogen and carbon monoxide, are not adsorbed. Water reacts directly with the adsorbed carbon species.

9.6 Dry Reforming of Methane (DRM)

Various rate models for the dry reforming of methane were fitted to the experimental data by numerically integrating the rate equations (Michael et al., 1997; El Solh et al., 2001).

The best agreement was obtained with a rate model based on simplified noncompetitive Langmuir-Hinshelwood (El Solh et al., 2001), which is the mechanism adopted in the present study. This mechanism assumes that carbon dioxide is associatively adsorbed on the catalyst surface in adsorption equilibrium. The slow and rate-determining step is the reaction of the adsorbed species with the other reactant from the gas phase, which leads directly to the products.

Reaction steps of the considered mechanistic model (El Solh et al., 2001) include the following:



where K is the thermodynamic equilibrium constant for the reforming reaction at the reaction temperature

9.7 Postulated “Additive” Rate Equation Model

The gathered gasification experimental data shows a negligible amount of carbon and C_2+ components in the product gas (i.e. < 0.5 wt% for glucose at 700°C , SB 0.6, and 10 seconds of contact time). As a result, the reaction involving the cracking of C_2+ hydrocarbon ($C_n H_{2m} + nH_2O \longrightarrow nCO + (n+m) H_2$), and the reaction including carbon ($C + H_2O \longleftrightarrow H_2 + CO$, $C + CO_2 \longleftrightarrow 2CO$ and $C + 2H_2 \longleftrightarrow CH_4$) can be neglected. Once the Eq (40), Eq (44), Eq (45) and Eq (46) are neglected the remaining ones are: a) water gas-shift reaction, Eq (41), b) steam reforming of methane, Eq (42), and c) dry reforming of methane, Eq (43).

Therefore, one can model using the Langmuir-Hinshelwood type rate equation, Eq (54), as an algebraic additive process of all relevant reactions involved as follow:

$$r_i = \sum r_{i,j} = r_{WGS} + r_{SR} + r_{DRM} \quad \text{Eq (58)}$$

were: r_{WGS} = water gas shift reaction rate contribution,

r_{SR} = steam reforming of methane reaction rate contribution, and

r_{DRM} = dry reforming of methane reaction rate contribution

Thus, one can obtain a set of differential equations to represent the catalytic steam gasification of biomass.

Firstly, the rate of formation and disappearance of hydrogen is given by the reaction rate contribution of WGS, SR and DRM as follow:

$$\begin{aligned} \frac{dp_{H_2}}{dt} = & \frac{k_{WGS} K_{CO_2}^A p_{CO} p_{H_2O}}{1 + K_{CH_4}^A p_{CH_4} + K_{CO_2}^A p_{CO_2}} \left(1 - \frac{p_{H_2} p_{CO_2}}{K_{WGS} p_{CO} p_{H_2O}} \right) + \\ & + \frac{k_{SR} K_{CH_4}^A p_{CH_4}}{1 + K_{CH_4}^A p_{CH_4}} \left(1 - \frac{p_{CO} p_{H_2}^3}{K_{SR} p_{CH_4} p_{H_2O}} \right) + \\ & - \frac{k_{DRM} K_{CO_2}^A K_{CH_4}^A p_{CO_2} p_{CH_4}}{1 + K_{CH_4}^A p_{CH_4} + K_{CO_2}^A p_{CO_2}} \left(1 - \frac{p_{CO}^2 p_{H_2}^2}{K_{DRM} p_{CO_2} p_{CH_4}} \right) \end{aligned} \quad \text{Eq (59)}$$

where k_{WGS} , k_{SR} and k_{DRM} are the kinetic constants for the water gas shift reaction (WGS), steam reforming reaction (SR) and dry reforming of methane reaction (DRM), respectively; K_{WGS} , K_{SR} and K_{DRM} are the thermodynamic equilibrium constants of the WGS, SR and DRM reactions at the reaction temperature; $K_{CH_4}^A$ and $K_{CO_2}^A$ are the adsorption constants for methane and carbon dioxide components; and p is the partial pressure of specie “ i .”

A similar equation can be written for each component in the product gas. The rate of formation and disappearance of carbon monoxide given by:

$$\frac{dp_{CO}}{dt} = - \frac{k_{WGS} K_{CO_2}^A p_{CO} p_{H_2O}}{1 + K_{CH_4}^A p_{CH_4} + K_{CO_2}^A p_{CO_2}} \left(1 - \frac{p_{H_2} p_{CO_2}}{K_{WGS} p_{CO} p_{H_2O}} \right) + \quad \text{Eq (60)}$$

$$+ \frac{k_{SR} K_{CH_4}^A p_{CH_4}}{1 + K_{CH_4}^A p_{CH_4}} \left(1 - \frac{p_{CO} p_{H_2}^3}{K_{SR} p_{CH_4} p_{H_2O}} \right) +$$

$$- \frac{k_{DRM} K_{CO_2}^A K_{CH_4}^A p_{CO_2} p_{CH_4}}{1 + K_{CH_4}^A p_{CH_4} + K_{CO_2}^A p_{CO_2}} \left(1 - \frac{p_{CO}^2 p_{H_2}^2}{K_{DRM} p_{CO_2} p_{CH_4}} \right)$$

For carbon dioxide, the reaction rate contribution of WGS, SR and DRM is written as:

$$\frac{dp_{CO_2}}{dt} = - \frac{k_{WGS} K_{CO_2}^A p_{CO} p_{H_2O}}{1 + K_{CH_4}^A p_{CH_4} + K_{CO_2}^A p_{CO_2}} \left(1 - \frac{p_{H_2} p_{CO_2}}{K_{WGS} p_{CO} p_{H_2O}} \right) +$$

$$- \frac{k_{DRM} K_{CO_2}^A K_{CH_4}^A p_{CO_2} p_{CH_4}}{1 + K_{CH_4}^A p_{CH_4} + K_{CO_2}^A p_{CO_2}} \left(1 - \frac{p_{CO}^2 p_{H_2}^2}{K_{DRM} p_{CO_2} p_{CH_4}} \right)$$
Eq (61)

For water, the reaction rate contribution of WGS and SR is given by:

$$\frac{dp_{H_2O}}{dt} = - \frac{k_{WGS} K_{CO_2}^A p_{CO} p_{H_2O}}{1 + K_{CH_4}^A p_{CH_4} + K_{CO_2}^A p_{CO_2}} \left(1 - \frac{p_{H_2} p_{CO_2}}{K_{WGS} p_{CO} p_{H_2O}} \right) +$$

$$- \frac{k_{SR} K_{CH_4}^A p_{CH_4}}{1 + K_{CH_4}^A p_{CH_4}} \left(1 - \frac{p_{CO} p_{H_2}^3}{K_{SR} p_{CH_4} p_{H_2O}} \right) +$$
Eq (62)

Finally, the rate of formation and disappearance of methane is given by the reaction rate contribution of SR and DRM as follow:

$$\frac{dp_{CH_4}}{dt} = - \frac{k_{SR} K_{CH_4}^A p_{CH_4}}{1 + K_{CH_4}^A p_{CH_4}} \left(1 - \frac{p_{CO} p_{H_2}^3}{K_{SR} p_{CH_4} p_{H_2O}} \right) +$$

$$- \frac{k_{DRM} K_{CO_2}^A K_{CH_4}^A p_{CO_2} p_{CH_4}}{1 + K_{CH_4}^A p_{CH_4} + K_{CO_2}^A p_{CO_2}} \left(1 - \frac{p_{CO}^2 p_{H_2}^2}{K_{DRM} p_{CO_2} p_{CH_4}} \right)$$
Eq (63)

These postulated rate expressions inevitably lead to mathematical models that are nonlinear with respect to their parameters, particularly when the adsorption constants appear both in the numerator and in the denominator of the expression. The nonlinearity in the parameters can result in overparametrization given a high degree of parameter correlation. One shall notice that this parameter correlation is amplified given the

mathematical form of the Hinselwood Langmuir equation where unknown parameters appear in the numerator and in the denominator.

This parameter correlation can be successfully eliminated using a procedure where the calculation of intrinsic kinetic parameters and adsorption constants is decoupled as the one that can be implemented with the CREC Riser Simulator's data, thereby improving the statistical confidence on the kinetic parameter estimates.

9.8 Parameter Estimation

Once a set of ordinary differential equations that describe the chemical reaction mechanism is established, the next step is to validate the model. This is done through the estimation of parameters in the equations by fitting parameters that have been obtained from experimental data. The mathematical model with the best parameter estimates can be used to predict the behaviour of the system.

For a system modeled with a set of ordinary differential equations, the mathematical representation of the model is given by (Englezos and Kalogerakis, 2001):

$$\frac{d\vec{C}(t)}{dt} = f(\vec{C}(t), \vec{u}, \vec{k}); \quad \vec{C}(t) = \vec{C}_0 \quad \text{Eq (64)}$$

$$y(t) = AC(t) \quad \text{Eq (65)}$$

where A is the $m \times n$ observation matrix which indicates the state variables that are measured experimentally.

$\vec{k} = [k_1, k_2, \dots, k_p]^T$ is a p -dimensional vector of parameters whose numerical values are unknown

$\vec{C} = [C_1, C_2, \dots, C_n]^T$ is a n -dimensional vector of state variable

$\vec{C}_0 = [C_{10}, C_{20}, \dots, C_{n0}]^T$ is a n -dimensional vector of initial conditions for the state variable

$\vec{u} = [u_1, u_2, \dots, u_r]^T$ is a r-dimensional vector of set or measured variables

$f = [y_1, y_2, \dots, y_n]^T$ is a n-dimensional vector of known form (differential equations)

$\vec{y} = [y_1, y_2, \dots, y_m]^T$ is an m-dimensional output vector (set of variables measured experimentally)

The parameters of the proposed model are estimated by minimizing the Least Squares objective function, defined as the sum of the squares of the residuals. For ordinary differential equations, the objective function is given by:

$$SSR = \sum_{i=1}^N \left[\hat{y} - \vec{y}(t_i, \vec{k}) \right]^T \left[\hat{y} - \vec{y}(t_i, \vec{k}) \right] \quad \text{Eq (66)}$$

where $\left[\hat{y} - \vec{y}(t_i, \vec{k}) \right]^T$ is the residuals for the i^{th} measurement defined as the difference

between the measured value, \hat{y} , and the calculated value using the model and the estimated parameters, $\vec{y}(t_i, \vec{k})$.

For the estimation of parameters using experimental data from more than one experiment, the objective function becomes:

$$SSR = \sum_{j=1}^{N_E} \sum_{i=1}^N \left[\hat{y} - \vec{y}(t_i, \vec{k}) \right]^T \left[\hat{y} - \vec{y}(t_i, \vec{k}) \right] \quad \text{Eq (67)}$$

where N_E is the number of experiments. As a result, two built-in MATLAB subroutines were used: “*nlinfit*” for the minimization of the objective function, and “*ode113*” for the numerical integration of the ordinary differential equation system.

9.9 Kinetic Parameter Estimation

The adsorption isotherms at various temperatures for methane and carbon dioxide were calculated independently using experimental data from the CREC Riser Simulator. This

calculation related the equilibrium partial pressure of pure species with the adsorbed amounts of the same species. More details of this calculation are provided in Appendix B.

Once the adsorption parameter and its dependence with temperature was established, the intrinsic kinetic constants were estimated using the non-linear least-squares regression routine “nlinfit.m,” available in the optimization toolbox of MATLAB, version 7.6. This routine uses the Gauss-Newton algorithm with Levenberg-Marquardt modifications for global convergence. The integration of the differential system (Eq (59)-Eq (63)), required in the parameter estimation, was performed numerically using the function “ode113”; and the function “nlparci” was used to produce 95% confidence intervals for each estimated parameter.

The reaction data, used to estimate the kinetic parameters corresponding to the surface reaction rates (k_i), was planned using Taguchi’s design of experiments involving four factors (steam biomass ratio, reaction temperature, contact time, and total pressure) and three levels for each of the factors. The conditions of the catalytic experiments were set as follows: a) using glucose as a model compound for the cellulose contained in biomass, 0.4, 0.6, 0.8 and 1.0 steam/biomass ratios (g/g) wt%, 2 atm. of argon, catalyst/feedstock ratio of ~25, residences times: 5, 10, 20, and 30 s, and reaction temperatures 600, 650, and 700°C, and b) using 2-methoxy-4-methylphenol as a model compound for the lignin contained in biomass, 0.4, 0.6, 0.8 and 1.0 steam/biomass ratios (g/g) wt%, 2 atm. of argon, catalyst/feedstock ratio of ~25, residences times: 5, 10, 20, and 30 s, and reaction temperatures 600, 650, and 700°C. As mentioned in previous chapters, the catalytic runs were repeated at least 3 times, and the mass balance closures were below 5%, being well in the range of typical closures achieved in the CREC Riser Simulator (de Lasa et al., 2006). A detailed discussion of these experimental results is presented in Chapter 6.

9.10 Kinetic Parameters as a Function of Temperature

A search for the kinetic parameters was initiated using the experimental data obtained at 600, 650 and 700°C. The MATLAB calculation procedure is explained in Section 9.9. An example of the kinetic parameters calculated at this adjustment is presented in Appendix E, while a selected set of results is displayed in Table 19. Table 19 reports the kinetic

parameters obtained for mixtures of 2-methyl-4-methoxyphenol in water at 700°C and S/B ratios of 0.4, 0.6, 0.8, and 1.0, with narrow 95% confidence limits.

Table 19. Kinetic parameters at 700°C for 2-methyl-4-methoxyphenol mixtures

2-Methyl-4-Methoxyphenol mixtures		
Parameter	Value	Error
$k_{WGS\ 1}^a$	1.30×10^{-5}	$\pm 8.09 \times 10^{-7}$
$k_{SR\ 1}^b$	2.99×10^{-9}	$\pm 5.66 \times 10^{-10}$
$k_{DRM\ 1}^a$	3.20×10^{-8}	$\pm 7.20 \times 10^{-10}$
$K_{CO_2}^c$	7.80×10^{-2}	$\pm 1.21 \times 10^{-3}$

^a [mol gcat⁻¹ s⁻¹], ^b [mol gcat⁻¹ s⁻¹ psia⁻¹], ^c [psia⁻¹].

9.11 Intrinsic Kinetic Parameters Estimation

To obtain the intrinsic kinetic parameters (activation energies and pre-exponential factors), the kinetic parameters k_i and K_{CO_2} (Eq (59)- Eq (63)) were allowed to vary with temperature using an Arrhenius relationship centered on an average temperature (650°C):

$$k_i = k_i^0 \exp \left(-\frac{E_i}{R} \left(\frac{1}{T} - \frac{1}{T_{avg}} \right) \right) \quad \text{Eq (68)}$$

$$K_{CO_2} = K_{CO_2}^0 \exp \left(-\frac{\Delta H_{ads}^{CO_2}}{R} \left(\frac{1}{T} - \frac{1}{T_{avg}} \right) \right) \quad \text{Eq (69)}$$

where k_i is the reaction rate constant of component i , k_i^0 is the pre-exponential factor or reaction rate constant at 650°C, E_i is the activation energy, $K_{CO_2}^0$ is the carbon dioxide adsorption equilibrium constant at 650°C, $\Delta H_{ads}^{CO_2}$ is the carbon dioxide heat of adsorption, R is the universal gas constant, and T_{avg} is the average temperature.

In terms of Eq (68) and Eq (69), one should notice that the centered Arrhenius form reduces the correlation between the pre-exponential factor and the activation energy,

thereby improving the statistical properties of the estimates for the pre-exponential factors.

Substitution of Eq (68) and Eq (69) in the proposed rate expressions (Eq (59)- Eq (63)), gives a new differential equation system to be solved, with the intrinsic kinetic parameters corresponding to the carbon dioxide adsorption, $K_{CO_2}^0$ and $\Delta H_{ads}^{CO_2}$, and the rate-limiting surface reaction rates, k_i^0 and E_i , as the parameters to be estimated.

Initial values of the kinetic parameters that were used to solve the new differential equation system were the ones derived in Section 9.10. In this sense, the kinetic parameters at 650°C were used as pre-exponential guess values ($K_{CO_2}^0$ and k_i^0). The initial activation energies (E_i) and heat of adsorption ($\Delta H_{ads}^{CO_2}$) values were obtained from linear regression of the Arrhenius expressions (Eq (68) and Eq (69)) in a semilogarithmic plot. Appendix E presents an example of the calculation, and Table 20 shows the results obtained for E_i and $\Delta H_{ads}^{CO_2}$, and their linear regression error (R^2).

Table 20. Activation energies and heat of adsorption guesses

2-Methyl-4-Methoxyphenol mixtures		
Parameter ^a	Value	R^2
E_{WGS}	18.4	0.809
E_{SR}	35.2	0.990
E_{DRM}	94.9	0.986
$\Delta H_{CO_2}^A$	-11.0	0.998

^a units [kJ/mol].

Finally, a total of 6 parameters (k_{WGS}^0 , E_{WGS} , k_{SR}^0 , E_{SR} , k_{DRM}^0 , and E_{DRM}) were adjusted simultaneously by nonlinear multivariable regression of experimental data using the MATLAB calculation procedure explained in Section 9.9 and the above guess values. Table 21 summarizes the intrinsic kinetic parameters estimated with their 95%

confidence interval, and the standard deviation of the residuals (σ), showing the quality of the fits.

Table 21. Intrinsic kinetic parameters of the proposed “additive” kinetic model with their 95% confidence

Parameter	Glucose		2-Methyl-4-Methoxyphenol	
	Value	Span for 95% confidence	Value	Span for 95% confidence
k_{WGS}^0 ^a	2.97 x10 ⁻⁶	±8.03 x10 ⁻⁸	1.05x10 ⁻⁶	±6.55 x10 ⁻⁷
E_{WGS} ^b	9.26	±0.94	23.43	±9.7
k_{SR}^0 ^c	1.80 x10 ⁻¹⁰	±8.87 x10 ⁻¹¹	2.43x10 ⁻⁹	±4.59 x10 ⁻¹⁰
E_{SR} ^b	96.20	±30.2	32.55	±25.3
k_{DRM}^0 ^c	9.58 x10 ⁻¹⁰	±6.42 x10 ⁻¹¹	1.84x10 ⁻⁸	±4.15 x10 ⁻¹⁰
E_{DRM} ^b	78.81	±10.4	90.88	±12.9
$K_{CO_2}^0$ ^d	8.43x10 ⁻²	±1.91x10 ⁻³	8.43x10 ⁻²	±1.91x10 ⁻³
$\Delta H_{CO_2}^A$ ^b	-11.01	±6.1	-11.01	±6.1
σ ^e	1.48 x10 ⁻³		3.17x10 ⁻³	
m	240		288	

^a [mol gcat⁻¹ s⁻¹ psia⁻¹]; ^b [kJ/mol]; ^c [mol gcat⁻¹ s⁻¹]; ^d [psia⁻¹];

^e $\sigma = \sqrt{\sum (X_{experimental} - X_{estimated})^2 / (m - p)}$, where m is the number of data points and p is the number of model parameters .

By inspecting the results of the parameter estimation it can be noticed that the standard deviation (σ), calculated from the summation of the squares of the residuals, shows the quality of the fit. This result is particularly relevant given the number of parameters adjusted, and it is reached due to the representative number of data points developed (m).

Moreover, the intrinsic kinetic parameters corresponding to the rate-limiting surface reaction rates, k_i^0 and E_i , are significant at the 95% confidence level, with this result showing that the re-parameterization and temperature centering were successful in reducing the overall correlation between the parameters.

The signs assigned to the activation energies are consistent with the expected dependence of these constants on temperature. A positive E_{SR} and E_{DRM} show a methane conversion intrinsic constant favored by higher temperatures while negative $\Delta H_{CO_2}^A$ shows a CO₂ adsorption process negatively affected by temperature increases.

Regarding the energies of activation (E_i), it is important to review the magnitude of the energy of activations obtained in the context of the present study and compare them with energies of activation for the same water gas shift, steam methane reforming and dry methane reforming reported in the literature. This comparison is presented in Table 22.

For the dry reforming of methane (DRM), Michael et al., 1997 report activation energies in the 93.3 to 123.2 kJ/mol range for similar nickel based catalysts. These values include the 78.8 and 90.9 kJ/mol activation energies calculated for DRM reaction using glucose and 2-methoxy-4-methyphenol model compounds. Thus, the calculated parameters are well in line with the data available in the literature.

Concerning water gas-shift reaction (WGS) activation energies, the values reported are in the 17.5 to 26.6 kJ/mol ranges when using a WGS rate formulation including chemical equilibrium and Langmuir-Hinshelwood type rate equation. Taking into consideration the span for 95% confidence reported, the parameter spans include the 9.2 and 23.4 kJ/mol activation energies calculated using glucose and 2-methoxy-4-methyphenol respectively. As a result the calculated parameters for WGS can be considered reasonably in line with the data from the literature.

Regarding steam reforming of methane (SRM), the activation energies for the dissociation of CH₄ on Ni range from 70 to 141 kJ/mol. As a result, the activation energy of 96.2 kJ/mol determined in the present study for glucose is in agreement with literature data. However, the 32 kJ/mol activation energy for SRM obtained for the 2-methoxy-4-

methyphenol gasification is considered outside the range of expected values. It is believed that this deviation of the SRM activation energy for 2-methoxy-4-methylphenol can be assigned to carbon species and their influence in the gasification kinetics. Carbon species are not included in the kinetic model to simplify the parameter calculation. While for glucose, carbon formation is minimal and as a result carbon effects can be reasonably neglected, for the 2-methoxy-4-methylphenol there is a greater amount of carbon formed (coke) and carbon species should be included in a more detailed kinetic model.

Table 22. Activation energy review with the reported in the literature [kJ/mol]

Water Gas-Shift reaction			
Glucose [L-H]	2-methoxy-4-methylphenol [L-H]	Literature WGS _{eq} form – [L-H]	Reference
9.26 [±0.9]	23.43 [±9.7]	17.5 [±13.3] - 26.6 [±14.2]	Michael et al., 1997
Steam Reforming of Methane reaction			
Glucose [L-H]	2-methoxy-4-methylphenol [L-H]	Literature [L-H] – [ER II]	Reference
96.20 [±30.2]	32.55 [±25.3]	70 - 141 [±51.0]	Nikolla et al., 2009; Jarosch et al., 2002
Dry Reforming of Methane reaction			
Glucose [L-H]	2-methoxy-4-methylphenol [L-H]	Literature [L-H] - Stepwise	Reference
78.81 [±10.4]	90.88 [±12.9]	93.2 [±27.9] - 123.2 [±4.7]	Michael et al., 1997

In conclusion, it can be stated that the proposed kinetic model provides sound energies of activations in the case of glucose for WGS, DRM and SRM reactions. This is encouraging because it allows one to argue that model parameters are more than fitting parameters conveying intrinsic reaction information. The proposed model shows however deficiency in the case of 2-methoxy-4-methylphenol for predicting the SRM energy of activation. This discrepancy is assigned to the lack of model accounting of coke species and their evolution during gasification.

9.12 Gasification Kinetic Modeling Results

The experimental and model-predicted values for 2-methoxy-4-methyphenol and glucose, using the intrinsic kinetic parameters reported in Table 21 are shown in Figure 57 through Figure 66.

One important issue to address while this model is applied is the initial conditions for the kinetic calculation given.

Thanks to the principle of operation of the CREC Riser Simulator where reaction time can be changed in a wide range of values, from 5 seconds to 30 seconds, and considering the gas composition at 5 seconds or the shortest reaction time various stoichiometric coefficients in Eq (24) were set at reaction time approaching zero. With this information and the intrinsic kinetic and adsorption parameters established in section 9.7 the various differential equations can be solved numerically.

Numerical solution of this equations show that the proposed kinetic model gives accurate predictions of product permanent gases (H_2 , CO, CO_2 , H_2O and CH_4). Figure 57 through Figure 66 report a reasonably random distribution of the product permanent gases with respect to the 45° perfect agreement case, with this result indicating that all individual products are predicted satisfactorily.

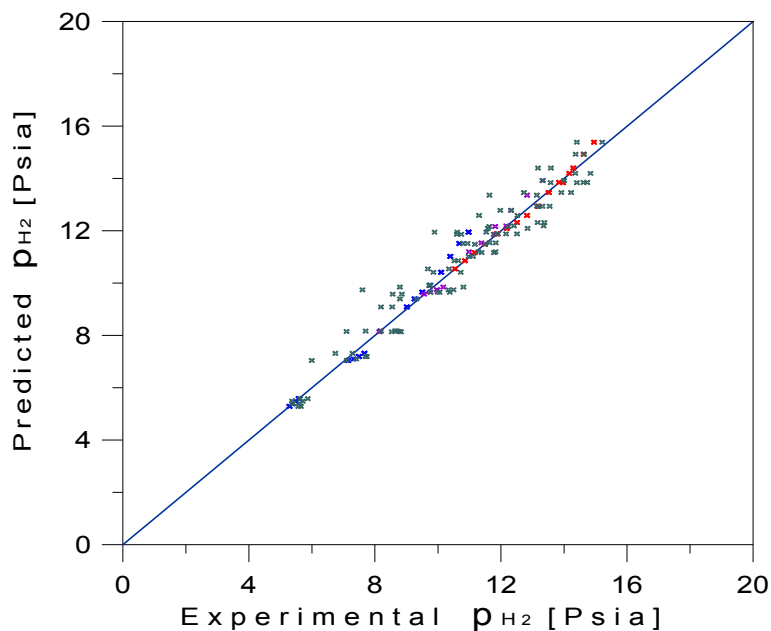


Figure 57. Predicted and experimental hydrogen yields from catalytic steam gasification of 2-methoxy-4-methylphenol over Ni/ α -alumina at various temperatures, residence times, and steam biomass ratios.

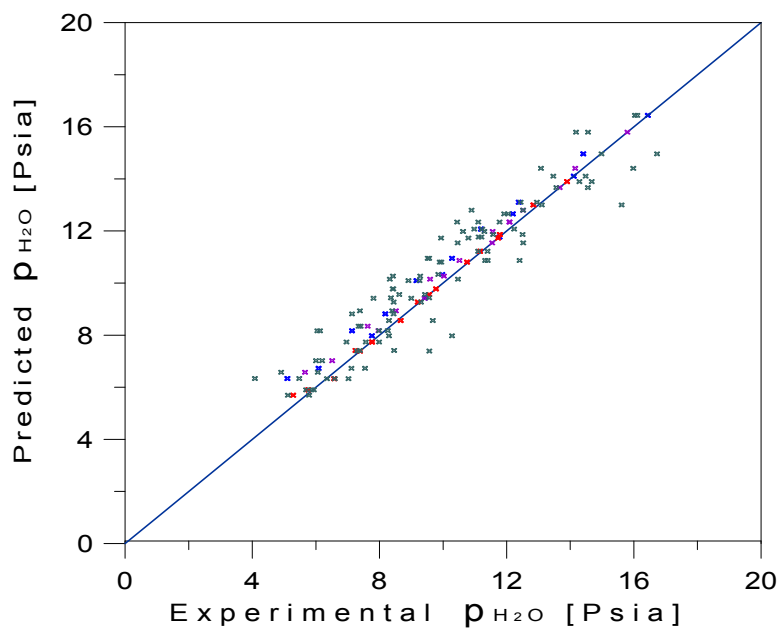


Figure 58. Predicted and experimental water yields from catalytic steam gasification of 2-methoxy-4-methylphenol over Ni/ α -alumina at various temperatures, residence times, and steam biomass ratios.

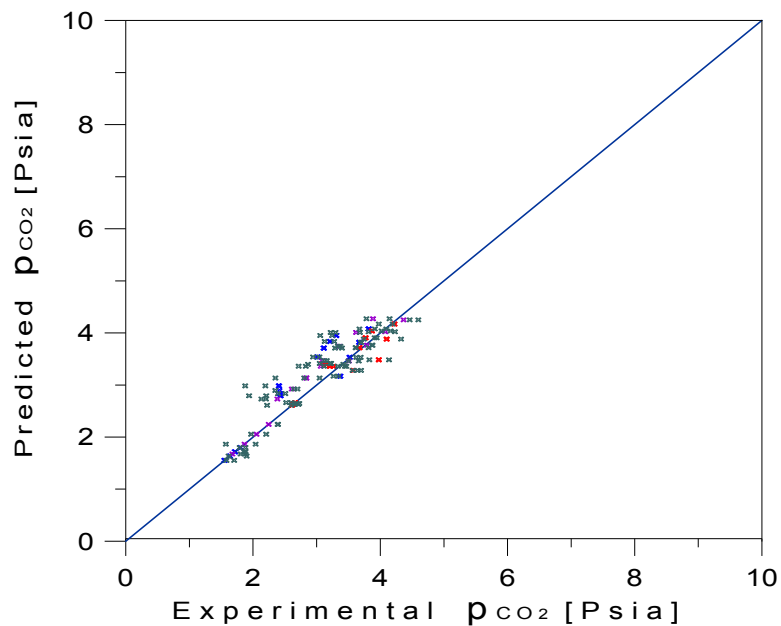


Figure 59. Predicted and experimental carbon dioxide yields from catalytic steam gasification of 2-methoxy-4-methylphenol over Ni/ α -alumina at various temperatures, residence times, and steam biomass ratios.

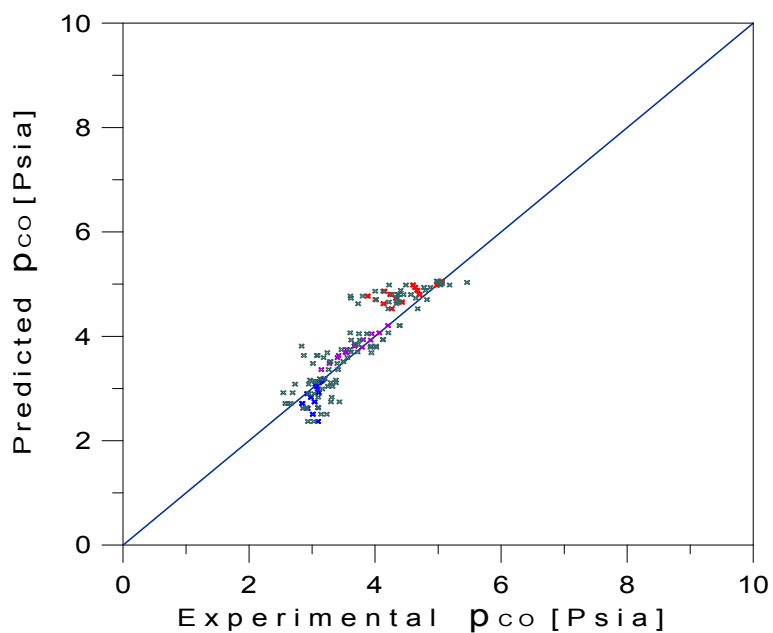


Figure 60. Predicted and experimental carbon monoxide yields from catalytic steam gasification of 2-methoxy-4-methylphenol over Ni/ α -alumina at various temperatures, residence times, and steam biomass ratios.

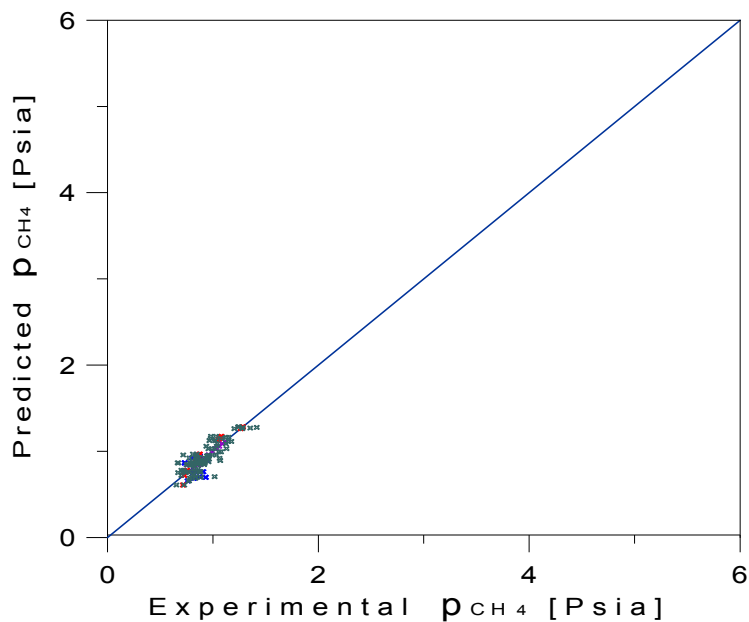


Figure 61. Predicted and experimental methane yields from catalytic steam gasification of 2-methoxy-4-methyphenol over Ni/ α -alumina at various temperatures, residence times, and steam biomass ratios.

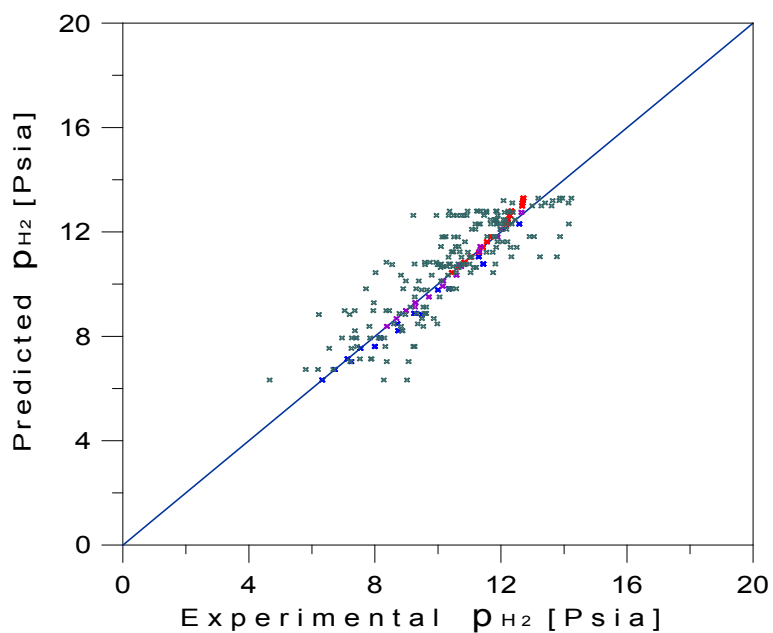


Figure 62. Predicted and experimental hydrogen yields from catalytic steam gasification of glucose over Ni/ α -alumina at various temperatures, residence times, and steam biomass ratios.

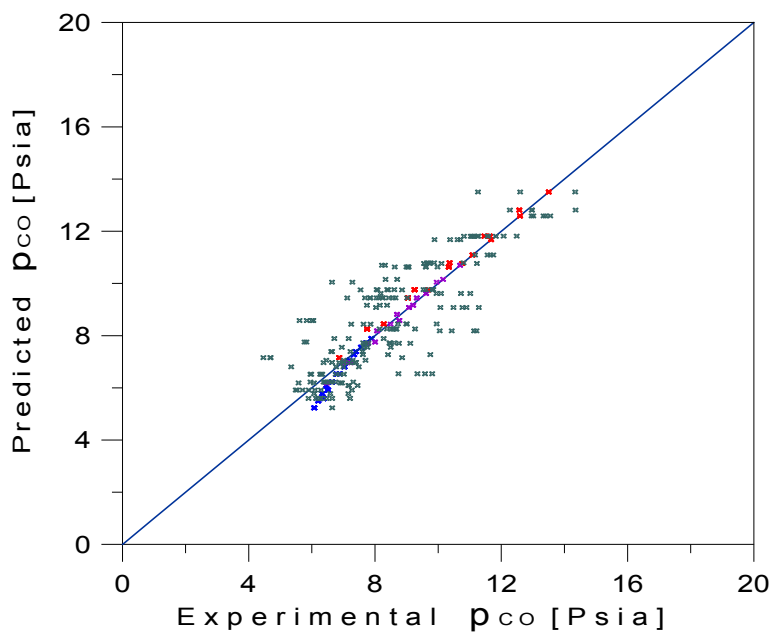


Figure 63. Predicted and experimental carbon monoxide yields from catalytic steam gasification of glucose over Ni/ α -alumina at various temperatures, residence times, and steam biomass ratios.

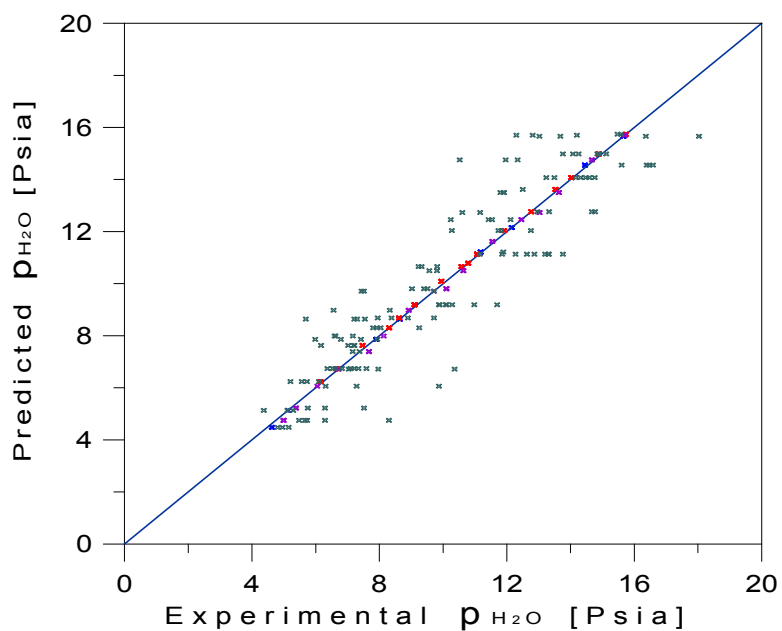


Figure 64. Predicted and experimental water yields from catalytic steam gasification of glucose over Ni/ α -alumina at various temperatures, residence times, and steam biomass ratios.

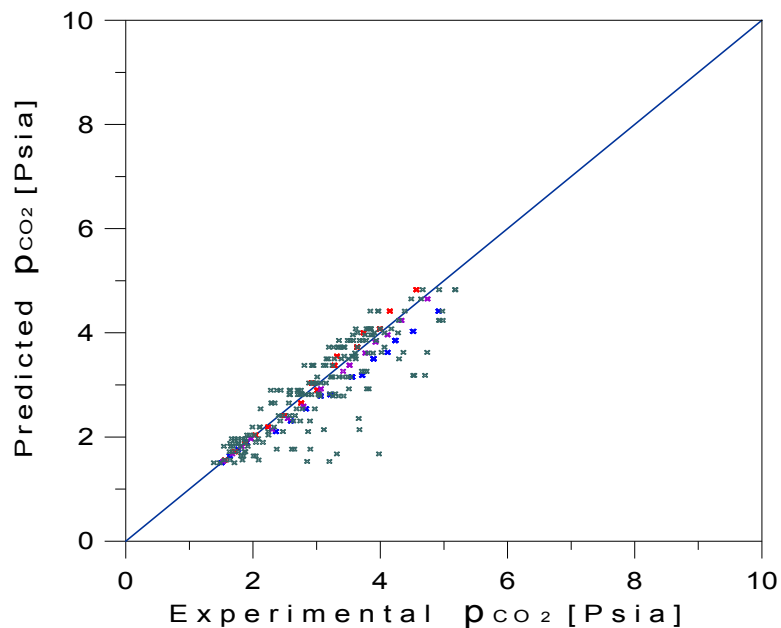


Figure 65. Predicted and experimental carbon dioxide yields from catalytic steam gasification of glucose over Ni/ α -alumina at various temperatures, residence times, and steam biomass ratios.

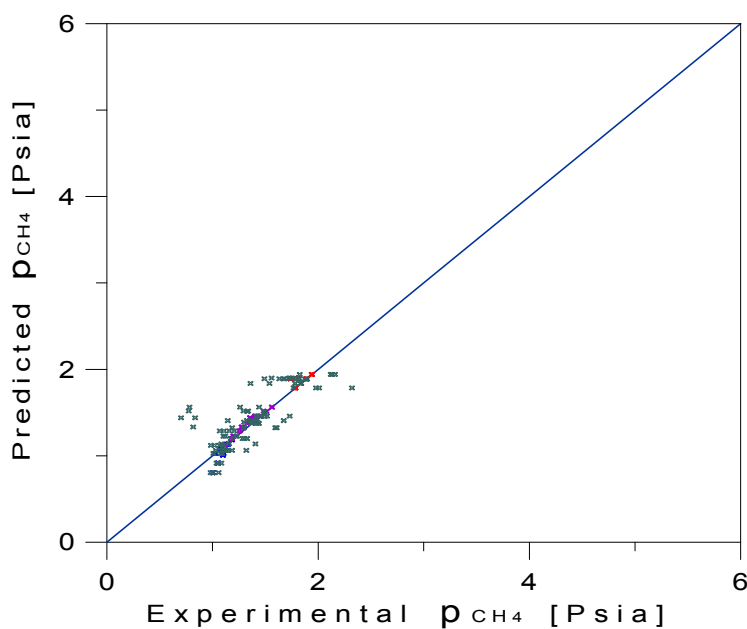


Figure 66. Predicted and experimental methane yields from catalytic steam gasification of glucose over Ni/ α -alumina at various temperatures, residence times, and steam biomass ratios.

On this basis, It can concluded that the set of adsorption and kinetic parameters established is adequate for predicting hydrogen, carbon monoxide, carbon dioxide, methane and water concentrations. It can also be concluded that proposed model can be safely used for prediction of biomass circulating fluidized bed gasifier operation.

9.13 Conclusions

- a. It is shown that a three reaction additive kinetic model is adequate to represent the steam gasification of glucose and 2-methoxy-4-methylphenol over Ni/ α -alumina. The reaction network accounts for all product gases (H_2 , CO, CO_2 , H_2O and CH_4).
- b. It is proven that the experimental-modeling procedure, where intrinsic kinetic parameters and adsorption constants are *decoupled* in their evaluation in the CREC Riser Simulator eliminates overparametrization with successfully parameter correlation.
- c. It is demonstrated that the centred Arrhenius form reduces the correlation between the pre-exponential factor and the activation energy, thereby improving the statistical properties of the estimates for the pre-exponential factors.
- d. It is proven that the resulting energies of activation in the case of glucose are in agreement in their magnitudes with those reported in the literature using single component reactions. This shows the likelihood that the proposed model includes physicochemically based parameters that can be linked to intrinsic reaction kinetics.
- e. It is shown that for the case of 2-methoxy-4-methylphenol gasification while the activation energies for DRM and WGS are satisfactory, for SMR there is discrepancy with literature data. This points to the need of a more elaborate kinetic reaction network where carbon species are accounted for.

Chapter 10 Conclusions and Recommendations

10 Conclusions and Recommendations

This Ph.D. dissertation reports a research study on the catalytic steam gasification of biomass using model compounds. This research allows elucidating the factors inherent to this process such as thermodynamic restrictions and mechanistic reaction steps. The ultimate aim is to establish the chemical reaction engineering tools that will allow the design and operation of large scale fluidized bed units for biomass steam catalytic gasification.

The performance of a prepared nickel supported on α -alumina catalyst towards biomass steam gasification was demonstrated using a CREC Riser Simulator under gasification conditions. The analytical system employed consists of GC, MS and total organic carbon analyzer which was considered the best arrangement to identify and quantify permanent gases and low level of tars and coke. To evaluate the steam gasification performance of the Ni/ α -alumina fluidizable catalyst, glucose was selected as a model compound for representing cellulose while 2-methoxy-4-methylphenol for representing lignin species

10.1 Main Contributions

The following are the most relevant contributions of the present Ph.D. dissertation:

1. It is shown that the CREC Riser Simulator of the present study offers a valuable tool for evaluation of catalytic steam gasification of biomass surrogate reactions. This unit provides minimum temperatures differences inside the reactor at any reaction time, with excellent contacting between catalyst and the vapor phase. The CREC Riser Simulator permits direct sampling of reaction products to the GC/MS, which allows an excellent repeatability of the experimental results.
2. It is proven that the fraction of tar and type of tar formed are closely related with the biomass or the model compound considered to represent the biomass to be gasified. This phenomenon was investigated at different gasification temperature,

SB ratio, catalyst and contact times. While for glucose gasification, there is minimal to no tar formation, for the 2-methoxy-4-methylphenol gasification there considerable amounts of tar obtained along with permanent gases being formed.

3. It is demonstrated that the thermodynamic equilibrium model developed, which involve a set of nine independent reactions is able to represent the molar fraction of various product species in a CREC Riser Simulator catalytic gasification unit for contact time greater than 30 seconds and a wide range of steam/glucose ratios and temperatures
4. It is established that a three reaction “additive” kinetic model is adequate to represent the steam gasification of glucose and 2-methoxy-4-methylphenol over Ni/ α -alumina. The reaction network accounts for all product gases (H₂, CO, CO₂, H₂O and CH₄).
5. It is proven that the experimental-modeling procedure, where intrinsic kinetic parameters and adsorption constants are decoupled in their evaluation in the CREC Riser Simulator eliminates overparametrization with successfully parameter correlation.
6. It is shown that the resulting energies of activation in the case of glucose are in agreement in their magnitudes with those reported in the literature using single component reactions. This shows the likelihood that the proposed model includes physicochemically based parameters that can be linked to intrinsic reaction kinetics.

10.1.1 Related Contributions

The incoming are the related contributions of the research study:

7. It is proven that the Ni/ α -alumina fluidizable displays optimum physical properties for good fluidization, with both weak and strong acid sites and mild total acidity,
8. It is demonstrated with the help of TPR/TPO studies that, the Ni/ α -alumina catalyst displays a single peak of reproducible magnitude centred at approximately 500°C.

This result indicates a reducible phase primarily composed by NiO. It is also shown with pulse chemisorption that nickel crystallite particles do not agglomerate under cyclic reduction-oxidation processes.

9. It is proven with BET analysis that the Ni/ α -alumina catalyst displays a moderate reduction in the total surface area of the catalyst after nickel is loaded on the α -alumina support. The decrease of the surface area is assigned to the plugging of some of the support pores by nickel species.

10.2 Recommendations

Considering the valuable results of this study the following is recommended:

1. The use of a γ -alumina with an appropriate stabilizer such as lanthanum, as suggested by Hossain and de Lasa 2007 for oxygen carrier materials for chemical looping combustion. This support can provide a higher surface area and as a result can increase the catalytic activity of the nickel-based catalyst.
2. A more extensive study is needed to characterize the tar products in more detailed manner. This more extensive study should also involve the kinetics and reaction pathways describing primary tar conversion into secondary and tertiary processes.
3. A more elaborate kinetic reaction network is advisable for the gasification of chemical species such 2-methoxy-4-methylphenol representing lignin and accounting for carbon formation/consumption reactions. This strategy will allow adequate prediction of all activation energies of the relevant gasification reactions

Bibliography

- Abatzoglou, N., Fernandez, J. C., Laramée, L., Jollez, P., Chornet, E., (1997). Application of Gasification to the Conversion of Wood, Urban and Industrial Wastes, *Developments in Thermochemical Biomass Conversion* 2, 960-972.
- Abu El-Rub, Z., Bramer, E. A., and Brem, G., (2004). Review of Catalysts for Tar Elimination in Biomass Gasification Processes. *Industrial & Engineering Chemistry Research* 43 (22), 6911-6919
- Albertazzi, S.; Basile, F.; Brandin, J.; Einvall, J.; Fornasari, G.; Hulteberg, C.; Sanati, M.; Trifirò, F.; Vaccari, A., (2009). Pt-Rh/MgAl(O) Catalyst for the Upgrading of Biomass-Generated Synthesis Gases. *Energy & Fuels* 23 (1), 573-579.
- Aldén, H., Espenäs, B. G., Rensfelt, E., (1988). Conversion of Tar in Pyrolysis Gas from Wood Using a Fixed Dolomite Bed. *Research in Thermochemical Biomass Conversion*, 987–1001.
- Altafini, C. R., Wander P. R., Barreto, R. M., (2003). Prediction of the working parameters of a wood waste gasifier through an equilibrium mode. *Energy Conversion and Management* 44 (17), 2763-2777.
- Antal, M. J., Allen, S. G., Schulman, D., Xu, X., (2000). Biomass Gasification in Supercritical Water. *Industrial & Engineering Chemistry Research* 39 (11), 4040-4053
- Askgaard, T. S., Nørskov, J. K., Ovesen, C. V., Stoltze, P., (1995). A Kinetic Model of Methanol Synthesis. *Journal of Catalysis* 156 (2), 229-242.
- Aznar, M. A., Caballero, M. A., Sancho, J. A., Frances, E., (2006). Plastic Waste Elimination by Co-Gasification with Coal and Biomass in Fluidized Bed with Air in Pilot Plant. *Fuel Processing Technology* 87 (5), 409-420.
- Aznar, M. P., Caballero, M. A., Gil, J., Martín, J. A., Corella, J., (1998). Commercial Steam Reforming Catalysts to Improve Biomass Gasification with Steam-Oxygen Mixtures: Catalytic Tar Removal. *Industrial & Engineering Chemistry Research* 37 (7), 2668-2680.
- Aznar, M. P., Corella, J., Delgado, J., Lahoz, J., (1993). Improved Steam Gasification of Lignocellulosic Residues in a Fluidized Bed with Commercial Steam Reforming Catalysts. *Industrial & Engineering Chemistry Research* 32 (1), 1-10.
- Baker, E. G., Brown, M. D., Elliott, D. C., Mudge, L. K., (1988). Characterization and Treatment of Tars from Biomass Gasifiers. *AIChE Summer National Meeting*, 1-11.
- Baker, E. G., Mudge, L.K., Brown, M. D., (1987). Steam Gasification of Biomass with Nickel Secondary Catalysts. *Industrial & Engineering Chemistry Research* 26 (7), 1335-1339.
- Balat, M., (2009). Bioethanol as a Vehicular Fuel: A Critical Review. *Energy Sources, Part A: Recovery, Utilization, and Environmental Effects* 31 (14), 1242-1255.

- Bangala, D. N., Abatzoglou, N., Chornet, E., (1998). Steam Reforming of Naphthalene on Ni- Cr/Al₂O₃ Catalysts Doped with MgO, TiO₂ And La₂O₃, *AIChE Journal* 44 (4), 927–936.
- Bangala, D. N., Abatzoglou, N., Martin, J. P., Chornet, E., (1997). Catalytic Gas Conditioning: Application to Biomass and Waste Gasification. *Industrial & Engineering Chemistry Research* 36 (10), 4184–4192.
- Banowetz, G. M.; Griffith, S. M.; El-Nashaar, H. M., (2009). Mineral Content of Grasses Grown for Seed in Low Rainfall Areas of the Pacific Northwest and Analysis of Ash from Gasification of Bluegrass (*Poa pratensis* L.) Straw. *Energy & Fuels* 23 (1), 502-506.
- Bartels, M., Lin, W., Nijenhuis, J., Kapteijn, F., Vanommen, J., (2008). Agglomeration in fluidized beds at high temperatures: Mechanisms, detection and prevention *Progress in Energy and Combustion Science* 34 (5), 633-666.
- Bartholomew, C., Weatherbee, G., Jarvi, G., (1980). Effects of Carbon Deposits on the Specific Activity of Nickel and Nickel Bimetallic Catalysts. *Chemical Engineering Communications* 5 (1-4), 125-134.
- Bartholomew, C., Sorensen, W., (1983). Sintering Kinetics of Silica- and Alumina-Supported Nickel in Hydrogen Atmosphere. *Journal of Catalysis* 81 (1), 131-141.
- Boissonnet, G., Bayle, J., Seiler, J. M., Chataing, T., Rouge, S., Bertrand, C., (2003). Comparison of Several Biomass Steam Gasification Routes and Technologies to Produce Hydrogen and Synfuels, First European Hydrogen Energy Conference, Grenoble, France.
- Boissonnet, G., Seiler, J. M., Chataing, T., Claudet, G., Brothier, M., Bertrand, C., (2002). CEA Activities on Biomass Gasification to Produce Synfuels: Pyrolysis and Gasification of Biomass and Waste, Expert Meeting, Strasbourg, France.
- Brown, D., Gassner, M., Fuchino, T., Maréchal, F., (2009). Thermo-economic analysis for the optimal conceptual design of biomass gasification energy conversion systems. *Applied Thermal Engineering* 29 (11-12), 2137-2152.
- Bryden, K. M., Ragland, K. W., Rutland, C. J., (2002). Modeling Thermally Thick Pyrolysis of Wood. *Biomass Bioenergy* 22 (1), 41–53.
- Caballero, M. A., Aznar, M. P., Gil, J., Martin, J. A., Frances, E., Corella, J., (1997). Commercial Steam Reforming Catalysts to Improve Biomass Gasification with Steam-Oxygen Mixtures. 1. Hot Gas Upgrading by the Catalytic Reactor. *Industrial & Engineering Chemistry Research* 36 (12), 5227-5239.
- Callaghan, C. A., Fishtik, I., Datta, R., Carpenter, M., Chmielewski, M., Lugo, A., (2003). An Improved Microkinetic Model for the Water Gas Shift Reaction on Copper. *Surface Science* 541 (1-3), 21-30.
- Campbell, C. T., Daube, K. A., (1987). A Surface Science Investigation of the Water-Gas Shift Reacton on Copper(111). *Journal of Catalysis*. 104 (1), 109-117.

- Chaiwat, W., Hasegawa, I., Mae, K., (2009). Examination of the Low-Temperature Region in a Downdraft Gasifier for the Pyrolysis Product Analysis of Biomass Air Gasification Industrial & Engineering Chemistry Research 48 (19), 8934-8943.
- Chen, H. P., Li, B., Yang, H. P., Yang, G. L., Zhang, S. H., (2008). Experimental investigation of biomass gasification in a fluidized bed reactor. Energy & Fuels 22 (5), 3493-3498.
- Chen, Y., Luo, Y., Wu, W., Su, Y., (2009). Experimental Investigation on Tar Formation and Destruction in a Lab-Scale Two-Stage Reactor. Energy & Fuels 23, 4659-4667
- Choudhary, V., Banerjee, S., Rajput, A. M., (2001). Continuous production of H₂ at low temperature from methane decomposition over Ni-containing catalyst followed by gasification by steam of the carbon on the catalyst in two parallel reactors operated in cyclic manner. Journal of Catalysis 198 (1), 136-141.
- Coll, R., Salvado, J., Farriol, X., Montane, D., (2001). Steam Reforming Model Compounds of Biomass Gasification Tars: Conversion at Different Operating Conditions and Tendency Towards Coke Formation. Fuel Processing Technology 74 (1), 19-31.
- Corella, J., Sanz A., (2005). Modeling Circulating Fluidized Bed Biomass Gasifiers: A Pseudo-Rigorous Model for Stationary State. Fuel Processing Technology 86 (9), 1021– 1053.
- Corella, J.; Aznar, M.; Gil, J.; Caballero, M. A., (1999). Biomass gasification in fluidized bed: Where to locate the dolomite to improve gasification?. Energy & Fuels 13 (6), 1122-1127.
- Corella, J., Aznar, M. P., Delgado, J., Martinez, M. P., Aragües, J. L., (1991). The Deactivation of Tar Cracking Stones (Dolomites, Calcites, Magnesites) and of Commercial Methane Steam Reforming Catalysts in the Upgrading of the Exit Gas from Steam Fluidized Bed Gasifiers of Biomass and Organic Wastes. Catalyst Deactivation 68 249–252.
- Corella, J., Herguido, J., Alday, F. J., (1988). Pyrolysis and Steam Gasification of Biomass in Fluidized Beds: Influence of the Type and Location of the Biomass Feeding Point on the Product Distribution. Research in Thermochemical Biomass Conversion, 384–398.
- Corella, J., Herguido, J., González-Sáiz, J., (1989). Steam Gasification of Biomass in Fluidized Bed: Effect of the Type of Feedstock. Pyrolysis and Gasification, 618–623.
- Corella, J., Toledo, J. M., Molina, G., (2007). A review on dual fluidized-bed biomass gasifiers. Industrial & Engineering Chemistry Research 46 (21), 6831-6839.
- CRE Group Ltd., (1997). Identification and Processing of Biomass Gasification Tars, Energy Technology Support Unit (ETSU), Department of Trade and Industry, DTI Contract No. B/T1/00418/00/00.

- Dalai, A. K., Sasaoka, E., Hikita, H., Ferdous, D., **(2003)**. Catalytic Gasification of Sawdust Derived from Various Biomass. *Energy & Fuels* 17 (6), 1456-1463.
- de Lasa, H., Riser Simulator for Catalytic Cracking Studies, Canadian Patent #1,284,017, **(1991)**. U.S. Patent # 5,102,678, **(1992)**.
- Demirbas, A. , **(2004)**. Trace element concentrations in ashes from various types of lichen biomass species. *Energy Sources* 26 (5), 499-506.
- Devi, L.; Ptasiniski, K. J.; Janssen, F. J., **(2003)**. A review of the primary measures for tar elimination in biomass gasification processes. *Biomass and Bioenergy* 24 (2), 125-140.
- Dhepe, P. L., Fukuoka, A., **(2008)**. Cellulose Conversion under Heterogeneous Catalysis . *ChemSusChem* 1 (12), 969-75.
- Di Blasi, C., **(2000)**. Dynamic Behaviour of Stratified Downdraft Gasifiers. *Chemical Engineering Science* 55 (15), 2931–2944.
- Dibbern, H., Olesen, P., Rostrup-Nielsen, J., Tottrup, P., and Udengaard, N., **(1986)**. Make low H₂/CO syngas using sulfur passivated reforming. *Hydrocarbon Processing* 65 (1), 71-74.
- Ekström, C., Lindman, N., Pettersson, R., **(1985)**. Catalytic Conversion of Tars, Carbon Black and Methane from Pyrolysis/Gasification of Biomass. *Fundamentals of Thermochemical Biomass Conversion*, 601–618.
- El Solh, T., **(2002)** Dry Reforming of Methane in a Fast Fluidized Bed Reactor Catalysis and Kinetics, PhD thesis, The University of Western Ontario, London, Ontario.
- El Solh, T., Jarosch, K., de Lasa, H., **(2001)** Fluidizable Catalysts for Methane Steam Reforming. *Applied Catalysis A-General* 210 (1-2), 315-324.
- Elliott, D. C., **(1986)**. Analysis and Comparison of Biomass Pyrolysis/Gasification Condensates— Final Report, Richland, WA: Battelle Memorial Institute. Biofuels and Municipal Waste Technology Division, PNL-5943.
- Elliott, D. C., **(1988)**. Relation of Reaction Time and Temperature to Chemical Composition of Pyrolysis Oils, ACS Symposium Series 376. *Pyrolysis Oils from Biomass*.
- Elliott, D. C., Baker, E. G., Butner, R. S., and Sealock, L. J. **(1993)**. Bench-Scale Reactor Tests of Low Temperature, Catalytic Gasification of Wet Industrial Wastes. *Journal of Solar Energy Engineering*, 115 (1), 52-56
- Englezos, P., Kalogerakis, N., **(2001)**. *Applied Parameter Estimation for Chemical Engineers*, Marcel Dekker, Inc. New York.
- Evans, R. J., Milne, T. A., **(1987)a**. Molecular Characterization of the Pyrolysis of Biomass. 1. Fundamentals. *Energy & Fuel* 1 (2), 123–138.
- Evans, R. J., Milne, T. A., **(1987)b**. Molecular Characterization of the Pyrolysis of Biomass. 2. Applications. *Energy & Fuels* 1 (4), 311–319.

- Evans, R. J., Milne, T. A., (1997). Chemistry of Tar Formation and Maturation in the Thermochemical Conversion of Biomass. *Developments in Thermochemical Biomass Conversion* 2, 803-816.
- Fagbemi, L., Khezami, L., Capart, R., (2001). Pyrolysis products from different biomasses: application to the thermal cracking of tar. *Applied Energy* 69 (4), 293-306.
- Fiaschi, D., Michelini, M., (2001). A Two-Phase One-Dimensional Biomass Gasification Kinetics Model. *Biomass and Bioenergy* 21 (2), 121-132.
- Fishtik, I., Datta, R., (2002). A UBI-QEP Microkinetic Model for the Water-Gas Shift Reaction on Cu(111). *Surface Science* 512 (3), 229-254.
- Flanigan, V. J., Sitton, O. C., Huang, W. E., (1988). The Development of a 20-Inch Indirect Fired Fluidized Bed Gasifier, Richland, WA: Pacific Northwest Laboratory, PNL-6520, 126.
- Franco, C., Pinto, F., Gulyurtlu, I., Cabrita, I., (2003). The Study of Reactions Influencing the Biomass Steam Gasification Process. *Fuel* 82 (7), 835-842.
- Gadalla, A. M., and Bower, B., (1988). The Role of Catalyst Support on the Activity of Nickel for Reforming Methane with CO₂. *Chemical Engineering Science* 43 (11), 3049-3062.
- Gaffney, T. R., Golden, T. C., Mayorga, S. G., Brzozowski, J. R., Talyer, F. W. (1999). Carbon Dioxide Pressure Swing Adsorption Process Using Modified Alumina Adsorbents, US Patent 5917136.
- Gao, N., Li, A., Quan, C., (2009). A Novel Reforming Method for Hydrogen Production from Biomass Steam Gasification. *Bioresource technology* 100 (18), 4271-4277.
- Garcia, L., Salvador, M.L., Arauzo, J., Bilbao, R., (1997). Coprecipitated Ni-Al Catalysts in the Pyrolysis and Steam Gasification of Biomass. *Biomass Gasification and Pyrolysis: State of the Art and Future Prospects*, 249-258.
- Garcia, X. A., Alarcon, N. A., Gordon, A. L., (1999). Steam Gasification of Tars Using a CaO Catalyst. *Fuel Processing Technology* 58 (2-3), 83-102.
- Gassner, M., Maréchal, F., (2009). Thermodynamic comparison of the FICFB and Viking gasification concepts *Energy*. 2009, 34 (10), 1744-1753.
- Geldart, D., (1973). Types of gas fluidization. *Powder Technology* 7 (5), 285-292.
- Gil, J., Corella, J., Aznar, M. P., Caballero, M. A., (1999). Biomass Gasification in Atmospheric and Bubbling Fluidized Bed: Effect of the Type of Gasifying Agent on the Product Distribution. *Biomass and Bioenergy* 17 (5), 389-403.
- Ginsburg, J., de Lasa, H., (2005). Catalytic Gasification of Biomass in CREC Fluidized Riser Simulator. *International Journal of Chemical Reactor Engineering* 3, A38.
- Golden, T. C., Talyer, F.W., Wang, A.W., Kalbassi, M.A., (1997). Base Treated Alumina in Pressure Swing Adsorption. US Patent 5656064.
- Golfier, F., Mermoud, F., Salvador, S., Dirion, J. L., Van de Steene, L., (2004). Modeling of Char Gasification at Particle Scale: How to Select the Best Assumptions in the

Scope of Fixed Bed Modeling, Second world conference on biomass for energy, industry and climate protection, Rome, Italy.

- Gordillo, G., Annamalai, K., Carlin, N., (2009). Adiabatic fixed-bed gasification of coal, dairy biomass, and feedlot biomass using an air-steam mixture as an oxidizing agent. *Renewable Energy* 34 (12), 2789-2797.
- Graham, R. G., Bain, R., (1993). Biomass Gasification: Hot-Gas Clean-Up, International Energy Agency, Biomass Gasification Working Group, 44.
- Gulyurthu, I., Franco, C., Mascarenhas, F., Cabrita, I., (1994). Steam Gasification Versus Fast Pyrolysis to Produce Medium Calorific Value Gaseous Fuel Advances in Thermochemical Biomass Conversion 2, 1187–1196.
- Han, J., Kim, H., (2008). The reduction and control technology of tar during biomass gasification/pyrolysis: An overview. *Renewable and Sustainable Energy Reviews* 12 (2), 397-416.
- Hasler P, Buehler R, Nussbaumer T., (1998). Evaluation of gas cleaning technologies for biomass gasification. 10th European Conference and Technology Exhibition on Biomass for Energy and Industry. Wurzburg, Germany. Biomass for Energy and Industry, 272-275.
- Herguido, J., Corella, J., Gonzalez-Saiz, J., (1992). Steam Gasification of Lignocellulosic Residues in a Fluidized Bed at a Small Pilot Scale: Effect of the Type of Feedstock. *Industrial & Engineering Chemistry Research* 31 (5), 1274-1282.
- Himmelblau, D. M., (1970). *Process Analysis by Statistical Methods*, New York: John Wiley & Sons, Inc.
- Hu, G., Xu, S., Li, S., Xiao, Ch., Liu, S., (2006). Steam Gasification of Apricot Stones with Olivine and Dolomite as Downstream Catalysts. *Fuel Processing Technology* 87 (5), 375 – 382.
- Huber, G. W.; Iborra, S.; Corma, A., (2006). Synthesis of transportation fuels from biomass: Chemistry, catalysts, and engineering. *Chemical Reviews* 106 (9), 4044-4098.
- Hossain, M. M., de Lasa, H. I., (2007). Reactivity and stability of Co-Ni/Al₂O₃ oxygen carrier in multicycle CLC: *AIChE Journal* 53 (7), 1817-1829.
- Jain, R., (1993). *Prepurification of Air for Separation*. US Patent 5232474.
- Jand, N., Brandani, V., and Foscolo, P., (2006). Thermodynamic Limits and Actual Product Yields and Compositions in Biomass Gasification Processes. *Industrial & Engineering Chemistry Research* 45 (2), 834-843.
- Jarosch, K., de Lasa, H., (1999) Novel Riser Simulator for Methane Reforming Using High Temperature Membranes. *Chemical Engineering Science* 54 (10), 1455-1460.
- Jarosch, K., El Soll, T., de Lasa, H., (2002). Modelling the Catalytic Steam Reforming of Methane: Discrimination Between Kinetic Expressions Using Sequentially Designed Experiments. *Chemical Engineering Science* 57 (16), 3439-3451.

- Jönsson, O., (1985). Thermal Cracking of Tars and Hydrocarbons by Addition of Steam and Oxygen in the Cracking Zone. *Fundamentals of Thermochemical Biomass Conversion*. Elsevier Applied Science, 733–746.
- Juutilainen, S. J., Simell, P. A., Krause, A. O. I., (2006). Zirconia: Selective Oxidation Catalyst for Removal of Tar and Ammonia from Biomass Gasification Gas. *Applied Catalysis B-Environmental* 62 (1-2), 86–92.
- Kersten, S. R. A., Prins, W., Van der Drift, A., Van Swaaij, W. P. M., (2002). Interpretation of Biomass Gasification by “Quasi”-Equilibrium Models, Twelfth European Conference on Biomass for Energy, Industry and Climate Protection, Amsterdam, The Netherlands.
- Khan, A., De jong, W., Jansens, P., Spliethoff, H., (2009). Biomass combustion in fluidized bed boilers: Potential problems and remedies. *Fuel Processing Technology* 90 (1), 21-50.
- Khodakov, A. Y., Griboval-Constant, A., Bechara, R., Zholobenko, K.L., (2002). Pore Size Effects in Fischer Tropsch Synthesis over Cobalt-Supported Mesoporous Silicas. *Journal of Catalysis* 206 (2), 230-241
- Kilpinen, P., Hupa, M., Leep alahiti, J., (1991). Nitrogen Chemistry at Gasification ± a Thermodynamic Analysis, Combustion Chemistry Research Group Report 91-14, Abo Academi University, Finland.
- Kinoshita, C. M., Wang, Y., Zhou, J., (1994). Tar Formation under Different Biomass Gasification Conditions. *Journal of Analytical and Applied Pyrolysis* 29 (2), 169–181.
- Kirubakaran, V., Sivaramakrishnan, V., Nalini, R., Sekar, T., Premalatha, M., Subramanian, P., (2009). A review on gasification of biomass. *Renewable and Sustainable Energy Reviews* 13 (1), 179–186
- Klimantos, P., Koukouzas, N., Katsiadakis, A., Kakaras, E., (2009). Air-blown biomass gasification combined cycles (BGCC): System analysis and economic assessment. *Energy* 34 (5), 708-714.
- Knight, R. A., (2000). Experience with Raw Gas Analysis from Pressurized Gasification of Biomass. *Biomass and Bioenergy* 18 (1), 67–77
- Koufopoulos, C. A., Papayannakos, N., (1991). Modelling of the Pyrolysis of Biomass Particles: Studies on Kinetics, Thermal and Heat Transfer Effects. *Canadian Journal of Chemical Engineering* 69 (4), 907–915.
- Lee, W., Nam, S. S., Kim, S. B., Lee, K. W., Choi, C. S., (2000). The Effect of Na_2CO_3 on the Catalytic Gasification of Rice Straw over Nickel Catalysts supported on kieselguhr. *Korean Journal of Chemical Engineering* 17 (2), 174-178.
- Li, X. T., Grace, J. R., Watkinson, A. P., Lim, C. J., Ergudenler, A., (2001). Equilibrium Modeling of Gasification: a Free Energy Minimization Approach and its Application to a Circulating Fluidized Bed Coal Gasifier. *Fuel* 80 (2), 195-207.

- Li, X. T., Grace, J. R., Lim, C. J., Watkinson, A. P., Chen, H. P., Kim, J. R., (2004). Biomass Gasification in a Circulating Fluidized Bed. *Biomass and Bioenergy* 26 (2), 171–193.
- Liao, C.; Wu, C.; Yan, Y., (2007). The characteristics of inorganic elements in ashes from a 1 MW CFB biomass gasification power generation plant. *Fuel Processing Technology* 88 (2), 149-156.
- Ligang, W., Shaoping, X., Zhang, L., Liu, C., Zhu, H., Liu, S., (2007). Steam Gasification of Biomass for Hydrogen-Rich Gas in a Free-Fall Reactor. *International Journal of Hydrogen Energy* 32 (1), 24 – 31.
- Lobachyov, K. V., Richter, H. J., (1998). An Advanced Integrated Biomass Gasification and Molten Fuel Cell Power System. *Energy Conversion Management* 39 (16-18), 1931-1943.
- Lopamudra, D., Krzysztof, J., Ptasinska, F., Janssen, J. J. G., Sander, V. B., Van Paasenb, P., Bergmanb, C. A., Kielb, J. H. A., (2005). Catalytic Decomposition of Biomass Tars: Use of Dolomite and Untreated Olivine. *Renewable Energy* 30, (4) 565–587.
- Luo, S., Xiao, B., Hu, Z., Liu, S., Guo, X., He, M., (2009). Hydrogen-rich gas from catalytic steam gasification of municipal solid waste (MSW): Influence of steam to MSW ratios and weight hourly space velocity on gas production and composition. *International Journal of Hydrogen Energy* 34 (5), 2191-2194.
- Lv, P. M, Chang, J., Wang, T. J., Wu, C. Z., Tsubaki, N., (2004). A Kinetic Study on Biomass Fast Catalytic Pyrolysis. *Energy & Fuels* 18 (6), 1865-1869.
- Ma, D., Lund, C.R.F., (2003). Assessing High-Temperature Water-Gas Shift Membrane Reactors. *Industrial & Engineering Chemistry Research* 42 (4), 711-717.
- Mahishi, M.j, Goswami, D., (2007). Thermodynamic optimization of biomass gasifier for hydrogen production. *International Journal of Hydrogen Energy* 32 (16), 3831-3840.
- Mark, M. F., and Maier, W. F., (1996). CO₂-Reforming of Methane on Supported Rh and Ir Catalysts. *Journal of Catalysis* 164 (1), 122-130.
- Mathieu, P., and Dubuisson, R., (2002). Performance Analysis of Biomass Gasifiers. *Energy Conversion and Management* 43 (9-12), 1291-1299.
- MATLAB version 7.6.0.324 (R2008a). The Mathworks Inc.
- Matsui, I., Kunii, D., Furusawa, T., (1985). Study of Fluidized Bed Steam Gasification of Char by Thermogravimetrically Obtained Kinetics. *Journal of Chemical Engineering of Japan* 18 (2), 105–113.
- McKendry, P., (2002)a. Energy Production from Biomass (part 1): Overview of Biomass. *Bioresource Technology* 83 (1), 37-46.
- McKendry, P., (2002)b. Energy production from biomass (part 2): conversion technologies. *Bioresource Technology* 83 (1), 47-54.

- McKendry, P., (2002)c. Energy production from biomass (part 3): gasification technologies. *Bioresource technology* 83 (1), 55-63
- Melgar, A., Perez, J., Laget, H., Horillo, A., (2007). Thermochemical Equilibrium Modeling of a Gasifying Process. *Energy Conversion and Management* 48 (1), 59-67.
- Michael, F. M., Franz, M., Wilhelm, F. M., (1997). Reaction Kinetics of the CO₂ Reforming of Methane. *Chemical Engineering & Technology* 20 (6) 361-370.
- Milne, A.; Evans, J.; Abatzoglou, N., (1998). Biomass Gasifier “Tars”: Their Nature, Formation and Conversion. NREL/TP-570-25357.
- Millar, G. J., Rochester, C. H., Howe, C., Waugh, K. C., (1991). A Combined Infrared, Temperature Programmed Desorption and Temperature Programmed Reaction Spectroscopy Study of CO₂ and H₂ Interactions on Reduced and Oxidized Silicasupported Copper Catalysts. *Molecular Physics* 76 (4), 833-849.
- Minowa, T., Inoue, S., (1999). Hydrogen Production from Biomass by Catalytic Gasification in Hot Compressed Water. *Renewable Energy* 16 (1-4), 1114-1117.
- Mohan, D., Pittman, C.U., Steele, P.H., (2006). Pyrolysis of wood/biomass for bio-oil: A critical review. *Energy & Fuels* 20 (3), 848-889.
- Mudge, L. K., Baker, E. G., Mitchell, D. H., Brown, M. D. (1985). Catalytic Steam Gasification of Biomass for Methanol and Methane Production. *Journal of Solar Energy Engineering* 107 (1), 88-92.
- Mukunda, H.S.; Dasappa, S.; Paul, P.J.; Rajan, N.K.S.; Shrinivasa, U., (1994)a. Gasifiers and Combustors for Biomass—Technology and Field Studies. *Energy for Sustainable Development* 1 (3), 27–38.
- Mukunda, H. S.; Paul, P. J.; Dasappa, S.; Shrinivasa, U.; Sharan, H.; Buehler, R., Hasler, P.; Kaufmann, H., (1994)b. Results of an Indo-Swiss Programme for Qualification and Testing of a 300-kW IISc-Dasag Gasifier. *Energy for Sustainable Development* 1 (4), 46–49.
- Munir, S., Daood, S., Nimmo, W., Cunliffe, A., Gibbs, B., (2009). Thermal analysis and devolatilization kinetics of cotton stalk, sugar cane bagasse and shea meal under nitrogen and air atmospheres. *Bioresource Technology* 100 (3), 1413-1418.
- Munster, P., Grabke, H., (1981). Kinetics of the Steam Reforming of Methane with Iron, Nickel and Iron–Nickel Alloys as Catalysts. *Journal of Catalysis* 72 (2), 279–287.
- Nagel, F. P., Schildhauer, T. J., McCaughey, N., Biollaz, S. M., (2009). Biomass-integrated gasification fuel cell systems - Part 2: Economic analysis. *International Journal of Hydrogen Energy* 34 (16), 6826-6844.
- Nakamura, J., Campbell, J.M., Campbell, C. T., (1990). Kinetics and Mechanism of the Water-Gas Shift Reaction Catalysed by the Clean and Cs-Promoted Cu (110) Surface: A Comparison with Cu (111). *Journal of the Chemical Society-Faraday Transactions* 86 (15), 2725-2734.

- Narvaez, I., Orio, A., Aznar, M.P., Corella, J., (1996). Biomass Gasification with Air in an Atmospheric Bubbling Fluidized Bed: Effect of Six Operational Variables on the Quality of the Produced Raw Gas. *Industrial & Engineering Chemistry Research* 35 (7), 2110-2120.
- Nieminen, M., Simell, P., Leppälahti, J., Ståhlberg, P., Kurkela, E., (1996). High-Temperature Cleaning of Biomass Derived Fuel Gas, *Biomass for Energy and Environment: Proceedings of the 9th European Bioenergy Conference*, 1080–1085.
- Nikolla, E., Schwank, J., Linic, S., (2009). Comparative study of the kinetics of methane steam reforming on supported Ni and Sn/Ni alloy catalysts: The impact of the formation of Ni alloy on chemistry. *Journal of Catalysis* 263 (2), 220–227
- Olivares, A., Aznar, M. P., Caballero, M. A., Gil, J., Frances, E., Corella, J., (1997). Biomass Gasification: Produced Gas Upgrading by In-Bed Use of Dolomite. *Industrial and Engineering Chemistry Research* 36 (12), 5220–5226.
- Ollis, D. F., Pelizzetti, E., Serpone, N., (1989). *Heterogeneous Photocatalysis in the Environment: Application to Water Purification. Photocatalysis Fundamentals and Applications*, Wiley Interscience, 603.
- Orfao, J., Antunes, J. M., and Figueiredo, J. L., (1999). Pyrolysis Kinetics of Lignocellulosic Materials – Three Independent Reactions Model. *Fuel* 78 (3), 349-358.
- Osowski, S., Fahlenkamp, H., (2006). Regenerative energy production using energy crops. *Industrial Crops and Products* 24 (3), 196-203
- Osowski, S., Neumann, J., Fahlenkamp, H., (2005). Gasification of biogenic solid fuels . *Chemical Engineering & Technology* 28 (5), 596-604.
- Ovesen, C. V., Clausen, B. S., Hammershoi, B. S., Steffensen, G., Askgaard, T., Chorkendorff, I., Norskov, J. T., Rasmussen, P. B., Stoltze, P., Taylor, P., (1996). A Kinetics and Catalysis of the Water-Gas-Shift Reaction: A Microkinetic and Graph Theoretic Approach. *Journal of Catalysis* 158 (1), 170-180.
- Ovesen, C. V., Stoltze, P., Norskov, J. K., Campbell, C. T., (1992). A Kinetic Model of the Water Gas Shift Reaction. *Journal of Catalysis* 134 (2), 445-468.
- Padban, N., (2000). PFB Air Gasification of Biomass: Investigation of Product Formation and Problematic Issues Related to Ammonia, Tar and Alkali, Ph.D. Thesis, Department of Chemical Engineering II, Lund University, Lund, Sweden.
- Pekediz, A., Kraemer, D. W., Chabot, J., deLasa, H. I., (1992). Mixing Patterns in a Novel Riser Simulator. *Applied Sciences* 225, 133-146
- Perez, P. P., Aznar, P. M., Caballero, M. A., Gil, J., Martin, J. A., and Corella, J., (1997). Hot Gas Cleaning and Upgrading with a Calcined Dolomite Located Downstream a Biomass Fluidized Bed Gasifier Operating with Steam – Oxygen Mixtures. *Energy and Fuels* 11 (6), 1194-1203.
- Peters, B., Bruch, C., (2003). Drying and Pyrolysis of Wood Particles: Experiments and Simulation. *Journal of Analytical and Applied Pyrolysis* 70 (2), 1–18.

- Prasad, B., Kuester, J. L., (1988). Process Analysis of a Dual Fluidized Bed Biomass Gasification System. *Industrial and Engineering Chemistry Research* 27 (2), 304-310.
- Pfeifer, C.; Puchner, B.; Hofbauer, H., (2009). Comparison of dual fluidized bed steam gasification of biomass with and without selective transport of CO₂. *Chemical Engineering Science* 64 (23), 5073-5083.
- Proll, T., Rauch, R., Aichernig, C., (2007). Fluidized bed steam gasification of solid biomass - Performance characteristics of an 8 MWth combined heat and power plant. Hofbauer, H. *International Journal of Chemical Reactor Engineering* 5 (A54), 1-19.
- Prokopiev, S., Aristov, Y., Parmon, V., Giordano, N., (1992). Intensification of Hydrogen Production via Methane Reforming and the Optimization of H₂:CO Ratio in a Catalytic Reactor with a Hydrogen Permeable Membrane Wall. *International Journal of Hydrogen Energy* 17 (4), 275-279.
- Pyle, D. L., Zaror, C. A., (1985). Heat Transfer and Kinetics in the Low Temperature Pyrolysis of Solids, *Chemical Engineering Science* 39 (1), 147-158.
- Radmanesh, R., Chaouki, J., Guy, C., (2006). Biomass Gasification in a Bubbling Fluidized Bed Reactor: Experiments and Modeling. *AIChE Journal* 52 (12), 4258-4272.
- Raman, P., Walawender, W. P., Fan, L. T., Chang, C. C., (1981). Mathematical Model for the Fluid-Bed Gasification of Biomass Materials: Application to Feedlot Manure. *Industrial & Engineering Chemistry Process Design and Development* 20 (4), 686-692.
- Rapagna, S., Jand, N., Kiennemann, A., Foscolo, P. U., (2000). Steam-Gasification of Biomass in a Fluidized-Bed of Olivine Particles. *Biomass Bioenergy* 19 (3), 187-197.
- Rapagna, S., Latif, A., (1997). Steam Gasification of Almond Shells in a Fluidized Bed Reactor: The Influence of Temperature and Particle Size on Product Yield and Distribution. *Biomass and Bioenergy* 12 (4), 281-288.
- Rapagna, S., Provendier, H., Petit, C., Kiennemann, A., Foscolo, P. U., (2002). Development of Catalysts Suitable for Hydrogen or Syngas Production from Biomass Gasification. *Biomass and Bioenergy* 22 (5), 377-388.
- Rhodes, C., Hutchings, G.J., Ward, A.M., (1995). Water-Gas Shift Reaction: Finding the Mechanistic Boundary. *Catalysis Today* 23 (1), 43-58.
- Rostrup-Nielsen, J., (1993). Production of Synthesis Gas. *Catalysis Today* 18 (4), 305-324.
- Rostrup-Nielsen, J., (1997). Industrial relevance of coking. *Catalysis Today* 37 (3), 225-232.
- Rostrup-Nielsen, J., Hansen, J. B., (1993). CO₂-Reforming of Methane over Transition Metals. *Journal of Catalysis* 144 (1), 38-49.

- Ruggiero, M., and Manfrida, G., (1999). An Equilibrium Model for Biomass Gasification Processes. *Renewable Energy* 16 (1-4), 1106-1109.
- Salaices, E., Serrano, B., de Lasa, H., (2010). Biomass Catalytic Steam Gasification Thermodynamics Analysis and Reaction Experiments in a CREC Riser Simulator. *Industrial & Engineering Chemistry Research* 49 (15)5, 6834-6844.
- Schumacher, N., Boisen, A., Dahl, S., Gokhale, A. A., Kandoi, S., Grabow, L. C., Dumesic, J. A., Mavrikakis, M., Chorkendorff, I., (2005). Trends in Low-Temperature Water-Gas Shift Reactivity on Transition Metals. *Journal of Catalysis*, 229 (2), 265-275.
- Schuster, G., Loffler, G., Weigl, K., and Hofbauer, H., (2001). Biomass Steam Gasification – An Extensive Parametric Modeling Study. *Bioresource Technology* 77 (1), 71-79.
- Sedor, K. E., Hossain, M. M., de Lasa, H., (2008). Reactivity and Stability of Ni/Al₂O₃ Oxygen Carrier for Chemical-Looping Combustion (CLC). *Chemical Engineering Science* 63 (11), 2994-3007.
- Sheth, P. N., Babu, B. V., (2009). Experimental studies on producer gas generation from wood waste in a downdraft biomass gasifier *Bioresource technology* 100 (12), 3127-33
- Shido, T., Iwasawa, Y., (1993). The Effect of Co-adsorbates in Reverse Water-Gas Shift Reaction on ZnO, in Relation to Reactant-Promoted Reaction Mechanism. *Journal of Catalysis* 140 (2), 575-584.
- Simell, P. A., Kurkela, E., Ståhlberg, P., (1993). Formation and Catalytic Decomposition of Tars from Fluidized-Bed Gasification. *Advances in Thermochemical Biomass Conversion* 1, 265–279.
- Simell, P. A., Leppalahti, J. K., Bredenberg, J. B., (1992). Catalytic Purification of Tarry Fuel Gas with Carbonate Rocks and Ferrous Materials. *Fuel* 71 (2), 211-218.
- Simmons, G.M., Gentry, M., (1986). Particle Size Limitations Due to Heat Transfer in Determining Pyrolysis Kinetics of Biomass. *Journal of Analytical and Applied Pyrolysis* 10 (2), 117–127.
- Singh, S. K., Walawender, W. P., Fan, L. T., Geyer, W. A., (1986). Steam Gasification of Cottonwood (Branches) in a Fluidized-Bed. *Wood and Fiber Science* 18 (2), 327-344.
- Skoulou, V., Swiderski, A., Yang, W., Zabaniotou, A., (2009). Process characteristics and products of olive kernel high temperature steam gasification (HTSG). *Bioresource technology* 100 (8), 2444-51.
- Smith, J.M., Van Ness, H.C., Abbott, M.M., (1996). Introduction to Chemical Engineering Thermodynamics, fifth Edition. The McGraw-Hill Companies, Inc.
- Sutton, D., Kelleher, B., Ross, J. R., (2001). Review of Literature on Catalysts for Biomass Gasification. *Fuel Processing Technology* 73 (3), 155-173.

- Swami, S. M., Abraham, M. A., (2006). Integrated catalytic process for conversion of biomass to hydrogen Energy & Fuels 20 (6), 2616-2622.
- Tasaka, K.; Furusawa, T.; Tsutsumi, A., (2007). Steam gasification of cellulose with cobalt catalysts in a fluidized bed reactor. Energy & Fuels 21 (2), 590-595.
- Tomishige, K., Asadullah, M., Kunimori, K., (2004). Syngas Production by Biomass Gasification Using Rh/CeO₂/SiO₂ Catalysts and Fluidized Bed Reactor. Catalysis Today 89 (4), 389-403.
- Trimm, D. (1997). Coke formation and minimisation during steam reforming reactions. Catalysis Today 37 (3), 233-238.
- Tserpe, E., Waugh, K. C., (1997). A Microkinetic Analysis of the Reverse Water Gas Shift Reaction. Dynamics of Surfaces and Reaction Kinetics in Heterogeneous Catalysis. Studies in Surface Science and Catalysis 109, 401-416.
- Tsuchida, T., (1993) Preparation of High Surface Area α -Al₂O₃ and its Surface Properties. Applied Catalysis A-General 105 (2), L141-L146.
- Villa, R., Cristiani, C., Groppi, G., Lietti, L., Forzatti, P., Cornaro, U., Rossini, S., (2003) Ni Based Mixed Oxide Materials for CH₄ Oxidation Under Redox Cycle Conditions. Journal of Molecular Catalysis A-Chemical 204, 637-646.
- Walawender, W. P., Hoveland, D. A., Fan, L. T., (1985). Fundamentals of Thermochemical Biomass Conversion. Amsterdam: Elsevier 813-817.
- Waldheim, L., Carpentieri, E., (2001). Update on the Progress of the Brazilian Wood BIG-GT Demonstration Project. Journal of Engineering for Gas Turbines and Power 123 (3), 525-536.
- Warnecke, R., (2000). Gasification of biomass: comparison of fixed bed and fluidized bed gasifier Biomass and Bioenergy 18 (6), 489-497.
- Wang, D., Czernik, S., Chornet, E., (1998). Production of Hydrogen from Biomass by Catalytic Steam Reforming of Fast Pyrolysis Oils. Energy & Fuels 12 (1), 19-24.
- Wang, Y.; Kinoshita, C.M., (1992). Experimental Analysis of Biomass Gasification with Steam and Oxygen. Solar Energy 49 (3), 153-158.
- Wang, S., and Lu, G. Q., (1998)a. Reforming of methane with carbon dioxide over Ni/Al₂O₃ catalysts: Effect of nickel precursor. Applied Catalysis A-General 169 (2), 271-280.
- Wang, S., and Lu, G. Q., (1998)b. CO₂ reforming of methane on Ni catalysts: Effects of the support phase and preparation technique. Applied Catalysis B-Environmental 16 (2), 269-277
- Wang, L.; Weller, C.; Jones, D.; Hanna, M., (2008). Contemporary issues in thermal gasification of biomass and its application to electricity and fuel production. Biomass & Bioenergy 32 (7), 573-581.
- Wang, W. Y., Ye, Z. C., Padban, N., Olofsson, G., Bjerle, I., (2000). Gasification of Biomass/Waste Blends in a Pressurized Fluidized-Bed Gasifier, AACM,

- Proceedings of the First World Conference on Biomass for Energy and Industry, Seville, Spain, 1698–1701.
- Waugh, K.C., (1999). Prediction of Global Reaction Kinetics by Solution of the Arrhenius Parameterised Component Elementary Reactions: Microkinetic Analysis. *Catalyst Today* 53 (2), 161-176.
- Wei, L., Xu, S., Zhang, L., Liu, C., Zhu, H., Liu, S., (2007). Steam Gasification of Biomass for Hydrogen-Rich Gas in a Free-Fall Reactor. *International Journal of Hydrogen Energy* 32 (1), 24-31.
- Wolfesberger, U., Aigner, I., Hofbauer, H., (2009). Tar Content and Composition in Producer Gas of Fluidized Bed Gasification of Wood-Influence of Temperature and Pressure. *Environmental Progress & Sustainable Energy* 28 (3), 372-379.
- Xu, G., Takahiro, M., Toshiyuki, S., Shigeru, K., Toshiro, F., (2005). Distinctive Effects of CaO Additive on Atmospheric Gasification of Biomass at Different Temperatures. *Industrial and Engineering Chemistry Research* 44 (15), 5864-5868.
- Xu, J., and Froment, G., (1989). Methane Steam Reforming, Methanation and Water–Gas Shift: Intrinsic Kinetics. *AIChE Journal* 35 (1), 88–96.
- Yan, Q. H., Guo, L. J., Lu, Y. J., (2006). Thermodynamic Analysis of Hydrogen Production from Biomass Gasification in Supercritical Water. *Energy Conversion and Management* 47 (11-12), 1515-1528.
- Zhang, R., Brown, R. C., Suby, A., and Cummer, K., (2004). Catalytic Destruction of Tar in Biomass Derived Producer Gas. *Energy Conversion and Management* 45 (7-8), 995-1014.
- Zhao, Y., Sun, S., Tian, H., Qian, J., Su, F., Ling, F., (2009). Characteristics of rice husk gasification in an entrained flow reactor. *Bioresource technology* 100 (23), 6040-6044.
- Zhou, J., Masutani, S. M., Ishimura, D. M., Turn, S. Q., Kinoshita, C. M., (2000). Release of Fuel-Bound Nitrogen During Biomass Gasification. *Industrial and Engineering Chemistry Research* 39 (3), 626–634.

Appendix A Volume Calculations

A.1. Volume of the Reactor

The Riser Simulator volume was determined using a mass balance. The volume determined included the reactor volume and the volume of the lines connecting the reactor to the 4-port valve (4PV), as shown in Figure A.1. Once leak tested, the reactor was kept at room temperature ($\sim 22.5^\circ\text{C}$), while a flow of helium was circulated through the system. After 15 minutes, the flow of helium was stopped and the pressure in the reactor was allowed to equilibrate to atmospheric pressure. Then the reactor was sealed by closing the 4PV. Finally, a known amount of air (~ 20.0 ml) was injected into the Riser Simulator using a calibrated gas tight Hamilton syringe. Based on the pressure rise inside the reactor as well as the known amount of air injected, the volume of the reactor could be assessed.

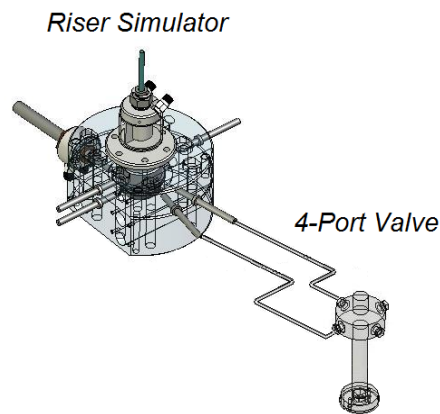


Figure A.1 Volume included in the reactor volume

A mass balance in the reactor and the syringe system can be summarized as follows:

$$m_{s,i} + m_{r,i} = m_{s,f} + m_{r,f} \quad \text{Eq A.1}$$

where:

$m_{s,i}$, initial mass of air contained in the syringe (g)

$m_{r,i}$, initial mass of helium trapped in the reactor (g)

$m_{s,f}$, final mass of air in the syringe after the injection, considered zero (g)

$m_{r,f}$, final mass of air and helium in the reactor after the injection (g)

Substitution of the ideal gas equation in the mass balance gives:

$$m_{s,i} + \frac{P_{r,i} V_r MW_{He}}{R T_r} = m_{s,f} + \frac{P_{r,f} V_r MW_{r,f}}{R T_r} \quad \text{Eq A.2}$$

Solving for the reactor volume yields the following expression:

$$V_r = \frac{m_{s,i} R T_r}{P_{r,f} MW_{r,f} - P_{r,i} MW_{He}} \quad \text{Eq A.3}$$

where:

V_r = reactor volume (cm³)

R = ideal gas constant (1206.3 cm³psia/gmol K)

T_r = reactor temperature (K)

$P_{r,i}, P_{r,f}$ = initial and final reactor pressure, respectively (psia)

MW_{He} = molecular weight of helium (g/gmol)

$MW_{r,f}$ = average molecular weight of mixture, helium and air, in the reactor (g/gmol)

The average molecular weight of the mixture in the reactor can be calculated as follows:

$$MW_{r,f} = \frac{1}{\frac{m_{r,i}}{(m_{r,i} + m_{s,i})} + \frac{m_{s,i}}{(m_{r,i} + m_{s,i})} \frac{MW_{Air}}{MW_{He}}} \quad \text{Eq A.4}$$

Table A.1 Helium and air properties

Molecular formula	Helium (He)	Air
Molar mass	4.0026 g/mol	28.97 g/mol
Density	0.1786 g/L	1.212 Kg·m ⁻³ @ 22.5 C
Boiling point	-268.93°C	-306.00°C

Because the average molecular weight of the mixture in the reactor is a function of the reactor volume, the reactor volume was calculated using an iterative procedure:

1. Guess of an initial V_r value.
2. Calculation of $MW_{r,f}$, equation a4.
3. Calculation of V_r equation a3.

Verify $V_{r,calculated} - V_{r,guessed} = 0$, if not, make $V_{r,guessed} = V_{r,calculated}$ and repeat steps 2 to 4.

Table A.2 summarizes the experimental data obtained following the described procedure.

Table A.2 Experimental data and reactor volume calculation

Observation #	$m_{s,i}$ (g)	T_r (°C)	$P_{r,i}$ (psia)	$P_{r,f}$ (psia)	V_r (cm³)
1	0.024	22.500	14.121	19.916	50.7561
2	0.024	22.500	14.127	19.962	50.4123
3	0.024	22.500	14.133	19.932	50.7175
4	0.024	22.500	14.131	19.974	50.3391
5	0.024	22.500	14.126	19.889	51.0415
6	0.024	22.500	14.126	19.896	50.9776

From the gathered data the following statistics were obtained:

Number of observations, n: 6

Number of degree of freedom, v: 5

Sample mean, x: 50.707

Sample standard deviation, s: 0.286

Then the confidence limits at the 99% confidence interval were established using the Student's t-distribution:

$$\mu = x \pm \left[t_{1-\alpha/2}(\nu) \right] \frac{s}{\sqrt{n}} \quad \text{Eq A.5}$$

where

μ = true population mean

α = fraction of area under the Student's t-distribution probability curve not included in the confidence interval

At the 99% confidential interval:

$$\mu = 50.707 \pm \left[t_{1-0.05/2}(5) \right] \frac{0.286}{\sqrt{6}}$$

From t-distribution tables (Himmelblau, 1970) $t_{1-0.05/2}(5) = 2.571$, thus:

$$\mu = 50.707 \pm 0.30 \text{ cm}^3$$

Hence the reactor volume was found to be $50.707 \pm 0.30 \text{ cm}^3$ at the 95 % confidence interval.

A.2. Volume of the Vacuum Box

The vacuum box volume was also determined by means of a mass balance, similar to the way in which the reactor volume was calculated. The volume of the vacuum box system includes the vacuum chamber, sample loop, Reactor 6PV, GCMS 2010 6PV, and connecting lines, as shown in Figure A.2.

The reactor was prepared in the same way as for the reactor volume determination procedure. The vacuum box was set at room temperature (22.5°C). The Helium flow was stopped and the vacuum pressure was allowed to equilibrate to atmospheric pressure.

Then the reactor was isolated by closing the 4PV. After that, the same amount of air (20 ml) was injected into the vacuum box. From the known amount of air injected, and from the initial and final pressure in the vacuum chamber, the volume of the vacuum box was calculated.

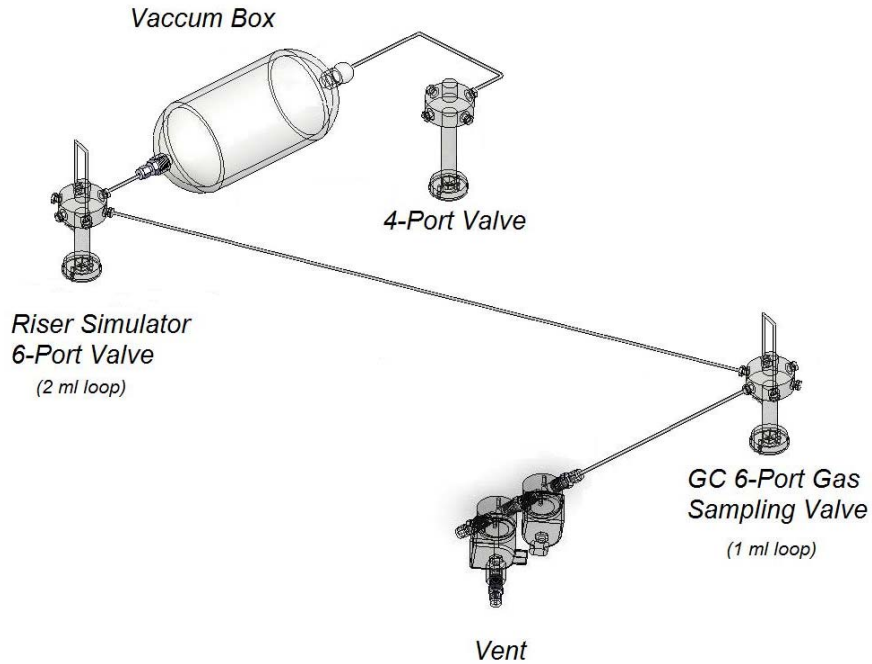


Figure A.2 Volume included in the vacuum box volume

Initially, before the injection of air into the reactor, there was only helium in the system. The total initial mass in the system was the sum of the mass of helium in the reactor and the mass of helium in the vacuum box:

$$m_{T,i} = m_{r,i} + m_{VB,i} \quad \text{Eq A.6}$$

where:

$m_{T,i}$, total initial mass in the system (g)

$m_{r,i}$, initial mass of helium trapped in the reactor (g)

$m_{VB,i}$, initial mass of helium trapped in the vacuum box (g)

The final mass in the system, after the pressure between the reactor and vacuum box reached equilibrium, can be expressed by:

$$m_{T,f} = m_{r,f} + m_{VB,f} \quad \text{Eq A.7}$$

where:

$m_{s,i}$, initial mass of air contained in the syringe (g)

$m_{T,f}$, total final mass in the system (g)

$m_{r,f}$, final mass of acetic acid and helium in the reactor after opening 4PV (g)

$m_{VB,f}$, final mass of acetic acid and helium in the reactor after opening 4PV (g)

The final mass in the system includes the mass of helium and air distributed throughout the system. Thus the difference between the total and initial mass is equal to the mass of air injected into the system:

$$m_{s,i} = m_{T,f} - m_{T,i} \quad \text{Eq A.8}$$

Substitution of the ideal gas equation in the mass balance gives:

$$m_{s,i} = \left(\frac{P_{r,fe} V_r MW_f}{RT_r} + \frac{P_{VB,fe} V_{VB} MW_f}{RT_{VB}} \right) - \left(\frac{P_{r,i} V_r MW_{He}}{RT_r} + \frac{P_{VB,i} V_{VB} MW_{He}}{RT_{VB}} \right) \quad \text{Eq A.9}$$

Finally, the vacuum box volume can be isolated, resulting in the following equation:

$$V_{VB} = \frac{m_{s,i} + \frac{P_{r,i} V_r MW_{He}}{RT_r} - \frac{P_{r,fe} V_r MW_f}{RT_r}}{\frac{P_{VB,fe} MW_f}{RT_{VB}} - \frac{P_{VB,i} MW_{He}}{RT_{VB}}} \quad \text{Eq A.10}$$

where:

V_{VB} = vacuum box volume (cm³)

V_r = reactor volume (cm³)

$m_{s,i}$ = initial mass of air contained in the syringe (g)

R = ideal gas constant (1206.3 cm³psia/gmol K)

T_r = reactor temperature (K)

T_{VB} = vacuum box temperature (K)

$P_{r,i}, P_{VB,i}$ = reactor and vacuum box initial pressures, respectively (psia)

$P_{r,fe}, P_{VB,fe}$ = reactor and vacuum box final pressures after opening 4PV, respectively (psia)

MW_{He} = molecular weight of helium (g/gmol)

MW_f = average molecular weight of mixture, helium and air, in the system
(g/gmol)

The average molecular weight of the mixture in the system is calculated as follows:

$$MW_f = \frac{1}{\frac{m_{r,i} + m_{VB,i}}{MW_{He}} + \frac{m_{s,i}}{MW_{AcAc}}} \quad \text{Eq A.11}$$

Because the average molecular weight of the mixture in the system is a function of the unknown vacuum box volume, the vacuum box volume was calculated using an iterative procedure:

1. Guess of an initial V_{VB} value.
2. Calculation of MW_f , equation a11.
3. Calculation of V_{VB} equation a10.

Verify $V_{VB,calculated} - V_{VB,guessed} = 0$, if not, make $V_{VB,guessed} = V_{VB,calculated}$ and repeat steps 2 to 4.

The experimental data obtained following the described procedure is summarized in Table A.3.

Table A.3 Experimental data and vacuum box volume calculation

Observation #	$m_{s,i}$ (g)	T_{vb} (°C)	$P_{vb,i}$ (psia)	$P_{vb,f}$ (psia)	V_{vb} (cm3)
1	0.0239	22.50	13.9735	14.2413	1098.2065
2	0.0239	22.50	13.9591	14.2267	1098.9795
3	0.0239	22.50	13.9764	14.2438	1099.7320
4	0.0239	22.50	13.9859	14.2552	1092.1800
5	0.0239	22.50	13.9858	14.2532	1099.9212
6	0.0239	22.50	13.9656	14.2321	1103.6125
7	0.0239	22.50	13.9752	14.2431	1097.8638
8	0.0239	22.50	13.9799	14.2476	1098.3570

From the obtained data the following statistics were calculated:

Number of observations, n : 8

Number of degree of freedom, v : 7

Sample mean, \bar{x} : 1098.772

Sample standard deviation, s : 3.728

At the 95% confidential interval:

$$\mu = 1098.772 \pm t_{1-0.05/2}(7) \frac{3.728}{\sqrt{8}}$$

From the t-distribution tables $t_{1-0.05/2}(7) = 2.365$, thus:

$$\mu = 1098.772 \pm 3.117 \text{ cm}^3$$

Thus, the vacuum box volume was found to be $1098.772 \pm 3.117 \text{ cm}^3$ at the 95% confidence interval.

Appendix B Adsorption Isotherms at High Temperatures

B.1. Adsorption of CO₂ on Ni/ α -alumina at High Temperatures

The kinetic modeling of catalytic steam biomass gasification requires the knowledge of adsorption isotherms at various temperatures. Therefore, experimental results of the adsorption of carbon dioxide on alumina and nickel/alumina are particularly interesting for both fundamental and applied research. Unfortunately, data for the adsorption of carbon dioxide on alumina in literature are very scarce (Gaffney et al., 1999, Jain, 1993 and Golden et al., 1997). The aim of this section is to present experimental isotherms of carbon dioxide on Ni/ α -alumina at high temperatures (600, 650 and 700°C).

B.1.2. Experimental Section

B.1.2.1. Materials and Reagents

In this study, a nickel catalyst supported on α -alumina was used. Representative characteristics of this catalyst are reported in Chapter 5. The carbon dioxide pure gas grade 3.0 (99.9 % carbon dioxide, product part CD 3.0) was from Praxair Canada Inc.

B.1.2.2 Apparatus

A schematic diagram of the experimental apparatus for the measurement of single adsorption isotherms is shown in Figure B.1. It has two major sections: the CREC Riser Simulator reactor, and the pressure data acquisition.

The CREC Riser Simulator is a bench scale internal recycle batch reactor. The main reactor body consists of a lower and an upper shell. The lower shell houses a basket that contains catalyst. When the impeller rotates, gas is forced outwards from the center of the impeller towards the walls. This creates a lower pressure region in the center of the reactor which induces an upwards gas flow through the catalyst in the basket. At the proper impeller speed, the gas up-flow intensively fluidizes the catalyst

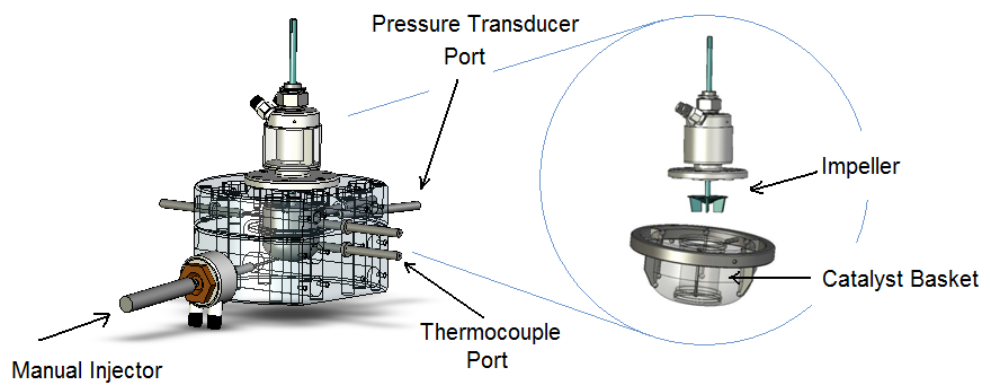


Figure B.1 Schematic of the RECAT CREC Riser Simulator

Mass measurements with 0.01 mg accuracy were performed with a microbalance (A) (CI-Robal, Wilshire, U.K.) in which a cage with samples inside is suspended in one of the arms (B).

A known amount of carbon dioxide was injected into the Riser Simulator using a calibrated gas tight Hamilton syringe. The varying reactor pressure was measured and displayed on an Omega DP series digital pressure display. The currently selected pressure transducers allow pressure readings up to 50 psi. The pressure data was saved on a computer disk using a Personal Daq acquisition card.

B.1.2.3. Procedure

Experiments for the single adsorption isotherms were carried out as follows: one gram of Ni/ α -alumina was introduced into the CREC Riser Simulator's catalyst basket. Once leak tested, the reactor was heated to the desired temperature (600, 650 and 700°C,) while circulating helium throughout the reactor. Once the reactor reached the set temperature, the flow of helium was stopped and the pressure in the reactor was allowed to equilibrate to atmospheric pressure. Then the reactor was sealed. After that, a known amount of carbon dioxide was injected to the Riser Simulator. Based on the pressure rise inside the reactor as well as the known volume of carbon dioxide injected, the total number of moles of carbon dioxide in the system was assessed. The same procedure was carried out with an empty catalyst basket. Table B.1 summarizes the experimental data obtained following the described procedure.

Table B.1 Experimental data for CO₂ adsorption

No - Catalyst				1.0 g - Catalyst		
Run	Pressure [psia]	Tr [°C]	CO ₂ [mol]	Pressure [psia]	Tr [°C]	CO ₂ [mol]
1	3.326	599.8	1.60E-04	3.290	601.9	1.56E-04
2	3.350	600.1	1.61E-04	3.317	599.8	1.58E-04
3	3.386	599.8	1.63E-04	3.331	600.3	1.59E-04
4	3.408	600.3	1.64E-04	3.125	599.8	1.49E-04
5	3.376	600.1	1.63E-04	3.352	600.0	1.60E-04
6	3.355	600.0	1.61E-04	3.319	600.2	1.58E-04
7	3.398	600.1	1.64E-04	3.312	600.1	1.58E-04
8	3.393	599.6	1.63E-04	3.001	600.5	1.43E-04
9	3.421	600.1	1.66E-04	3.392	599.9	1.62E-04
10	3.410	600.1	1.64E-04	3.352	600.0	1.60E-04
1	3.480	650.1	1.58E-04	3.572	650.1	1.61E-04
2	3.527	650.1	1.61E-04	3.540	650.2	1.60E-04
3	3.525	650.1	1.61E-04	3.559	650.1	1.60E-04
4	3.538	650.1	1.61E-04	3.548	650.0	1.60E-04
5	3.547	650.0	1.62E-04	3.544	650.1	1.60E-04
6	3.552	650.1	1.67E-04	3.555	650.3	1.60E-04
7	3.489	650.0	1.59E-04	3.464	650.0	1.56E-04
8	3.5170	650.5	1.60E-04	3.518	650.1	1.59E-04
1	3.745	699.7	1.62E-04	3.646	701.7	1.56E-04
2	3.747	700.2	1.62E-04	3.742	700.1	1.60E-04
3	3.765	700.3	1.63E-04	3.714	700.1	1.59E-04
4	3.804	700.2	1.64E-04	3.695	700.1	1.58E-04
5	3.776	700.7	1.62E-04	3.468	699.9	1.48E-04
6	3.710	699.8	1.60E-04	3.627	700.4	1.55E-04
7	3.788	699.9	1.64E-04	3.674	700.4	1.57E-04

B.1.2.4. Langmuir-Hinshelwood Formulation

During the catalytic adsorption process, a species “A” in the gas phase finds a free site, “S” and adsorbs on the surface forming the “AS” species



where $A_{(g)}$ is the adsorbing gas molecule,

S is an adsorption site, and

AS is the chemisorption complex.

The rate of adsorption can be described as:

$$-r_a = k_a P_a \Theta_v + k_d \Theta_A \quad \text{Eq B.1}$$

where r_a is the rate of adsorption,

k_a is the adsorption constant,

P_a is the partial pressure of the gas,

k_d is the desorption constant,

Θ_v represent the concentration of unoccupied (free) sites, and

Θ_A represents the sites occupied by gas A.

A conservation of total number of sites are assumed

$$1 = \Theta_A + \Theta_v \quad \text{Eq B.2}$$

To describe the adsorption-desorption event, a formulation consistent with a chemisorption isotherm at adsorption-desorption equilibrium is used. As a result of this,

Eq B.1 becomes

$$k_a P_a \Theta_v = k_d \Theta_A$$

$$\Theta_A = \frac{k_a}{k_d} P_a \Theta_v$$

$$\Theta_A = K_A P_a \Theta_v \text{ with } K_A = \frac{k_a}{k_d} \quad \text{Eq B.3}$$

Substituting Eq B.2 into Eq B.3, we have:

$$\Theta_A = K_A P_a (1 - \Theta_A)$$

$$\Theta_A = K_A P_a - \Theta_A K_A P_a$$

$$\Theta_A (1 + K_A P_a) = K_A P_a$$

Finally,

$$\Theta_A = \frac{K_A P_a}{1 + K_A P_a} \quad \text{Eq B.4}$$

At maximum adsorption a monolayer of adsorbate is formed on the catalyst; molecules of adsorbate do not deposit on other, already adsorbed, molecules of adsorbate, only on the free surface of the catalyst.

$$\Theta_A = \frac{V_{ads}}{V_m} \quad \text{Eq B.5}$$

Substituting Eq B.5 into Eq B.4, we have:

$$\frac{V_{ads}}{V_m} = \frac{K_A P_a}{1 + K_A P_a}$$

$$V_{ads} = \frac{K_A P_a V_m}{1 + K_A P_a}$$

$$\frac{1}{V_{ads}} = \frac{1 + K_A P_a}{K_A P_a V_m}$$

$$\frac{1}{V_{ads}} = \frac{1}{V_m} + \frac{1}{K_A V_m} \frac{1}{P_a} \quad \text{Eq B.6}$$

Eq B.6 represents an expression for a straight line. Using the slope one can obtain $\frac{1}{K_A V_m}$,

where K_A and V_m are constants for each adsorbent/adsorbate pair at a given temperature.

The volume of the monolayer (V_m) of the Ni/ α -alumina catalyst was measured using an ASAP 2010 analyzer (from Micromeritics). Before the measurements, samples weighing from 0.15 to 0.2 g were degassed at 643K for 4 h. Adsorption isotherms were measured under the relative pressure range from $\sim 10^{-6}$ to 1.

The Langmuir catalyst surface area (BET) and volume of the monolayer observed were $31.1314 \text{ m}^2/\text{g}$ and $7.151396 \text{ cm}^3/\text{g}$, respectively.

Figure B.2 shows the data obtained during carbon dioxide adsorption experiments in the CREC Riser Simulator at 600°C .

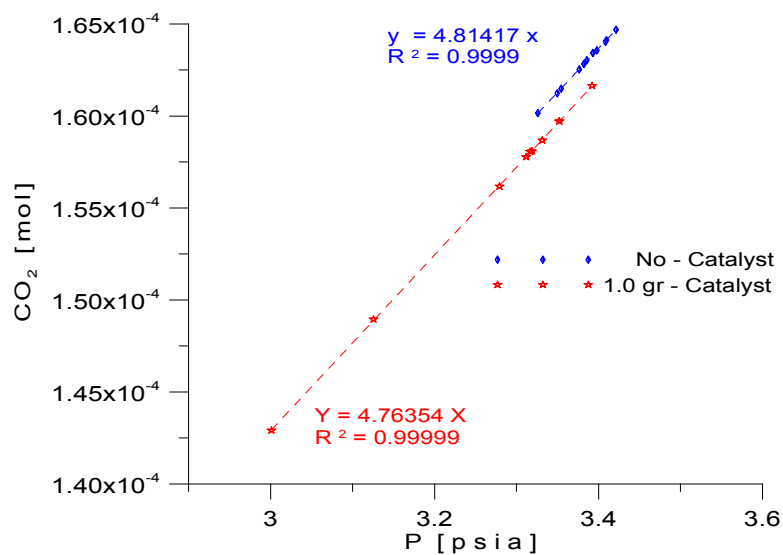


Figure B.2 Carbon dioxide adsorption experiments in the CREC Riser Simulator at 600°C

Linear regression of Figure B.2 gives the adsorption constant of carbon dioxide,

$K_{CO_2}^A$ at 600°C, as follows:

$$V_m = 7.151396 \text{ cm}^3/\text{g STP}$$

$$\text{slope} = \frac{1}{K_A V_m} = 1.533$$

$$K_{CO_2}^A = \frac{1}{(7.151)(1.5329)} = 0.0912 \text{ psia}^{-1}$$

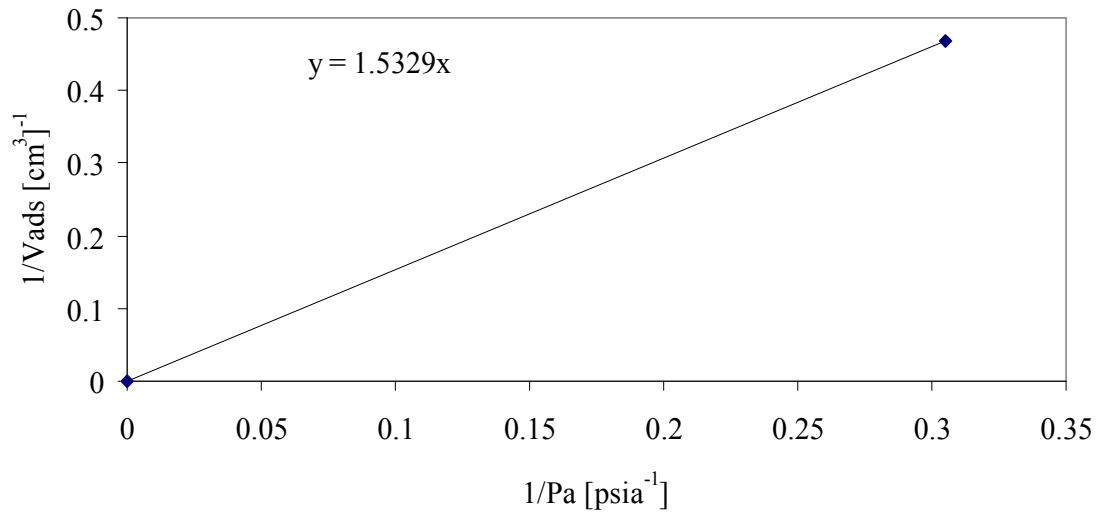


Figure B.3 Linear regression of carbon dioxide adsorption experiments at 600°C

Table B.2 presents the carbon dioxide adsorption constants at 600, 650 and 700°C when one gram of Ni/ α -alumina was introduced into the CREC Riser Simulator's catalyst basket.

Table B.2 Adsorption constant for carbon dioxide as a function of reaction temperature

T [°C]	700	650	600
$K_{CO_2}^A$ ^a	0.0780	0.0843	0.0912

B.2. Adsorption of CH₄ on Ni/ α -alumina at High Temperatures

This study concluded that at high temperatures and using the same procedure than for adsorption of CO₂ on Ni/ α -alumina, there was no evident adsorption of methane on Ni/ α -alumina at 600°C and above. Table B.3 tabulates the findings that support this conclusion.

Table B.3 Experimental data for CH₄ adsorption at 600°C

Run	No - Catalyst			1.0 g - Catalyst		
	Pressure [psia]	T _r [°C]	CH ₄ [mol]	Pressure [psia]	T _r [°C]	CH ₄ [mol]
1	3.380	602.3	1.62E-4	3.430	600.1	0.042
2	3.411	599.8	1.64E-4	3.460	600.1	0.042
3	3.404	599.9	1.64E-4	3.504	600.0	0.042
4	3.416	600.2	1.64E-4	3.493	600.5	0.042
5	3.402	600.1	1.64E-4	3.533	600.0	0.042
6	3.444	600.2	1.66E-4	3.507	600.1	0.042
7	3.424	600.1	1.65E-4	3.560	600.0	0.042

Based on the differences in reactor pressure when no catalyst is used and when 1.0g of catalyst is used for the injection of pure CH₄, this study shows no empirical evidence of CH₄ adsorption on Ni/ α -alumina at temperatures above 600°C.

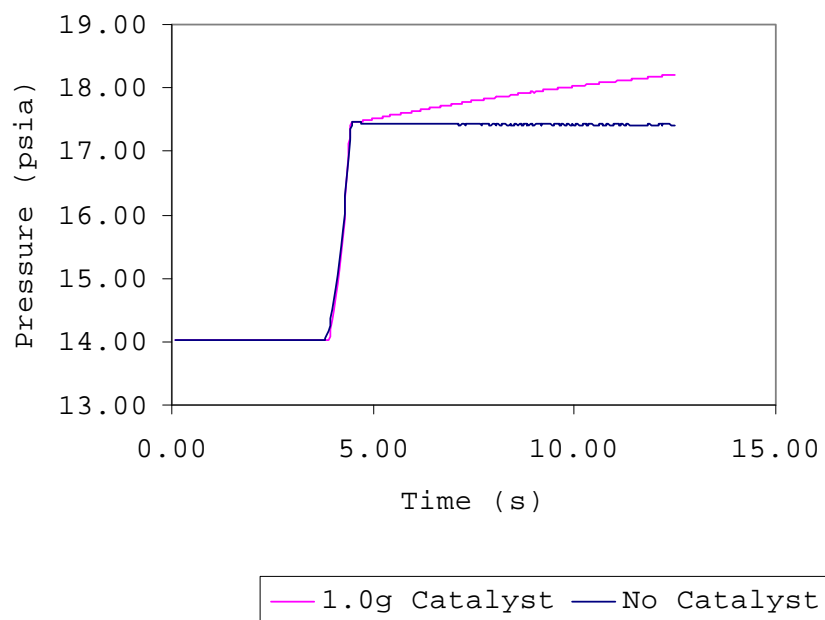


Figure B.4 Pressure profile in CREC Riser Simulator for CH₄ injection at 600°C

Appendix C Calibration Curves

Calibration curves of Hydrogen (H_2), Carbon Monoxide (CO), Carbon Dioxide (CO_2), Methane (CH_4), Ethylene (C_2H_4), Ethane (C_2H_6), Propylene (C_3H_6), Propane (C_3H_8), 1-Butene (C_4H_8), N-Butane (C_4H_{10}), 1-Pentene (C_5H_{10}), N-Pentane (C_5H_{12}), 1-Hexene (C_6H_{12}), and N-Hexane (C_6H_{14}), were carried out using the Shimadzu GC/TCD configuration presented in Figure C.1.

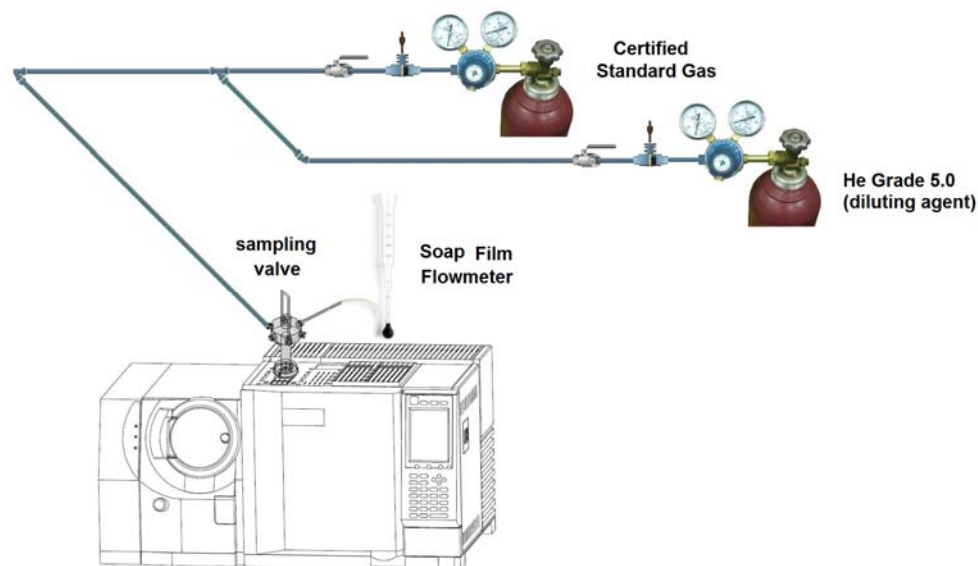


Figure C.1 Shimadzu GC/TCD gas calibration curves configuration

After a certified gas standard was connected to the system, a 1 ml sample of certified gas standard was injected into the Shimadzu GC/TCD through the gas sampling six-port valve (6PV). For different gas concentrations (dilutions with helium), both the certified gas standard and the helium flow were controlled using a micro-regulating valve. The gas flow was measured at the exit of the gas sampling 6PV using a Hewlett Packard Soap Film Flowmeter, which allows accurate calculation of gas flow, by measuring the time it takes a soap film to pass between two marks. The two marks indicate a known volume, and the time of passage allows calculation of volume flow per unit time. Measurements at each gas concentration were repeated at least 10 times to secure reproducibility.

C.1. Calibrated Components

C.1.1. Hydrogen

The hydrogen (H_2) calibration curve that correlates the H_2 concentration with its TCD (Thermal Conductivity Detector) response was determined using: a) Multi-Component Certified Gas Mixture (4.001% H_2 , 5.024% N_2 , 4.986% O_2 , 5.004% CO , 5.006% CO_2 and 4.008% CH_4 , balance gas helium, product part GMT10404TC, Alltech Associates, Inc., a Grace Company), b) Certified Standard Hydrogen (10.0% H_2 Certified concentration balanced with helium, product part HE HY10C-K, Praxair Canada inc), c) Hydrogen Pure Gas Grade 5.0 (99.999 % Hydrogen, product part HY 5.0MF, Praxair Canada inc), and, for different hydrogen dilutions, d) Helium Pure Gas Grade 5.0 (99.999 % Helium Ultra High Purity, product part HE 5.0UF, Praxair Canada inc). A 1 ml gas sample with a known H_2 concentration was injected into the Shimatzu GC/TCD through the 6PV at standard conditions (25°C and 1 atm).

The area corresponding to the injected H_2 , as measured by the TCD allows correlating this hydrogen area with its concentration in moles as it is shown in Figure C.2. The H_2 concentration in the mixture that was injected was varied from 4.0 wt% to 16.8 wt% as it is reported in Table C.1. Measurements at each H_2 concentration were repeated at least 3 times to ensure reproducibility. The H_2 retention time (3.357 min) and detector intensity at different concentrations are presented in Figure C.3.

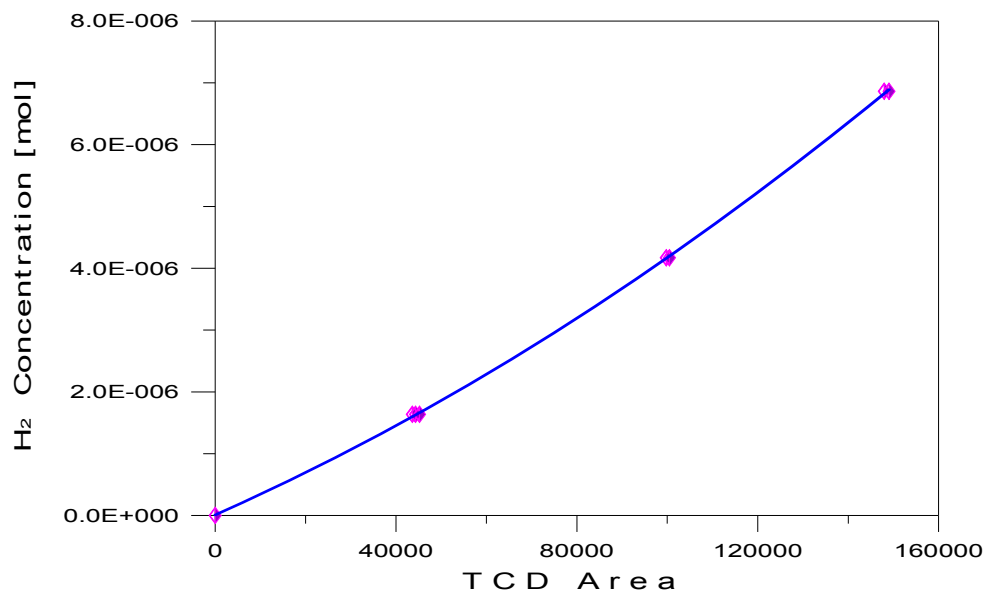
Figure C.2 TCD calibration curve for H₂

Table C.1 CO calibration data

Pressure [atm]				1
Temperature [K]				298.15
Injection No.	1	2	3	
Gas mixture H ₂ Content [%]	4.001	10.200	16.790	
Gas Sample Volume [ml]	1.00	1.00	1.00	
H ₂ moles	1.64E-06	4.17E-06	6.86E-06	
	GC/TCD Area			
Repetition 1	43604.2	97038.7	152353.0	
Repetition 2	44307.0	99769.0	147944.3	
Repetition 3	45208.0	100487.0	149025.0	

Eq C.1 reports the equation for the calibration curve that was obtained from the GC/TCD data. The corresponding coefficient of determination, R^2 , was 0.9999, which indicates that the proposed quadratic model adequately represents the experimental data.

$$y_{H_2} = 9.078^{-11} A^2 + 3.253^{-5} A \quad \text{Eq C.1}$$

where y_{H_2} is the H₂ concentration (mol) and A the TCD area.

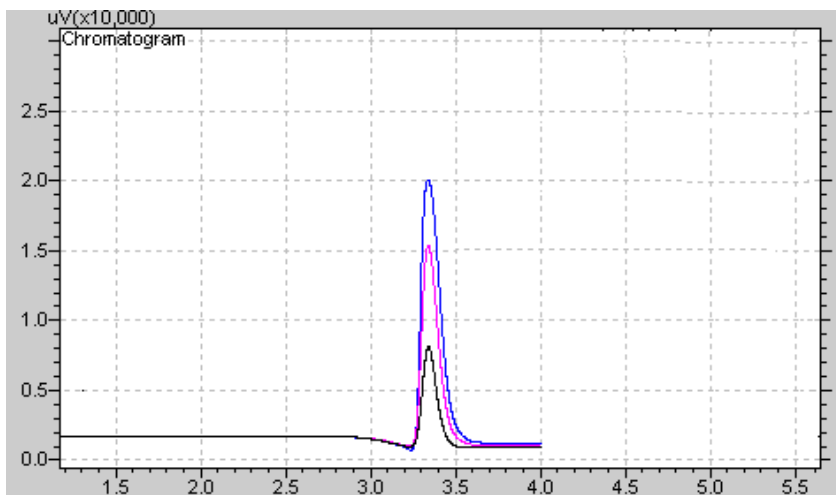


Figure C.3 H₂ retention time and TCD intensity at different H₂ concentrations

C.1.2. Carbon Monoxide

The carbon monoxide (CO) calibration curve was carried out using: a) Multi-Component Certified Gas Mixture (4.001% H₂, 5.024% N₂, 4.986 O₂, 5.004% CO, 5.006% CO₂ and 4.008% CH₄, balance gas helium, product part GMT10404TC, Alltech Associates, Inc., a Grace Company), b) 20.2 % Carbon Monoxide Certified Concentration balanced with Helium, product part HE HY10C-K, Praxair Canada inc), and for different CO dilutions, c) Helium Pure Gas Grade 5.0 (99.999 % Helium Ultra High Purity, product part HE 5.0UF, Praxair Canada inc). A 1 ml gas sample with a known CO concentration was injected to the Shimatzu GC/TCD through the 6PV.

The CO area measured by the TCD is presented in Figure C.4. The CO concentration in the injected mixture was varied from 5.0 wt% to 20.2 wt% as it is reported in Table C.2. The CO retention time (4.882 min) and detector intensity at different concentrations are presented in Figure C.5.

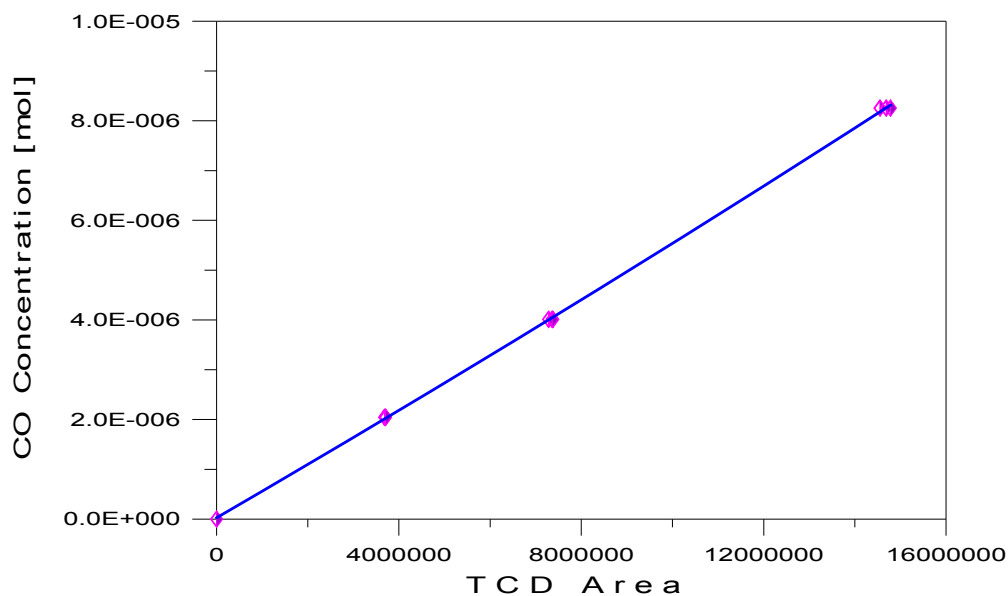


Figure C.4 TCD calibration curve for CO

Table C.2 CO calibration data

Pressure [atm]				1
Temperature [K]				298.15
Injection No.	1	2	3	
Gas mixture CO Content [%]	5.004	9.816	20.200	
Gas Sample Volume [ml]	1.00	1.00	1.00	
CO moles	2.05E-06	4.01E-06	8.26E-06	
	GC/TCD Area			
Repetition 1	3703957.6	7281830.5	14552667.2	
Repetition 2	3686364.0	7374934.0	14686619.0	
Repetition 3	3707626.0	7356785.0	14781556.0	

Eq C.2 reports the equation that represents the calibration curve obtained from the GC/TCD data for CO. The coefficient of determination for this relationship, R^2 , was 0.9999, which verifies that the proposed quadratic model adequately represents the data.

$$y_{CO} = 1.553^{-15} A^2 + 5.372^{-7} A \quad \text{Eq C.2}$$

where y_{CO} is the CO concentration (mol) and A the TCD area.

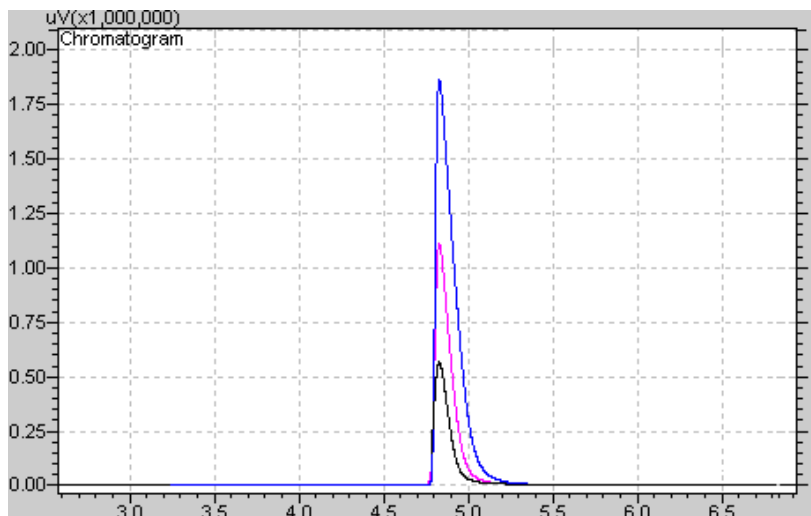
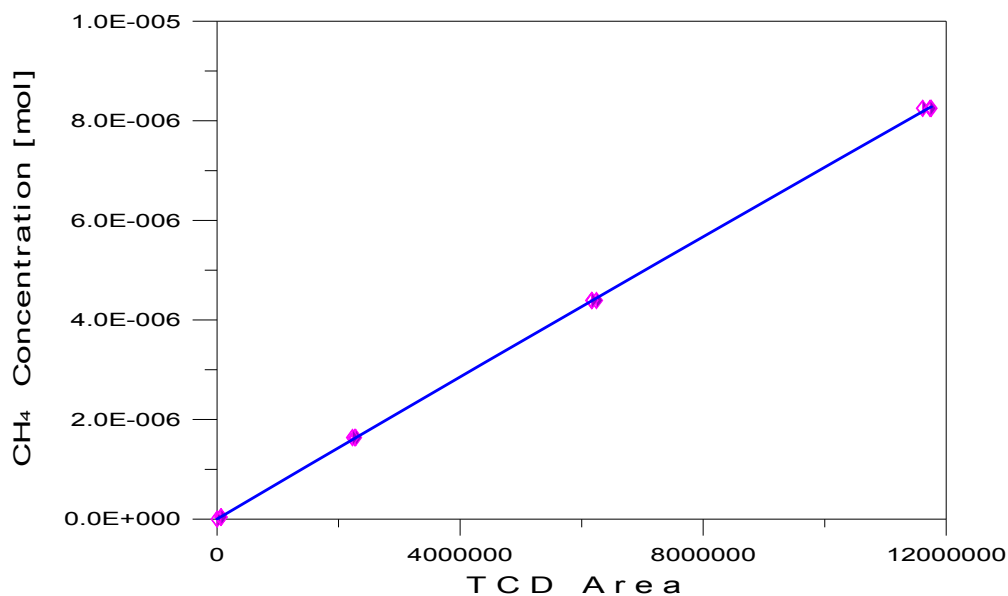


Figure C.5 Retention time and TCD intensity of different CO concentrations

C.1.3. Methane

The methane (CH_4) calibration curve was determined using: a) Multi-Component Certified Gas Mixture (ppm V: 1002 CH_4 , 995 C_2H_6 , 994 C_3H_8 , 1000 C_4H_{10} , 1003 C_5H_{12} , and 988 C_6H_{14} , balance with helium), b) Multi-Component Certified Gas Mixture (4.001% H_2 , 5.024% N_2 , 4.986 O_2 , 5.004% CO , 5.006% CO_2 and 4.008% CH_4 , balance gas helium, product part GMT10404TC, Alltech Associates, Inc., a Grace Company), c) Methane Pure Gas Grade 2.0 (99.0 % Methane, product part ME 2.0, Praxair Canada inc), and for different CH_4 dilutions, d) Helium Pure Gas Grade 5.0 (99.999 % Helium Ultra High Purity, product part HE 5.0UF, Praxair Canada inc). A 1 ml gas sample with a known CH_4 concentration was injected to the Shimadzu GC/TCD through the 6PV at standard conditions (25°C and 1 atm).

The CH_4 area measured by the TCD is displayed in Figure C.6. The concentration of CH_4 in the mixture was varied from 0.1002 wt% to 20.1825 wt% as it is reported in Table C.3. The retention time (7.014 min) and detector intensity for CH_4 at different concentrations are shown in Figure C.7.

Figure C.6 TCD calibration curve for CH₄Table C.3 CH₄ calibration data

Pressure [atm]					1
Temperature [K]					298.15
Injection #	1	2	3	4	
Gas mixture CH ₄ Content [%]	0.1002	4.0080	10.7457	20.1825	
Gas Sample Volume [ml]	1.00	1.00	1.00	1.00	
CH ₄ moles	4.10E-08	1.64E-06	4.39E-06	8.25E-06	
	GC/TCD Area				
Repetition 1	66067.0	2264387.7	6246781.0	11610088.0	
Repetition 2	68724.0	2282403.0	6171727.0	11750493.0	
Repetition 3	63409.0	2229742.0	6164982.0	11734603.0	

Eq C.3 reports the equation that represents the calibration curve obtained from the data pertaining to the GC/TCD area for CH₄. Its coefficient of determination, R^2 , was 0.9999, which indicates that the proposed quadratic model adequately represents the data.

$$y_{CH_4} = 1.010^{-15} A^2 + 1.1809^{-7} A \quad \text{Eq C.3}$$

where y_{CH_4} is the CH₄ concentration (mol) and A the TCD area.

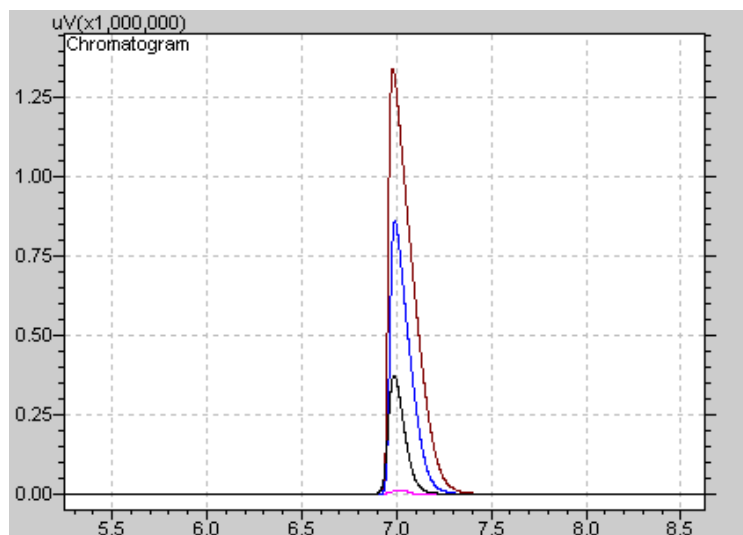
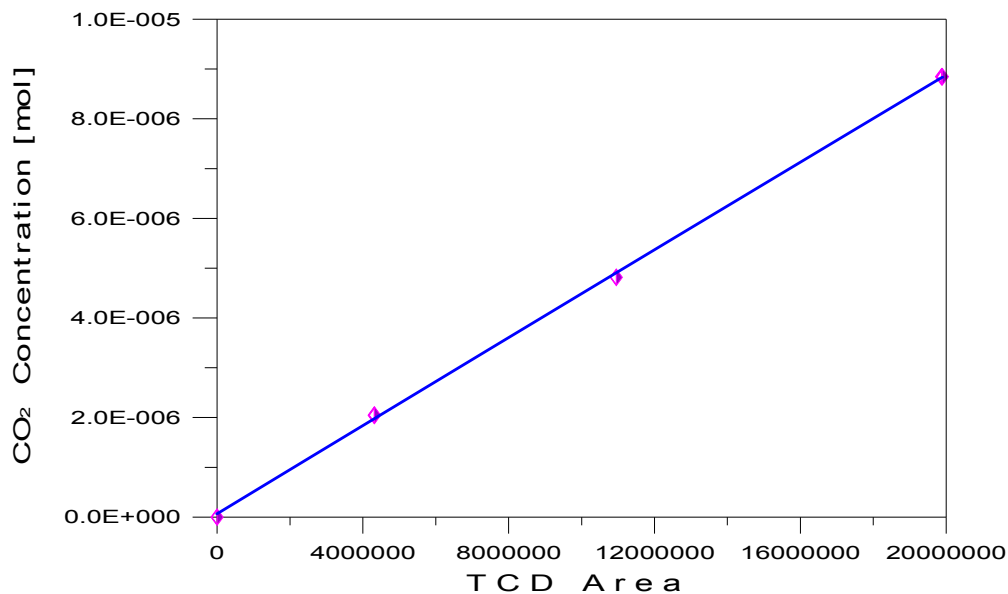


Figure C.7 CH₄ retention times and TCD intensity at different CH₄ concentrations

C.1.4. Carbon Dioxide

The carbon dioxide (CO₂) calibration curve was accomplished using: a) Multi-Component Certified Gas Mixture (4.001% H₂, 5.024% N₂, 4.986 O₂, 5.004% CO, 5.006% CO₂ and 4.008% CH₄, balance gas helium, product part GMT10404TC, Alltech Associates, Inc., a Grace Company), b) Carbon Dioxide Pure Gas Grade 3.0 (99.9 % Carbon Dioxide, product part CD 3.0, Praxair Canada inc), and for different CO₂ dilutions, c) Helium Pure Gas Grade 5.0 (99.999 % Helium Ultra High Purity, product part HE 5.0UF, Praxair Canada inc). A 1 ml gas sample with a known CO₂ concentration was injected to the Shimadzu GC/TCD through the 6PV at standard conditions (25°C and 1 atm).

The CO₂ area measured by the TCD is presented in Figure C.8. The CO₂ concentration in the injected mixture was varied from 5.006 wt% to 21.641 wt% as it is reported in Table C.4. The retention time (9.275 min) and detector intensity for CO₂ at different concentrations are shown in Figure C.9.

Figure C.8 TCD calibration curve for CO₂Table C.4 CO₂ calibration data

Pressure [atm]				1
Temperature [K]				298.15
Injection No.	1	2	3	
Gas mixture CO ₂ Content [%]	5.006	11.779	21.641	
Gas Sample Volume [ml]	1.00	1.00	1.00	
CO ₂ moles	2.05E-06	4.81E-06	8.85E-06	
	GC/TCD Area			
Repetition 1	4292306.9	11389932.3	19774171.1	
Repetition 2	4306853.0	11400329.9	19877331.0	
Repetition 3	4320734.0	10949611.0	19897896.0	

Eq C.4 reports the equation for the calibration curve that was obtained from the GC/TCD data for CO₂. Its coefficient of determination, R^2 , was 0.9994, which indicates that the proposed quadratic model adequately represents the obtained data.

$$y_{CO_2} = 3.0843 \cdot 10^{-16} A^2 + 4.5001 \cdot 10^{-7} A \quad \text{Eq C.4}$$

where y_{CO_2} is the CO₂ concentration (mol) and A the TCD area.

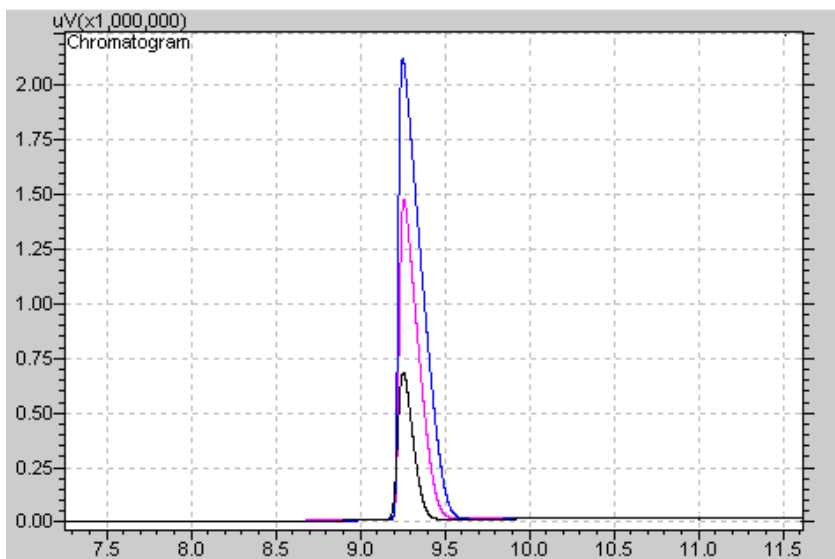
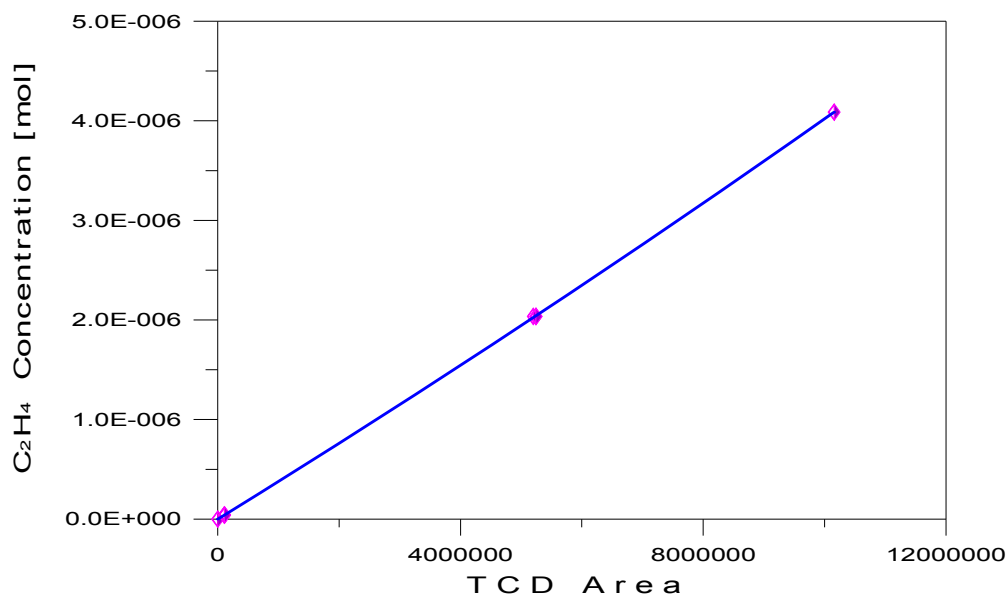


Figure C.9 CO₂ retention time and TCD intensity at different CO₂ concentrations

C.1.5. Ethylene

The ethylene (C₂H₄) calibration curve was determined using: a) Multi-Component Certified Gas Mixture (ppm V: 1003.0 C₂H₄, 1003.0 C₃H₆, 999.2 C₄H₈, 999.9 C₅H₁₀, and 1000.5 C₆H₁₂, balance with helium, product part GMT10358TC, Alltech Associates, Inc., a Grace Company), b) Certified Standard Ethylene (10.0 % Ethylene Certified Concentration balanced with Helium, product part HE EY10C-AS, Praxair Canada inc), and for different C₂H₄ dilutions, c) Helium Pure Gas Grade 5.0 (99.999 % Helium Ultra High Purity, product part HE 5.0UF, Praxair Canada inc). A 1 ml gas sample with a known C₂H₄ concentration was injected into the Shimatzu GC/TCD through the 6PV at standard conditions (25°C and 1 atm).

The C₂H₄ area measured in the TCD is presented in Figure C.10. The C₂H₄ concentration in the injected mixture was varied from 0.1003 wt% to 10.0000 wt% as it is reported in Table C.5. The C₂H₄ retention time (11.839 min) and detector intensity are shown Figure C.11.

Figure C.10 TCD calibration curve for C₂H₄Table C.5 C₂H₄ calibration data

Pressure [atm]				1
Temperature [K]				298.15
Injection No.	1	2	3	
Gas mixture C ₂ H ₄ Content [%]	0.1003	4.9812	10.0000	
Gas Sample Volume [ml]	1.00	1.00	1.00	
C ₂ H ₄ moles	4.10E-08	2.04E-06	4.09E-06	
	GC/TCD Area			
Repetition 1	108703.0	5197620.0	9930235.0	
Repetition 2	108339.1	5244155.0	10107286.1	
Repetition 3	109567.0	5244848.0	10155599.0	

Eq C.5 reports the calibration curve equation obtained from the GC/TCD data for C₂H₄. Its coefficient of determination, R², was 1.0000, which indicates that the proposed quadratic model adequately represents the experimental data.

$$y_{C_2H_4} = 2.9034^{-15} A^2 + 3.7299^{-7} A \quad \text{Eq C.5}$$

where $y_{C_2H_4}$ is the C₂H₄ concentration (mol) and A the TCD area.

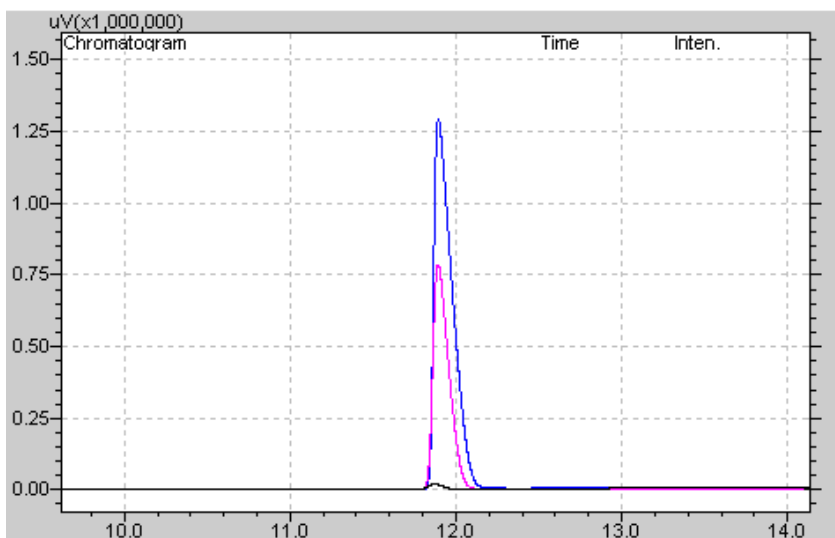


Figure C.11 C_2H_4 retention times and TCD intensity at different C_2H_4 concentrations

C.1.6. Propylene

The propylene (C_3H_6) calibration curve was performed using: a) Multi-Component Certified Gas Mixture (ppm V: 1003.0 C_2H_4 , 1003.0 C_3H_6 , 999.2 C_4H_8 , 999.9 C_5H_{10} , and 1000.5 C_6H_{12} , balance with helium, product part GMT10358TC, Alltech Associates, Inc., a Grace Company), b) Certified Standard Propylene (10.0 % Propylene Certified Concentration balanced with Helium, product part HE EY10C-AS, Praxair Canada inc), and for different C_3H_6 dilutions, c) Helium Pure Gas Grade 5.0 (99.999 % Helium Ultra High Purity, product part HE 5.0UF, Praxair Canada inc). A 1 ml gas sample with a known C_3H_6 concentration was injected into the Shimatzu GC/TCD through the 6PV at standard conditions (25°C and 1 atm).

The C_3H_6 area measured by the TCD is presented in Figure C.12. The C_3H_6 concentration in the injected mixture was varied from 0.1003 wt% to 10.000 wt% as it is reported in Table C.6. The C_3H_6 retention time (15.450 min) and detector intensity are shown Figure C.13.

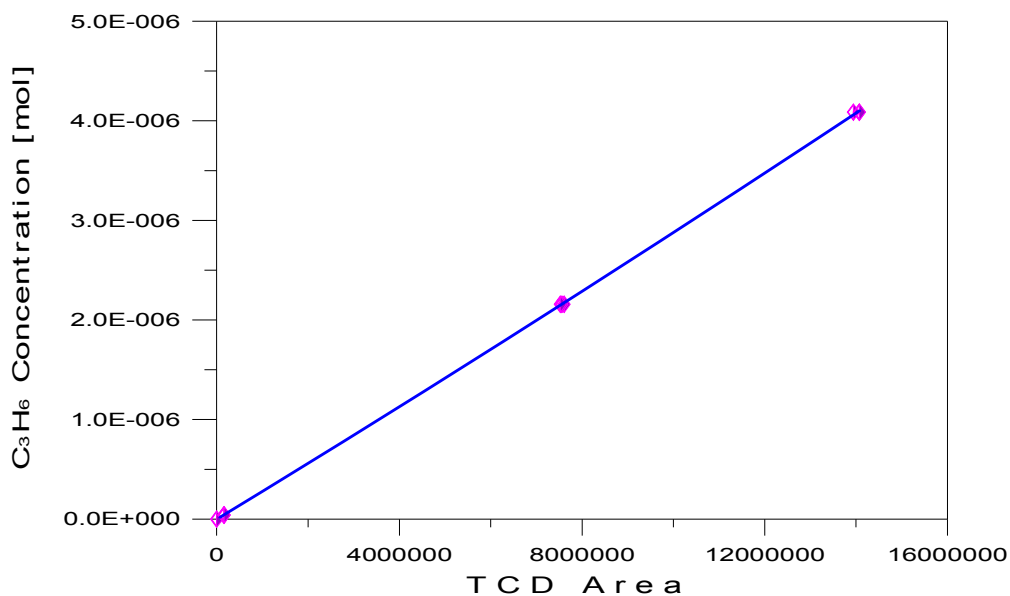


Figure C.12 TCD calibration curve for C_3H_6

Eq C.6 reports the calibration curve obtained from the GC/TCD data for C_3H_6 . Its coefficient of determination, R^2 , was 0.9999, signifying that the proposed quadratic model adequately represents the data.

$$y_{C_3H_6} = 6.3699^{-16} A^2 + 2.8149^{-7} A \quad \text{Eq C.6}$$

where $y_{C_3H_6}$ is the C_3H_6 concentration (mol) and A the TCD area.

Table C.6 C_3H_6 calibration data

Pressure [atm]				1
Temperature [K]				298.15
Injection No.	1	2	3	
Gas mixture C_3H_6 Content [%]	0.1003	5.2812	10.000	
Gas Sample Volume [ml]	1.00	1.00	1.00	
C_3H_6 moles	4.10E-08	2.16E-06	4.09E-06	
	GC/TCD Area			
Repetition 1	163354.0	7604939.7	14068933.9	
Repetition 2	155160.3	7556343.0	13940871.5	
Repetition 3	162917.0	7521953.0	14072840.0	

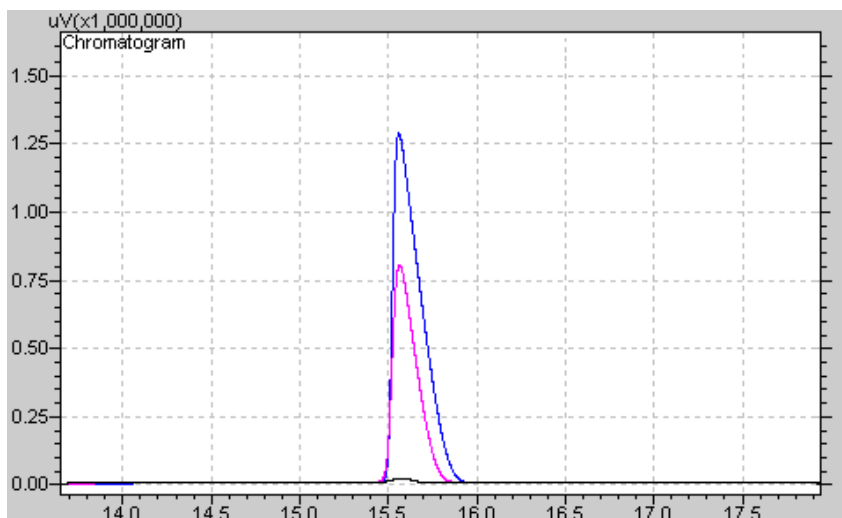


Figure C.13 C_3H_6 retention time and TCD intensity at different C_3H_6 concentrations

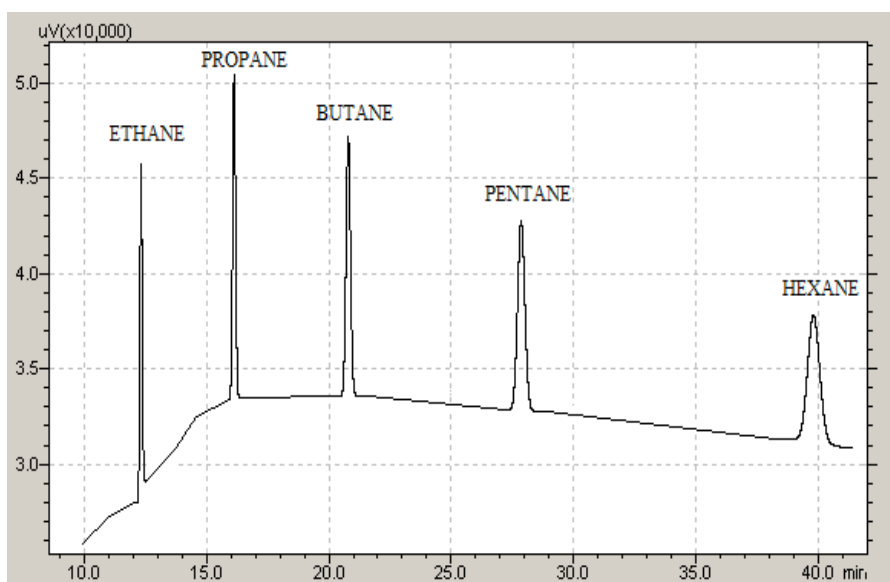
C.1.7. Ethane, Propane, Butane, Pentane, and Hexane

The ethane (C_2H_6), propane (C_3H_8), butane (C_4H_{10}), pentane (C_5H_{12}) and hexane (C_6H_{14}) calibration curves were determined using Multi-Component Certified Gas Mixture (ppm V: 1002 CH_4 , 995 C_2H_6 , 994 C_3H_8 , 1000 C_4H_{10} , 1003 C_5H_{12} , and 998 C_6H_{14} , balance with helium, product part GMT10411TC, Alltech Associates, Inc., a Grace Company) A 1 ml gas sample with a known concentration was injected into the Shimadzu GC/TCD through the 6PV at standard conditions (25°C and 1 atm).

The C_2H_6 , C_3H_8 , C_4H_{10} , C_5H_{12} and C_6H_{14} concentration and areas measured by the TCD are reported in Table C.7 The C_2H_6 , C_3H_8 , C_4H_{10} , C_5H_{12} and C_6H_{14} retention times (12.303, 16.009, 20.781, 27.781, and 39.693 minutes, respectively) and intensities are presented in Figure C.14.

Table C.7 C₂H₆, C₃H₈, C₄H₁₀, C₅H₁₂ and C₆H₁₄ calibration data

Pressure [atm]	1				
Temperature [K]	298.15				
Component	C ₂ H ₆	C ₃ H ₈	C ₄ H ₁₀	C ₅ H ₁₂	C ₆ H ₁₄
Gas mixture content [%]	0.0995	0.0994	0.1000	0.1003	0.998
Gas Sample Volume [ml]	1.00	1.00	1.00	1.00	1.00
Moles	4.07E-08	4.06E-08	4.09E-08	4.10E-08	4.08E-08
	GC/TCD Area				
Repetition 1	113343.3	146987.4	177299.8	206380.3	192711.0
Repetition 2	112281.00	146305.0	174798.0	200294.0	213146.0
Repetition 3	115725.0	144490.0	173823.0	200216.0	190937.0

Figure C.14 C₂H₆, C₃H₈, C₄H₁₀, C₅H₁₂ and C₆H₁₄ retention times and TCD intensities at 1000 ppm.

C.1.8. Butene, Pentene, and Hexene

The butene (C₄H₈), pentene (C₅H₁₀) and hexene (C₆H₁₂) calibration curves were determined using Multi-Component Certified Gas Mixture (ppm V: 1003.0 C₂H₄, 1003.0 C₃H₆, 999.2 C₄H₈, 999.9 C₅H₁₀, and 1000.5 C₆H₁₂, balance with helium, product part

GMT10358TC, Alltech Associates, Inc., a Grace Company), A 1 ml gas sample with a known concentration was injected into the Shimadzu GC/TCD through the 6PV.

The C_4H_8 , C_5H_{10} , and C_6H_{12} concentration and areas measured in the TCD are reported in Table C.8. The C_4H_8 , C_5H_{10} and C_6H_{14} retention times (20.210, 26.883 and 38.294 minutes, respectively) and intensities are presented in Figure C.15.

Table C.8 C_4H_8 , C_5H_{10} , and C_6H_{12} calibration data

Pressure [atm]	1		
Temperature [K]	298.15		
Component	C_4H_8	C_5H_{10}	C_6H_{12}
Gas mixture content [%]	0.09992	0.09999	0.10005
Gas Sample Volume [ml]	1.00	1.00	1.00
Moles	4.08E-08	4.09E-08	4.09E-08
	GC/TCD Area		
Repetition 1	165692.0	174502.0	154202.0
Repetition 2	161947.2	172368.2	157746.0
Repetition 3	163282.0	173680.0	151022.0

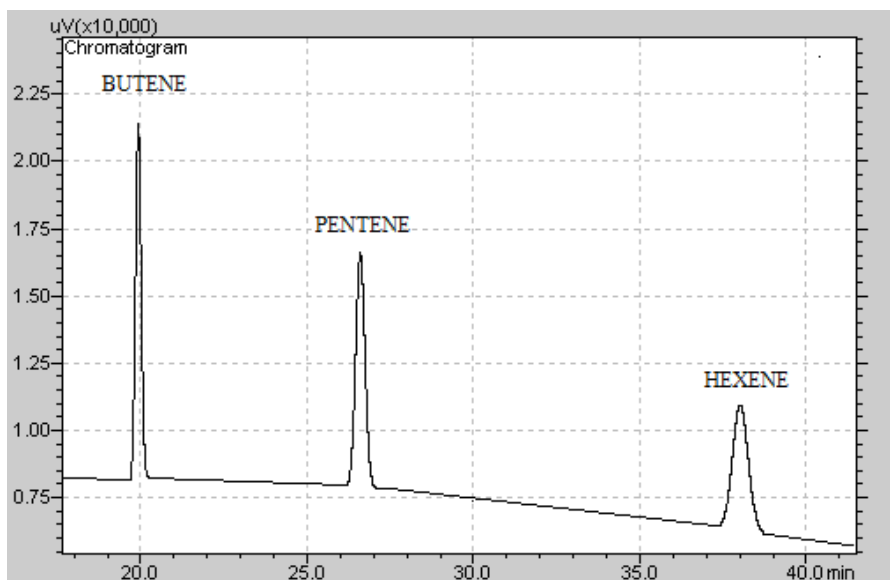


Figure C.15 C_4H_8 , C_5H_{10} , and C_6H_{12} retention time and TCD intensity at 1000 ppm.

C.1.9. Water

For the water (H_2O) calibration curve, the CREC Riser Simulator and the Shimatzu GC/TCD-MS system was used. Once leak tested, the reactor was heated to 150°C while circulating a helium flow through the system. The reactor temperature was well above the boiling point of H_2O (100°C) assuring that the entire sample injected was evaporated. When the reactor reached the set temperature, the flow of helium was stopped and the pressure in the reactor was allowed to equilibrate to atmospheric pressure. Then the reactor was sealed by closing the 4PV.

After that, a known amount of H_2O was injected into the Riser Simulator using a calibrated gas tight Hamilton syringe. After 5 seconds the 4PV valve was opened and the reactor was emptied due to the pressure difference between the reactor and the vacuum box. The CREC Riser Simulator 6PV valve and the Shimatzu GC/TCD gas sampling 6PV, which were initially in the load position, were turned to the inject position to send the gas sample to both the GC/TCD and MS simultaneously.

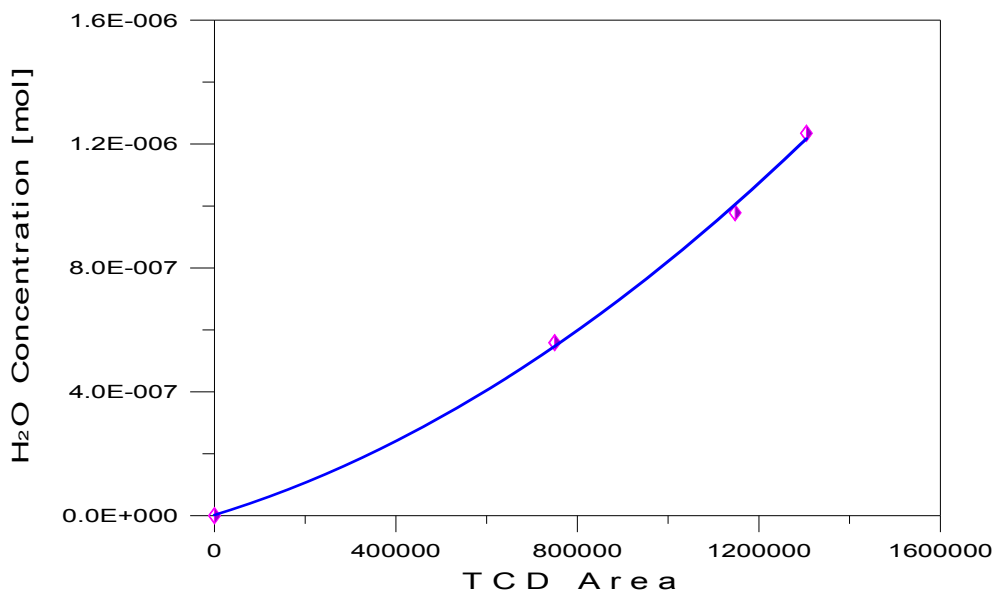


Figure C.16 TCD calibration curve for H_2O

The H_2O area measured by the TCD is shown in Figure C.16. The H_2O mixture was varied from concentrations of $5.59\text{E}-07$ to $1.23\text{E}-06$ moles of H_2O as it is reported in

Table C.9. The H₂O retention time (13.187 min) and detector intensities are shown Figure C.17.

Eq C.7 reports the equation for the calibration curve obtained from the GC/TCD data for H₂O. Its coefficient of determination, R^2 , was 0.9776, with this result indicating that the proposed quadratic model adequately represents the data.

$$y_{H_2O} = 9.3888^{-14} A^2 + 7.9399^{-7} A \quad \text{Eq C.7}$$

where y_{H_2O} is the H₂O concentration (mol) and A the TCD area.

Table C.9 H₂O calibration data

Pressure [atm]	0.2		
Temperature [K]	423.15		
Gas Sample Volume [ml]	1.00	1.00	1.00
H ₂ O moles	5.59E-07	9.78E-07	1.23E-06
	GC/TCD Area		
Average	726547	1147808	1304862

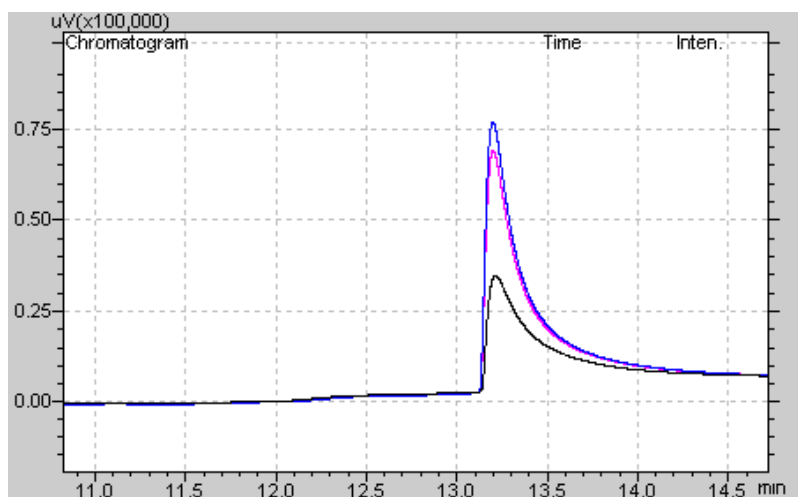


Figure C.17 H₂O retention time and TCD intensity at different H₂O concentrations

Appendix D Thermodynamic Equilibrium Model for Steam Gasification of Biomass

D.1. Introduction

A thermodynamic equilibrium model based on evaluations involving C, H and O element balances and various product species up to C₆ hydrocarbons is reported in this Appendix. This model establishes the effects of biomass composition, temperature, and steam on the various gas product molar fractions. On this basis, the most significant parameters determining the chemical interconversion and distribution of chemical species can be identified.

D.2. Evaluation of Product Species Molar Fraction at Equilibrium

The product species considered for the equilibrium calculations are: H₂, CO, CO₂, H₂O, CH₄, C₂H₄, C₂H₆, C₃H₈, C₄H₁₀, C₅H₁₂, and C₆H₁₄ and the presence of solid carbon. From the elemental analysis of different biomass, it can be shown that the compositions of nitrogen and sulphur species evolving from the reactor are negligible in terms of the equilibrium calculations [(Ginsburg and de Lasa, 2005); (Schuster et al., 2001)]. The formation of tar was neglected in thermodynamic calculations because of its low concentration, although it has to be considered in plant operation. Thus, the simplified overall mass balance for the gasification reaction can be written as follows:

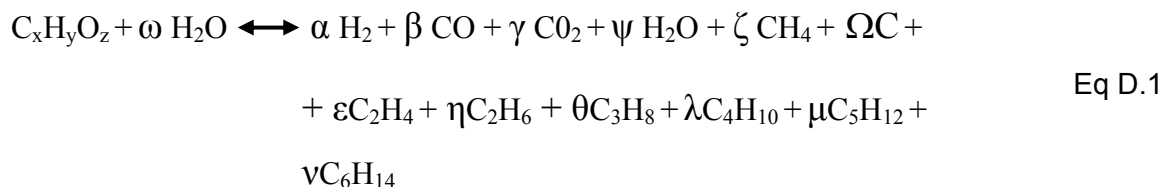


Figure D.1 presents the gas phase reactions occurring after volatilization of the biomass, which are considered to be at equilibrium:

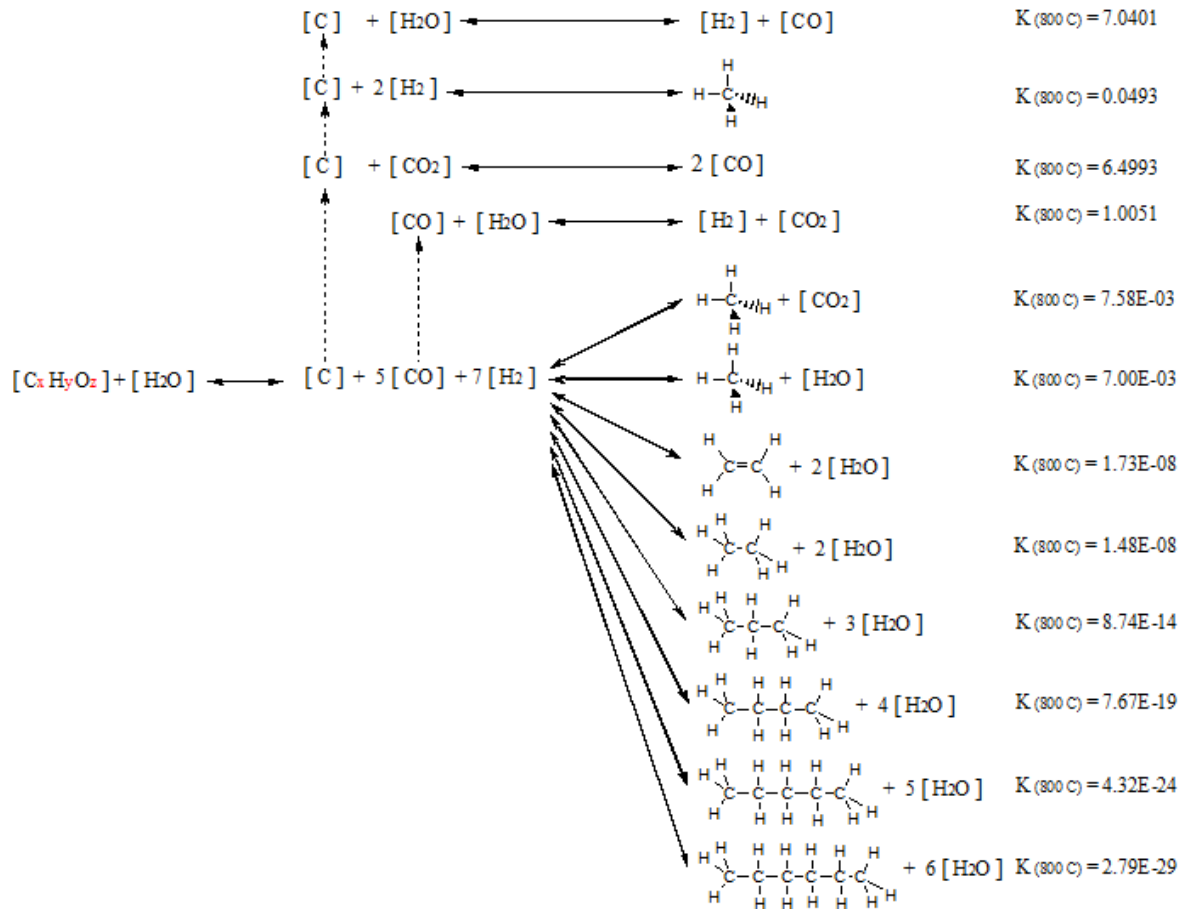


Figure D.1 Equilibrium reactions considered in the gasification of biomass

It can be seen in Eq D.1 that there are 11 unknown variables, thus 11 equations are required to solve this system:

D.3. Reforming of Methane

The relation between equilibrium constants and composition is given by:

$$K = \prod_i \left(\frac{\hat{f}_i}{f_i^o} \right) = \prod_i (y_i \phi_i P [\text{bar}])^{v_i}$$

where:

K = equilibrium constant

\prod_i = signifies the product over all species i

\hat{f}_i = fugacity coefficient of species i in an ideal gaseous solution

f_i^o = fugacity coefficient of pure species i

y_i = moles fraction of species i

ϕ_i = fugacity coefficient of species i

ν_i = stoichiometric coefficient of specie i

P = total reactor pressure (bar)

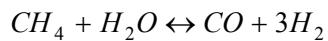
$$\square K = \prod_i (y_i)^{\nu_i} \prod_i (\phi_i)^{\nu_i} \prod_i (P)^{\nu_i}$$

For low pressure (all species are considered as ideal gases):

$$K = \left[\prod_i (y_i)^{\nu_i} \right] P^{\nu}$$

So, for reforming of methane, we have:

Steam Reforming of Methane



$$K_{CH_4} = \frac{y_{CO} y_{H_2}^3}{y_{CH_4} y_{H_2O}} (P)^2$$

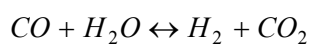
Eq D.2

Dry Reforming of Methane



$$K_{CH_4} = \frac{y_{CO}^2 y_{H_2}^2}{y_{CH_4} y_{CO_2}} (P)^2$$

D.4. Water-Gas Shift

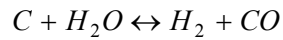


Eq D.3

$$K_{WGS} = \frac{y_{H_2} y_{CO_2}}{y_{CO} y_{H_2O}}$$

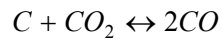
D.5. Carbon Reactions

Heterogeneous Water-Gas Shift Reaction



$$K_C = \frac{y_{CO} y_{H_2}}{y_{H_2O}}$$

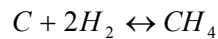
Boudouard Equilibrium



Eq D.4

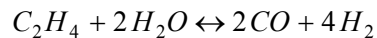
$$K_C = \frac{y_{CO}^2}{y_{CO_2}}$$

Hydrogenating Gasification



$$K_C = \frac{y_{CH_4}}{y_{H_2}^2} (P)^{-2}$$

D.6. Ethylene



Eq D.5

$$K_{C_2H_6} = \frac{y_{CO}^2 y_{H_2}^4}{y_{C_2H_6} y_{H_2O}^2} (P)^3$$

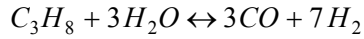
D.7. Ethane



Eq D.6

$$K_{C_2H_6} = \frac{y_{CO}^2 y_{H_2}^5}{y_{C_2H_6} y_{H_2O}^2} (P)^4$$

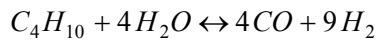
D.8. Propane



Eq D.7

$$K_{C_3H_8} = \frac{y_{CO}^3 y_{H_2}^7}{y_{C_3H_8} y_{H_2O}^3} (P)^6$$

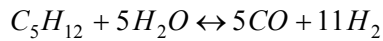
D.9. Butane



Eq D.8

$$K_{C_4H_{10}} = \frac{y_{CO}^4 y_{H_2}^9}{y_{C_4H_{10}} y_{H_2O}^4} (P)^8$$

D.10. Pentane



Eq D.9

$$K_{C_5H_{12}} = \frac{y_{CO}^5 y_{H_2}^{11}}{y_{C_5H_{12}} y_{H_2O}^5} (P)^{10}$$

D.11. Hexane



Eq D.10

$$K_{C_6H_{14}} = \frac{y_{CO}^6 y_{H_2}^{13}}{y_{C_6H_{14}} y_{H_2O}^6} (P)^{12}$$

Since all species are accounted for in Eq D.1, the molar fractions can be expressed as:

$$y_{H_2} = \frac{\alpha}{\alpha + \beta + \gamma + \psi + \zeta + \varepsilon + \Omega + \eta + \theta + \lambda + \nu + \nu} \quad \text{Eq D.11}$$

$$y_{CO} = \frac{\beta}{\alpha + \beta + \gamma + \psi + \zeta + \varepsilon + \Omega + \eta + \theta + \lambda + \nu + \nu} \quad \text{Eq D.12}$$

$$y_{CO_2} = \frac{\gamma}{\alpha + \beta + \gamma + \psi + \zeta + \varepsilon + \Omega + \eta + \theta + \lambda + \nu + \nu} \quad \text{Eq D.13}$$

$$y_{H_2O} = \frac{\psi}{\alpha + \beta + \gamma + \psi + \zeta + \varepsilon + \Omega + \eta + \theta + \lambda + \nu + \nu} \quad \text{Eq D.14}$$

$$y_{CH_4} = \frac{\zeta}{\alpha + \beta + \gamma + \psi + \zeta + \varepsilon + \Omega + \eta + \theta + \lambda + \nu + \nu} \quad \text{Eq D.15}$$

$$y_C = \frac{\Omega}{\alpha + \beta + \gamma + \psi + \zeta + \varepsilon + \Omega + \eta + \theta + \lambda + \nu + \nu} \quad \text{Eq D.16}$$

$$y_{C_2H_4} = \frac{\varepsilon}{\alpha + \beta + \gamma + \psi + \zeta + \varepsilon + \Omega + \eta + \theta + \lambda + \nu + \nu} \quad \text{Eq D.17}$$

$$y_{C_2H_6} = \frac{\eta}{\alpha + \beta + \gamma + \psi + \zeta + \varepsilon + \Omega + \eta + \theta + \lambda + \nu + \nu} \quad \text{Eq D.18}$$

$$y_{C_3H_8} = \frac{\theta}{\alpha + \beta + \gamma + \psi + \zeta + \varepsilon + \Omega + \eta + \theta + \lambda + \nu + \nu} \quad \text{Eq D.19}$$

$$y_{C_4H_{10}} = \frac{\lambda}{\alpha + \beta + \gamma + \psi + \zeta + \varepsilon + \Omega + \eta + \theta + \lambda + \nu + \nu} \quad \text{Eq D.20}$$

$$y_{C_5H_{12}} = \frac{\nu}{\alpha + \beta + \gamma + \psi + \zeta + \varepsilon + \Omega + \eta + \theta + \lambda + \nu + \nu} \quad \text{Eq D.21}$$

$$y_{C_6H_{14}} = \frac{\nu}{\alpha + \beta + \gamma + \psi + \zeta + \varepsilon + \Omega + \eta + \theta + \lambda + \nu + \nu} \quad \text{Eq D.22}$$

Substituting equations Eq D.11 to Eq D.22 in the various equilibrium reaction equations, gives:

$$K_{WGS} = \frac{\alpha\gamma}{\psi\beta} \quad \text{Eq D.23}$$

$$K_{CH_4} = \frac{\alpha^3 \beta}{\zeta \psi (\alpha + \beta + \gamma + \psi + \zeta + \varepsilon + \Omega + \eta + \theta + \lambda + \nu + \nu)^2} (P)^2; \quad \text{Eq D.24}$$

$$K_{CH_4} = \frac{\alpha^2 \beta^2}{\gamma \psi (\alpha + \beta + \gamma + \psi + \zeta + \varepsilon + \Omega + \eta + \theta + \lambda + \nu + \nu)^2} (P)^2$$

$$K_C = \frac{\alpha \beta}{\psi} (P); \quad K_C = \frac{\beta^2}{\gamma} (P); \quad \text{Eq D.25}$$

$$K_C = \frac{\zeta (\alpha + \beta + \gamma + \psi + \zeta + \Omega + \varepsilon + \eta + \theta + \lambda + \nu + \nu)^2}{\alpha^2} (P)^{-1}$$

$$K_{C_2H_4} = \frac{\alpha^4 \beta^2}{\varepsilon \psi (\alpha + \beta + \gamma + \psi + \zeta + \Omega + \varepsilon + \eta + \theta + \lambda + \nu + \nu)^3} (P)^3 \quad \text{Eq D.26}$$

$$K_{C_2H_6} = \frac{\alpha^5 \beta^2}{\eta \psi (\alpha + \beta + \gamma + \psi + \zeta + \Omega + \varepsilon + \eta + \theta + \lambda + \nu + \nu)^4} (P)^4 \quad \text{Eq D.27}$$

$$K_{C_3H_8} = \frac{\alpha^7 \beta^3}{\theta \psi (\alpha + \beta + \gamma + \psi + \zeta + \Omega + \varepsilon + \eta + \theta + \lambda + \nu + \nu)^6} (P)^6 \quad \text{Eq D.28}$$

$$K_{C_4H_{10}} = \frac{\alpha^9 \beta^4}{\lambda \psi (\alpha + \beta + \gamma + \psi + \zeta + \Omega + \varepsilon + \eta + \theta + \lambda + \nu + \nu)^8} (P)^8 \quad \text{Eq D.29}$$

$$K_{C_5H_{12}} = \frac{\alpha^{11} \beta^5}{\nu \psi (\alpha + \beta + \gamma + \psi + \zeta + \Omega + \varepsilon + \eta + \theta + \lambda + \nu + \nu)^{10}} (P)^{10} \quad \text{Eq D.30}$$

$$K_{C_6H_{14}} = \frac{\alpha^{13} \beta^6}{\nu \psi (\alpha + \beta + \gamma + \psi + \zeta + \Omega + \varepsilon + \eta + \theta + \lambda + \nu + \nu)^{12}} (P)^{12} \quad \text{Eq D.31}$$

In addition, from the carbon, hydrogen, and oxygen mole balances of the overall gasification reaction, Eq D.1, the following relationships are acquired:

$$x = \beta + \gamma + \zeta + \varepsilon + \Omega + \eta + \theta + \lambda + \mu + \nu$$

$$y + 2\omega = 2\alpha + 2\psi + 4\zeta + 4\varepsilon + 6\eta + 8\theta + 10\lambda + 12\mu + 14\nu$$

$$z + \omega = \beta + 2\gamma + \psi$$

Furthermore, expressing ζ , α and ψ , as a function of the other parameters:

$$\zeta = x - \beta - \gamma - \varepsilon - \Omega - \eta - \theta - \lambda - \mu - \nu$$

$$\alpha = \frac{1}{2}y - 2x - z + 3\beta + 4\gamma - \eta - 2\theta - 3\lambda - 4\mu - 5\nu$$

$$\psi = z + \omega - \beta - 2\gamma$$

Substituting ζ , α , and ψ into equations Eq D.23 to Eq D.31, it is possible to eliminate three of the parameters, leaving a system of nine independent non-linear equations with nine unknowns (β , γ , Ω , ε , η , θ , λ , μ , ν), as follows:

$$K_{WGS} = \frac{(0.5y - 2x - z + 3\beta + 4\gamma - \eta - 2\theta - 3\lambda - 4\nu - 5\nu)\gamma}{\beta(z + \omega - \beta - 2\gamma)} \quad \text{Eq D.32}$$

$$K_{CH_4} = \frac{(0.5y - 2x - z + 3\beta + 4\gamma - \eta - 2\theta - 3\lambda - 4\nu - 5\nu)^3 \beta^2}{(x - \beta - \gamma - \varepsilon - \Omega - \eta - \theta - \lambda - \nu - \nu)(z + \omega - \beta - 2\gamma)} \cdot \frac{1}{(0.5y - x + \omega + 2\beta + 2\gamma - \eta - 2\theta - 3\lambda - 4\nu - 5\nu)^2} (P)^2 \quad \text{Eq D.33}$$

$$K_C = \frac{(0.5y - 2x - z + 3\beta + 4\gamma - \eta - 2\theta - 3\lambda - 4\nu - 5\nu)\beta}{(z + \omega - \beta - 2\gamma)} (P) \quad \text{Eq D.34}$$

$$K_{C_2H_4} = \frac{(0.5y - 2x - z + 3\beta + 4\gamma - \eta - 2\theta - 3\lambda - 4\nu - 5\nu)^4 \beta^2}{\varepsilon(z + \omega - \beta - 2\gamma)(0.5y - x + \omega + 2\beta + 2\gamma - \eta - 2\theta - 3\lambda - 4\nu - 5\nu)^3} (P)^3 \quad \text{Eq D.35}$$

$$K_{C_2H_6} = \frac{(0.5y - 2x - z + 3\beta + 4\gamma - \eta - 2\theta - 3\lambda - 4\nu - 5\nu)^5 \beta^2}{\eta(z + \omega - \beta - 2\gamma)(0.5y - x + \omega + 2\beta + 2\gamma - \eta - 2\theta - 3\lambda - 4\nu - 5\nu)^4} (P)^4 \quad \text{Eq D.36}$$

$$K_{C_3H_8} = \frac{(0.5y - 2x - z + 3\beta + 4\gamma - \eta - 2\theta - 3\lambda - 4\nu - 5\nu)^7 \beta^3}{\theta(z + \omega - \beta - 2\gamma)(0.5y - x + \omega + 2\beta + 2\gamma - \eta - 2\theta - 3\lambda - 4\nu - 5\nu)^6} (P)^6 \quad \text{Eq D.37}$$

$$K_{C_4H_{10}} = \frac{(0.5y - 2x - z + 3\beta + 4\gamma - \eta - 2\theta - 3\lambda - 4\nu - 5\nu)^9 \beta^4}{\lambda(z + \omega - \beta - 2\gamma)(0.5y - x + \omega + 2\beta + 2\gamma - \eta - 2\theta - 3\lambda - 4\nu - 5\nu)^8} (P)^8 \quad \text{Eq D.38}$$

$$K_{C_5H_{12}} = \frac{(0.5y - 2x - z + 3\beta + 4\gamma - \eta - 2\theta - 3\lambda - 4\nu - 5\nu)^{11} \beta^5}{\nu(z + \omega - \beta - 2\gamma)(0.5y - x + \omega + 2\beta + 2\gamma - \eta - 2\theta - 3\lambda - 4\nu - 5\nu)^{10}} (P)^{10} \quad \text{Eq D.39}$$

$$K_{C_6H_{14}} = \frac{(0.5y - 2x - z + 3\beta + 4\gamma - \eta - 2\theta - 3\lambda - 4\nu - 5\nu)^{13} \beta^6}{\nu(z + \omega - \beta - 2\gamma)(0.5y - x + \omega + 2\beta + 2\gamma - \eta - 2\theta - 3\lambda - 4\nu - 5\nu)^{12}} (P)^{12} \quad \text{Eq D.40}$$

Nine independent nonlinear equations with nine unknowns result from algebraic manipulation of this system of twelve variables ($\alpha, \beta, \gamma, \psi, \zeta, \Omega, \varepsilon, \eta, \theta, \lambda, \mu, \nu$). The Newton-Raphson (NR) model is used to solve the nonlinear system of equations containing constrained variables. The NR method uses a truncated Taylor series estimate of the function values to obtain better estimates of the unknowns.

D.12. Parameter Initial Guesses and Constraints

To solve the nonlinear equation system, initial guesses of $\beta, \gamma, \varepsilon, \eta, \theta, \lambda, \mu,$ and ν are made with the following constraints: $K_{WGS}, K_{CH_4}, K_{C_2H_4}, K_{C_2H_6}, K_{C_3H_8}, K_{C_4H_{10}}, K_{C_5H_{12}},$ and $K_{C_6H_{14}} \rightarrow 0$. This holds true if $\beta, \gamma, \varepsilon, \eta, \theta, \lambda, \mu,$ and ν are selected using the following procedure:

- i) The minimum allowable value of β for a given value of γ is found by taking the limit of $K_{WGS} \rightarrow 0$

$$K_{WGS \rightarrow 0} = \frac{y_{H_2} y_{CO_2}}{y_{CO} y_{H_2O}} = \frac{\alpha \gamma}{\psi \beta} = \frac{(0.5y - 2x - z + 3\beta + 4\gamma - \eta - 2\theta - 3\lambda - 4\nu - 5\nu) \gamma}{\beta (z + \omega - \beta - 2\gamma)}$$

$$\alpha > 0$$

$$0.5y - 2x - z + 3\beta_{\min} + 4\gamma - \eta - 2\theta - 3\lambda - 4\nu - 5\nu > 0$$

$$\beta_{\min} > \frac{1}{3} [2x + z - 0.5y - 4\gamma + \eta + 2\theta + 3\lambda + 4\nu + 5\nu]$$

- ii) The maximum allowable value of β for a given value of γ is found by taking the limit of $K_{WGS} \rightarrow \infty$.

$$K_{WGS \rightarrow \infty} = \frac{y_{H_2} y_{CO_2}}{y_{CO} y_{H_2O}} = \frac{\alpha \gamma}{\psi \beta} = \frac{(0.5y - 2x - z + 3\beta + 4\gamma - \eta - 2\theta - 3\lambda - 4\nu - 5\nu) \gamma}{\beta (z + \omega - \beta - 2\gamma)}$$

$$\psi > 0$$

$$(z + \omega - \beta_{\max} - 2\gamma) > 0$$

$$\beta_{\max} > z + \omega - 2\gamma$$

iii) To ensure that for a given value of γ , $\beta_{\max} > \beta_{\min}$ the following inequality must be satisfied:

$$\beta_{\max} > \beta_{\min}$$

$$\left[\frac{2}{3}x + \frac{1}{3}z - \frac{1}{6}y - \frac{4}{3}\gamma_{\max} + \frac{1}{3}\eta + \frac{2}{3}\theta + \lambda + \frac{4}{3}\nu + \frac{5}{3}\nu \right] < [z + \omega - 2\gamma_{\max}] \text{ and}$$

$$\gamma_{\max} < \frac{3}{2} \left[\frac{2}{3}z + \omega - \frac{2}{3}x + \frac{1}{6}y - \frac{1}{3}\eta - \frac{2}{3}\theta - \lambda - \frac{4}{3}\nu - \frac{5}{3}\nu \right]$$

Additionally, numerical solution of the above set of partial equations (steam reforming of methane, Eq D.2 and water-gas shift reaction, Eq D.3) was carried out using Aspen HYSYS[®] package to check the adequate solution of the proposed model.

D.13. Equilibrium Constants

D.13.1. Effect of Temperature on the Equilibrium Constant

Since the standard-state temperature is that of the equilibrium mixtures, the standard property changes of reaction, such as ΔG° and ΔH° , vary with the equilibrium temperature.

The dependence of ΔG° on T is given by:

$$\frac{d(\Delta G^\circ / RT)}{dT} = \frac{-\Delta H^\circ}{RT^2} \quad \text{Eq D.41}$$

According to the definition of the *standard Gibbs energy change of reaction* (Smith et al., 1996):

$$\frac{d\Delta G^\circ}{RT} = -\ln K \quad \text{Eq D.42}$$

$$\text{with: } \Delta G^\circ = \Delta H_0^\circ - \frac{T}{T_0}(\Delta H_0^\circ - \Delta G_0^\circ) + R \int_{T_0}^T \frac{\Delta Cp^\circ}{R} dT - RT \int_{T_0}^T \frac{\Delta Cp^\circ}{R} \frac{dT}{T} \quad \text{Eq D.43}$$

Therefore:

$$\frac{d \ln K}{dT} = \frac{-\Delta H^\circ}{RT^2} \quad \text{Eq D.44}$$

Eq D.22 establishes the effect of temperature on the equilibrium constant, and hence on the equilibrium conversion. Figure D.2 to Figure D.5 display the effect of temperature on the equilibrium constant for all reactions considered in this model. Table D.1 shows additionally, the standard enthalpy of formation $\Delta h_{f(298)}^\circ$, Standard Gibbs free energy $\Delta g_{f(298)}^\circ$, and the thermodynamic equilibrium constant K at 800°C.

D.13.2 Effect of Pressure on the Equilibrium Gas Composition

At reaction equilibrium, the gas species composition is a function of temperature and pressure. An analysis of this composition can be made by applying Le Chatelier's principle to the reaction network.

$$\frac{K}{\left[\prod_i (\phi_i)^{v_i}\right]} = \left[\frac{(y_{A3})^{v3} (y_{A4})^{v4}}{(y_{A1})^{v1} (y_{A2})^{v2}} \right] P^{v_T} \quad \text{Eq D.44}$$

Figure D.2 displays the equilibrium constant for the water-gas-shift reaction at temperatures ranging from 400 - 950°C with a $K_{eq(800\text{ C})}$ of 1.0051.

Figure D.3 shows the effect of temperature on the equilibrium constant for the steam reforming and dry reforming of methane, resulting in an equilibrium constant at 800°C, and a $K_{eq(800\text{ C})}$ of 7.00e-03 (steam reforming) and 7.58e-03 (dry reforming). The equilibrium constants for the higher hydrocarbons cracking reactions considered in the steam gasification of biomass is shown in Figure D.4.

Finally, Figure D.5 presents the equilibrium constant for the carbon reaction considered in the equilibrium model at temperatures ranging from 450 to 950°C.

Table D1 Thermodynamic properties and equilibrium constant at 800°C for all reactions considered in the equilibrium model

Reaction Equations	$\Delta g_{f(298)}^{\circ}$ [kJ/ mol]	$\Delta h_{f(298)}^{\circ}$ [kJ/ mol]	$K_{\text{eq}} (800 \text{ C})$
$CO + H_2O \leftrightarrow H_2 + CO_2$	-28.538	-42.200	1.005
$CO + 3H_2 \leftrightarrow CH_4 + H_2O$	140.098	205.310	142.959
$2CO + 3H_2 \leftrightarrow CH_4 + CO_2$	168.635	123.760	131.856
$C + H_2O \leftrightarrow H_2 + CO$	89.824	130.414	7.0401
$C + CO_2 \leftrightarrow 2CO$	118.362	172.615	6.499
$C + 2H_2 \leftrightarrow CH_4$	-50.273	-74.900	0.049
$2CO + 4H_2 \leftrightarrow C_2H_4 + 2H_2O$	111.651	104.256	5.754E+07
$2CO + 5H_2 \leftrightarrow C_2H_6 + 2H_2O$	212.787	172.779	6.780E+07
$3CO + 7H_2 \leftrightarrow C_3H_8 + 3H_2O$	293.149	165.051	1.144E+13
$4CO + 9H_2 \leftrightarrow C_4H_{10} + 4H_2O$	376.793	161.968	1.304E+18
$5CO + 11H_2 \leftrightarrow C_5H_{12} + 5H_2O$	457.916	159.719	2.314E+23
$6CO + 13H_2 \leftrightarrow C_6H_{14} + 6H_2O$	539.699	158.303	3.591E+28

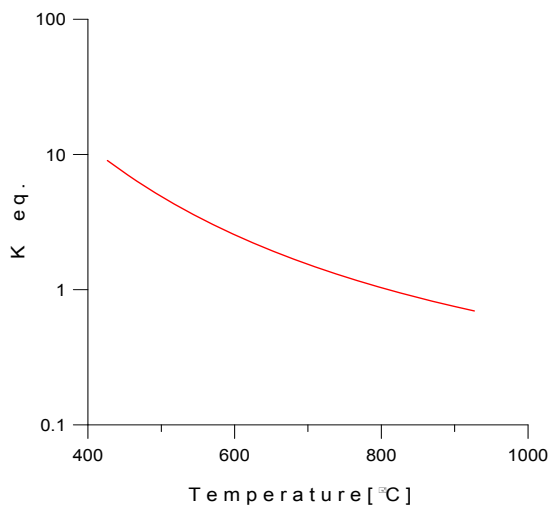


Figure D.2 Effect of temperature on the equilibrium constant for the water gas-shift reaction

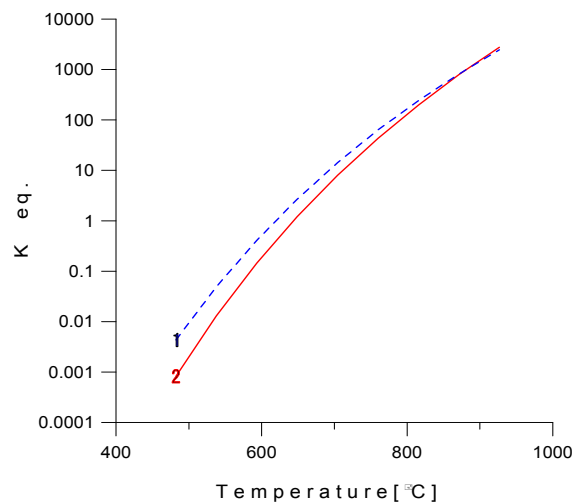


Figure D.3 Effect of temperature on the equilibrium constant for: 1 steam reforming of methane and 2 dry reforming of methane

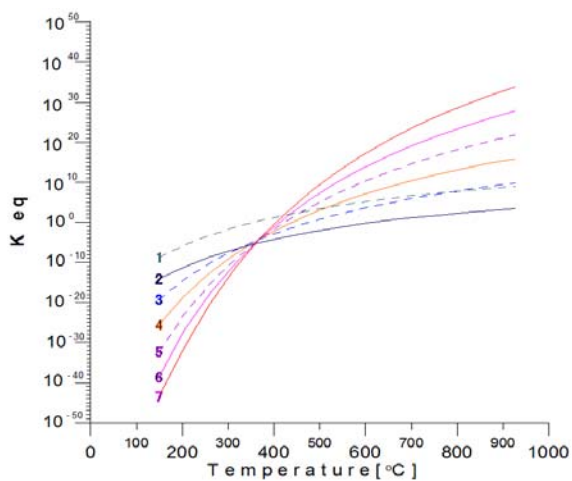


Figure D.4 Effect of temperature on the equilibrium constant for: 1 ethylene, 2 methane 3 ethane, 4 propane, 5 butane, 6 pentane and 7 hexane

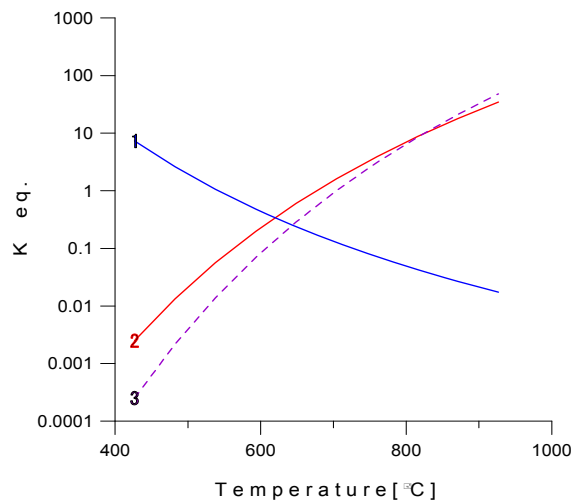


Figure D.5 Equilibrium constant at different temperatures for 1 hydrogenating gasification, 2 water-gas shift and 3 Boudouard reaction

Appendix E Kinetic Parameters Estimation Example

E.1. Kinetic Parameters as a Function of Temperature

Once a first set of kinetic parameters was obtained, a new search for the kinetic parameters was initiated following the procedure explained in Chapter 9. Tables E.1 and E.2 present a selected set of results.

Table E1 Kinetic parameters for mixtures of 2-methyl-4-methoxyphenol in water at S/B ratios of 0.4, 0.6, 0.8, and 1.0, as a function of the reaction temperature

T [°C]	600	650	700
k_{WGS}^a	9.49E-06	1.05E-05	1.30E-05
k_{SR}^b	2.02E-09	2.43E-09	2.99E-09
k_{DRM}^a	8.42E-09	1.84E-08	3.20E-08
$K_{CO_2}^c$	9.12E-02	8.43E-02	7.80E-02

^a [mol gcat⁻¹ s⁻¹], ^b [mol gcat⁻¹ s⁻¹ psia⁻¹], ^c [psia⁻¹].

E.2 Intrinsic Kinetic Parameters Estimation

To obtain the intrinsic kinetic parameters (activation energies and pre-exponential factors), the kinetic parameters k_i were allowed to vary with temperature using an Arrhenius relationship centered on an average temperature (refer to Eq (68) and Eq (69), Chapter 9); thus, giving a new differential equation system to be solved in order to estimate the intrinsic kinetic parameters corresponding to the rate-limiting surface reaction rates, k_i^0 and E_i .

Initial values for these intrinsic kinetic parameters to solve the new differential equation system were necessary. In this sense, the kinetic parameters at 650°C (Table E.1) were used as pre-exponential guess values (k_i^0). Moreover, the initial activation energy (E_i) values were obtained from linear regression of the Arrhenius expressions (Eq (68) and Eq

(69), Chapter 9) in a semilogarithmic plot. Figures E.1 and E.2, present a calculation example for E_i and $\Delta H_{CO_2}^A$

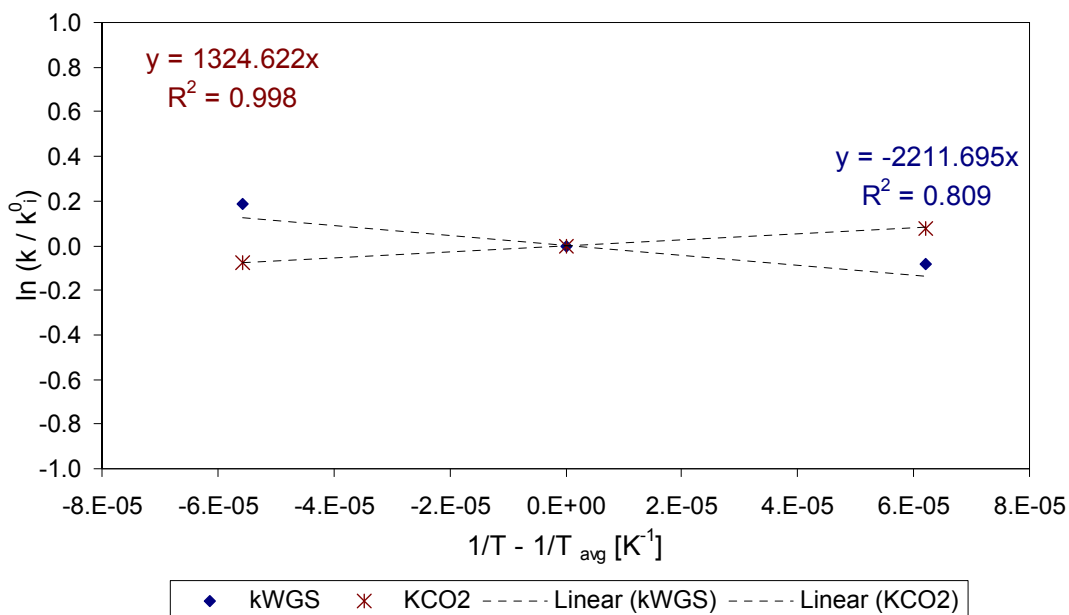


Figure E.1 Semilogarithmic plot of Arrhenius expression for water-gas shift reaction and carbon dioxide adsorption, from catalytic steam gasification of mixtures of 2-methyl-4-methoxyphenol in water at S/B ratios of 0.4, 0.6, 0.8, and 1.0, C/O=25.

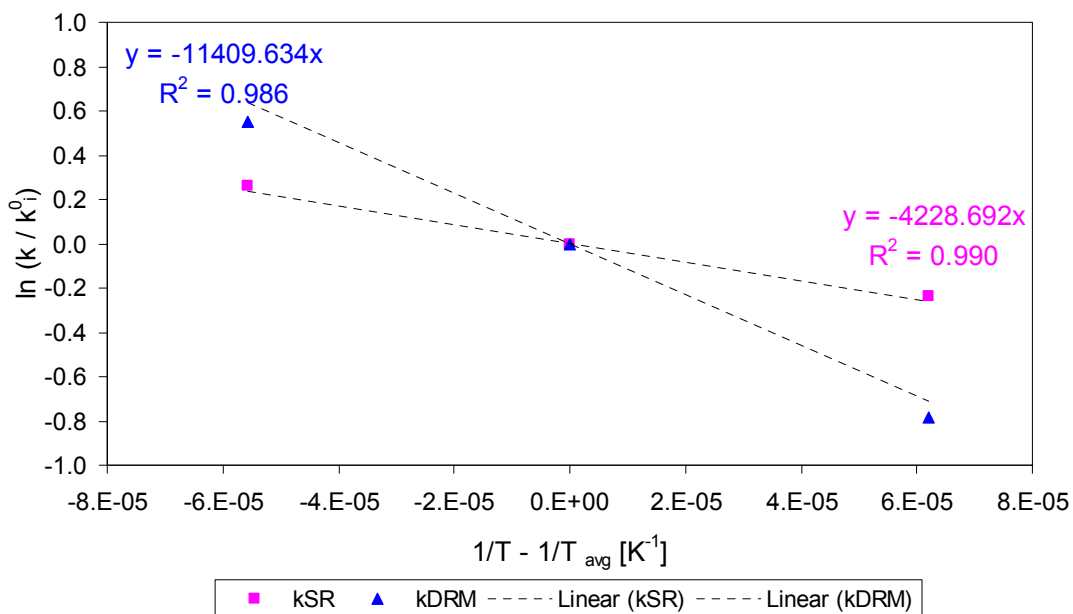


Figure E.2 Semilogarithmic plot of Arrhenius expression for steam and dry reforming of methane, from catalytic steam gasification of mixtures of 2-methyl-4-methoxyphenol in water at S/B ratios of 0.4, 0.6, 0.8, and 1.0, C/O=25.

Linear regression of data reported in Figure E.1 and E.2 gives the initial activation energies for water-gas shift reaction, steam reforming of methane, dry reforming of methane, as well carbon dioxide heat of adsorption, as follows:

$$\frac{-E_{WGS}}{R} = -2211.695 \Rightarrow E_{WGS} = 18.4 \text{ kJ / mol} \quad \text{Eq E.1}$$

$$\frac{-E_{SR}}{R} = -4228.692 \Rightarrow E_{SR} = 35.2 \text{ kJ / mol} \quad \text{Eq E.2}$$

$$\frac{-E_{DRM}}{R} = -11409.63 \Rightarrow E_{DRM} = 94.9 \text{ kJ / mol} \quad \text{Eq E.3}$$

$$\frac{-\Delta H_{CO_2}^A}{R} = 1324.22 \Rightarrow \Delta H_{CO_2}^A = -11.0 \text{ kJ / mol} \quad \text{Eq E.4}$$

Regarding the coefficient of determination (R^2) from the linear regression of Figures E.1 and E.2, it is observed that their values are close to 1, with this result indicating that the estimated parameters adequately represent the experimental data.

Finally, a total of 6 parameters were adjusted simultaneously by nonlinear multivariable regression of experimental data using the MATLAB calculation procedure explained in section 9.9 (Chapter 9), and the above guess values. Table 21 (Chapter 9) summarizes the intrinsic kinetics parameters estimated with their 95% confidence interval, and the standard deviation of the residuals (σ), showing the quality of the fits.

Appendix F Mass Balances

This appendix reports the experimental data for catalytic steam gasification of biomass, including: molar fraction compositions of the major product species, tars, coke deposited over the catalyst, reaction temperature, and pressure in the reactor and vacuum box. An important observation from these runs was that the mass balance closures, which included all chemical species being fed to and removed from the reactor, were in the $\pm 5\%$ range.

The first section of this appendix is devoted to the mass balance closure calculation procedure. Section F.2 displays the gasification experimental results when glucose is used as a feedstock. Section F.3 shows the experimental data for catalytic steam gasification of 2-methoxy-4-methylphenol. Finally, Section F.4 provides the experimental results for gasification of mixtures of glucose-2 methoxy 4 methylphenol-water at 700°C.

F.1. Mass Balance Calculation Procedure

The mass balance closure was defined as:

$$MB = \frac{m_i - m_p - m_c}{m_i} \times 100 \quad \text{Eq F.1}$$

where:

MB : mass balance closure (%)

m_i : total mass of reactants injected (g)

m_p : total mass of reaction products (g)

m_c : coke over catalyst (g)

The exact amount of reactant injected was calculated as the difference between the mass of the syringe before (m_{bef}) and after (m_{aft}) performing the injection. The mass of products was determined calculating the total product moles in the system with ideal gas law and

using the average molecular weight of product mixture in an argon free basis. The following expression was obtained:

$$n_p = \frac{V_{VB}}{RT_{VB}}(P_{VB,f} - P_{VB,i}) + \frac{V_r}{RT_r}(P_{r,fe} - P_{r,i}) \quad \text{Eq F.2}$$

$$m_p = MW_p n_p \quad \text{Eq F.3}$$

where:

MW_p = average molecular weight of product mixture, Ar free basis (g/gmol)

V_{VB} = vacuum box volume (cm³)

V_r = reactor volume (cm³)

n_p = total product moles in the reactor and vacuum box (gmol)

R = ideal gas constant (1206.3 cm³psia/gmol K)

T_r = reactor temperature (K)

T_{VB} = vacuum box temperature (K)

$P_{r,i}, P_{VB,i}$ = reactor and vacuum box initial pressures, respectively (psia)

$P_{r,fe}, P_{VB,f}$ = reactor and vacuum box final pressures, respectively (psia)

The average molecular weight of the product mixture was calculated using the molecular weight of the individual species and the weight fractions as follows:

$$MW_p = \frac{1}{\sum \frac{w_i}{MW_i}} \quad \text{Eq F.4}$$

with w_i and MW_i representing the weight fraction and molecular weight (g/gmol) of each product species respectively. The separation and quantification of permanent gases (H₂, CO, CO₂, H₂O and CH₄), water, and light hydrocarbons up to C₆ were performed in a Shimatzu 2010 GC with thermal conductivity detector using calibration curves. The components present in the tars were identified using a Shimatzu 2010 with a mass

spectrometer detector. The coke deposited on the catalysts after the experimental run was measured in a total organic carbon analyzer from Mandel. A detailed experimental method is presented in Chapter 4.

F.2. Glucose - Mass Balance

Catalytic runs with Ni/ α -alumina catalyst were performed in a CREC fluidized riser simulator. Mixtures of glucose-water at steam biomass ratios of 0.4, 0.6, 0.8 and 1.0 (g/g) wt%, 2 atm. of argon, catalyst/biomass ratio of ~25, residence times of 5, 10, 20, and 30 s, and reaction temperatures 600, 650, and 700°C. The impeller velocity was set at 6000 rpm to get a well fluidized bed. No tars were identified when glucose was used as a feedstock.

Table F.1 through Table F.3 report the mass balances calculated for a selected set of catalytic runs of catalytic steam gasification of glucose at 600, 650 and 700°C.

Table F1. Catalytic experimental runs for glucose at 700oC, S/B ratios of 0.4 and 0.6, reaction times of 5, 10, 20, and 30s

Date	22/05/09	22/05/09	4/05/09	21/05/09	26/05/09	26/05/09	01/05/09	21/05/09
S/B	0.4				0.6			
Reaction Time (s)	5	10	20	30	5	10	20	30
Mole Fractions (mol%)								
Hydrogen	0.302	0.265	0.3243	0.371	0.307	0.327	0.326	0.375
Carbon Monoxide	0.360	0.410	0.321	0.333	0.358	0.345	0.250	0.235
Methane	0.052	0.050	0.056	0.041	0.050	0.045	0.051	0.037
Carbon Dioxide	0.052	0.067	0.086	0.102	0.046	0.074	0.081	0.113
Ethylene	0.003	0.003	0.002	0.002	0.003	0.002	0.002	0.002
Ethane	0.005	0.005	0.007	0.004	0.006	0.005	0.006	0.003
Water	0.226	0.201	0.206	0.149	0.229	0.203	0.284	0.236
Coke wt% (gcoke/gcat)								
Coke wt% (gcoke/gcat)	0.018	0.016	0.013	0.009	0.016	0.015	0.012	0.009
Mass Injected (g)								
Mass Injected (g)	0.033	0.033	0.052	0.034	0.033	0.033	0.57	0.035
Tr (°C)								
Tr (°C)	700	700	700	700	700	700	700	700
Tv (°C)								
Tv (°C)	153	152	165	163	151	150	150	150
P _{ri} (psia)								
P _{ri} (psia)	13.28	13.96	13.99	13.96	13.94	14.04	14.07	14.00
P _{rf} (psia)								
P _{rf} (psia)	2.94	2.96	2.95	2.94	2.95	2.94	2.96	2.95
P _{vi} (psia)								
P _{vi} (psia)	4.01	3.97	4.52	4.09	4.04	4.00	4.67	4.11
P _{vf} (psia)								
P _{vf} (psia)	3.97	3.93	4.50	4.04	4.00	3.96	4.64	4.07
CMB								
CMB	-0.84	-0.63	-0.25	-0.35	-0.81	-2.68	-1.45	-1.80

Table F2. Catalytic experimental runs for glucose at 650oC, S/B ratios of 0.8 and 1.0, reaction times of 5, 10, 20, and 30s

Date	07/08/09	05/08/09	06/08/09	06/08/09	04/08/09	05/08/09	10/08/09	19/05/09
S/B	0.8				1.0			
Reaction Time (s)	5	10	20	30	5	10	20	30
Mole Fractions (mol%)								
Hydrogen	0.207	0.356	0.298	0.328	0.213	0.272	0.293	0.332
Carbon Monoxide	0.323	0.254	0.260	0.215	0.302	0.295	0.213	0.186
Methane	0.051	0.039	0.033	0.036	0.045	0.034	0.038	0.029
Carbon Dioxide	0.056	0.133	0.111	0.146	0.056	0.079	0.111	0.133
Ethylene	0.003	0.000	0.000	0.000	0.002	0.000	0.000	0.001
Ethane	0.004	0.003	0.003	0.000	0.002	0.004	0.003	0.003
Water	0.356	0.215	0.296	0.275	0.380	0.315	0.342	0.317
Coke wt% (gcoke/gcat)								
Coke wt% (gcoke/gcat)	0.015	0.014	0.014	0.013	0.014	0.014	0.014	0.013
Mass Injected (g)								
Mass Injected (g)	0.036	0.036	0.036	0.036	0.039	0.039	0.038	0.038
Tr (°C)								
Tr (°C)	650	650	650	650	650	650	650	650
Tv (°C)								
Tv (°C)	140	159	161	151	150	154	150	150
Pri (psia)								
Pri (psia)	13.76	13.63	13.66	13.72	13.65	13.52	13.87	13.60
Prf (psia)								
Prf (psia)	2.97	2.96	2.96	2.93	2.96	2.95	2.96	2.96
Pvi (psia)								
Pvi (psia)	4.03	4.12	4.06	4.03	4.07	4.16	4.14	4.11
Pvf (psia)								
Pvf (psia)	4.00	4.08	4.07	4.02	4.09	4.12	4.10	4.13
CMB								
CMB	-2.28	0.34	0.34	0.24	-1.26	-0.13	-0.37	-1.73

Table F3. Catalytic experimental runs for glucose at 600°C, S/B ratios of 0.8 and 1.0, reaction times of 5, 10, 20, and 30s

Date	30/05/09	28/05/09	29/04/09	19/05/09	11/05/09	25/05/09	05/05/09	20/05/09
S/B	0.8				1			
Reaction Time (s)	5	10	20	30	5	10	20	30
Mole Fractions (mol%)								
Hydrogen	0.282	0.209	0.314	0.332	0.101	0.187	0.316	0.331
Carbon Monoxide	0.303	0.206	0.221	0.207	0.214	0.255	0.189	0.178
Methane	0.030	0.030	0.045	0.052	0.027	0.026	0.029	0.035
Carbon Dioxide	0.104	0.082	0.124	0.142	0.061	0.089	0.108	0.133
Ethylene	0.002	0.002	0.001	0.001	0.003	0.001	0.001	0.000
Ethane	0.002	0.003	0.003	0.003	0.003	0.001	0.002	0.001
Water	0.262	0.459	0.292	0.263	0.583	0.431	0.355	0.322
Propylene	0.000	0.001	0.000	0.000	0.001	0.001	0.000	0.000
Acetylaldehyde	0.016	0.008	0.000	0.000	0.008	0.009	0.001	0.000
Coke wt% (gcoke/gcat)								
Coke wt% (gcoke/gcat)	0.016	0.016	0.016	0.016	0.015	0.015	0.016	0.016
Mass Injected (g)								
Mass Injected (g)	0.034	0.33	0.038	0.036	0.035	0.039	0.039	0.034
Tr (°C)								
Tr (°C)	600	600	600	600	600	600	600	600
Tv (°C)								
Tv (°C)	150	140	140	150	150	150	150	165
Pr (psia)								
Pr (psia)	13.92	14.47	13.74	13.54	14.06	13.54	14.05	13.66
Prf (psia)								
Prf (psia)	2.95	2.96	2.96	2.95	2.96	2.95	2.98	2.95
Pvi (psia)								
Pvi (psia)	3.93	4.05	4.13	4.09	3.99	4.10	4.20	4.11
Pvf (psia)								
Pvf (psia)	3.92	3.94	4.08	4.05	3.92	4.06	4.21	4.07
CMB								
CMB	-6.29	-1.66	-1.44	-1.22	-5.71	0.27	0.02	-0.14

F.3. 2-methoxy-4-methylphenol - Mass Balances

In addition, catalytic runs using Ni/a-alumina catalyst were performed for mixtures of 2-methoxy-4-methylphenol-water at steam biomass ratios of 0.4, 0.6, 0.8 and 1.0 (g/g) wt%, 2 atm. of argon, catalyst/biomass ratio of ~25, residences times of 5, 10, 20, and 30

s, and reaction temperatures 600, 650, and 700°C. The impeller velocity was set at 6000 rpm to get a well fluidized bed.

Table F.4 through Table F.6 report the mass balances calculated for a selected set of catalytic runs of catalytic steam gasification of 2-methoxy-4-methylphenol at 600, 650 and 700°C.

Table F4. Catalytic experimental runs for 2-methoxy-4-methylphenol at 600°C, S/B ratios of 0.4 and 0.6, reaction times of 5, 10, 20 and 30s.

Date	22/09/09	18/09/09	16/09/09	15/09/09	22/09/09	18/09/09	16/09/09	15/09/09
S/B	0.4				0.6			
Reaction Time (s)	5	10	20	30	5	10	20	30
Mole Fractions (mol%)								
Hydrogen	0.262	0.338	0.377	0.438	0.242	0.313	0.385	0.442
Carbon Monoxide	0.159	0.128	0.137	0.131	0.136	0.134	0.142	0.127
Methane	0.045	0.037	0.039	0.039	0.040	0.037	0.042	0.038
Carbon Dioxide	0.084	0.104	0.134	0.149	0.083	0.099	0.136	0.146
Ethylene	0.000	0.000	0.000	0.000	0.000	0.000	0.000	0.000
Ethane	0.000	0.000	0.000	0.000	0.000	0.000	0.000	0.000
Water	0.450	0.394	0.314	0.243	0.498	0.416	0.295	0.247
Coke wt% (gcoke/gcat)								
Coke wt% (gcoke/gcat)	0.025	0.025	0.023	0.022	0.025	0.024	0.022	0.021
Tar (g)	0.010	0.010	0.009	0.007	0.008	0.008	0.007	0.006
Mass Injected (g)								
Mass Injected (g)	0.028	0.027	0.027	0.027	0.030	0.030	0.030	0.029
Temperatures (°C)								
T _r (°C)	600	600	600	600	600	600	600	600
T _v (°C)	304	301	299	302	304	304	306	303
Pressures (psia)								
P _{ri} (psia)	13.27	13.30	13.36	13.16	13.10	13.15	13.01	13.08
P _{rf} (psia)	2.96	2.96	2.96	2.96	2.96	2.96	2.96	2.95
P _{vi} (psia)	3.88	3.79	3.92	3.94	3.89	3.92	3.92	3.96
P _{vf} (psia)	3.74	3.75	3.80	3.79	3.77	3.81	3.82	3.84
Mass Balance Closure (%)								
MB Closure (%)	1.20	0.60	-0.25	1.90	1.12	3.04	0.75	-1.88

Table F5. Catalytic experimental runs for 2-methoxy-4-methylphenol at 650oC, S/B ratios of 0.4 and 0.6, reaction times of 5, 10, 20 and 30s.

Date	14/09/09	11/09/09	10/09/09	09/09/09	14/09/09	11/09/09	10/09/09	09/09/09
S/B	0.4				0.6			
Reaction Time (s)	5	10	20	30	5	10	20	30
Mole Fractions (mol%)								
Hydrogen	0.341	0.365	0.446	0.480	0.328	0.389	0.423	0.433
Carbon Monoxide	0.176	0.160	0.146	0.146	0.158	0.155	0.124	0.129
Methane	0.047	0.041	0.037	0.036	0.042	0.040	0.032	0.031
Carbon Dioxide	0.072	0.091	0.125	0.144	0.077	0.099	0.119	0.140
Ethylene	0.001	0.001	0.000	0.000	0.001	0.001	0.000	0.000
Ethane	0.002	0.002	0.001	0.001	0.003	0.002	0.001	0.001
Water	0.360	0.341	0.245	0.193	0.392	0.316	0.301	0.266
Coke wt% (gcoke/gcat)								
Coke wt% (gcoke/gcat)	0.020	0.020	0.019	0.018	0.019	0.018	0.017	0.016
Tar (g)	0.008	0.008	0.007	0.006	0.007	0.007	0.006	0.005
Mass Injected (g)								
Mass Injected (g)	0.027	0.027	0.027	0.028	0.030	0.030	0.030	0.030
T _r (°C)								
T _r (°C)	650	650	650	650	650	650	650	650
T _v (°C)								
T _v (°C)	301	308	308	302	304	305	301	304
P _{ri} (psia)								
P _{ri} (psia)	13.19	13.20	13.29	13.15	13.38	13.43	13.47	13.49
P _{rf} (psia)								
P _{rf} (psia)	2.95	2.95	2.96	2.96	2.96	2.95	2.96	2.96
P _{vi} (psia)								
P _{vi} (psia)	3.82	3.77	3.88	3.95	3.97	4.05	4.07	4.10
P _{vf} (psia)								
P _{vf} (psia)	3.79	3.79	3.83	3.83	3.85	3.86	3.90	3.89
MB Closure (%)								
MB Closure (%)	-0.76	-2.45	-5.94	0.33	0.00	0.55	-0.23	-1.20

Table F6. Catalytic experimental runs for 2-methoxy-4-methylphenol at 700oC, S/B ratios of 0.8 and 1.0, reaction times of 5, 10, 20 and 30s.

Date	2/09/09	2/09/09	2/09/09	2/09/09	31/08/09	8/09/09	8/09/09	8/09/09
S/B	0.8				1.0			
Reaction Time (s)	5	10	20	30	5	10	20	30
Mole Fractions (mol%)								
Hydrogen	0.363	0.405	0.455	0.442	0.322	0.323	0.401	0.420
Carbon Monoxide	0.161	0.147	0.135	0.146	0.144	0.121	0.112	0.111
Methane	0.041	0.035	0.026	0.022	0.036	0.028	0.023	0.021
Carbon Dioxide	0.087	0.106	0.122	0.131	0.073	0.081	0.116	0.122
Ethylene	0.001	0.000	0.001	0.001	0.001	0.000	0.000	0.001
Ethane	0.003	0.002	0.001	0.001	0.002	0.002	0.000	0.001
Water	0.344	0.304	0.260	0.255	0.423	0.446	0.349	0.324
Coke wt% (gcoke/gcat)	0.022	0.021	0.021	0.020	0.022	0.021	0.020	0.020
Tar (g)	0.005	0.005	0.004	0.004	0.004	0.004	0.003	0.002
Mass Injected (g)	0.031	0.031	0.031	0.031	0.032	0.032	0.032	0.032
T _r (°C)	700	700	700	700	700	700	700	700
T _v (°C)	306	305	306	302	303	300	303	306
P _{ri} (psia)	13.46	13.36	13.58	13.56	13.33	13.26	13.53	13.48
P _{rf} (psia)	2.96	2.96	2.95	2.96	2.96	2.96	2.96	2.96
P _{vi} (psia)	3.90	3.93	4.00	3.96	3.92	4.00	4.03	3.98
P _{vf} (psia)	3.94	3.97	3.97	4.00	3.99	4.00	4.03	4.00
MB Closure (%)	0.07	2.58	-2.12	1.25	0.18	0.59	-0.67	-6.48

F.4. Model Compound Mixtures - Mass Balances

Finally, catalytic runs over Ni/a-alumina catalyst were carried out for mixtures of glucose-2 methoxy 4 methylphenol-water at 0.4, 0.6, 0.8 and 1.0 steam/biomass ratios

(g/g) wt%, 2 atm. of argon, catalyst/feedstock ratio of ~25, residences times of 5, 10, 20, and 30 s, and reaction temperature of 700°C.

Table F.7 through Table F.8 present the mass balances calculated for catalytic runs for glucose and 2-methoxy-4-methylphenol mixtures at 700°C, S/B ratios of 0.4 and 0.6, reaction times of 5, 10, 20 and 30s.

Table F7. Catalytic experimental runs for glucose and 2-methoxy-4-methylphenol mixtures at 700oC, S/B ratios of 0.4 and 0.6, reaction times of 5, 10, 20 and 30s.

Date	30/09/09	30/09/09	25/09/09	24/09/09	30/09/09	30/09/09	25/09/09	24/09/09
S/B	0.4				0.6			
Reaction Time (s)	5	10	20	30	5	10	20	30
Mole Fractions (mol%)								
Hydrogen	0.388	0.440	0.483	0.516	0.362	0.421	0.446	0.474
Carbon Monoxide	0.305	0.307	0.281	0.260	0.269	0.266	0.238	0.230
Methane	0.067	0.059	0.054	0.048	0.050	0.046	0.043	0.041
Carbon Dioxide	0.065	0.098	0.103	0.115	0.066	0.089	0.115	0.124
Ethylene	0.002	0.000	0.000	0.000	0.002	0.001	0.000	0.000
Ethane	0.002	0.002	0.000	0.000	0.003	0.003	0.000	0.000
Water	0.172	0.094	0.079	0.062	0.249	0.172	0.159	0.132
Coke wt% (gcoke/gcat)								
Coke wt% (gcoke/gcat)	0.030	0.031	0.028	0.028	0.036	0.035	0.034	0.033
Tar (g)	0.008	0.008	0.008	0.007	0.007	0.007	0.006	0.005
Mass Injected (g)								
Mass Injected (g)	0.035	0.035	0.033	0.032	0.036	0.035	0.035	0.035
Tr (°C)								
Tr (°C)	700	700	700	700	700	700	700	700
Tv (°C)								
Tv (°C)	300	301	303	302	303	300	301	304
Pr (psia)								
Pr (psia)	13.71	13.72	13.73	13.72	13.67	13.71	13.69	13.70
Prf (psia)								
Prf (psia)	2.96	2.95	2.96	2.95	2.96	2.95	2.96	2.96
Pvi (psia)								
Pvi (psia)	4.04	3.97	3.95	4.15	4.12	4.02	4.04	4.07
Pvf (psia)								
Pvf (psia)	3.95	3.95	3.94	3.94	4.00	4.00	4.02	4.02
MB Closure (%)								
MB Closure (%)	1.29	0.77	0.44	0.44	0.93	1.16	0.34	-1.80

Table F8. Catalytic experimental runs for glucose and 2-methoxy-4-methylphenol mixtures at 700oC, S/B ratios of 0.4 and 0.6, reaction times of 5, 10, 20 and 30s.

Date	30/09/09	30/09/09	25/09/09	24/09/09	30/09/09	30/09/09	25/09/09	24/09/09
S/B	0.8				1.0			
Reaction Time (s)	5	10	20	30	5	10	20	30
Mole Fractions (mol%)								
Hydrogen	0.360	0.352	0.432	0.451	0.323	0.372	0.393	0.424
Carbon Monoxide	0.250	0.211	0.208	0.202	0.231	0.223	0.200	0.191
Methane	0.046	0.036	0.035	0.032	0.042	0.038	0.033	0.028
Carbon Dioxide	0.083	0.090	0.128	0.140	0.076	0.091	0.112	0.121
Ethylene	0.001	0.001	0.000	0.000	0.001	0.001	0.001	0.001
Ethane	0.003	0.001	0.000	0.000	0.003	0.002	0.002	0.001
Water	0.257	0.309	0.197	0.176	0.324	0.274	0.259	0.235
Coke wt% (gcoke/gcat)								
Coke wt% (gcoke/gcat)	0.038	0.037	0.036	0.034	0.037	0.036	0.034	0.032
Tar (g)								
Tar (g)	0.006	0.006	0.005	0.004	0.004	0.004	0.004	0.003
Mass Injected (g)								
Mass Injected (g)	0.038	0.037	0.037	0.037	0.38	0.038	0.38	0.038
T _r (°C)								
T _r (°C)	700	700	700	700	700	700	700	700
T _v (°C)								
T _v (°C)	301	305	302	302	303	300	303	301
P _{ri} (psia)								
P _{ri} (psia)	13.64	13.66	13.69	13.68	13.81	13.83	13.87	13.89
P _{rf} (psia)								
P _{rf} (psia)	2.97	2.95	2.96	2.96	2.97	2.96	2.96	2.96
P _{vi} (psia)								
P _{vi} (psia)	4.22	4.15	4.13	4.20	4.25	4.12	4.18	4.27
P _{vf} (psia)								
P _{vf} (psia)	4.08	4.05	4.07	4.08	4.13	4.11	4.13	4.13
MB Closure (%)								
MB Closure (%)	-0.46	1.20	-1.4	-2.33	-2.60	-1.95	-2.24	-5.70

Curriculum Vitae

Name: Enrique Salaices

Post-secondary Education and Degrees: Universidad Autonoma de Zacatecas
Zacatecas, Zacatecas, Mexico
1987-1992 B.Sc.

The University of Western Ontario
London, Ontario, Canada
2006-2010 Ph.D.

Honors and Awards: Council for Science and Technology Scholarship
CONACyT- Mexico
2006-2010

Faculty of Graduate Studies Scholarship
The University of Western Ontario, Canada
2006-2010

Graduate Student Teaching Award
The Society of Graduate Students of The University of
Western Ontario, Canada
2008

Related Work Experience: Research Assistant
The University of Western Ontario, Canada
2006-2010

Teaching Assistant
The University of Western Ontario, Canada
2006-2009

Technological & Scientific Researcher
Electrical Research Institute, Mexico
1993-2006

Scientific Researcher
Electric Power Research Institute, CA, USA
1997-2000

Publications:

Salaices E, Serrano B, de Lasa H. (2010). Biomass Catalytic Steam Gasification: Thermodynamics Analysis and Reaction Experiments in a CREC Riser Simulator. *Industrial & Engineering Chemistry Research*, 49, 6834-6844

Salaices E, Serrano B, de Lasa H. (2010). Biomass Catalytic Steam Gasification: A Kinetics Approach. *Industrial & Engineering Chemistry Research*. Accepted for publication.

Salaices E, Serrano B, de Lasa H. (2010). Catalytic Steam Gasification of Biomass: Catalysts, Thermodynamics and Kinetics. *Chemical Reviews*. Accepted for publication.

Salaices E, Serrano B, de Lasa H. (2010). Biomass Catalytic Steam Gasification: Thermodynamics Analysis and Reaction Experiments in a CREC Riser Simulator. *AIChE's 2010 Annual Meeting, Salt Lake City, USA*. November 7-12, 2010

Salaices E, Serrano B, de Lasa H. (2010). Biomass Catalytic Steam Gasification: Thermodynamics Analysis and Reaction Experiments in a CREC Riser Simulator. Research Bridges Symposium, Sarnia, Canada. May 6, 2010

Salaices E, Serrano B, de Lasa H. (2009). Steam Gasification of Biomass: Parametric Model Analysis. 8th World Congress of Chemical Engineering (WCCE8), Montréal, Canada. August 23–27, 2009

Solis J., Ramos J. C., Salaices E. (1998). Validation of the Laguna Verde RETRAN-03 model for pressurization transients. Nuclear Technology, 121, 237-244.

Morales J. B., Salaices E., Lorenzano F., Torbeck J. E., Healzer J. M. (1997). TRACG sensitivity analysis of the SBWR MSL LOCA to different non-condensable mixing conditions. VIII Congress Mexican Nuclear Society